Cellulose Nanocrystal - Electronically Conducting Polymer Nanocomposites for Supercapacitors

Soon Yee Liew, MEng (Hons)

Thesis submitted for the degree of Doctor of Philosophy

August 2012

Abstract

This thesis describes the use of cellulose nanocrystals for the fabrication of porous nanocomposites with electronic conducting polymers for electrochemical supercapacitor applications. The exceptional strength and negatively charged surface functionalities on cellulose nanocrystals are utilised in these nanocomposites. The negatively charged surface functionalities on cellulose nanocrystals allow their simultaneous incorporation into electropolymerised, positively charged conducting polymer for charge balancing, i.e. co-electrodeposition occurs. The exception is the case of polyaniline-cellulose nanocomposites which formed with uncharged cellulose nanocrystals. As a result, the cellulose nanocrystals form the structural backbone of the nanocomposites in which the mechanical integrity of the nanocomposites becomes significantly improved. In Chapter 1, supercapacitors and the electrode materials are introduced. The equations relating to the characterisation of supercapacitor materials and devices are also introduced in Chapter 1. In the first half of Chapter 2, the basics of electrochemistry and electrochemical methods used in this work are discussed. In the second half, the preparation of the cellulose nanocrystals is reported. Chapters 3 and 4 report the fabrication and characterisation of polypyrrole-cellulose nanocrystal composites with respect to their capacitance, stability and charging characteristics. Chapter 5 discusses the making of the

polypyrrole-cellulose nanocomposites at a practical scale for supercapacitors, and consequently reports the making and testing of a laboratory prototype supercapacitor. Chapter 6 extends the PPy work to other ECPs by the fabrication and characterisation of polyaniline and poly(3,4-ethylenedioxythiophene) nanocomposites with cellulose nanocrystals. Finally, Chapter 7 contains the closing conclusions that I have made for this thesis, and in Chapter 8, I have made some suggestions for future work in this area.

In this project, the materials were characterised using mainly scanning electron microscopy and a range of electrochemical techniques. Specifically, the performance of the polypyrrole-cellulose nanocomposites was compared against that of polypyrrole-carbon nanotube nanocomposites, current state-of-the-art materials for supercapacitor. The performance of all the nanocomposites described in this thesis was also critically compared against that of the best available similar materials in literature, to assess the viability of these materials for applications in supercapacitor devices. Significantly, to the best of my knowledge, this is the first time that the nanocomposites of electronic conducting polymers with non-conducting rod-like nanoparticles fabricated using the co-electrodeposition method were described. The performance of conducting polymer composites was significantly enhanced by the presence of the cellulose nanocrystals as the backbone. This work also proves, for the first time, that conducting polymer composite containing non-conducting nanofillers can also achieve high performance. This is a very interesting finding, compared to previous work reported in the literature for similar materials, such as those developed using carbon nanotubes as the composite filler.

Preface

The work reported in this PhD thesis is the original work of the author and has not been published elsewhere except for the following publication (at the time this thesis is written).

Soon Yee Liew, Wim Thielemans and Darren Walsh, 'Electrochemical Capacitance of Nanocomposite Polypyrrole/Cellulose Films', 2010, Journal of Physical Chemistry C, 114**,** 17926-17933.

Acknowledgements

I like to thank my supervisors, Dr. Wim Thielemans and Dr. Darren Walsh for providing good supervision, guidance and motivation throughout the course of my PhD. It has been my pleasure to work with them, and also the others within their groups for providing a friendly environment to work in and for their help, many times, over the years. Specifically, I owe a lot to Dr. Lee Johnson for providing excellent tutorials on electrochemistry at the earlier stages of my PhD. There were also many interesting discussions among us that I will remember for a long time. Within the groups I work in, I would like to thank Dr. Marianne Labet, Samuel Eyley, Lindy Heath, Shi Hong Lee, Dr. Kevin Lovelock and Andinet Ejigu. Among other colleagues within the department, I also like to thank Dr. Jaouad El Harfi, Hui Deng and Dr. Di Hu for their help in numerous occasions in the past few years.

I like to thank The University of Nottingham's Dean of Engineering International Research Scholarship for 3 years of funding. It is a dream come true for me and I still remember the joy my family and I had when I found out this scholarship was awarded to me. I also like to thank the Department of Inorganic Chemistry for awarding me the Barker prize for the best presentation when I participated in the 3rd year student colloquia. These awards mean a lot to me and could change my life, if not already.

I owe a lot to my parents, Dr. Liew Yin Chai and Dr. Siow Yon Yin, and my brothers, Soon Khong and Justin Soon Jiat. Specifically, I thank my parents for asking a lot out of me (and my brothers of course) since I was

young, although high expectations mean they have also had to work hard to keep the pressure on us. Besides, I learnt a lot from my parents directly because they are simply good examples to follow. Thus I like to take this opportunity to show my appreciation for everything they have provided me with. In that respect, I like to thank my brothers even just for spending time with my parents and taking care of the family during my absence. I also like to thank, and dedicate this thesis to my late grand father, Siow Kwee Jin, who unfortunately passed away a few days after I earned the Barker's prize. I missed a few stories from him about the history of my family, which I heard from my brothers, he delivered every detail with full of passion and a lot of energy. Perhaps, those were the presentation skills that I inherit from him.

Last but not least, I like to thank Hoi Lam Helen Lui, my girlfriend for many years even before I started my PhD project. I cannot imagine coming through these years without her understanding, support and encouragement. May god bless us, I hope we will have a good future.

Other than the people mentioned above, there are many others that I like to thank but I shall do so in person. My success definitely does not belong to myself only, but also to you all. In fact, I am also grateful for having to work until late nights/early mornings in the office in the 4th year, finishing any time between 2-6 am. However, the late nights become easy with the accompaniment of wonderful music by the Girls' Generation, so I like to thank them too. Besides, when I walk home after work I usually get to see beautiful stars, to listen to nature's best melody, and simply enjoy the peace. Surely many others do not 'have', and may not appreciate the chance!!

Contents

Chapter 1. Introduction, background review and project objectives

1.1. Introduction

The ability to store and use energy efficiently has become ever more important. As the world population continues to grow, so does the energy demands required for sustainable socio-economic growth. Modern day energy usage is still highly reliant on fossil fuel burning, either directly for transport, heating and cooking, or for the generation of electricity. The cost of energy has risen steeply as crude oil and gas prices continue to rise. Although the use of renewable energy sources such as solar, wind and hydroelectric has increased over recent years, the technology associated with electricity generation from these energy sources remains expensive. In addition, despite the high and ever increasing cost of energy, the use of energy has been generally inefficient. Typical electricity supply and demand characteristics is an example; while the electricity demand fluctuates over the course of the day, the electricity generation on the contrary is usually fixed and tends to cover the peak in demands. As the demand drops, some energy may be wasted, unless it is stored for later use. Similarly, the utilization of renewable energy sources also poses a problem. Take for example the use of solar power; as electricity generation during the night time is generally not possible but may be surplus during the day. An effective means of utilizing this form of energy would be storing whenever possible for later use.

The above mentioned scenarios highlight the need for energy storage, to act as a buffer between supply and demand, at the large scale. The same is true for smaller scale applications, especially those that are operated with electrical energy and which are required to be mobile. For example, mobile phones, mobile computers (laptops), global positioning system devices (GPS), digital cameras and even electric cars, all require a mobile source of energy. Thus the need for energy storage devices, either stationary or mobile, is inevitable. Among various energy storage devices, supercapacitors are devices that store a relatively large amount of charge which can be rapidly drained and re-charged, thereby giving rise to high energy and power density.[1] Like any other energy storage devices, the performance of a supercapacitor device is strongly dependent on the material from which it is constructed. Electronically conducting polymers (ECPs) are a class of material proposed for the fabrication of supercapacitor devices due to the ease of preparation and relatively low cost. However, there are weaknesses associated with the use of conducting polymers for this application. The more recently emerged field of nanotechnology has very much benefited the construction of higher performance supercapacitors, as researchers can now relate the performance of a supercapacitor material to its structure and morphology. Within this effort, this thesis is concerned with the fabrication and characterization of a novel conducting polymer nanocomposite for supercapacitor devices. In the following section, supercapacitors and conducting polymers, and their composites relevant to supercapacitors are introduced in detail. The fundamentals of capacitance, and power and energy delivered, or stored in a

capacitor, in mathematical forms will also be introduced in this chapter to complement the understanding of the topic.

1.1.1 Supercapacitors

Supercapacitors are most commonly described as devices that fit the gap between conventional batteries and conventional capacitors.[1] Supercapacitors can store considerably large amounts of charge or energy, giving rise to high energy storage density, but in principle operate no different than capacitors. As the charge can be stored and removed rapidly, supercapacitors are capable of delivering high power. Supercapacitors have been known since many years and the first ever supercapacitor patent was dated to 1957, which described the making of a carbon-carbon capacitor.[2] Unfortunately, interest in supercapacitors, either research or commercial, was narrow until the late 1980s when supercapacitors became famous due to interest in hybrid electric vehicles, and has since become a widely studied topic.[2] In the literature, supercapacitors are also widely known as ultracapacitors, electrochemical capacitors, electric double-layer capacitors (EDLC), or electrochemical double-layer capacitors (ECDLC). To avoid confusion and for convenience, the term 'supercapacitor' will be used throughout this thesis. Moreover, the use of the terms EDLC and ECDLC, strictly speaking, refer to a specific type of supercapacitors. It is however unfortunately misused quite often and will be discussed in more detail later. The energy storage density and power delivery capability of various systems are summarized in a Ragone plot shown as Figure 1.1. Typical supercapacitors are capable of storing up to 1 – 10 Wh kg^{-1} of energy and

deliver up to 10^5 W kg^{-1} of power. In comparison, the specific energy contained in conventional capacitors and batteries amount to less than 0.1 and up to a few hundred Wh kg^{-1}, respectively. Likewise, conventional capacitors are capable of delivering up to 10^7 W kg^{-1} of power, whereas batteries have up to about 10^3 W kg^{-1} of specific power capability.

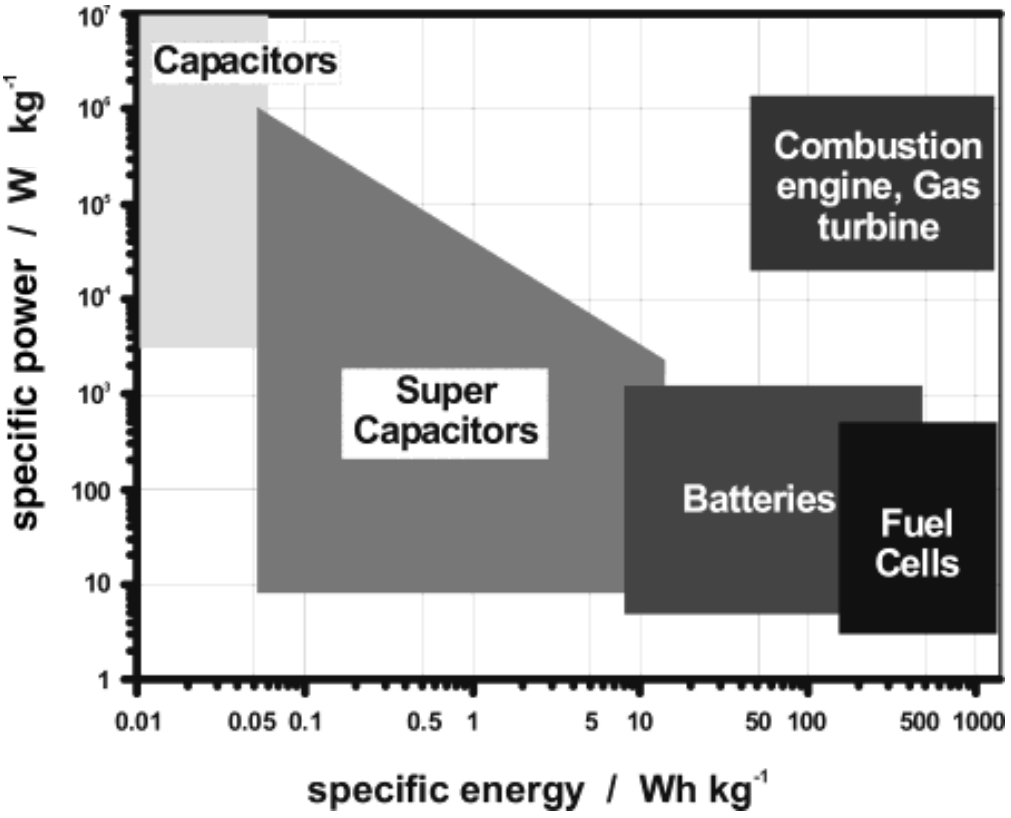

Figure 1.1. Ragone plot of various energy storage and conversion devices. Figure from Winter and Brodd.[3]

The plot area covered by supercapacitors overlaps at both ends with that of capacitors (at the high power, low energy end) and that of batteries (at the high energy, low power end). Fuel cells and internal combustion engines are also included for comparison purposes, but these systems convert energy that

is stored in other forms into electrical energy or mechanical work. For example, the most common fuel cells convert energy stored in the form of chemical bonds, under controlled conditions, while most internal combustion engines utilize the energy stored in chemical bonds of fossil fuel sources such as petrol (or gasoline) and diesel through combustion, which is an uncontrolled oxidation reaction. Strictly speaking, batteries and supercapacitors employing pseudo-capacitance (explained in text below) are also conversion devices as they convert chemical energy via redox reactions that take place at the electrodes. However, both energy storage and conversion occur in the same compartment in the case of batteries and supercapacitors. Therefore, they are closed energy storage and conversion systems. In contrast, fuel cells and internal combustion engines convert energy delivered from outside of the device, and also discharge waste in the process such as water (hydrogen fuel cells) and carbon dioxide (combustion engines), and are thus open energy conversion systems.[3] Notably, the characteristics of internal combustion engines are almost always present in Ragone plots because they have the performance that researchers attempt to match using various other systems. More importantly, the information provided in Ragone plots for supercapacitors and batteries most often only refer to the capability of the active materials. Actual device performance may be quite significantly lower, as in those cases the weight of the electrolyte, current collectors and device housing, need to be considered.

Other than powering electric/hybrid vehicles, there is also wide interests in supercapacitors for applications in mobile and portable devices and as buffers for distributed power generation.[3] It should be noted however, that in

many of these applications, supercapacitors do not function as the sole power source component; more often they are used together with other devices to form hybrid systems. For example, the battery-supercapacitor hybrid,[4] the fuel cell-supercapacitor hybrid,[5] and the fuel cell-battery-supercapacitor hybrid[6,7] have been investigated for use in electric vehicles. The application of supercapacitors in hybrid or electric vehicles is currently an extremely active area for research,[8-10] but these examples also highlight that none of the individual batteries, supercapacitors or fuel cell units could perform up to the required energy and power standards in cars. In these cases, owing to the high power capability of supercapacitors, energy and current is drawn preferentially when the vehicle requires acceleration, while batteries or fuel cell units can be used during constant speed cruising as they store more energy and therefore prolong the drive distance. Supercapacitors have also been used in vehicles for regenerative braking, with braking energy recovery close to 70 %.[5]

A supercapacitor consists of two electrodes with high capacitance and a strong electrolyte. When both electrodes are made of the same material, the device is called a symmetrical supercapacitor. Otherwise the device is called an asymmetrical supercapacitor. In symmetrical supercapacitors, either electrode may be used as the positive electrode or negative electrode. For asymmetrical supercapacitors, the electrode material which operates at the more positive potential region is used as the positive electrode, and the negative electrode is the electrode material which operates at the more negative potential region. Common symmetrical supercapacitors are made of carbon,[11-13] while asymmetrical supercapacitors are usually made of carbon as the negative electrode whereas a wide range of materials are used for the positive

electrode including metal oxides[11,14-16] or electronically conducting polymers (ECPs).[15,17-19] Asymmetrical supercapacitors can also be made of two different metal oxide or two different ECP electrodes.[19-21] The performance of most of the supercapacitors are usually reported as that of a single cell only. However, in application, they can be stacked to achieve a higher operational voltage.[20,22,23]

Energy in supercapacitors is stored either through the double-layer (termed double-layer capacitance), or as the result of a faradaic process (termed pseudo-capacitance, or pseudo-faradaic capacitance), or a combination of both. For double-layer capacitance, charge storage occurs at the interface of a polarisable electrode and an ionic solution. The charging process does not involve electron transfer, i.e. it is a non faradaic charging process, and is ascribed to the effect of ionic and electronic charge separation at the electrode/electrolyte interface when the voltage between the two capacitor electrodes is varied. As the storage of charge in a double-layer is electrostatic in nature, i.e. the opposite charge of the electrode and the ions at a charged interface (cations accumulate at a negatively charged electrode and likewise anions at a positively charge electrode),[24,25] the charging and draining process can take place very rapidly and with high reversibility.[25,26]

In contrast to double-layer capacitance, pseudo-capacitance occurs as a result of an electron transfer process, it is a faradaic process. Unlike double-layer capacitance, which only involves charging the surface of a material, pseudo-capacitance occurs on materials that may be reversibly oxidised and reduced. The redox process can be accompanied by either absorption or expulsion of counterions to maintain electroneutrality. In this

case, the charge can be stored throughout the volume of the pseudo-capacitive material provided there is sufficient electrolyte access for counterion diffusion. However, although the role of the counterions is to maintain electroneutrality of the charged material, the quick faradaic charge transfer process results in concentration or depletion of ions of a particular charge.[25] In this case it is similar to double-layer capacitance, and hence the birth of the term 'pseudo-capacitance'.[25] The cause for pseudo-capacitance occurring on carbon materials is different from those for metal oxides and ECPs. On carbon materials, it is due to the redox active groups on the carbon surfaces, which usually have fixed redox potentials and therefore present current peaks in cyclic voltammograms (CVs). On the contrary, metal oxides and ECPs presents pseudo-capacitance across a broad range of potentials, and the resulting CVs do not have sharp current peaks. Such behaviour for metal oxides and ECPs is explained using the band theory which will be discussed in section 1.1.3.2.

The utilization of the double-layer capacitance of electrode interfaces for storing electrical energy was initiated in the early 1960s from the early work on carbon supercapacitors.[2] Yet, as mentioned above, it was only until the late 1980s and early 1990s, due to the surge in demands and interest in the automobile sector, that commercial interest began to manifest itself for the development of supercapacitors based on the large double-layer capacitance at high surface area carbon electrodes.[2,24,27] The taxonomy of supercapacitor materials is shown in Figure 1.2. The idea of pseudo-capacitance, in comparison, was first introduced in the mid 1970s, but only began to gain considerable attention at the late 1990s.[24,27,28] Earlier examples of

supercapacitors mainly make use of the double-layer effect in porous carbon materials, as they existed before the pseudo-capacitive effect in various materials was understood and utilised. However, researchers have ever since shifted their attention towards pseudo-capacitive materials as mass-specific capacitance can be substantially higher in these materials. That brings back, briefly, the earlier discussion of the use of terms EDLC and ECDLC.

The terms 'supercapacitor', EDLC and ECDLC are very often treated equally, especially for cases where carbon is used as the active electrode material. The word 'double-layer' contained in terms EDLC and ECDLC imply the mechanism of charge storage;[29] whereas the term 'supercapacitor' describes a charge storage device with specific performance criteria with no indication of the charge storage mechanism. Thus describing supercapacitors as EDLC and ECDLC was always correct for earlier generations of supercapacitors, as they employ only the double-layer effect and they meet the 'supercapacitor' performance criteria. However, ever since supercapacitors can also utilize pseudo-capacitance in addition to the double-layer capacitance, these terms are strictly not equal anymore and their use requires caution. In carbon materials, often the pseudo-capacitive effect was introduced to enhance of the gravimetric capacitance, but either the device was still referred to as either EDLC or ECDLC, or the capacitance specifically referred to as double-layer capacitance.[30-37] Moreover, a recent review mentioned ECPs as a type of EDLC materials.[38] Such referencing, in my opinion, is highly inappropriate and may be misleading to the amateur reader, and regrettably, shows a misunderstanding of either the topic or the basics within the scientific community. Nevertheless those mistakes marked just how science was

developed, as terms were only developed after the science and not otherwise. However, as the field of supercapacitor research is not in its infancy anymore, clear boundaries between different terms should be drawn. At present, significantly more has to be done, not only to define different terms that may cause confusion, but also to clarify issues such as characterisation and calculations where many examples of misuse will be shown in later sections for the benefit of the field itself, for future scientists, and to a greater extent, science and humanity.

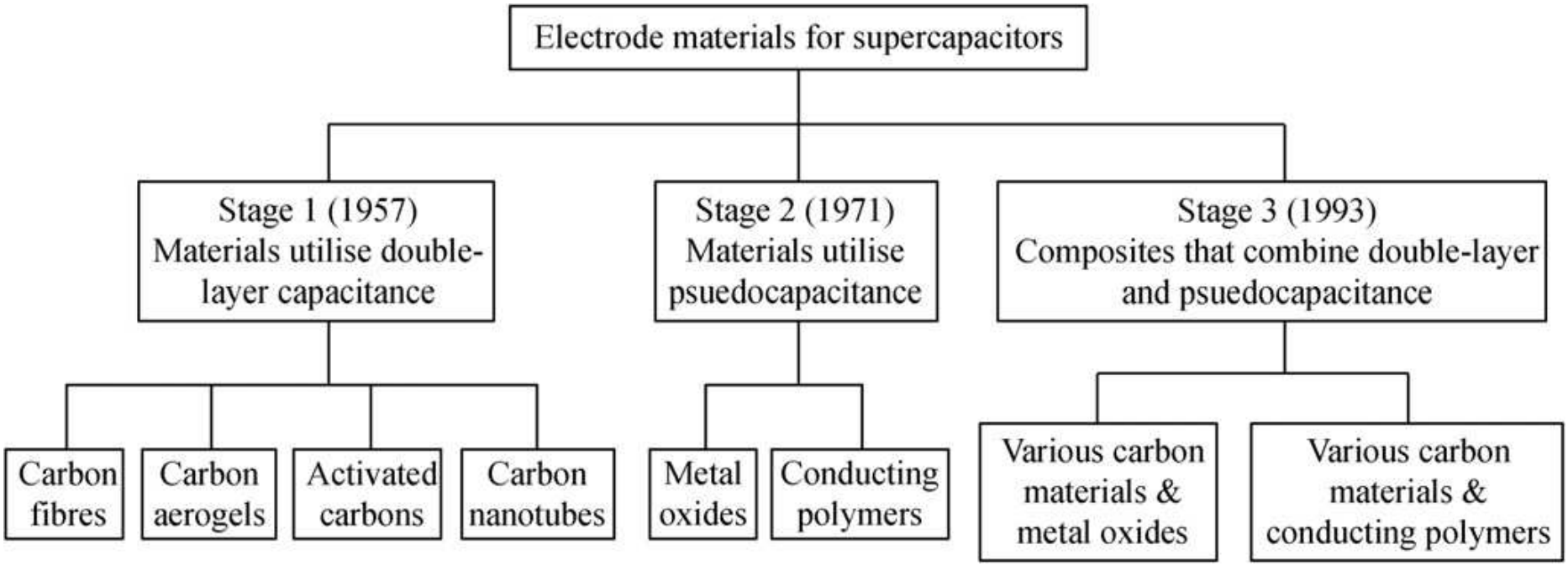

Figure 1.2. Taxonomy of supercapacitor materials. From Peng et al. 2008.[39]

1.1.2 Capacitance, Power and Energy calculations

The equations introduced in this section are those that will be used throughout this thesis for the calculation of capacitance and energy. Other equations which may be less commonly encountered in this thesis will be introduced when appropriate.

1.1.2.1 Capacitance

The capacitance, C, in units of farads (F) is related to charge, Q, in coulombs (C) and voltage, V, in volts (V), or joules per coulomb, by the following equation.

$$C = \frac{dQ}{dV} \tag{1.1}$$

And equally, when the charge and voltage is expressed in time-derivatives,

$$C = \frac{dQ/dt}{dV/dt} \tag{1.2}$$

since dQ/dt, the time derivative of charge is the current, i, in unit of amperes (A), therefore

$$C = \frac{i}{dV/dt} \tag{1.3}$$

where dV/dt is the voltage scan rate, or the potential scan rate. This form of equation is the most commonly used one for the characterisation of capacitive

materials. For example, the CV and galvanostatic methods for capacitive materials would produce results that fit the equation directly. In the case of CVs, i is the capacitive current response of the material for a given dV/dt. For the galvanostatic method, dV/dt is the rate of potential change in response to a set charge/discharge current i. It should be noted that Equation 1.3 also implies that for an ideal capacitor, both i and dV/dt should have constant values giving rise to a rectangular shaped CV and a symmetrical triangular shaped galvanostatic charge/discharge cycle. When the capacitance is divided by the mass of the electrode material, specific capacitance C_{sp} (F g^{-1}) is obtained. Likewise, when i is replaced with mass-specific current i_s (A g^{-1}) in Equation 1.3, the capacitance is also specific to mass. Back calculation can also be performed using the C_{sp} to obtain the response i_s.

Alternatively, for data acquired using electrochemical impedance spectroscopy (EIS), or alternating current (AC) impedance spectroscopy, the following equation is used,

$$C = -\frac{1}{\omega Z''} = -\frac{1}{2\pi f Z''} \tag{1.4}$$

Where ω is the angular frequency of the driving AC potential wave form and the response, f is the frequency in hertz (Hz), and Z'' is the imaginary complex impedance, in ohms (Ω) which is at 90˚ (for an ideal case) phase angle in comparison with the driving AC potential wave form. The simplest derivation for this equation is as follows, by applying a Laplace transformation to the equation

$$i = C\frac{dV}{dt} \tag{1.5}$$

One obtains

$$i(s) = C(sV(s) - V_o) \tag{1.6}$$

Where i(s) and V(s) are the current and the voltage in the Laplace domain, respectively, and V_o is initial voltage. When V_o is 0, the impedance, Z(s) is

$$Z(s) = \frac{V(s)}{i(s)} = \frac{1}{Cs} \tag{1.7}$$

Substituting $s = j\omega$, for a transformation from the Laplace domain to the frequency domain, thus gives

$$C = \frac{1}{j\omega Z} = -\frac{1}{2\pi f Z''} \tag{1.8}$$

The presence of the complex number j in Equation 1.8 implies that the capacitive current response occurs with a +90˚ phase angle ahead of the applied potential wave form. In the simplest explanation, as the AC potential waveform and its time derivation are

$$V = V_o \sin(\omega t) \tag{1.9}$$

$$dV/dt = \omega V_o \cos(\omega t) = \omega V_o \sin(\omega t + \pi/2) \tag{1.10}$$

As

$$i = C\frac{dV}{dt} \tag{1.5}$$

The current is thus

$$i = C\omega V_o \sin(\omega t + \pi/2) \tag{1.11}$$

The + $\pi/2$ in the sine-function is the 90˚ phase angle.

Figure 1.3 shows the results expected from each different characterisation for an ideally capacitive electrode or device. The figure was obtained directly from an excellent review published recently by Snook and co-workers.[40] The equations related to each of the characterisation method are also included in the figure. There is a mistake in the equation written for Figure 1.3c where it says $C = (Z''.2\pi f)$ from the original paper. However, $C = 1/slope$ also written in the figure is correct, as the slope equals -$Z''.2\pi f$ and therefore $C = -1/(Z''.2\pi f)$.

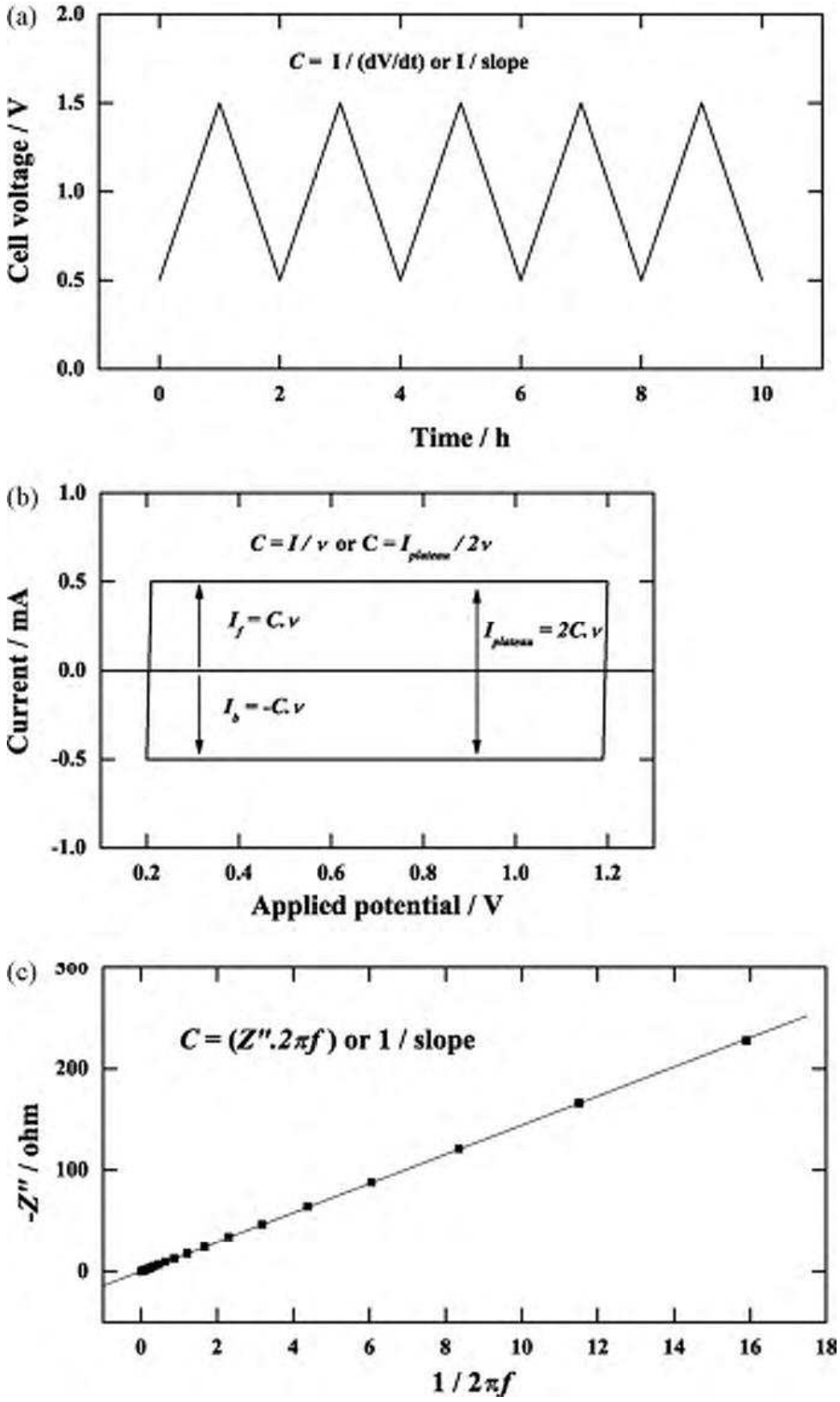

Figure 1.3. Idealised schematic representation showing measurement of capacitance of supercapacitor devices and electrodes from (a) galvanostatic measurements; (b) cyclic voltammetry and (c) imaginary impedance data from EIS. Symbols in this figure C is capacitance (F), I is current (A), v is scan rate (V s^{-1}), *Z''* is imaginary impedance (ohm), f is frequency (Hz). Figure from Snook et al. 2011.[40]

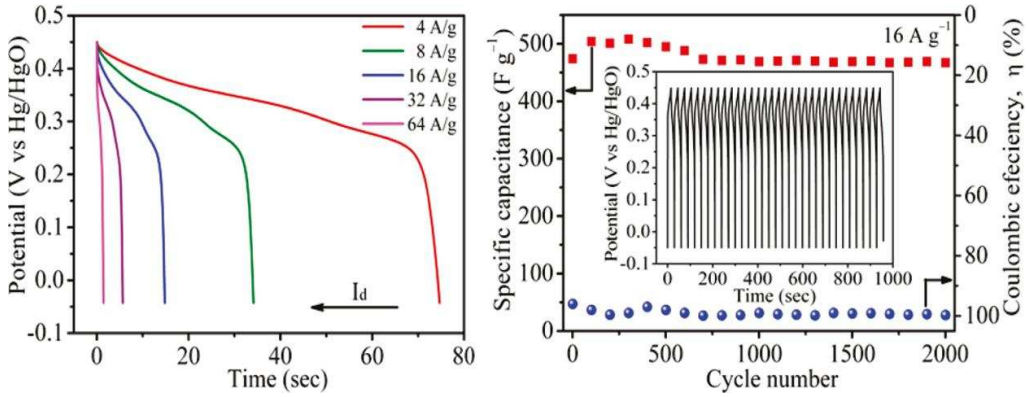

Figure 1.4. (Left) Charge-discharge plots of Co_3O_4 electrode at different current densities. (Right) Specific capacitance and Coulombic efficiency as a function of cycle number. Figure from Meher et al. 2011.[41]

Examples of rather interesting interpretation of electrochemical data for evaluation of capacitance nonetheless occur. For example, Figure 1.4 (left) shows the discharge-time plots of a Co_3O_4 electrode at different current densities. At 8 A g^{-1} discharge current density, a mass specific capacitance of 548 F g^{-1} was reported.[41] The calculation was based upon a potential window of 0.5 V (from -0.05 V to 0.45 V). However, the discharge curve across the potential range was not a straight line. Two different slopes are distinct in the discharge curves, and the potential at which the switch occurs is ca. 0.3 V. In the same study, EIS at bias potential of 0.4 V measured specific capacitance of 900 F g^{-1}; comparing to 100 F g^{-1} at 0.2 V. The observation is rather easily rationalised; at potentials negative of 0.3 V, the Co_3O_4 electrode is significantly less capacitive than at potentials positive of 0.3 V. Thus, the potential range selected for the galvanostatic characterisation of the electrode in that case was inappropriate. More interestingly, the above mentioned case was not an isolated one, similar calculations were presented by Lang et al. in 2011[42] and Yuan et al. in 2009.[43] Remarkably, these examples are

demonstrated only for metal oxide based electrode material. Bizarrely, specific capacitance calculated from CV peak current also seemed to be acceptable.[44] When the peak current is used for the calculation, it would result in a highly overestimated specific capacitance. For any CVs that present peaks, the total charge passed should be employed for specific capacitance calculation.

1.1.2.2 Power and energy

The equation to calculate electrical power, P, in unit watts (W) or joules per second is as follows

$$P = V \times i \tag{1.12}$$

It follows that for constant voltage and current, the energy, W, in joules (J) is a simple integration of P with respect to time. It is noteworthy that the symbol E is also commonly used for energy, however for the case of this thesis it has been used for potential, hence W is used for energy. So:

$$W = \int_0^t P\,dt = \int_0^t Vi\,dt = Vit \tag{1.13}$$

The $W = Vit$ equation can be used only if both V and i are constants, which occurs in batteries but not in capacitors. For capacitors, neither V nor i are constants in the same test but inter-related by Equation 1.5. By substituting the capacitive current into the power expression, one gets

$$P = CV\frac{dV}{dt} \tag{1.14}$$

The time-integral of power would be substituted for a volt-integral, hence

$$W = \int_0^t CV \frac{dV}{dt} dt = \int_0^V CV\, dV = \frac{1}{2} CV^2 \quad (1.15)$$

Alternatively, W can also be derived from the equation

$$C = \frac{Q}{V} \quad (1.1)$$

As $V = dW/dQ$, substituting into the above equation gives

$$C = \frac{Q}{dW} dQ \quad (1.16)$$

By separating the variables and integrating both sides,

$$\int_0^W dW = W = \int_0^Q \frac{Q}{C} dQ = \frac{Q^2}{2C} \quad (1.17)$$

This form of energy equation contains no information on the voltage. By replacing Q= CV, the equation becomes $W = \frac{1}{2} CV^2$. This equation describes the energy stored in a capacitor for a given C and V. When C is normalised to mass, i.e. the total mass specific capacitance, C_{ssp} (F g^{-1}) is used, the specific energy, W_{sp} results, in units of J kg^{-1}, or more commonly expressed in units of Wh kg^{-1}. For the calculation of W_{sp}, C_{ssp} is the capacitance recorded in a two electrode configuration, divided by the sum of both electrodes' mass. In this way, the W_{sp} value reflects that of an operational supercapacitor device. The variation of W_{sp} for devices having different C_{ssp} and different operating voltage is plotted in Figure 1.5.

Traditionally, supercapacitors have a symmetrical configuration, especially those made of carbon materials. The overall capacitance, C_{ov}, can

be calculated, considering two capacitive electrodes connected in series, as follows:

$$\frac{1}{C_{ov}} = \frac{1}{C_1} + \frac{1}{C_2} \tag{1.18}$$

C_1 and C_2 refer to the capacitance values of either of the electrodes that make up the cell. If C_1 equals C_2, usually in the case for symmetrical cells as maximum cell capacitance is to be achieved, then C_{ov} is $C_1/2$. If the mass of each electrode is m, then $C_{ssp} = C_{ov}/2m = C_1/4m$. In this case, C_1/m is the specific capacitance, C_{sp} for characterisation performed in the 3 electrode configuration.

In the 3-electrode configuration, the measured capacitance is expressed in a similar way as C_{ov}. However, the series connection now has the working electrode with a certain capacitance and a counter electrode which only supplies current into the system. In this case, the counter electrode would have supposedly infinite capacitance. Thus the capacitance of the system becomes the following, considering $C_2 = \infty$,

$$\frac{1}{C_{ov}} = \frac{1}{C_1} + \frac{1}{\infty} = \frac{1}{C_1} \tag{1.19}$$

$$C_{ov} = C_1 \tag{1.20}$$

Thus W_{sp} calculation based on C_{sp} for a single electrode resulting from a 3-electrode characterisation, and V the potential window of a material is inappropriate. Nevertheless higher C_{sp} and wider potential window for any materials also imply higher energy storage capability, but in cases of 3-electrode characterisation these values should strictly be reported

independently. There are cases where a symmetrical supercapacitor configuration is assumed when W_{sp} is calculated based on 3-electrode measurements, by assuming $C_{ssp} = C_1/4m = C_{sp}/4$, and V as the potential window for the material. The information provided in this way of calculation is acceptable, as it shows exactly the expected W_{sp} for symmetrical devices based on the material.

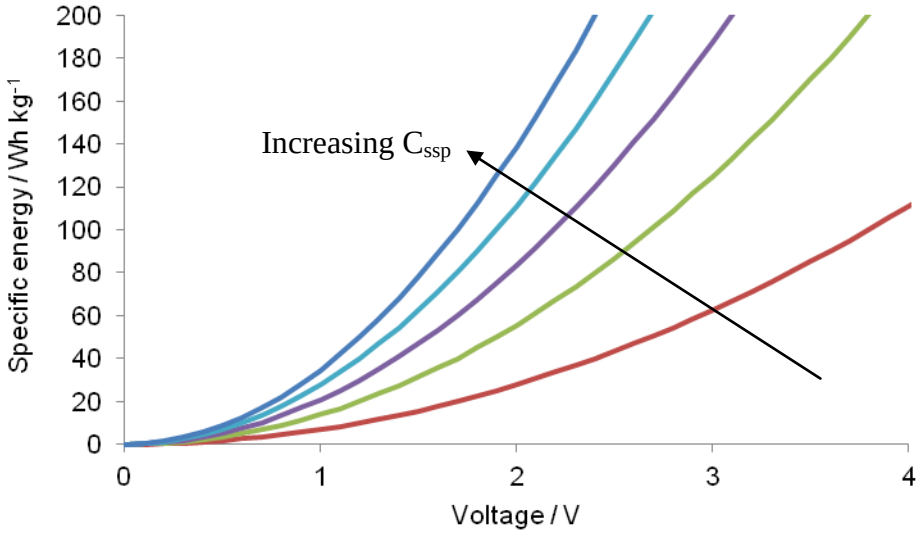

Figure 1.5. Variation of W_{sp} for supercapacitor devices against operating voltages, for cells with different C_{ssp}. The increasing C_{ssp} is indicated with an arrow, starting with bottom line for 50, 100, 150, 200 and 250 F g^{-1}.

Table 1.1 shows some examples of the W_{sp} reported in the literature for supercapacitor devices or electrode materials. The 'Case' column shows how the W_{sp} in each reference was calculated. Case 1 is the most appropriate, as 2-electrode devices are put together and tested in the same way as they would be used in applications. Case 2 is acceptable, as the characterisation indicates the expected W_{sp} if a symmetrical device is assembled. Values reported under

Case 3 can be misleading, but discussions will be provided below. Finally, Case 4 is fundamentally inappropriate, as the W expression does not describe that of a capacitor. Case 5, although the calculation was unclear, showed a bizarrely high specific energy unexpected even by the researchers reporting the work.[45]

In my opinion, Case 3 is inappropriate; justified above considering 2 serially connected capacitors and which 1 of the 2 has, in relative terms, infinite capacitance. However, it is worth mentioning that the reported W_{sp} is nonetheless, in theory, achievable but only under 2 very strict conditions:

(1) the supercapacitor has an asymmetrical configuration, with the second electrode connected in series having the same C_{sp} as the first; (2) the potential range for the second electrode must be at least equally wide, but not overlapping that of the first. In that way $C_{ssp} = C_{sp}/4$, but as the voltage is double now the energy increases by exactly 4 times, in this case the calculation of W_{sp} could result in the same value. It should be very easy to appreciate that such circumstances are extremely difficult to realise.

Table 1.1. Some examples of specific energy reported for supercapacitor devices and materials in the literature.

Supercapacitor/electrode material	Specific Energy reported	case#	Specific Capacitance	Voltage/potential range	Ref.
RuO_2	26.7 Wh kg^{-1}	1	768 F g^{-1}	1 V	23
V_2O_5 nanofibers	78 Wh kg^{-1} ($LiClO^4$ in PC) 5 Wh kg^{-1} (2 M KCl (aq.))	1	250 F g^{-1} 190 F g^{-1}	3 V 0.9 V	46
PPy/graphene	10 Wh kg^{-1}	1	280 F g^{-1}	1 V	47
PANi – Activated carbon	18 Wh kg^{-1}	1	320 F g^{-1}	1.3 V	48
MnO_2/graphene - graphene	11.4 Wh kg^{-1}	1	328 F g^{-1}	1 V	14
Nanoporous carbon	20 Wh kg^{-1}	1	400 F g^{-1}	1.2 V	49
Activated graphene	70 Wh kg^{-1}	1	166 F g^{-1}	3.5 V	50
RuOx/PTFE	17.6 Wh kg^{-1}	2	Ca.500 F g^{-1}	1 V	51
Graphene	28.5 Wh kg^{-1}	3	205 F g^{-1}	1 V	52
PANi Nanowire Arrays	130 Wh kg^{-1}	3		0.7 V	53
MnOx	Ca. 40 Wh kg^{-1}	3	200-400 F g^{-1}	0.9 V	54
PANi/SnO_2	42.4 Wh kg^{-1}	3	Ca. 300 F g^{-1}	1 V	55
Poly(tris(thiophenylphenyl)amine)	42.3 Wh kg^{-1}	3	Ca. 500 F g^{-1}	0.8 V	44
PANi/sulfonated graphene	83 Wh kg^{-1}	3	931 F g^{-1}	0.8 V	56
V_2O_5/CNT	851 Wh kg^{-1}	3	981 F g^{-1}	2.5 V	57
PANi	100 Wh kg^{-1}	4	800 F g^{-1}	0.7 V	58
Graphene	20 Wh kg^{-1}	4*	150-200 F g^{-1}	0.8 V	59
PANi/SWCNT nanocomposite	228 Wh kg^{-1}	4**	485 F g^{-1}	0.7 V	60
PPy	250 Wh kg^{-1}	5	400 F g^{-1}	1 V	45

#Case 1	Reported from 2-electrode testing, specific capacitance = C_{ssp}
Case 2	Reported from 3-electrode testing, but assuming a symmetrical configuration capacitor, i.e. $C_{ssp}=C_{sp}/4$
Case 3	Reported from 3-electrode testing, assuming $C_{ssp}=C_{sp}$. And V = potential range of characterisation
Case 4	Reported from 3-electrode testing, with W=Vit
Case 4* and 4**	*Same as 4, W=Vit however with an averaged V, which was halved the potential range. **Same as 4, but with a mistake at unit conversion from J kg^{-1} to Wh kg^{-1}
Case 5	W calculation was unclear

1.1.3 Supercapacitor materials

The discussions in the previous section have shown the strong dependence of the performance of a supercapacitor device on the material from which it is constructed. As either the double-layer capacitance or pseudo-capacitance could arise from a range of materials, different configurations of a supercapacitor may be required to effectively utilise these materials. Perhaps, the most common materials for the construction of supercapacitors have been mentioned in the above paragraphs and Figure 1.2, i.e. carbon, metal oxides and ECPs. Different electrolyte systems also have crucial effects on the performance of supercapacitors. The use of carbon and metal oxides for supercapacitor construction, and the use of different electrolytes will be discussed briefly in following sections, whereas ECPs will be introduced afterwards in more detail, considering their relevance to the current work.

1.1.3.1 Carbon

Carbon, in its various forms, is the most widely used commercial material for supercapacitors.[2,39,61] In fact, as mentioned above, the first supercapacitor was a carbon-carbon one.[2,3] The reasons for the popularity of carbon materials as supercapacitor electrodes include low cost, high conductivity, high capacitance, good corrosion resistance, high temperature stability, availability and established electrode production technologies.[2,12]

The predominant charge storage mechanism on carbon is through double-layer charging. High surface area pure carbon such as activated carbon, mesoporous carbon, carbon nanotubes and graphene can exhibit high double-layer capacitance, and capacitors built with these pure carbon materials can be called ECDLC or EDLC.[2] When surface functional groups are introduced onto these carbon materials, they give rise to pseudo-capacitance.[2] Surface functional groups are in general present on activated carbons; however the electrochemical response either by double-layer charging or pseudo-capacitance may depend on the electrolyte used.

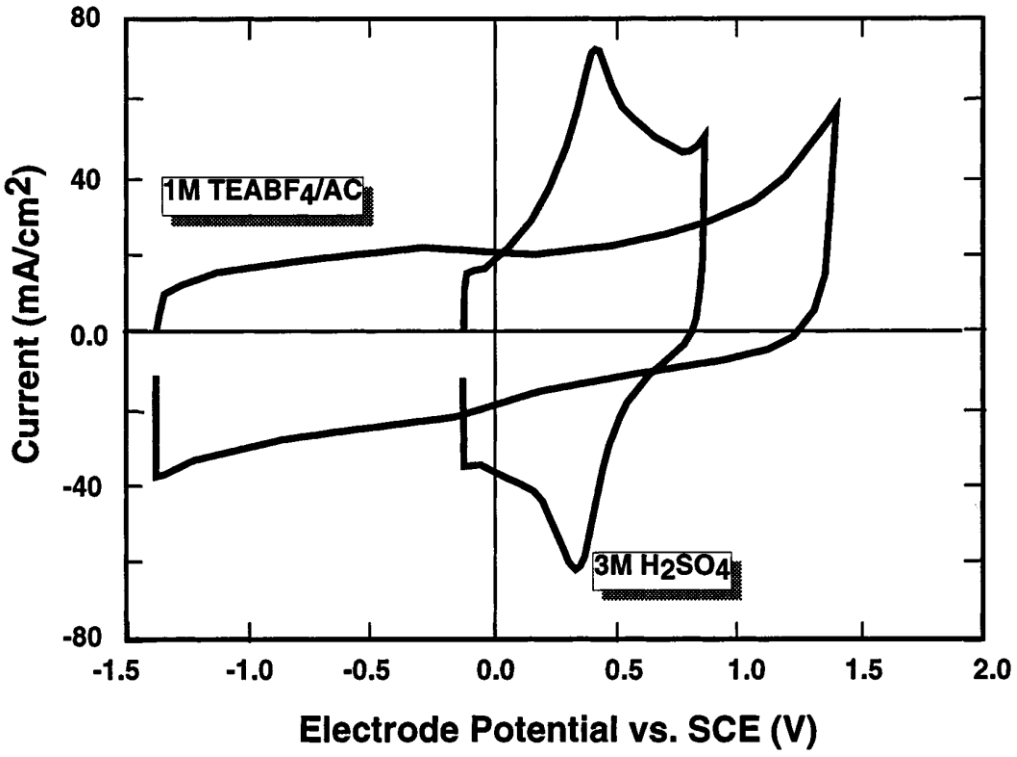

Figure 1.6. Cyclic voltammograms of activated glassy carbon electrodes at 100 mV s^{-1} in 3 M H_2SO_4 and 1 M tetraethylammoniumtetrafluoroborate ($TEABF_4$) in acetonitrile. Both electrodes received the same electrochemical activation. Figure from Kotz and Carlen.[2]

Figure 1.6 shows cyclic voltammograms (CVs) of two electrochemically activated glassy carbon electrodes in aqueous and non-aqueous electrolytes.

The treatment for both electrodes was the same, and thus they should have similar electrochemical behaviour. However, the CV in acetonitrile does not show the redox peaks such as those present in the CV in H_2SO_4. When acetonitrile was used, the CV has a highly rectangular shape, characteristic of double-layer capacitance. The redox peak for the CV in 3 M H_2SO_4 illustrates the contribution from the pseudo-capacitive surface functional groups. The CV also shows that the response was predominantly pseudo-capacitive (consider pure double-layer response as a rectangle that is fitted within that CV, refer to Figure 1.3).[59,62] Hence, a device using this system (activated carbon in H_2SO_4) is strictly not an ECDLC, or EDLC. The redox peak is reduced significantly in organic electrolyte due to the absence of protons.[2] This simple example also shows the difference between the potential window for aqueous and organic electrolytes. The potential window is smaller for aqueous systems (1-1.4 V), whereas organic electrolytes allow a much wider potential window.

Porous carbon materials with high specific capacitance can be obtained through the pyrolysis of various carbon materials such as coal,[63] wood,[64,65] pitch,[13,66] pistachio shells,[67] coconut shells,[68] bamboo,[69] seaweed,[70] rice husks,[34] used coffee beans,[49] or polymers.[32,71-74] The processes used to make them may differ. The most common process for making high surface area carbon involves an alkaline agent-activating process to create the highly porous structure.[63,75] Processes without the activation step are also common, such as those prepared by using various templates, such as zeolites and silicas.[76-78] An alternative process of making porous carbon by using magnesium oxide (MgO) as the substrate ceramic was suggested.[32] The MgO process was proposed in light of the complication of dissolving the zeolite and

silica templates, as the zeolite and silica templating process require use of hazardous hydrofluoric acid[76] in large amounts, whereas the MgO substrate is soluble in less harmful sulphuric acid.[32] Carbonization of organic aerogels to produce mesoporous carbons for supercapacitors has also been reported.[79,80]

The performance of many carbon materials, owing to its predominant double-layer charging effect, is crucially affected by their specific area, surface and pore structure. In brief, a higher surface area exposes more electrode/electrolyte interface it therefore influences the charge storage capability while the pore structure affects the power density. As a result, various studies on the performance of carbon materials for supercapacitors have been focusing on the carbon specific area, surface and pore structure.[32,34,63,74,76,81-83] Notably, the specific capacitance in porous carbon materials may not increase linearly with specific surface area.[34,63,76] A previous study has even suggested that the use of very high surface area carbons (1200 $m^2 g^{-1}$) for the EDLCs were not beneficial.[84] First it needs to be mentioned that higher specific area not only corresponds to more pores in a sample, but also to smaller pores.[76] Next to consider is the principal difference between different measurement techniques. The Brunauer Emmett Teller (BET) method is the most common for surface area determination, which measures equilibrium values. However most, if not all electrochemical measurements are dynamic in nature and as a result, the measured capacitance values can differ quite significantly at different potential scan rates, current loadings, and frequency in EIS measurement.[76] The effect could be rather easily rationalised as follows, and would explain the results in ref. 84 where capacitance did not increase for the higher surface area carbon. During the

measurements, the capacitive responses depend on how fast the electrolyte can respond to the potential perturbation applied to the electrode. Thus, for more efficient access and release of the electrolyte, a larger pore size is preferable, which does not directly translate to higher total specific area. As expected, when characterised using low frequency measurements, the materials of higher specific area always achieve higher specific capacitance.[32,76] All the capacitance values measured in ref. 84 were however, performed at the same scan rate, and it was likely that the scan rate favoured the materials with larger pore size. It has been shown that the mesopore size range, between 3 nm to several tens of nanometres allowed most efficient charging at high current density (also high scan rate, high frequency). Smaller pore size which contributed to higher specific area however, may not be accessible to electrolyte within a short time frame as they posed increased length for ion diffusion.[32,34,76] The case is different if a low current loading is employed. As more time is given for the electrolyte to travel into smaller pores, the system may approximate equilibrium, which explains the correlation between low frequency capacitance with the BET surface area.[32,76,82] Thus carbon materials with more of larger pores are more suitable for high power supercapacitor applications because charge can be stored and removed faster, giving rise to higher power, although they stores less energy.[82]

Even though charge storage on carbon materials occurs typically through the double-layer, pseudo-capacitance is often introduced to enhance their capacitive performance. The origin of pseudo-capacitance on carbon materials may be the oxidation/reduction of surface quinoidal[33,71] or carbonyl[71] groups.

These groups are also some times collectively called 'oxygen groups'.[71] The proposed reactions on these surface groups are depicted as follows:[77]

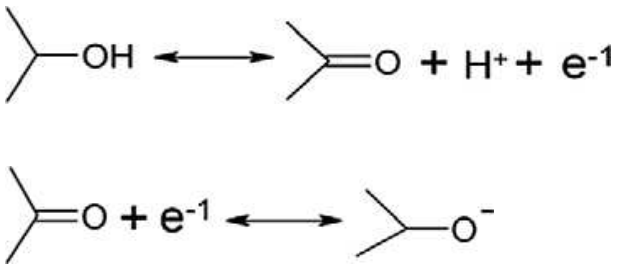

Scheme 1. Proposed reaction on carbon surface groups.[77]

The proposed reaction explains the absence of pseudo-capacitive effect when organic electrolyte is used as there are no protons, and it is also significantly reduced if basic media are used.[2,85] Notably, the presence of various oxygen functional groups can also enhance the carbon surface wettability which also favours better capacitive performance.[39,63,71,77] However pseudo-capacitance should not be confused with surface chemistry; as pseudo-capacitance has to arise, strictly, from electron transfer reactions whereas some surface chemistry may result in increasing capacitance by giving better compatibility with the electrolyte, and consequently higher double-layer capacitance.[79] Therefore the introduction of oxygen functional groups may increase the capacitance arising from both pseudo-capacitance and improved wettability.[39,63,71] Pseudo-capacitive reactions other than the above shown quinone/hydroquinone type can also be activated by base oxygen species in the high pH range.[31] In basic media, the pseudo-capacitive effect is ascribed to pyrone functionalities.[31] There are many ways to introduce surface oxygen

functional groups onto carbon materials. In fact, they are generally present in activated carbon prepared through the alkaline-activation process.[63,85] By using seaweed as the carbon precursor, the as-pyrolysed porous carbon already contained a high amount of oxygenated surface functionalities and did not require an activation process.[70] Recently, it became recognised that nitrogen-containing carbon materials may also contribute to a high pseudo-capacitance.[68,72,73,86] The nitrogen species responsible for the faradaic reactions are pyridinic and pyrrolic nitrogen.[68]

The pseudo-capacitive effect on carbon materials however, is not limited to surface groups on carbon surfaces. A recent report showed that the total capacitance on high surface carbon was enhanced by grafting electroactive anthraquinone groups.[62] Pseudo-capacitive charge storage based on redox active mediators as the electrolyte has also been proposed.[87] $Fe(CN)_6^{4-}$ was used as the electrolyte which participated during the double-layer charging of the porous carbon. Once adsorbed, the electron transfer that takes place on the mediator contributes to pseudo-capacitance.[87]

Carbon nanotubes (CNTs)[33,88] and graphene[14,52,89-92] are different forms of carbon widely studied as electrode materials in supercapacitors. There are different ways of making pristine CNTs and graphene; they are however beyond the scope of this discussion. In comparison to porous carbon, the advantage of using CNTs is that they form a more open porous structure for electrolyte transport.[93] Pristine CNTs usually have lower capacitance due to lower specific surface area (hundreds of $m^2\ g^{-1}$) in comparison with porous carbons (>1000 $m^2\ g^{-1}$), and are usually modified before use as the electrode.[37,93-95] In comparison, graphene has a marked advantage in high

surface area (a single graphene sheet has 2630 $m^2 g^{-1}$ of surface area) and high conductivity.[96] The development of CNTs and graphene for supercapacitor applications are generally not different than those for porous carbon and thus will not be mentioned further.

To briefly conclude, the capacity of pseudo-capacitance based carbon materials is generally greater than those based on pure double-layer capacitance. It has been suggested that faradaic reactions cause phase changes within the electrode and may cause shorter life time in those materials, and generally slower charge/discharge resulting in a lower power density.[96] Contradicting suggestions also exist. For example, nitrogen-containing carbon showed enhanced capacitance particularly at higher current loading (high power density),[68] and frequency response of oxygen functionalised carbon fiber was superior compared to unmodified ones.[97] There was also suggestion that oxygenated groups on the carbon surface are stable, at least up to 10000 cycles.[32,72]

Carbon will continue to be studied, and used as the electrode material for supercapacitors due to the many reasons mentioned earlier, and especially encouraged by the interest of using renewable materials, such as bamboo and seaweed, and also waste product such as rice husks and used coffee beans. New discoveries are still being made all the time, such as the case for the seaweed derived porous carbons which are naturally rich in oxygen functionalities without the need for further activation.[70] A wider potential range, translating to higher operational voltage was also achieved in cases employing aqueous systems as a result of better understanding on the role of surface functionalities on carbon materials.[70] Utilizing pseudo-capacitance

based on redox active electrolyte was also encouraging.[87] However, the evaluation of the specific capacitance may be questionable as mass of the 'active' material in those cases should include the mass of the redox active electrolyte.[87] Moreover redox active mediators are usually expensive, and therefore the 'cost per unit capacitance' in those devices may be less attractive.[87] Advances in new materials such as graphene would certainly benefit the field, as the potential of such materials are not fully understood yet at present, and 'much more is expected from this revolutionising material within the near future'.[98,99] Details of some of the carbon materials reported for use as supercapacitor materials are shown in Table 1.2.

Other than being used directly as the electrode material in supercapacitors, carbon materials are also widely used to form composite materials with metal oxides and ECPs to form very high capacitance materials. These discussions will follow in the sections for metal oxides and ECP composites.

Table 1.2. Specific capacitances of a selection of carbon materials in the literature. Electrolytes are aqueous based unless otherwise stated.

Year reported	Material	Electrolyte	Capacitance (F g^{-1})	Comments / Notes	Scan rate/ current load	Ref.
1993	Carbon foam	4 M KOH	≈ 40	Derived from organic aerogel, the device was also called 'aerocapacitor'		80
2001	Porous carbon	1 M H_2SO_4	199	Porous carbon prepared from defluorination of PTFE with lithium metal	40 mA g^{-1}	74
2002	Activated Carbon fabrics	1 M H_2SO_4	120-150	Suggested mechanism/reaction for pseudo-capacitance on Carbon	ca. 100 mA g^{-1}	71
2002	SWCNT	1 M $LiClO_4$ in propylene carbonate	60		10 mA g^{-1}	95
2003	Activated Carbon	1 M $LiClO_4$ in propylene carbonate	220		40 mA g^{-1}	63
2004	Integrated CNTs	6 M KOH	207	CNTs directly grown on ammonia etched nickel substrates	1 V s^{-1}	100
2004	Activated carbon	0.5 M H_2SO_4	142	Carbon from wood	≈ 2.5 A g^{-1}	65
2005	Carbon aerogels	1.5 M Et_3MeNBF_4	>100	Pyrolysis was performed in CO_2 for the carbon activation	>48 mA cm^{-2}	79
2005	MWCNTs	1 M H_2SO_4	335	Acid treated		33
2006	Mesoporous carbon	30 wt% KOH	160-210	Higher surface area in pores larger than 3 nm Good high frequency response	50 mV s-1 (ca. 10 A g^{-1})	76
2006	Porous carbons	1 M H_2SO_4	210	Specific area = 1500 – 2000 m^2/g Porous carbon prepared without stabilisation and activation process.	1 A g^{-1}	32
2006	MWCNTs	1 M Et_4NBF_4 in propylene carbonate	28	MWCNTs were mass produced		94
2007	Activated carbon	0.5 M H_2SO_4 1 M $NaNO_3$	122 81	Prepared from pistachio shell	25 mV s^{-1}	67
2008	Porous carbon	1 M H_2SO_4	368	Derived from waste coffee beans treated with $ZnCl_2$	50 mA g^{-1}	49
2008	Graphene	5.5 M KOH Et_4NBF_4 in	135 99		1.333 A g^{-1}	96

Table 1.2. Specific capacitances of carbon materials.

		acetonitrile				
2009	Porous carbon	Et_4NBF_4 in acetonitrile	146	Carbon was prepared by chemical vapour deposition on template	250 mA g^{-1}	78
2009	Graphene	30 wt% KOH	205		100 mA g^{-1}	52
2010	Porous carbon	1 M H_2SO_4 6 M KOH 0.5 M Na_2SO_4	255 201 125	Carbon derived from seaweed, without activation process High operating voltage in aqueous systems	200 mA g^{-1}	70
2010	Activated carbon	6 M KOH	235; 160	Prepared from polyaniline, extremely stable after cycling for 10000 times	1 A g^{-1}; 11 A g^{-1}	72
2011	Activated carbon nanospheres	0.5 M H_2SO_4	240	Prepared from polypyrrole, by KOH activation Stable for 3000 cycles	100 mV s^{-1}	73
2011	Mesoporous carbon spheres	2 M H_2SO_4 Et_4NBF_4 in propylene carbonate	208;146 97		500 mA g^{-1}; 30A g^{-1} 500 mA g^{-1}	77
2011	Activated carbon	0.1 M $K_4Fe(CN)_6$	272		250 mA g^{-1}	87
2011	CNT	1 M H_2SO_4	47	Nitrogen-containing CNTs	500 mA g^{-1}	88
2011	Reduced graphene oxide	6 M KOH	41.5	Measurement performed using 2 electrode cell	100 mA g^{-1}	91
2011	Activated Graphene	Ionic liquid/acetonitrilc mixture	166		5.7 A g^{-1}	50
2011	Porous carbons	1 M Et_4NBF_4 in acetonitrile	≈200	Hydrothermal carbonization was performed to obtain the carbon	1 A g^{-1}	64
2011	Graphene	1 M H_2SO_4	276		100 mA g^{-1}	59
2011	Graphene oxide-MWCNT MWCNT Graphene oxide	1 M H_2SO_4	251 85 60			101

1.1.3.2 Metal Oxides

Many metals such as ruthenium,[102,103] cobalt,[41,42,104-106] nickel,[43,104,107-110] manganese,[20,22,111] tungsten,[103,112,113] iron,[21,114] titanium,[115,116] tin,[20,55,117,118] and vanadium[46,57,119,120] have either oxides or hydroxides which may be conducting or semiconducting and exhibit a large capacitance, ascribed to the pseudo-capacitance effect. They form the metal oxides family of materials for supercapacitor applications. They are desirable because of the possibility of providing higher energy density supercapacitors than carbon based-ones, and better stability than ECP-based supercapacitors.[121] Usually, supercapacitors using metal oxides have an asymmetrical configuration.[1,108,113] In this section, the performance of ruthenium and manganese based supercapacitor materials will be reviewed in detail, as they are the most common systems. Nevertheless, the challenges posed by utilizing other types of metal oxides or hydroxides as supercapacitor materials are somewhat similar to that of either ruthenium and/or manganese based systems.[121]

Figure 1.7 depicts a cyclic voltammogram showing the multiple redox reaction for manganese dioxide (MnO_2) related to the oxidation from Mn(III) to Mn(IV), taking place over a 0.9 V potential range.[1] This example highlights a requirement for metal oxides in supercapacitor applications; they have to co-exist between two or more oxidation states without irreversible phase change.[121] As each of the multiple redox reactions plays a part in the overall charge transfer over the wide window, the transition between multiple oxidation states for these materials is continuous.[102] An alternative

explanation of the pseudo-capacitive effect on metal oxides was also offered in two recent reviews, described in the view of the band theory.[122,123]

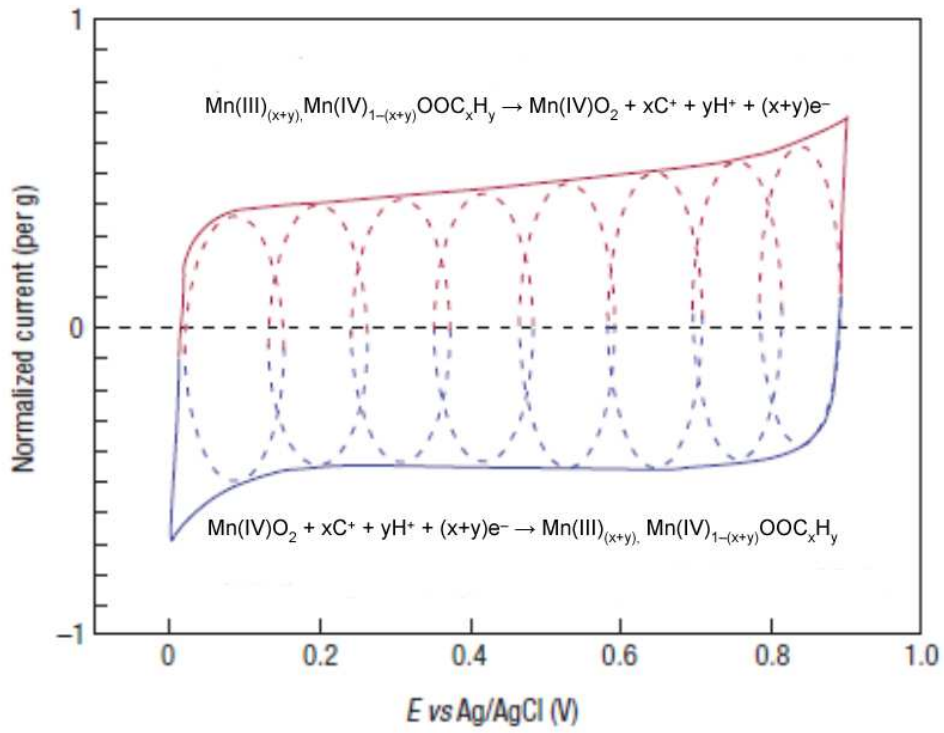

Figure 1.7. Cyclic voltammetry for a MnO_2 electrode cell in 0.1 M K_2SO_4 showing the successive multiple redox reactions leading to the pseudo-capacitive charge storage mechanism. From Simon and Gogotsi.[1]

Figure 1.8 shows the distribution of energy states in three different classes of materials: conductors (metals), semiconductors and insulators. The complete overlap of electron energy states for metals allows free electron mobility in response to an electric field, thus charge storage at any fixed energy state is impossible as electrons are free to move.[122,123] At the other extreme, charges in insulators are localised, as there is no electron transfer between neighbouring sites. Thus, the energy levels of the filled and vacant states are singular, resulting a fixed potential for electron transfer.[122-124] In the

case for semiconductors, such as metal oxides, or ECPs, when the applied potential is sufficient, the localised electrons are excited into, and become delocalised in the conduction band. As the electrons become delocalised, they do so among redox sites which are in close vicinity of each other. As these redox sites also interact with each other, they give rise to a broad range of energy states (or a band of energy states) with very small differences between neighbouring energy states. The consequence of this whole process is the observed pseudo-capacitive behaviour.[122,123] The absence of irreversible phase change allows the process to be repeated.[121] The near constant current response of these materials towards a linearly increasing potential occurs because electron transfer into each energy state in the conduction band is continuous over a range of potentials, i.e. electron transfer proceeds in the same manner with changing potential.[122,123] As a result, rectangular CVs are observed for many metal oxides and conducting polymers.[122]

The main disadvantage of pure metal oxide materials for use in supercapacitor electrodes is the low conductivity. The poor conductivity of these metal oxide materials limits the loading on electrodes, and as a result the attainable electrode capacitance. The situation is improved by forming composite materials with conducting materials such as carbon.[11,102,122] It is also noteworthy that for all cases of metal oxide materials, higher specific surface area is preferred. Although the charge storage is pseudo-capacitive in nature, high surface area gives more accessible redox active sites, as a result of exposure of more metal centres and also a shortened diffusion distance.[121]

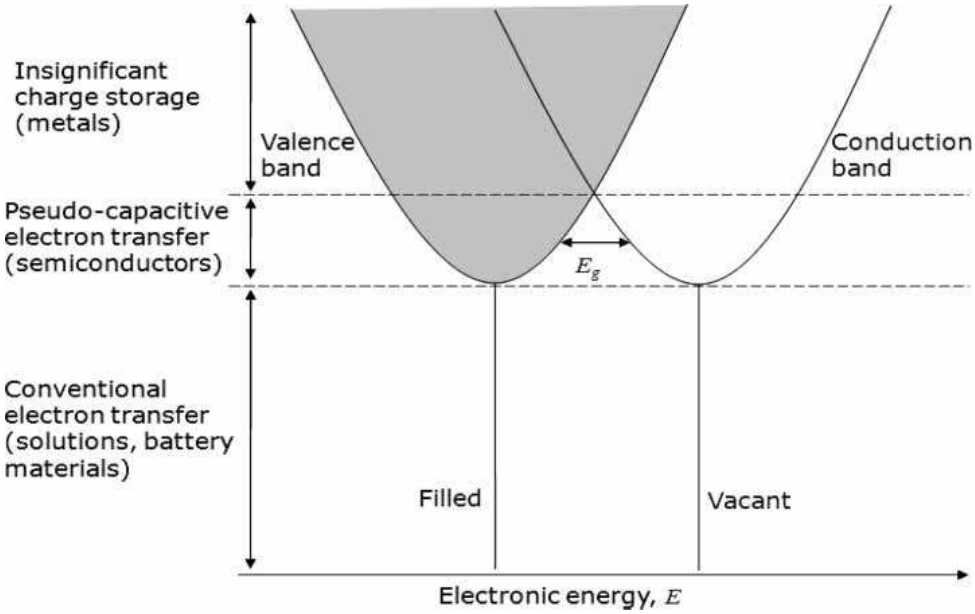

Figure 1.8. Illustration of band theory for different materials. Figure from Chae et al.[123]

1.1.3.2.1 Ruthenium oxide (RuO_2)

RuO_2 is the material most popular in the supercapacitor field due to its high capacitance. For example, amorphous RuO_2 was reported to have specific capacitance values of 720,[103] 900,[125] 954,[126] and 1300 F g^{-1}.[127] The values differ due to the different characterisation methods and the loading of the electrode material. A recent review highlighted the main factors affecting the performance of RuO_2 as a supercapacitor material.[121] Other than the specific surface area of RuO_2 materials, the extent of hydration and crystallinity are critical for their performance.[121] Briefly, de-hydrated RuO_2 has poor capacitance due to the inability to conduct protons/cations. As the pseudo-capacitive reaction on RuO_2 is the following,

$$RuO_2 + xH^+ + xe^- \leftrightarrow RuO_{2-x}(OH)_x \quad (1.24)$$

the capacitance will suffer if proton conduction is poor. For example, hydrous RuO_2 has a high capacitance of 900 F g^{-1} while anhydrous RuO_2 has a capacitance of 0.75 F g^{-1}.[125] The close relationship between the capacitance of RuO_2 materials and their crystallinity also arises from the same effect. Generally, a crystalline structure poses difficulty to expand or contract, thus preventing protons/cations from permeating the bulk material, leading to diffusion limitations.[121,128] As expected, the amorphous structure allows the bulk to participate in the redox reaction, thus providing far superior performance.[128] However, a recent study revealed that crystalline RuO_2 too, has a high capacitance of 950 F g^{-1}.[126] The hydrous RuO_2 nanocrystallites were prepared by templating using hexagonal self-ordered mesoporous SiO_2.[126] The results showed that crystalline RuO_2 can also have superior charge transfer due to the coexistance of smooth proton exchange pathways and good electronic conductivity.[126] Arrays of crystalline RuO_2 electrodeposited into an anodic aluminium oxide template also exhibited a high capacitance of 1300 F g^{-1}.[127] The extraordinary performance is ascribed to the combination of morphology, hydrous nature and metallic conductivity.[127] A high energy and power density supercapacitor stack of 5 cells, built with hydrous RuO_2 mixed with 20 wt% carbon delivered 634 F g^{-1} of capacitance, and was stable over 60000 cycles.[23]

1.1.3.2.2 Manganese oxide (MnO_x)

MnO_x is another widely studied supercapacitor electrode material due to its abundance, environmentally friendliness and high theoretical specific

capacitance up to 1300 F g^{-1}.[121,122,129] The capacitance of MnO_x, like RuO_2, is ascribed to pseudo-capacitance (Figure 1.7), between the Mn(III) and Mn(IV) states.[1,20]

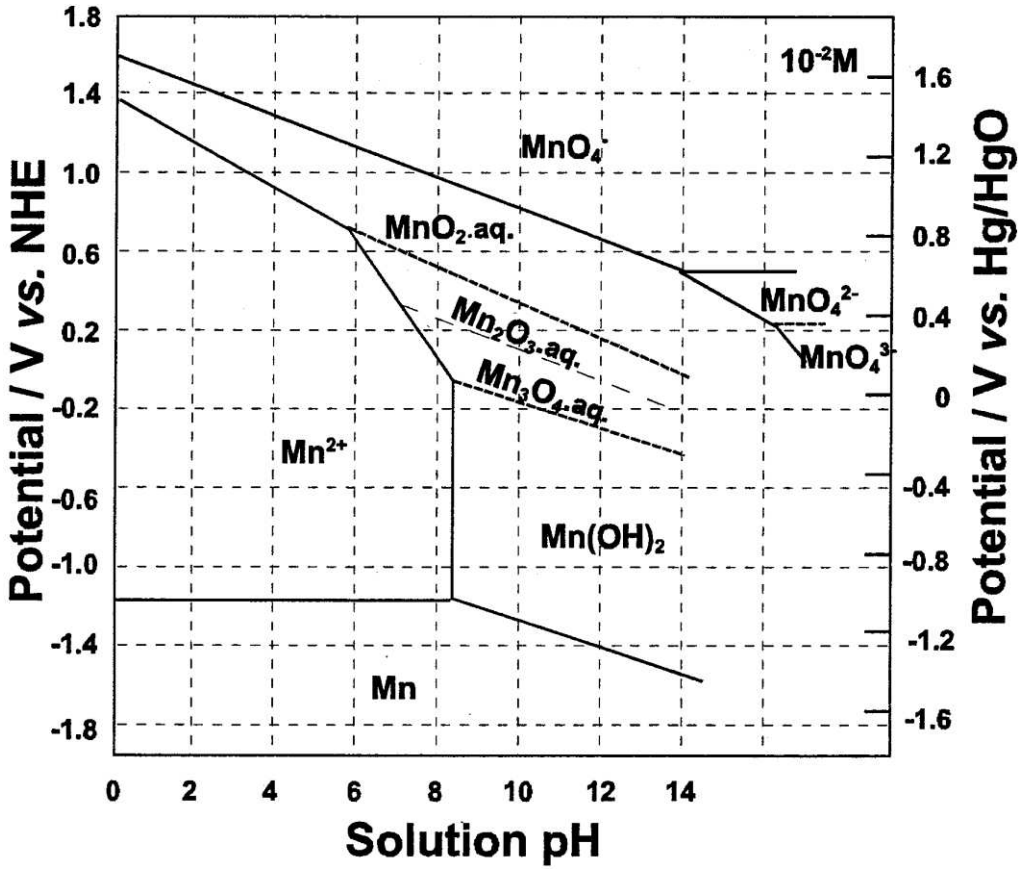

Figure 1.9. Potential pH diagram of manganese in aqueous medium at 25˚C. Figure from Messaoudi 2001.[129]

Figure 1.9 shows the potential-pH diagram of manganese in aqueous medium, which shows the different phases for manganese species at different oxidation states and different pH. The phase behaviour of manganese oxides has a significant consequence on their application in supercapacitors. As Mn(II) and Mn(VII) are soluble in aqueous solutions, they must be avoided as

they lead to partial dissolution of the electrode and a loss in capacitance.[122] The formation of Mn(II) can be prevented by avoiding acidic electrolyte, while the formation of Mn(VII) requires control by electrochemical means. At any pH, the potential at which Mn(VII) forms is the positive potential limit for operation without incurring the dissolution of the electrode.[122,130] The conductivity of MnO_x also changes with pH. Under neutral conditions, MnO_2 is in the semiconducting state and exhibits near ideal pseudo-capacitive behaviour. Thus, most MnO_2-based supercapacitors have neutral aqueous electrolyte, such as KCl or K_2SO_4. At high pH conditions, MnO_2 is reduced to $Mn(OH)_2$ which is a poor conductor.[131] As a result the response of manganese in alkaline solutions resembles battery-like systems.[129] Several other factors that affect the capacitance performance of MnO_x have been highlighted in a recent review.[121] Like RuO_2, the performance of MnO_x is highly dependent on its crystallinity and morphology. Briefly, all these factors affect the cation or proton transport which complements the pseudo-capacitive reaction on MnO_x and this is similar to the case for RuO_2.[121,122]

The main challenge posed by using MnO_2 as the electrode material for supercapacitors is the loading, due to poor electrical conductivity of MnO_2. As a result, the specific capacitance decreases when thicker films of MnO_2 are prepared. For example, at an electrode loading of 50 μg cm^{-2}, a specific capacitance of 400 F g^{-1} was recorded.[54] This value dropped to 177 F g^{-1} when the loading was increased to 200 μg cm^{-2}.[54] For a very thin layer (less than 2 μm thick) of MnO_2, a specific capacitance of 1380 F g^{-1} was reported.[132] In general, specific capacitance values of around 200-300 F g^{-1} were most commonly reported in the literature due to higher electrode loading.[133,134]

1.1.3.2.3 Ruthenium and manganese oxide composites

The main disadvantage of RuO_2 is the rarity of ruthenium and consequently the high cost of the material.[135] This issue is usually addressed by forming composite electrodes with other materials, such as carbon,[102,136-138] ECPs,[139-142] or other metal oxides.[103,143] Moreover, as the electrode loading of RuO_2 is increased, the gravimetric capacitance decreases due to significantly smaller specific surface area.[144] Such findings imply that when smaller amounts of RuO_2 are used, they become more effective, and clearly make the case for composite electrodes. For example, at 35 Ru wt% in a RuO_2 carbon aerogel composite, a specific capacitance >200 F g^{-1} was achieved.[137] Amorphous tungsten oxide/ruthenium oxide with a tungsten content of 50 wt% displayed a specific capacitance of around 560 F g^{-1}.[103] At 60 wt% of RuO_2 in a RuO_2-carbon black composite, the specific capacitance achieved was 647 F g^{-1}, corresponding to 988 F g^{-1} contributed by RuO_2 in the composite.[145] More recently, a RuO_2-carbon nanofibre composite electrode, of 33 wt% Ru displayed a specific capacitance of 1017 F g^{-1} for the RuO_2 portions.[136]

The issue of poor conductivity on MnO_2 is overcome by making composites of MnO_2 with highly conductive supports such as carbon and ECPs.[20,22,111,146-148] Carbon, in various forms, is the most popular conducting material used for the fabrication of manganese oxide composites. As an example, a Mn_2O_3-carbon nanocomposite electrode recorded a total specific capacitance of 160 F g^{-1}.[146] However, the capacitance utilization of Mn_2O_3 in the composite was very effective, up to 600 F g^{-1}.[146] Carbon-supported MnO_2 nanorods showed specific capacitance values of 165 F g^{-1} and the contribution

of MnO_2 was 458 F g^{-1}.[149] The composite electrode gave a highly reversible performance for up to 10000 potential cycles.[149]

CNTs are widely used for making MnO_x composites due to the high conductivity, the consistency of the composite, and the formation of an open porous structure for enhanced electrolyte accessibility.[122] A MnO_2-activated CNT composite which showed specific capacitance of 250 F g^{-1} also had an enhanced cycle performance as the CNTs were able to alleviate the stress on the MnO_2 caused by the potential cycling.[150] When MnO_2 was electrodeposited into a 'forest' of vertically aligned CNTs, the resulting vertically aligned MnO_2-CNT composite achieved a gravimetric capacitance of 642 F g^{-1}.[151] Similarly, graphene is commonly used for making MnO_2 composites due to the high conductivity and high surface area.[152] For example, a graphene-MnO_2 composite of 78 wt% MnO_2 displayed a specific capacitance of 310 F g^{-1} at a scan rate of 5 mV s^{-1},[152] and an electrodeposited MnO_2 on graphene had a specific capacitance of 328 F g^{-1}.[14]

Other than composites with carbon materials, mixed metal oxides of MnO_2 with other metal oxides are also common. For instance, manganese-cobalt (Mn-Co) oxide,[153,154] manganese-nickel (Mn-Ni) oxide,[154] and Mn-Ni oxide-CNTs[155] composites have been prepared. Generally, these composites exhibited not only high capacitance, but also a good cycling performance.[154]

In short, metal oxides are attractive for supercapacitor applications due to the high mass specific capacitance. However, the high mass specific capacitance values are largely limited to very thin films only, due to the

resistivity of these materials at high loading. High accessible surface area for the electrolyte is also required for good performance. When thicker electrode materials are tested, the electrolyte diffusion limits the pseudo-capacitive reaction at the interfacial surface whereas the underlying materials are non-responsive. The development of nanostructured metal oxides, or metal oxide nanocomposites overcomes this problem by allowing a more effective utilization of the metal oxide portions. However, the over-emphasis on the utilization of the metal oxide component within a composite can be misleading. The specific capacitance values normalised to the metal oxide component within the composite may be inappropriate, as the composite performance is the result of the combination of multiple components. Details of some of the metal oxide materials reported for use as supercapacitor materials are shown in Table 1.3.

Table 1.3. Specific capacitances of a selection of metal oxide and metal oxide composite materials in the literature. Electrolytes are aqueous based unless otherwise stated.

Year reported	Material	Electrolyte	Capacitance (F g^{-1})	Comments / Notes	Scan rate/ current load	Ref.
1995	Amorphous RuO_2	0.5 M H_2SO_4	720	Capacitance stable over 4000 cycles	1.14-2 A g^{-1}	128
1996	RuO_2-carbon	39 wt% H_2SO_4	634	RuO_2:Carbon = 8:2		23
1999	Amorphous, hydrated RuO_2	0.5 M H_2SO_4	900		≈ 1 A g^{-1}	125
2001	50% tungsten oxide: ruthenium oxide Amorphous ruthenium oxide	10 M H_2SO_4	560 720		50 mA g^{-1}	103
2003	MnO_2	2 M KCl	240	Prepared by electrochemical deposition on carbon substrate	1.2 A g^{-1}	134
2003	MnO_2 Fe_3O_4	0.1 M K_2SO_4	150 75	A supercapacitor was fabricated with the MnO_2 as the anode and Fe_3O_4 as the anode	1.5 A g^{-1} 0.75 A g^{-1}	21
2004	Mn-Ni oxide Mn-Co oxide	1 M Na_2SO_4	685 560	Electrode prepared by electrodeposition	≈4 A g^{-1}	
2004	SnO_2	0.1 M Na_2SO_4	285 101	Electrode loading was 0.28 mg cm^{-2}	2.85 A g^{-1} 20.2 A g^{-1}	118
2005	MnO_2 nanowire	0.1 M Na_2SO_4	350	Synthesized by using CV deposition	≈1 A g^{-1}	156
2005	MnO_2	1 M Na_2SO_4	50	High electrode loading ≈ 9 C cm^{-2}		157
2005	Mn-Co Oxide	0.1 M Na_2SO_4 pH4	139		3.475 A g^{-1}	158
2005	(Mn-Ni) oxide-CNT	0.1 M Na_2SO_4	410		2.08 A g^{-1}	155
2006	MnO_x	2 M KCl 2 M $(NH_4)_2SO_4$	275 310	MnO_x formed by electrodeposition	15.5 A g^{-1} 13.75 A g^{-1}	159
2006	MnO_2-SWCNT	1 M Na_2SO_4	≈200	Higher specific capacitance for less SWCNT content, however less stable cycling performance	2 A g^{-1}	160
2006	RuO_2-arrays	1 M H_2SO_4	1300	RuO_2 arrays were electrodeposited	>1.3 A g^{-1}	127

Table 1.3. Specific capacitances of metal oxide and metal oxide composites

				into anodic aluminium oxide templates		
2006	RuO_2-PTFE	1 M H_2SO_4	599		5.99 A g^{-1}	51
2006	RuO_2-carbon black	0.5 M H_2SO_4	647		1.29 A g^{-1}	145
2006	Hydrous RuO_2 in PEDOT:PSS	0.5 M H_2SO_4	653	RuO_2 was inserted into the conducting polymer by electrochemical means	32.6 A/g	139
2006	Vanadium nitride	1 M KOH	1340;554		2.68 A g^{-1}; 55.4 A g^{-1}	120
2006	NiO_x	7 M KOH	696	High surface area NiO_x xerogel, stable mesopore structure		110
2007	RuO_2-polyaniline-Nafion	1 M H_2SO_4	475; 375		47.5 A g^{-1} ; 375 A g^{-1}	142
2007	RuO_2-carbon nanofibre	1 M H_2SO_4	1017;824	Good cycleability over 10000 cycles. Gravimetric capacitance was calculated on the mass basis of ruthenium oxide only.	≈7 A g^{-1} ; 700 A g^{-1}	136
2007	MnO_2	0.1 M Na_2SO_4	400	Low electrode loading about 50 μg cm^{-2}	2 A g^{-1}	54
2007	MnO_2-carbon	0.5 M Na_2SO_4	165	Highly reversible over 10000 potential cycles	0.8 A g^{-1}	149
2008	Mn-Co oxides	2 M KCl	135-177	Electrode loading was near 1 mg cm^{-2}, prepared by electrodeposition	≈ 2 A g^{-1}	153
2009	Mn_2O_3-mesoporous carbon	6 M KOH	160		0.8 A g^{-1}	146
2009	Fe_3O_4-activated carbon supercapacitor	6 M KOH	37.9	Capacitance was calculated using a 2 electrode configuration and mass basis of both electrode	0.5 mA cm^{-2}	114
2009	Nanocrystalline RuO_2	1 M H_2SO_4	954	Crystallite size of ≈ 6 nm was prepared from SBA-15 template	2.37 A g^{-1}	126
2009	TiO_2-CNT composite TiO_2	1 M H_2SO_4	110 180	Capacitance of TiO_2 was estimated from the total capacitance of the composite		116

Table 1.3. Specific capacitances of metal oxide and metal oxide composites

2009	MnO_2-activated CNT	1 M Na_2SO_4	250; 184		2.5 A g^{-1}; 18.4 A g^{-1}	150
2009	MnO_2-PEDOT-MWCNT	0.5 M Na_2SO_4	375	PEDOT was utilized to bridge the MnO_2 with the CNTs	1.87 A g^{-1}	148
2009	NiO_x	6 M KOH	710		1 A g^{-1}	43
2009	SnO_2-PANi	1 M H_2SO_4	305		1 A g^{-1}	55
2010	MnO_2-graphene	1 M Na_2SO_4	310	Composite easily prepared by mixing potassium permanganate with graphene under microwave irradiation	1.5 A g^{-1}	152
2010	MnO_2-PEDOT co-axial core/shell rods Co-deposited MnO_2-PEDOT MnO_2	0.5 M Na_2SO_4	285 195 185			147, 161
2010	RuO_x/PPy	0.1 M H_2SO_4	681	RuO_x was electrodeposited on preformed PPy nanorods	≈ 1.5 A g^{-1}	140
2010	RuO_2-PEDOT	1 M H_2SO_4	664	The composite has nanotube structure	15.4 A g^{-1}	162
2011	MnO_2-activated graphene	1 M KCl	328	MnO_2 nanoflowers were electrodeposited onto the activated graphene sheets	0.25 A g^{-1}	14
2011	MnO_2-vertically aligned CNT	0.2 M Na_2SO_4	642	Composite has stability issue, only stable up to 800 cycles	6.42 A g^{-1}	151
2011	$Co(OH)_2$	1 M KOH	2650	Ultrathin $Co(OH)_2$ sample electrodeposited on roughened Ni surface, capacitance contribution of roughened Ni was not mentioned.	13.25 A g^{-1}	106
2011	Co_3O_4-MWCNT	2 M KOH	418		0.625 A g^{-1}	42
2011	Co_3O_4	1 M KOH	548	Co_3O_4 has ultrathin layered structure that enhances surface area; electrode loading was 1 mg cm^{-2}.	8 A g^{-1}	41

1.1.3.3 Electrolytes for supercapacitors

The electrolyte provides an ionic conduction path as well as a physical separation of the positive and negative electrodes for the cell operation. It is an essential component of a supercapacitor. The influence of different electrolytes to the performance of a supercapacitor material was illustrated in Figure 1.6 for carbon materials.[2] The performance parameters affected by different electrolytes are, among others, limits of ideal polarizability, power performance and series resistance.[163] Common electrolyte systems for supercapacitors are separated into three types, aqueous, organic and ionic liquid electrolytes.

1.1.3.3.1 Aqueous electrolytes

Aqueous electrolytes are popular due to their high conductivity, non-flammability, low cost and environmental friendliness. The high conductivity of aqueous electrolytes arises from their high dielectric constant, which favours stable and smaller sizes of solvated ionic species.[3,121] This effect gives rise to a higher capacitance, and especially a higher power capability. Acidic electrolytes such as aqueous H_2SO_4 are used extensively for porous carbon materials to achieve higher capacitance due to the participation of protons in the pseudo-capacitive reactions which take place on surface quinodal or carbonyl groups (Scheme 1).[77] Aqueous H_2SO_4 is also commonly used for RuO_2 and for ECPs. (Table 1.3 and Table 1.4) PANi for example has

always been characterised in aqueous acid solutions due to the protonation induced conductivity.[164] However, acidic electrolytes present many technical disadvantages mainly due to their corrosiveness towards the metallic components in a supercapacitor.[70] Furthermore, acidic electrolytes cannot be used for MnO_x based materials due to the dissolution of manganese oxide in acid solutions. Consequently, alkaline solutions are more favourable because of better stability of metallic current collectors. The effect of pseudo-capacitance contribution for carbon materials is markedly reduced, although studies showed that surface pyrone groups on carbon become activated in high pH solutions.[31] Neutral aqueous electrolytes are the most desirable in terms of environmental friendliness. Although less commonly used for carbon materials, neutral electrolytes are widely used for metal oxides and ECP materials such as PPy and PEDOT (Table 1.4). Neutral electrolytes are used especially for MnO_2 based electrode materials as the use of either acidic or alkaline electrolytes are inappropriate, as the former causes dissolution of the electrode, while manganese forms non-conducting species in the latter.[131] In comparison, as ECPs do not present the dissolution problem, or the pH dependent conductivity (except for PANi), there is more flexibility in terms of aqueous electrolyte choice for ECP systems.

A major disadvantage of aqueous electrolytes is the relatively low voltage, and consequently a lower energy storage density, which is limited by the potential window for the decomposition of water, i.e. 1.23 V. This disadvantage is overcome by selecting electrode materials that have high overpotentials for hydrogen and/or oxygen evolution, to expand the stability limit of water through kinetic effects.[3,20] For example, by using activated

carbon as the negative electrode and MnO_x as the positive electrode, a practical cell voltage of 2 V has been achieved.[11] With MnO_x-CNT nanocomposites as the positive electrode and SnO_2-CNT nanocomposites as the negative electrode, a supercapacitor had an operating voltage of 1.7 V.[20] A supercapacitor based on seaweed-derived carbon also had an operating voltage up to 1.6 V; as the surface functionality influenced the overpotentials of hydrogen evolution and carbon oxidation.[70] An asymmetrical supercapacitor using a polyaniline positive electrode and an activated carbon negative electrode was tested at 1.6 V.[48] Also worth mentioning is the long proven example of the lead acid battery that has a single cell voltage of ≈ 2 V.[20]

1.1.3.3.2 Organic electrolytes

Organic electrolytes have the merit of allowing a higher voltage window (up to 3.5 V) which means much higher energy storage density for a given capacitance value.[121] Aprotic solvents such as acetonitrile and propylene carbonate are popular electrolyte candidates for carbon materials due to the hydrophobicity of carbon materials (Table 1.2). In those cases the electrolytes typically contain either lithium perchlorate ($LiClO_4$) or tetraalkylammonium tetrafluoroborate as the ionic species (Table 1.2). Due to the lower dielectric constants in organic solvents, ion pair formation is possible even at low salt concentration, which results in lower conductivity as ions are not all free, but instead partly bound to each other.[3] For that reason, salts with less symmetric structures, which have a lower crystal-lattice energy, show increased solubility.[121] The disadvantages of organic electrolytes, compared to aqueous

systems, include higher cost, lower conductivity and much less environmentally friendly.[61] Moreover, the purity of organic solvents can be an issue, i.e. slight water 'contamination' (3-5 ppm) reduces the stability voltage window significantly, compared to the use of pure solvents.[121] As a result, strict controls on the preparation process of these organic solvents are required.[61,121]

1.1.3.3.3 Ionic liquid electrolytes

Ionic liquids (ILs) are salts present in liquid form at room temperature. ILs are salts with melting temperatures below 100˚C, and they usually consist of highly asymmetric combinations of anions and cations. ILs are attractive candidates as supercapacitor electrolytes for their unique properties, such as high thermal and electrochemical stability (up to 6 V potential window[165]), non-flammability and very low vapour pressure.[61] As there are solvation shells in ILs, ILs also offer a well identified ion size.[121,166] Hydrophobic ionic liquids are commonly used due to the relative ease of achieving high levels of purity as water contamination is reduced.[61] The disadvantage posed by utilization of ionic liquids is similar to that of using organic solvents; as they are usually less conducting and more viscous than aqueous electrolytes, capacitance and power performance are generally lower. The disadvantages of ILs also include high cost, difficulty in synthesis and safety concerns due to the possible toxicity of certain ionic liquids. To achieve a higher power density, mixtures of ionic liquids and organic solvents are used.[50] In conjunction with higher power performance, these electrolyte mixture also provide a high energy storage

density (operating voltage of 3.5 V).[50] However, this approach also combines the disadvantages of both organic electrolytes and ionic liquids, such as potential flammability and toxicity.[121]

1.1.3.3.4 General trends and observations

A recent review summarized two principal factors contributing to the conductivity of the electrolyte: (1) the ability of salt dissociation to give out free charge carriers; and (2) the mobility of the dissociated ions in the electrolyte systems.[61] From this point of view, aqueous electrolytes have distinct advantages, and they are also more cost efficient and environmentally friendly. Organic and ionic liquid electrolytes provide the possibility of higher voltage and energy storage density but have disadvantages in terms of cost and environmental concerns. In addition, when organic or ionic liquid electrolytes are used, the supercapacitors suffer from lower power performance due to a significantly lower conductivity. The difference between the capacitance and power capability of materials characterised in aqueous, organic or ionic liquid electrolytes were also clearly manifested in the different applied current loading or scan rate for capacitance measurements (refer to Table 1.2). For example, the current loading for mesoporous carbon spheres (ref. [77]), when characterised in an aqueous system, could be close to 2 orders of magnitude higher than in an organic solvent system (30 A g^{-1} in 2 M H_2SO_4, 0.5 A g^{-1} in Et_4NBF_4-propylene carbonate), yet still resulted in a higher capacitance performance (146 F g^{-1} vs 97 F g^{-1}, respectively). Although the pseudo-capacitance contribution is markedly higher in the acidic electrolyte,

the huge difference in capacitance values corresponding to the current loading is clearly ascribed also to the nature of the electrolyte.[77] Thus, the choice of electrolyte can be made according to the performance requirement of a supercapacitor; aqueous systems are desirable for higher power, and organic/ionic electrolyte systems favour higher energy density. However, strictly speaking the choice is available mainly for porous carbon materials, whereas purely pseudo-capacitive materials such as metal oxides or ECPs tend to favour aqueous systems rather distinctively, as the complete charging of these materials require ions to diffuse into thicker layers than those present in carbon.

1.1.4 Conducting polymer and their nanocomposites for supercapacitors

ECPs are polymers which have a π-conjugated backbone, which consists of a regularly alternating single (C-C) and double (C=C) bonds. The π-conjugated backbone is responsible for the generation and propagation of charge carriers, making the polymers intrinsically conducting. Thus all ECPs share the π-conjugated structure.[26] The understanding of the conductivity in ECPs was first developed by the trio of Heeger, MacDiarmid and Shirakawa in the 1970s, based on the example of polyacetylene, which is the simplest form of any ECPs.[164,167] Upon doping with bromine, the polyacetylene film showed a dramatic conductivity increase.[167] The doping in that case corresponds to oxidation of the ECP (p-doping), and de-doping corresponds to the reduction of ECPs. Thus p-type ECPs are conducting in the oxidised state, while being

largely insulating in the neutral state. Taking such behaviour into consideration, the name 'semiconducting polymers' may be more appropriate as it better describes the nature of the material's conductivity. It is due to the semiconducting nature of ECPs that charge storage occurs in these materials, as outlined using band theory (Figure 1.8).

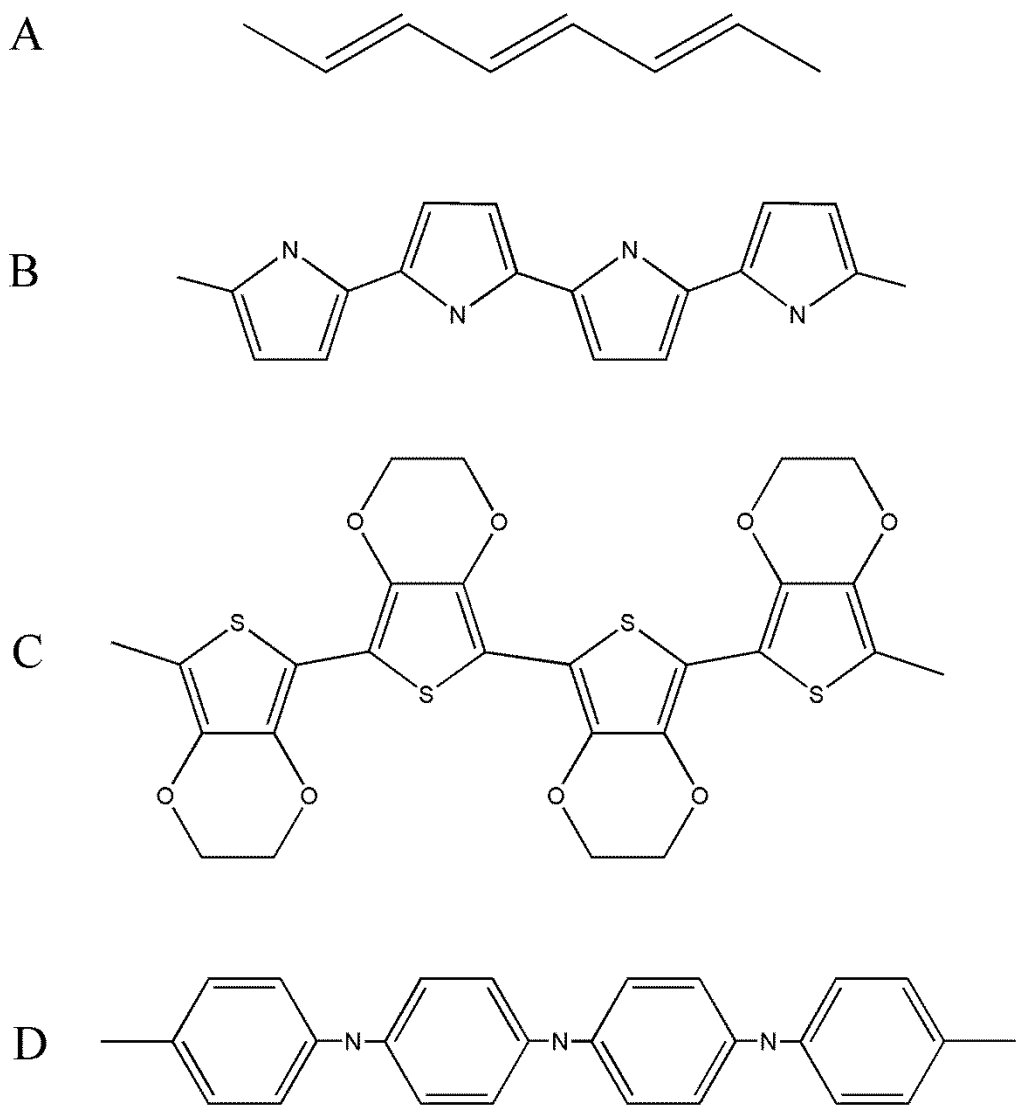

Figure 1.10. Chemical structures of some most common ECPs in their neutral state, hydrogen atoms are omitted for clarity. (A) trans-polyacetylene, (B) PPy, (C), PEDOT and (D) PANi.

Charge storage in ECP materials occurs when (considering an initially reduced, insulating state) electrons are removed from the π-conjugated backbones (oxidation), and vice versa. When ECPs are placed or grown on electrodes, they can be electrochemically oxidised or reduced. The insulating-conducting switching potential in ECPs presents the negative potential limit for its application in supercapacitors, while the positive limit is set either by the water oxidation potential or the potential where the ECP undergoes irreversible degradation, termed "overoxidation". The most popular ECPs for supercapacitor applications are polypyrrole (PPy), polyaniline (PANi) and poly(ethylenedioxythiophene) (PEDOT) due to their high conductivity, ease of preparation, cost effectiveness and their relatively light weight, which translate to higher specific capacitance.[39,168] The three common ECPs mentioned above are all p-type ECPs. Although n-type ECPs also exist, such as certain polythiophene derivatives, they are far less popular in comparison.[121] Although polyacetylene is lighter than any other ECPs, it is not commonly used in supercapacitors due to its relative instability and difficulties in synthesis.[169,170] While ECPs are used in many other applications, the following review will focus only in the context of supercapacitor ECP materials while other ECP applications may be mentioned whenever relevant.

The ability to draw high power from supercapacitors is attributed to the fast and simple electrochemistry of the electrode material.[168] As the redox processes in ECPs (an example illustrated in Figure 1.11) can proceed at very fast rates, which give rise to rapid charging and discharging, they are attractive materials for supercapacitors.[168]

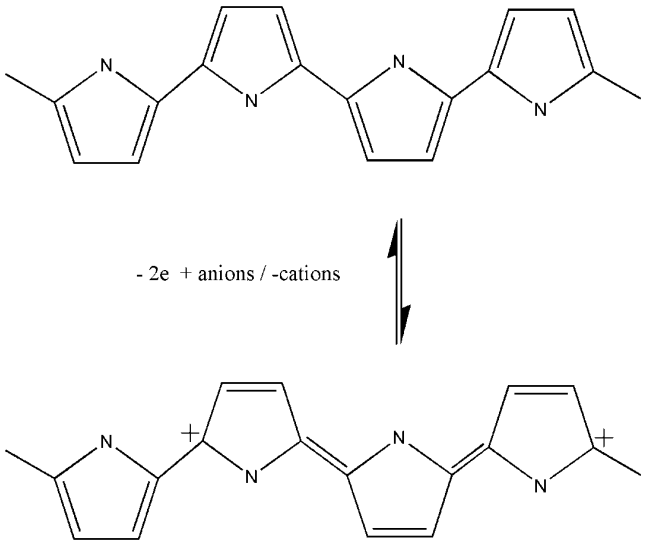

Figure 1.11. Oxidation and reduction of PPy.

The redox processes that take place on the ECP electrodes are accomplished by counterion movements for charge balancing, either ingress into the ECP or expulsion from it. In fact, in most cases the counter ion movement is the limiting kinetic factor of how fast an ECP material is charged. Thus electrolyte access is the key to higher performance ECPs.[39] The other challenge posed by ECP application in supercapacitors is the relatively poor mechanical stability. As they are rapidly charged and discharged, the ECPs go through volume or dimensional changes as the result of ion and solvent movements, which generate mechanical stress and can cause physical degradation to the ECP, consequently resulting in declining capacitance.[39,168] Generally, a porous structure is desirable not only for better electrolyte access into the ECP which result in higher capacitance, but also for higher cycling stability as there is less volumetric stress on the ECP material during the charging/discharging process. The main attribute of ECP nanocomposites formed with materials such as CNTs is the highly porous structure which

favours the capacitance and stability performance of ECPs.[39,168,171] As these supporting materials are also extremely strong mechanically, the mechanical integrity of the ECP composites becomes significantly enhanced. The synthesis, characterisation and performance of ECPs and ECP composites will be reviewed in following paragraphs. Notably, the volume and/or dimensional changes of the ECP materials as a result of the redox processes are reasons behind the utilization of these ECP materials for construction of electrochemical actuators.[172,173]

1.1.4.1 Synthesis of ECPs and ECP composites

There are two main ways of synthesizing ECPs or their composites; either by chemical or by electrochemical synthesis. Either way involves an oxidation process of the corresponding monomers, in the presence of a counterion species (either small, mobile ions such as Cl^- or large immobile ionic species such as acid treated CNTs[168,174]) for the doping process. Chemical synthesis of ECPs is achieved by oxidation of the monomers using an oxidizing agent; while electrochemical synthesis involves deposition of the conducting polymer on an electrode surface. For ECP composite formation, the chemical synthesis involves mixing the monomer of an ECP with the doping or supporting material prior to the oxidation step. The electrochemical synthesis, on the contrary, can proceed in two ways, either by deposition of the ECP on a pre-formed layer of the supporting material on an electrode, or by co-electrodeposition in which the electrochemical deposition of the ECP and the adhesion of the doping material to the deposited ECP occurs

simultaneously. The main advantage of chemical synthesis of ECPs is the ease of mass production, but the ECP product is always present in powder form. To make an electrode using such ECP products requires the use of a binder. The use of the binder material or the presence of reduction products of the oxidizing agent may also affect the overall performance of the material.[168] As the ECPs are directly formed on the electrode surface during the electrochemical synthesis process, there is no need for a binder. The contact resistance within the polymer material and between the ECP and the current collector is also significantly reduced, as they grow on the electrode substrate directly.[168] The amount of material loading on the electrode is also easily controlled by varying the deposition charge.

1.1.4.2 Polypyrrole (PPy)

After polyacetylene, PPy is one of the simplest ECP. The π-conjugated backbone of a neutral PPy resembles that of cis-polyacetylene, except PPy has an additional nitrogen heteroatom every 4 carbon atoms, linking between the 1st and 4th carbon atom (Figure 1.10B).[164] The nitrogen heteroatom and the ring structure of the repeating unit stabilize the polymer molecular structure. PPy is very attractive for supercapacitor applications due to the ease of processing as the Py monomer is soluble in water, and the polymer has good conductivity and environment stability. The main disadvantage of PPy is the weak potential cycling stability. Among other most commonly used ECPs for supercapacitors such as PANi and PEDOT electrodes, PPy has the worst cycling performance.[168] The relatively poor cycling performance is related to

the structure of PPy. Usually, PPy films have dense structures which consist of 'large' micrometer sized particles, which are commonly visible on the surface as typical 'cauliflower-like' or 'muffin-like' structures.[168] Such a dense structure is not favourable for electrolyte access during the potential cycling, and furthermore, the particulate structures may collapse easily as they undergo swelling and shrinkage repeatedly. In comparison, PANi and PEDOT have a more porous structure, and consequently a better cycling performance.[168]

Pulse polymerised PPy electrodes exhibiting a specific capacitance of 400 F g^{-1} when measured using a 2-electrode configuration, has been previously reported.[45] The electrode was said to display a specific capacitance of 1100 F g^{-1} in a 3-electrode cell.[45] The high capacitance was due to a lower density of defects in polymer structures during polymerisation by the pulsed technique.[45] A lower polymerisation rate set by the 'pulse on' time resulted in a lower reactivity of the radicals, and which resulted in better conjugation and higher electronic conductivity.[45,175] However, the exceptionally high specific capacitance (higher than theoretically achievable using PPy) may have been an overestimation as the loading (0.02 mg) on the electrode was very low.[45] The double-layer capacitance of the underlying electrode (graphite plate, size not mentioned) in the electrolyte (0.5 M H_2SO_4) may have been included into the estimation of 'specific capacitance' for the PPy.[45] Porous PPy electrodes can also be easily synthesized on titanium foil from cyclic voltammetry deposition at fast scan rate in oxalic acid solution.[176] At an electrode loading of 0.6 mg cm^{-2}, the porous PPy electrode exhibited 480 F g^{-1} specific capacitance.[176]

PPy-MWCNT nanocomposites synthesized chemically have shown a specific capacitance of 495 F g^{-1}.[171] Pellet electrodes were pressed from the nanocomposites, without any polymer binder, for the characterisation.[171] Remarkably, the pellet composite electrodes pressed at 500 kg cm^{-2} retained their porous internal structure to allow fast ion diffusion and migration as a result of the strength contributed by the MWCNTs.[171] Notably, composites containing less than 20 wt% MWCNT presented dense structures similar to that of pure polymer, which resulted in an inferior performance.[171] When a 5 nm PPy layer was deposited on a preformed CNT electrode, the specific capacitance increased from 50 F g^{-1} for the pristine CNTs to 163 F g^{-1} for the composite electrode.[177]

For co-electrodeposited PPy-MWCNT films, the capacitance of the composites was found to be twice that of pristine PPy films for all deposition charges.[178] The electrode capacitance, per unit area of the underlying electrode, for the composite was 1 F cm^{-2}, while the mass averaged capacitance was 192 F g^{-1}.[178] The composition of CNTs in the deposition solution for producing co-electrodeposited PPy-MWCNT films was also optimised to a CNT content of 0.4 wt% in the aqueous solutions.[179] Later studies also demonstrated that a electrode specific capacitance of 2.35 F cm^{-2} was achieved with a co-electrodeposited PPy-CNT composite, measured using CV.[168] Using an electrochemical quartz crystal microbalance, the effect of counterions during the redox cycling of co-electrochemical deposited PPy-CNT was studied.[45] A mix of cation expulsion and anion uptake upon oxidation of the composite was observed when aqueous KCl was used as the electrolyte. However, when

tetrabutylammonium bromide was used as the electrolyte salt, only uptake of Br^- was observed.[180]

Nanocomposites of PPy with vapour grown carbon fibers (VGCF) having PPy layers with a thickness of 5 nm gave a PPy-mass average capacitance of 588 F g^{-1}.[181] When thicker layers (> 10 nm) were deposited, the specific capacitance dropped significantly as the surface structure of the composite became comprised of the typical, unfavourable 'cauliflower-like' or 'muffin-like' structure.[181]

PPy composites with graphene materials are also gaining significant amounts of attention recently. Composite films of sulfonated graphene and PPy were co-electrodeposited from aqueous solutions containing Py monomer, sulfonated graphene and dodecylbenzene sulfonic acid.[182] For a film formation charge of 2 C cm^{-2}, the film showed a specific capacitance of 285 F g^{-1} at a current density of 0.5 A g^{-1}.[182] However, when a higher film formation charge of 4 C cm^{-2} was employed, the specific capacitance of the PPy-graphene composite decreased to 215 F g^{-1}.[182] Thus the effect of higher loading on the specific capacitance of ECP materials is similar to the case for metal oxides materials discussed in Section 1.1.3.2. Layered graphene oxide nanostructures with sandwiched PPy synthesized chemically in the presence of surfactant, showed capacitance over 500 F g^{-1} when characterised at 0.3 A g^{-1}.[183]

1.1.4.3 Polyaniline (PANi)

Polyaniline (PANi) is an ECP discovered in 1934 as aniline black. PANi is a unique ECP as the transition from insulator to metallic conductivity not only depends on the oxidation state, but it is also induced by protonation.[164] PANi has been, and continues to be one of the most important ECPs.[164] Due to the requirement of protons for PANi to become conducting, and to enable proper charging and discharging, protic solvents are required. Aqueous acidic solutions are the most common electrolyte used for PANi material characterisation. The main advantage of using PANi is its significantly higher capacitance, as the reversible redox reaction of PANi can remove up to one electron per two monomer units, in comparison with the maximum one electron every three monomer units in the case of PPy. Theoretically, the specific capacitance of polyaniline, considering the pseudo-capacitive contribution only, is 964 F g^{-1}.[184] A theoretical specific capacitance for PANi of 1700 F g^{-1} has also been reported.[185] This value however is incorrect as the mechanism of the redox switching of PANi was neglected and the assumption of one electron removal per monomer unit taking place across 0.61 V is wrong.[185]

The other advantage of using PANi is the ease of making porous films, which consist of PANi nanofibers by simple potentiostatic deposition.[168,184,185] For example, specific capacitance values for PANi were measured at 608 F g^{-1}, 445 F g^{-1} and 524.9 F g^{-1} using cyclic voltammetry, electrochemical impedance spectroscopy and galvanostatic methods, respectively.[185] Average specific capacitance values of electrodeposited PANi films between 700-825 F g^{-1} have

been measured between different potential windows by integrating the current recorded in CVs.[184] Using vertically aligned PANi nanowire arrays, specific capacitance of 780 F g^{-1} was measured at 40 A g^{-1} current loading.[53] In fact, it has been shown that co-electrodeposited PANi-CNT nanocomposites did not improve the capacitive performance, as the pristine PANi films also have a very porous structure.[168] However, the potential cycling stability was significantly enhanced by the presence of CNTs in the composite, as they alleviate stress generated by the electrolyte movements during potential cycling.[168] A significantly higher electrode capacitance was also achieved for the PANi-CNT (3.5 F cm^{-2}) composites than for pristine PANi (2.3 F cm^{-2}).[186] An earlier study which performed electrodeposition of PANi onto pre-formed CNT electrodes demonstrated 485 F g^{-1}, in comparison to the pristine electrodeposited PANi which only showed a specific capacitance of about 260 F g^{-1}.[60] Surprisingly, there was a lack of discussion on the low specific capacitance (260 F g^{-1}) recorded for the pristine PANi in the report,[60] as the same group published specific capacitance values for electrodeposited PANi films in excess of 740 F g^{-1} measured using either cyclic voltammetry[187] or the galvanostatic method[58]. A PANi-CNT array composite electrode, of which the PANi coating was only 7 nm on the surfaces of CNTs vertical arrays, displayed a high specific capacitance of 1030 F g^{-1} at 5.9 A g^{-1} current loading.[188] The composite also showed a very good stability, with only 5.5 % initial capacity lost after 5000 potential cycles at 5.9 A g^{-1} current loading.[188] Chemically synthesized PANi-CNT composites, pressed into a pellet formed without using any polymeric binder, also exhibited a specific capacitance of 650 F g^{-1}.[171]

1.1.4.4 Poly(3,4-ethylenedioxythiophene) (PEDOT)

Next to PPy and PANi, PEDOT is the most commonly used ECP for supercapacitors. PEDOT was developed during the late 1980s, at the Bayer AG research laboratories in Germany.[189] The original intention was to produce a soluble conducting polymer that lacked the presence of undesired α-β and β-β coupling like those usually present in PPy.[189] The undesired couplings do not take place during polymerisation of PEDOT as both of the β positions are occupied by the ethylenedioxy functionalities. As a result, a higher conjugation length is achieved, giving rise to a higher intrinsic electronic conductivity. The ethylenedioxy functionalities also result in higher stability of the polymer in the oxidised state. PEDOT was initially found to be insoluble, but this was overcome by using poly(styrenesulfonate) (PSS) as the dopant during polymerisation. The latter is soluble in water, and the combination of PEDOT:PSS becomes soluble as well.[189] PEDOT:PSS is commercially available, known as BAYTRON P from the Bayer company.[189]

For application as supercapacitor materials, it appears that PEDOT materials have been given less attention than PPy and PANi due to its relatively small theoretical mass specific capacitance, which arises from two effects: (1) larger molar mass of the monomer unit, and (2) wider charging potential range.[190] However, the wider potential ranges can at least compensate, or even improve the performance over other ECP materials, when the energy storage density is considered.[19,174] PEDOT is also compatible with aqueous, organic and ionic electrolytes, making it a very versatile ECP.[190-193] A disadvantage of using PEDOT however is that electrochemical synthesis of

PEDOT from aqueous deposition solutions is not possible as the monomer is water-insoluble. On the contrary, thick PEDOT films can be made easily by using potentiostatic deposition from acetonitrile solutions; the electrode capacitance, normalised to electrode area, can reach 5 F cm^{-2}.[194] The electrodeposited PEDOT films on Pt electrodes presents a porous structure, made up of fairly loosely connected aggregates of nanoparticles.[168,194]

PEDOT nanotubes and nanowires electrochemically synthesized in the cylindrical pores of an alumina template membrane exhibited 130 F g^{-1} specific capacitance at 1 V s^{-1} scan rate.[195] PEDOT exhibiting a high stability in 1 M H_2SO_4 has been electrodeposited from an ionic liquid solution of the monomer.[193] The PEDOT film had an enhanced cycling life time up to 70,000 cycles with near 80 % capacitance retention.[193] The capacitance performance of PEDOT was also highly improved by forming composites with CNTs electrochemically. The capacitance of an electrochemically synthesized PEDOT-CNT nanocomposite was more than twice that of pristine PEDOT synthesized using the same deposition charge.[168] However, thicker films of PEDOT-CNT could not be made using electrochemical co-deposition due to the phase separation of the deposition solution, which consists of an aqueous/acetonitrile mixture, after long deposition times.[168] The oxidised CNTs are dispersed in the aqueous phase whereas the EDOT monomer is only soluble in acetonitrile.[168] The aqueous solubility issue is not present for chemical synthesis of PEDOT-CNT composites.[190] An asymmetrical supercapacitor built using the PEDOT-carbon composite as the positive electrode and activated carbon as the negative electrode, containing organic

electrolyte exhibited average mass specific capacitance of 160 F g^{-1} over a voltage of 1.5 V, and a stable performance for over 20000 cycles.[190]

1.1.4.5 General trends and observations

To achieve high capacitance performance using ECP materials, high surface area is required. Attempts to achieve high surface area ECPs are wide ranging. For example, either by strict control of an electropolymerisation process for making PPy nanotubes[45] or electrodeposition into porous alumina templates to make PEDOT nanowires.[195] Alternatively, the porous structure is achieved by forming composites between ECPs and rod like nanoparticles such as CNTs. In the latter case, the CNTs also contribute strength towards the overall mechanical robustness of the composite, which is especially important during extended potential cycling. For example, the comparison between electrodeposited PANi and PANi-CNT only showed significant improvement in the potential cycling stability test.[168] This is due to the similar porous structure of electrodeposited PANi films which provide sufficient electrolyte pathways for high capacitance initially.[168] For making composites, in particularly those with CNTs, there are notable differences between the materials achieved by chemical or electrochemical synthesis routes. The prospect of the chemical route for large scale production is unquestionable, and CNTs in those cases do not require charge on the surface. However, the disadvantage of chemical synthesis of ECP-CNT composites is the inability to achieve a constant level of homogeneity and integrity in the composite product as polymerisation of the ECP tends to proceed on the polymer itself.[26,196]

Electrochemical deposition can produce ECP composites with a more defined and reproducible morphology. As a result these composites are preferred for electrochemical studies.[168] In the electrochemical process for making an ECP composite, the co-electrodeposition of CNTs,[168] or graphene,[182] happens as they bear negatively charged surface groups which allow their incorporation into the positively charged ECP during the polymerisation process. On preformed CNT electrodes, for example the vertical CNT arrays, surface charge is not necessary as the ECPs can nucleate on the conducting CNT surface.[188]

Generally, there has also been an overemphasis on the mass specific capacitance for ECP materials for supercapacitors. In this case, reporting only the mass specific capacitance may be misleading because the total electrode capacitance may not increase linearly with increasing amounts of material.[168,178,194] For example, Lota measured the mass specific capacitance values for very thin films of PEDOT at 180 F g^{-1}.[190] However, this value reduced to 80-100 F g^{-1} when larger amounts of the material (10-20 mg) were pressed into pellet form. It is not surprising that a lot of ECP materials, especially those synthesized electrochemically and with high capacitance are reported when only very small amounts of the material are applied on the test electrodes, while the electrode specific capacitance may be too low for practical purposes. When a very small amount of an ECP material is used, a very high capacitance can be easily achieved as the performance is not limited by kinetics. For example, a symmetrical supercapacitor built using poly(2,2-dimethyl-3,4-propylene-dioxythiophene) (PProDOT-Me_2) had an overall mass specific capacitance of 55 F g^{-1} (which equals 220 F g^{-1} for a 3

electrode system), which was reasonably good; but the electrode specific capacitance was impracticably low, at 6.5 mF cm^{-2}.[197] Similarly, a PEDOT-PProDOT-based supercapacitor containing ionic liquids demonstrated a high performance and high cycleability over 50000 cycles, retaining 98 % of its initial capacity.[198] However this was for a 150 nm thick film.[198] The overall capacity however, was only 1.35 mC cm^{-2} for each electrode, corresponding to 2.7 mF cm^{-2} capacitance for each electrode.[198] In contrast, electrode specific capacitance on the order of F cm^{-2} have been widely reported for many other ECP materials. This is very important because, for supercapacitors, a high electrode specific capacitance value is necessary as it translates directly into the device capacitance.[40] Thus a comprehensive material study requires characterisation simply at different electrode loadings and, ideally, a material will have linearly increasing electrode specific capacitance with the amount of material, which corresponds to constant mass specific capacitance over the range of deposited ECP amounts.

It is also interesting to briefly revise the band theory in relation to the theoretical specific capacitance for the three most commonly used ECP supercapacitor materials. The capacitance, is defined as $C = \frac{dQ}{dV}$, and the theoretical specific capacitance, as $C_{tmsp} = \frac{nF}{(\Delta V \times M_W)}$ where F is the Faraday's constant, 96485 Coulombs mol^{-1}, n is the number of electrons transferred per unit monomer, ΔV is the potential across which the charging occurs, and M_W is the relative molecular weight per monomer unit. The Faraday's constant is the charge stored per mole of electrons. Regardless of the relative molecular weight, C_{tmsp} is also inversely proportional to the potential window. Interestingly, the potential window for an ECP is dependent on the conjugation

length, and so is the conductivity.[199] As ECPs reach a higher conjugation length, the π-band, which results from the interaction (linear combination) of the π-orbital wave functions of the π-conjugated backbone, is wider as there are more interactions per unit polymer.[164] The first implication is a higher electronic conductivity. Secondly, there is a higher number of allowed redox states for the ECP, manifested by a larger potential window.[200] Finally, a fixed amount of charge stored at a larger potential window means a lower capacitance. For example, PPy and PEDOT have the same maximum n of 0.33 (1 electron every 3 monomeric unit). For PPy, complete charging occurs over 0.8 V whereas for PEDOT, it is 1.2 V due to a higher conjugation length.[190] The conductivity values measured for these materials presents an opposite trend in comparison to the C_{tmsp} values; i.e. conductivity of PEDOT > Ppy > PANi; potential window of PEDOT > Ppy > PANi; and C_{tmsp} of PANi > Ppy > PEDOT.[40,190] It is interesting that the band theory explanation that distinguishes between the two extremes of conductors and insulators also extend to the case of ECPs and even the metal oxides which are semiconducting. For a semiconductor, the capacitance is higher for a more resistive material. In the case of metal oxides, nickel oxide (10^{-4}-10^{-5} S cm^{-1},[201] average reported mass specific capacitance = 500-1000 F g^{-1} and C_{tmsp} = 3750 F g^{-1} [121]) cobalt oxide (≈10^{-4} S cm^{-1},[202] average reported mass specific capacitance = 500-800 F g^{-1} [121]) and manganese oxide (≈10^{-3} S cm^{-1},[143] average reported mass specific capacitance = 200-300 F g^{-1} [121]) show highly contrasting capacitance and conducting properties. The effective utilisation of the metal oxides of high specific capacitance however, is limited by low conductivity, but which is the origin of high specific capacitance from the band

theory point of view. There is also an analogy between C_{tmsp} for ECPs and metal oxides and the relative density of states described in the d-band theory for the case of metals. Details of some of the ECPs used as supercapacitor materials are shown in Table 1.4.

Table 1.4. Specific capacitances of a selection of ECP and ECP composite materials reported in the literature. Electrolytes are aqueous based unless otherwise stated.

Year reported	Material	Electrolyte	Capacitance (F g^{-1})	Comments / Notes	Current load	Ref.
2001	Ppy-MWCNT	1 M H_2SO_4	163	Ppy of 5 nm thickness was electrodeposited onto pre-formed CNT electrodes.	0.17 A g^{-1}	177
2002	Ppy-MWCNT	0.5 M KCl	192	Co-electrodeposited films of Ppy-MWCNT. 192 F g^{-1} was averaged for the film which showed 1 F cm^{-2} electrode capacitance.		178
2003	PANi-carbon	1 M H_2SO_4	230	PANi electrodeposited on carbon polyacrylonitrile aerogel electrodes		203
2005	Ppy-SWCNT	6 M KOH	350	SWCNTs were arylsulfonic acid functionalized, composites were chemically synthesized	2 A g^{-1}	204
2005	Ppy-MWCNT PANi-MWCNT	1 M H_2SO_4	495 650	Chemically synthesized ECP nanocomposites, pressed into pellet form for characterisation	0.208 A g^{-1} 0.37 A g^{-1}	171
2005	PANi	1 M H_2SO_4	742	Film thickness was around 20 μm	23 A g^{-1}	58
2005	PANi-CNT PANi	1 M HCl – 0.5 M $LiClO_4$ mixture		3.5 F cm^{-2} 2.3 F cm^{-2}		186
2005	PEDOT	1 M H_2SO_4	(A) 100 (B) 72	Chemically synthesized, (A) with ultrasonication and (B) mechanical stirring	0.45 A g^{-1}	205
2006	Ppy	Polymer gel electrolyte	200	Ppy with higher stability was produced after irradiation with 160 MeV Ni^{12+}		206
2006	PPy	1 M KCl	480 200	Porous PPy deposited on Ti foil in oxalic acid solution.	4.8 A g^{-1} 100 A g^{-1}	176
2006	Ppy-VGCF	6 M KOH	588	5 nm Ppy on the carbon fibers	17.64 A g^{-1}	181
2006	PANi	1 M H_2SO_4	775	Film thickness was around 20 μm	7.75 A g^{-1}	187
2006	PANi PANi-CNT	1 M H_2SO_4	260 485	Deposition solution contains H_2SO_4 PANi deposited on pre-formed CNTs		60
2007	PEDOT	0.5 M KCl		5 F cm-2 electrode capacitance, measured using CV and EIS		194
2008	PPy	0.5 M H_2SO_4	1100	Pulse deposited, very low electrode loading and		45

Table 1.4. Specific capacitances of ECPs and ECP composite materials

				double-layer effect of underlying electrode was not included		
2008	Ppy-MnO2 Ppy	0.5 M Na_2SO_4	620 250	Composites formed by electrodepostion	31 A g^{-1} 12.5 A g^{-1}	207
2008	PEDOT	1 M $LiClO_4$ 1 M Et_4NBF_4	130 125	PEDOT nanotubes synthesized in alumina template	130 A g^{-1} 16 A g^{-1}	195
2008	PEDOT	1 M H_2SO_4	130	PEDOT electrodeposited from ionic liquid solution	6.5 A g^{-1}	193
2008	PEDOT-activated carbon	β-naphtalene-sulfonic acid	158	PEDOT was electrodeposited on preformed carbon electrodes	1.58 A g^{-1}	208
2008	PANi-CNT	1 M H_2SO_4	1030 978 789	7 nm PANi layers on vertically arrayed CNTs	5.9 A g^{-1} 118 A g^{-1} 294 A g^{-1}	188
2009	PANi	1 M H_2SO_4	608	Potentiostatically deposited films	12.1 A g^{-1}	185
2009	Poly(tris(4-(thio-phen-2-yl)phenyl)amine) (PTTPA)	0.1 M Et_4NBF_4 in acetonitrile	950 ± 49 (peak - capacitance)	Dendritic conducting polymer		44
2010	Layered PPy-graphene	1 M NaCl	165	Stable for at least 1000 cycles	1 A g^{-1}	209
2010	PPy-graphene	2 M H_2SO_4	528 255	Surfactant assisted synthesis of layered structure	0.3 A g^{-1} 5 A g^{-1}	183
2010	PPy-graphene	1 M KCl	285	Electrochemically co-deposited film	0.5 A g^{-1}	182
2010	PANi	1 M HClO4 1 M LiTFSI EMITFSI	780 ≈500 ≈200	Vertically aligned PANi arrays electrochemically deposited without use of templates	40 A g^{-1}	184
2010	PANi-graphene	2 M H_2SO_4	480 210	Relatively dense structure of PANi, low capacitance at higher current loading	0.1 A g^{-1} 1 A g^{-1}	196
2010	PProDOT-Me_2	Ionic liquid- PC blend	55 (2 electrodes)	Electrode capacitance was only 6.5 mF cm^{-2}.		197
2011	PANi	1 M HCl	825	Measured by integrating CV current	16.5 A g^{-1}	184
2011	PANi-graphene		300-500	Composite synthesized chemically	0.1 A g^{-1}	210

1.1.5 Cellulose nanocrystals

Recently, renewable materials have been gaining unprecedented attention. The advantages of using renewable materials, other than such resources being virtually unlimited, are ascribed to their environmental friendliness, biocompatibility, biodegradability and low cost, among others.[211,212] Cellulose is the most abundant renewable material present. As a result, there has been a significant increase in research devoted to the applications of cellulose.[213-215] Cellulose consists of repeating β-(1-4)-D-glucopyranose units (Figure 1.12). The abundance of cellulose derives from the fact that it is the main component in the structural framework of plant cell walls, and it contributes towards the mechanical strength of plant materials. The strength of cellulosic material has been utilised in many applications such as building and clothing materials, which does not require too much introduction. There is also the potential to derive biofuels from cellulosic materials. Other than in plants, cellulose also occurs in a wide variety of living species as the structural reinforcement material.[216]

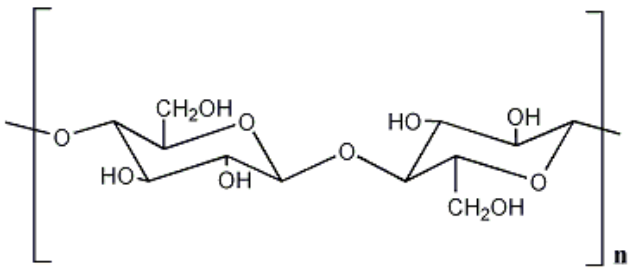

Figure 1.12. Chemical structure of cellulose

Natural cellulose contains both amorphous and crystalline regions. In natural cellulosic material, the crystalline cellulose portions are embedded in a matrix which can be mainly the amorphous cellulose. This is the case for cotton. In the case of wood, the amorphous matrix is mainly composed of lignin and hemicellulose, in simplified terms.[216] Although applications are found for cellulosic materials of different sizes, the use of natural cellulose is generally limited to the aforementioned cases (building and clothing). For more sophisticated utilization of cellulosic materials, the natural material is usually broken down to smaller units, so that further processing becomes much easier due to higher accessible surface area.

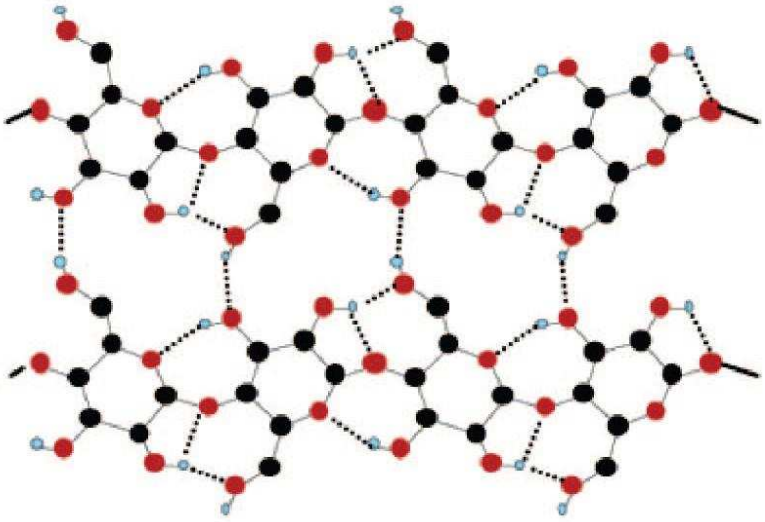

Figure 1.13. Lateral hydrogen bonding model for the cellulose I_β (which is present for cotton) allomorph. Red circles denote oxygen atoms, black circles are carbon atoms and blue circles are the hydrogen bonding-participating hydrogen atoms. Figure from Sturcova et al. 2004.[217]

In this project, cellulose is utilized in its crystalline form, which is the product after the removal of the amorphous fractions. This crystalline form of cellulose is also widely referred to as cellulose nanowhiskers or cellulose

nanocrystals (CNXLs). For clarity, CNXLs will be used through out the rest of this thesis. CNXLs are bundles of cellulose molecules stabilized laterally by hydrogen bonds formed between hydroxyl groups and oxygens of adjacent molecules to form the crystalline fibres (Figure 1.13). The bonds are formed as the cellulose molecules are synthesized in parallel by enzymes.[216,218] The separation or extraction of CNXLs from the amorphous regions is accomplished by acid hydrolysis. In this mass transfer controlled process, the amorphous regions are preferentially hydrolyzed due to lower density and higher free volume accessibility, and the resulting solids are CNXLs.[219,220] The applications of CNXLs will be the main focus in this introduction due to their direct relevance to this work. Figure 1.14 shows the cross-section of a cotton-derived CNXL.

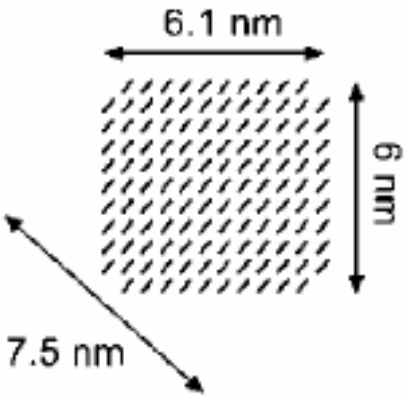

Figure 1.14. Cross section of an elementary CNXL derived from cotton, deduced from the analysis of peak broadening in wide angle X-ray scattering profiles. Figure adapted from Elazzouzi-Hafraoui et al. 2008.[221]

For different sources of cellulose and acids used for the hydrolysis process, CNXLs of different size and shapes (Figure 1.15) can be produced. Common sources of cellulose for extraction of CNXLs include cotton and

tunicates.[216] The CNXLs prepared by H_2SO_4 hydrolysis present a negatively charged surface, while those prepared by HCl hydrolysis are not charged.[222] The negatively charged surface of the CNXLs arise from substitution of some of the primary hydroxyl groups on the CNXLs by sulfate groups as a side reaction of the hydrolysis process, introducing surface sulfate half esters ($ROSO_3^-$) on the CNXLs. The surface sulphate half esters de-protonate easily to give negatively charged surfaces on the CNXLs. The negatively charged surfaces enable stabilisation of aqueous dispersion of CNXLs.[223] Other than acid hydrolysis, enzymatic reactions are also commonly used for the extraction of CNXLs, in which the disordered portions of the natural material are preferentially hydrolysed. The conditions used for the enzymatic reaction can also result in CNXLs of different lengths.[224]

Figure 1.15 shows the rod-like structures of CNXLs from different sources resulting in different dimensions. It has been shown that these CNXLs have rectangular cross-sections.[221] For example, an elementary crystallite of CNXLs derived from cotton has a cross sectional dimension of 6.1 nm x 6 nm (Figure 1.14) and that of tunicin-derived CNXLs is 12 nm x 10 nm.[221] Lengths of CNXLs can range from 100 nm to several microns. As they are made of straight chains of polysaccharides and contain practically no defects, these elementary CNXLs are very strong. CNXLs have modulus values similar to those of aramid fibers such as Kevlar (100 - 150 GPa), and strength on the order of 10 GPa.[216,225,226] There are wide fundamental and industrial interests for the exceptional strength and the nano-dimensions of CNXLs; they have been popular structural enhancing components in construction materials[227,228] and composites.[218,219,223,229-241] Furthermore, because these particles are

naturally occurring, stable and believed to be physiologically inert, they also have good potential for applications in the pharmaceuticals and food industry,[216] separation of biomolecules[242] and purification of proteins.[243]

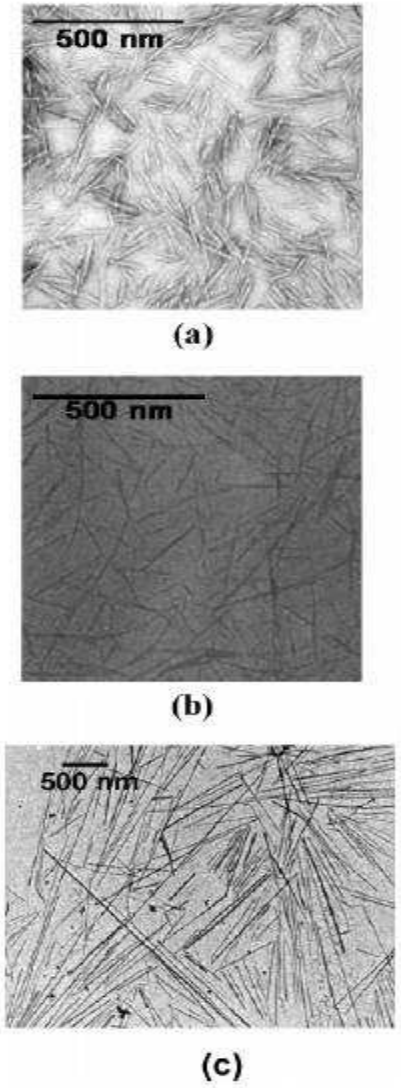

Figure 1.15. Transmission electron micrograph from a dilute suspension of hydrolyzed (a) cotton, (b) sugar-beet pulp and (c) tunicin. Figure from Samir et al. 2005.[216]

CNXLs have been used to make composites with a wide range of polymers. For example, composites of CNXLs with polyethylene glycol,[233] chitosan,[244] polyallylamine hydrochloride,[234] polylactic acid,[245] poly(methyl vinyl ether-co-maleic acid),[246] poly(diallyldimethylammonium

chloride) (PDDAC),[240] cellulose acetate-butyrate and rubber,[247] poly(styrene-co-hexylacrylate),[248] starch,[249] polystyrene,[250] polycaprolactone,[229,251,252] and a range of oligoether chains[253] have been reported. Solution casting is the most common method for producing CNXL-polymer composites. The compatibility of the CNXLs towards the polymer matrix is very important as the polymers used are often hydrophobic and have poor compatibility with CNXLs. This may result in a poor CNXL/matrix interface and, consequently, poor mechanical properties.[253] The shortcoming can be overcome by increasing the hydrophobicity of CNXLs,[230,254] by grafting reactive groups on CNXLs to form covalent linkage with the matrix,[247] by mixing in a compatible solvent,[233] or by grafting the polymers onto CNXL surfaces.[229,250,252,255] By grafting polymers onto CNXL surfaces, the compatibility issue is eradicated as the polymer is introduced as the surface functionality of the CNXL.

High toughness papers have been prepared by vacuum filtration of an aqueous dispersion of CNXLs (0.2 wt%) and subsequent drying under applied pressure.[224] The CNXLs formed a porous network structure in the nanopaper.[224] The overall structure displayed very high mechanical performance, which was dependent on the lengths of the individual CNXLs and the relative porosity of the paper.[224] Transparent nanopaper has been made from CNXLs using a similar filtering and drying procedure, with an additional polishing step.[256] As the transparent CNXL paper is highly flexible and foldable, they are very attractive for use as substrate materials for manufacturing electronic devices, considering their exceptional mechanical properties.[256]

Owing to the high surface area and aspect ratio of CNXLs, they are very attractive materials for making aerogels. Aerogels composed of CNXLs (50 nm wide) have been made from either freeze-drying directly a CNXL hydrogel or a solvent exchanged CNXL hydrogel (alcogel).[257] The aerogels displayed specific surface area of 70 - 120 $m^2 g^{-1}$ and 160 - 190 $m^2 g^{-1}$, respectively.[257] The pore collapsing caused by freeze-drying was reduced significantly when the drying was performed in a supercritical carbon dioxide environment.[258] The resulting aerogel displayed average specific surface area above 400 $m^2 g^{-1}$.[258] It is however note worthy that the lateral dimensions for the CNXL used in this case was also smaller, which translate to a higher surface area.[258]

The high density of surface hydroxyl functionalities on CNXLs can be very useful when they are modified. One of the simplest surface modifications takes place during the H_2SO_4 hydrolysis of a native cellulose species, where some of the surface hydroxyls are substituted with sulfate half esters. Acetate and butyrate functionalities are also easily attached onto the surface of CNXLs by similar substitution which takes place during the CNXL extraction using acetic acid or butyric acid hydrolysis.[241,254] The surface hydroxyls can be converted to either aldehyde[259] or carboxylate[260-262] functionalities by subjecting the CNXLs to a 2,2,4,4-tetramethylpiperidinyl-1-oxyl (TEMPO)-mediated oxidation process, but the former case was achieved only under careful control. TEMPO-mediated oxidised CNXLs have became a class of most widely studied CNXLs,[260,262-264] and have been applied in many different areas. For example, as templates for silver nanoparticle deposition,[265] to make transparent gas-insulating films[266] and to make and support nanocomposite oxygen reduction electrocatalysts.[267] The fabrication of pH sensing CNXLs

has also been reported where CNXLs are grafted with pH sensitive fluorophores.[268] An imidazolium salt was also grafted to CNXLs to give high anionic absorption or exchange capabilities.[269]

Stable and rigid films of CNXLs have also been formed on glassy carbon electrodes for electrochemical studies. The CNXL films demonstrated permselectivity based on charge and possibilities of utilising the negative surface charge on CNXLs for electrochemical applications.[223] Composite films of CNXLs and poly-(diallyldimethylammoniumchloride) (PDDAC) were formed on the surface of a glassy carbon electrode for the accumulation and detection of triclosan, an antibacterial and antifungal agent.[240] PDDAC was readily embedded into the network of hydrogen bonded CNXLs and imparted anion permselectivity to allow binding and transport of hydrophobic anions.[240] Later, CNXL-chitosan composite film electrodes were fabricated to study the competitive binding of triclosan, $Fe(CN)_6^{3-/4-}$ and sodium dodecylsulfate surfactant.[270] CNXLs have also been modified with boronic acid dendrimers, for electrochemical sensing purposes.[239] Thin carbon film electrodes were made using a simple procedure of pyrolysing a CNXL film formed by drop coating on ITO electrodes.[271] Notably, most, if not all of the renewable carbon precursors used to make porous carbon for supercapacitor applications are cellulosic-based.

At present, most of the research articles still cite cost and environmental friendliness as the main attractiveness of cellulose. The case always holds true when considering the preparation and/or manufacturing products which contain cellulose. However, the importance of cost becomes secondary if the materials are not useful. It becomes easy to forget that these cellulosic

materials are genuinely functional, or may outperform any other similar materials derived from non-sustainable resources, which means they are indeed practical. All of the advantages ascribed to CNXLs mentioned above, such as high specific surface area, high surface functionalities and exceptional mechanical properties are utilized in the work described in this thesis.

1.2. Project objectives

As discussed previously, the development of energy storage systems is becoming ever more important. Supercapacitor devices allow a considerable amount of stored energy to be delivered rapidly, giving rise to high power capability in conjunction with medium to high energy storage density. Such versatile characteristics of supercapacitors make them a very attractive class of devices. Carbon, metal oxides and ECPs are the most common materials used for the construction of supercapacitors. Of course, none of these materials are ideal, and each of them has advantages and shortcomings. In case of the shortcomings, some may be circumvented however others are inherent to the material itself.

The advantages of ECPs are generally associated with their high conductivity, high capacitance, flexibility and ease of fabrication. The downside of using these materials however, is the relatively poor stability, ascribed to their structural weakness. The poor stability can be improved by making a more porous structure which enhances electrolyte transport and reduces stress and volumetric changes on the material during potential cycling,

and at the same time improving their capacitance performance. When the porous structure is achieved by forming ECP composites with CNTs, the stability enhancement was enormous as CNTs also donate strength towards the composite.[168] Of course, the capacitance performance of the ECP-CNT composites is also improved in comparison with the ECP counterpart.[168]

Considering all the pre-requisites in order to use CNTs for the formation of ECP-CNT composites, CNXLs can offer an alternative as the ECP filler material. For example, CNXLs have extraordinary strength (at the same order of magnitude as CNTs) and have linear nanofibrillar structure which can aid the formation of open porous network with high specific surface area. Most importantly, negatively charged functionalities can be easily introduced to the CNXL exterior. The cost and environmental benefits of applying CNXLs in comparison to any other materials are beyond doubt, but such consideration comes after proving the usefulness of the ECP-CNXL composites.

The present investigation begins with the fabrication of an ECP-CNXL composite by co-electrochemical deposition. PPy is chosen as the first ECP for the study as the monomer is soluble in water, and as it is the weakest of the commonly used ECPs. Thin and thick PPy-CNXL films will be tested as the properties of ECP films may vary significantly for films of different thicknesses. Comparison is made against PPy films containing a small anion (Cl^-) electrodeposited using a smilar procedure. The cycling stability is also compared against an electrochemically co-deposited PPy-CNT composite, which is considered state-of-the-art at present.[168] The study then extends into making CNXL composites with PANi and PEDOT. A laboratory prototype symmetric supercapacitor made of PPy-CNXL is also assembled and tested.

Specific energy calculations are performed for the prototype supercapacitor. However, optimum application of such electrode materials in supercapacitors may be achieved using the asymmetric configuration as discussed in the introduction.

1.3. References

1. P. Simon and Y. Gogotsi, Nat. Mater., 2008, **7**, 845-854.
2. R. Kotz and M. Carlen, Electrochim. Acta, 2000, **45**, 2483-2498.
3. M. Winter and R. J. Brodd, Chem. Rev., 2004, **104**, 4245-4269.
4. B. Frenzel, P. Kurzweil and H. Roennebeck, J. Power Sources, 2011, **196**, 5364-5376.
5. R. Kotz, S. Muller, M. Bartschi, B. Schnyder, P. Dietrich, F. N. Buchi, A. Tsukada, G. G. Scherer, P. Rodatz, O. Garcia, P. Barrade, V. Hermann and R. Gallay, in Batteries and Supercapacitors, 2003, pp. 564-575.
6. A. K. Shukla, C. L. Jackson and K. Scott, Bull. Mater. Sci., 2003, **26**, 207-214.
7. G. Pede, A. Iacobazzi, S. Passerini, A. Bobbio and G. Botto, J. Power Sources, 2004, **125**, 280-291.
8. M. Mastragostino and F. Soavi, J. Power Sources, 2007, **174**, 89-93.
9. D. Iannuzzi and Ieee, in Iecon 2007: 33rd Annual Conference of the Ieee Industrial Electronics Society, Vols 1-3, Conference Proceedings, Ieee, New York, 2007, pp. 539-544.
10. D. Iannuzzi and P. Tricoli, in SPEEDAM 2010 International Symposium on Power Electronics, Electrical Drives, Automation and Motion, Pisa, Italy, 2010.
11. V. Khomenko, E. Raymundo-Pinero and F. Beguin, J. Power Sources, 2006, **153**, 183-190.
12. A. G. Pandolfo and A. F. Hollenkamp, J. Power Sources, 2006, **157**, 11-27.
13. M.-x. Wang, C.-y. Wang, M.-m. Chen, Y.-s. Wang, Z.-q. Sh, X. Du, T.-q. Li and Z.-j. Hu, New Carbon Materials, 2010, **25**, 285-290.
14. Q. Cheng, J. Tang, J. Ma, H. Zhang, N. Shinya and L. C. Qin, Carbon, 2011, **49**, 2917-2925.
15. V. Khomenko, E. Raymundo-Pinero, E. Frackowiak and F. Beguin, Appl. Phys. A: Mater. Sci. Process., 2006, **82**, 567-573.
16. T. Brousse, P.-L. Taberna, O. Crosnier, R. Dugas, P. Guillemet, Y. Scudeller, Y. Zhou, F. Favier, D. Belanger and P. Simon, J. Power Sources, 2007, **173**, 633-641.

17. D. Villers, D. Jobin, C. Soucy, D. Cossement, R. Chahine, L. Breau and D. Belanger, J. Electrochem. Soc., 2003, **150**, A747-A752.
18. K. S. Ryu, Y. G. Lee, Y. S. Hong, Y. J. Park, X. L. Wu, K. M. Kim, M. G. Kang, N. G. Park and S. H. Chang, Electrochim. Acta, 2004, **50**, 843-847.
19. E. Frackowiak, V. Khomenko, K. Jurewicz, K. Lota and F. Beguin, J. Power Sources, 2006, **153**, 413-418.
20. K. C. Ng, S. W. Zhang, C. Peng and G. Z. Chen, J. Electrochem. Soc., 2009, **156**, A846-A853.
21. T. Brousse and D. Belanger, Electrochem. Solid-State Lett., 2003, **6**, A244-A248.
22. S. Zhang, C. Peng, K. C. Ng and G. Z. Chen, Electrochim. Acta, 2010, **55**, 7447-7453.
23. J. P. Zheng and T. R. Jow, J. Power Sources, 1996, **62**, 155-159.
24. B. E. Conway, V. Birss and J. Wojtowicz, J. Power Sources, 1997, **66**, 1-14.
25. E. Frackowiak and F. Beguin, Carbon, 2001, **39**, 937-950.
26. C. Peng, Electrochemical synthesis of composites of conducting polymers and carbon anotubes for supercapacitors, The University of Nottingham, Nottingham, 2007.
27. B. E. Conway and W. G. Pell, J. Solid State Electrochem., 2003, **7**, 637-644.
28. B. E. Conway, J. Electrochem. Soc., 1991, **138**, 1539-1548.
29. P. W. Ruch, L. J. Hardwick, M. Hahn, A. Foelske, R. Koetz and A. Wokaun, Carbon, 2009, **47**, 38-52.
30. M. S. Michael and S. R. S. Prabaharan, J. Power Sources, 2004, **136**, 250-256.
31. C.-W. Huang, C.-H. Hsu, P.-L. Kuo, C.-T. Hsieh and H. Teng, Carbon, 2011, **49**, 895-903.
32. T. Morishita, Y. Soneda, T. Tsumura and M. Inagaki, Carbon, 2006, **44**, 2360-2367.
33. H. S. Ye, X. Liu, H. F. Cui, W. D. Zhang, F. S. Sheu and T. M. Lim, Electrochem. Commun., 2005, **7**, 249-255.
34. Y. P. Guo, J. R. Qi, Y. Q. Jiang, S. F. Yang, Z. C. Wang and H. D. Xu, Mater. Chem. Phys., 2003, **80**, 704-709.
35. C. S. Li, D. Z. Wang, T. X. Liang, X. F. Wang and L. Ji, Mater. Lett., 2004, **58**, 3774-3777.
36. D. Y. Qu, J. Power Sources, 2002, **109**, 403-411.
37. C.-C. Hu, J.-H. Su and T.-C. Wen, J. Phys. Chem. Solids, 2007, **68**, 2353-2362.
38. P. Sharma and T. S. Bhatti, Energy Conversion and Management, 2010, **51**, 2901-2912.
39. C. Peng, S. W. Zhang, D. Jewell and G. Z. Chen, Prog. Nat. Sci., 2008, **18**, 777-788.
40. G. A. Snook, P. Kao and A. S. Best, J. Power Sources, 2011, **196**, 1-12.
41. S. K. Meher and G. R. Rao, J. Phys. Chem. C, 2011, **115**, 15646-15654.
42. J. W. Lang, X. B. Yan and Q. J. Xue, J. Power Sources, 2011, **196**, 7841-7846.

43. C. Yuan, X. Zhang, L. Su, B. Gao and L. Shen, J. Mater. Chem., 2009, **19**, 5772-5777.
44. M. E. Roberts, D. R. Wheeler, B. B. McKenzie and B. C. Bunker, J. Mater. Chem., 2009, **19**, 6977-6979.
45. R. K. Sharma, A. C. Rastogi and S. B. Desu, Electrochem. Commun., 2008, **10**, 268-272.
46. G. Wee, H. Z. Soh, Y. L. Cheah, S. G. Mhaisalkar and M. Srinivasan, J. Mater. Chem., 2010, **20**, 6720-6725.
47. D. Zhang, X. Zhang, Y. Chen, P. Yu, C. Wang and Y. Ma, J. Power Sources, 2011, **196**, 5990-5996.
48. J. H. Park and O. O. Park, J. Power Sources, 2002, **111**, 185-190.
49. T. E. Rufford, D. Hulicova-Jurcakova, Z. H. Zhu and G. Q. Lu, Electrochem. Commun., 2008, **10**, 1594-1597.
50. Y. Zhu, S. Murali, M. D. Stoller, K. J. Ganesh, W. Cai, P. J. Ferreira, A. Pirkle, R. M. Wallace, K. A. Cychosz, M. Thommes, D. Su, E. A. Stach and R. S. Ruoff, Science, 2011, **332**, 1537-1541.
51. J. H. Jang, K. Machida, Y. Kim and K. Naoi, Electrochim. Acta, 2006, **52**, 1733-1741.
52. Y. Wang, Z. Shi, Y. Huang, Y. Ma, C. Wang, M. Chen and Y. Chen, J. Phys. Chem. C, 2009, **113**, 13103-13107.
53. K. Wang, J. Huang and Z. Wei, J. Phys. Chem. C, 2010, **114**, 8062-8067.
54. N. Nagarajan, M. Cheong and I. Zhitomirsky, Mater. Chem. Phys., 2007, **103**, 47-53.
55. Z.-A. Hu, Y.-L. Xie, Y.-X. Wang, L.-P. Mo, Y.-Y. Yang and Z.-Y. Zhang, Mater. Chem. Phys., 2009, **114**, 990-995.
56. Q. Hao, H. Wang, X. Yang, L. Lu and X. Wang, Nano Research, 2011, **4**, 323-333.
57. I. H. Kim, J. H. Kim, B. W. Cho and K. B. Kim, J. Electrochem. Soc., 2006, **153**, A1451-A1458.
58. V. Gupta and N. Miura, Electrochem. Solid-State Lett., 2005, **8**, A630-A632.
59. Z. Y. Lin, Y. Liu, Y. G. Yao, O. J. Hildreth, Z. Li, K. Moon and C. P. Wong, J. Phys. Chem. C, 2011, **115**, 7120-7125.
60. V. Gupta and N. Miura, Electrochim. Acta, 2006, **52**, 1721-1726.
61. L. L. Zhang and X. S. Zhao, Chem. Soc. Rev., 2009, **38**, 2520-2531.
62. G. Pognon, T. Brousse and D. Belanger, Carbon, 2011, **49**, 1340-1348.
63. D. Lozano-Castello, D. Cazorla-Amoros, A. Linares-Solano, S. Shiraishi, H. Kurihara and A. Oya, Carbon, 2003, **41**, 1765-1775.
64. L. Wei, M. Sevilla, A. B. Fuertes, R. Mokaya and G. Yushin, Adv. Energy Mater., 2011, **1**, 356-361.
65. F. C. Wu, R. L. Tseng, C. C. Hu and C. C. Wang, J. Power Sources, 2004, **138**, 351-359.
66. Y. J. Kim, Y. Horle, Y. Matsuzawa, S. Ozaki, M. Endo and M. S. Dresselhaus, Carbon, 2004, **42**, 2423-2432.
67. C.-C. Hu, C.-C. Wang, F.-C. Wu and R.-L. Tseng, Electrochim. Acta, 2007, **52**, 2498-2505.
68. D. Hulicova-Jurcakova, M. Seredych, G. Q. Lu and T. J. Bandosz, Adv. Funct. Mater., 2009, **19**, 438-447.

69. Y. J. Kim, B. J. Lee, H. Suezaki, T. Chino, Y. Abe, T. Yanagiura, K. C. Park and M. Endo, Carbon, 2006, **44**, 1592-1595.
70. M. P. Bichat, E. Raymundo-Pinero and F. Beguin, Carbon, 2010, **48**, 4351-4361.
71. C. T. Hsieh and H. Teng, Carbon, 2002, **40**, 667-674.
72. L. Li, E. Liu, J. Li, Y. Yang, H. Shen, Z. Huang, X. Xiang and W. Li, J. Power Sources, 2010, **195**, 1516-1521.
73. F. B. Su, C. K. Poh, J. S. Chen, G. W. Xu, D. Wang, Q. Li, J. Y. Lin and X. W. Lou, Energy Environ. Sci., 2011, **4**, 717-724.
74. S. Shiraishi, H. Kurihara, H. Tsubota, A. Oya, Y. Soneda and Y. Yamada, Electrochem. Solid-State Lett., 2001, **4**, A5-A8.
75. H. S. Teng, Y. J. Chang and C. T. Hsieh, Carbon, 2001, **39**, 1981-1987.
76. W. Xing, S. Z. Qiao, R. G. Ding, F. Li, G. Q. Lu, Z. F. Yan and H. M. Cheng, Carbon, 2006, **44**, 216-224.
77. Q. Li, R. Jiang, Y. Dou, Z. Wu, T. Huang, D. Feng, J. Yang, A. Yu and D. Zhao, Carbon, 2011, **49**, 1248-1257.
78. C. Portet, Z. Yang, Y. Korenblit, Y. Gogotsi, R. Mokaya and G. Yushin, J. Electrochem. Soc., 2009, **156**, A1-A6.
79. Y. Z. Wei, B. Fang, S. Iwasa and M. Kumagai, J. Power Sources, 2005, **141**, 386-391.
80. S. T. Mayer, R. W. Pekala and J. L. Kaschmitter, J. Electrochem. Soc., 1993, **140**, 446-451.
81. K. Honda, T. N. Rao, D. A. Tryk, A. Fujishima, M. Watanabe, K. Yasui and H. Masuda, J. Electrochem. Soc., 2000, **147**, 659-664.
82. D. Y. Qu and H. Shi, J. Power Sources, 1998, **74**, 99-107.
83. G. Lota, T. A. Centeno, E. Frackowiak and F. Stoeckli, Electrochim. Acta, 2008, **53**, 2210-2216.
84. O. Barbieri, M. Hahn, A. Herzog and R. Kotz, Carbon, 2005, **43**, 1303-1310.
85. V. Ruiz, C. Blanco, E. Raymundo-Pinero, V. Khomenko, F. Beguin and R. Santamaria, Electrochim. Acta, 2007, **52**, 4969-4973.
86. X. X. Xiang, E. H. Liu, L. M. Li, Y. J. Yang, H. J. Shen, Z. Z. Huang and Y. Y. Tian, J. Solid State Electrochem., 2011, **15**, 579-585.
87. Y. Tian, J. Yan, R. Xue and B. Yi, J. Electrochem. Soc., 2011, **158**, A818-A821.
88. J. I. Kim and S. J. Park, J. Solid State Chem., 2011, **184**, 2184-2189.
89. C.-T. Hsieh, S.-M. Hsu, J.-Y. Lin and H. Teng, J. Phys. Chem. C, 2011, **115**, 12367-12374.
90. Y. Q. Sun, Q. O. Wu and G. Q. Shi, Energy Environ. Sci., 2011, **4**, 1113-1132.
91. Z. Lei, N. Christov and X. S. Zhao, Energy Environ. Sci., 2011, **4**, 1866-1873.
92. J. J. Yoo, K. Balakrishnan, J. Huang, V. Meunier, B. G. Sumpter, A. Srivastava, M. Conway, A. L. M. Reddy, J. Yu, R. Vajtai and P. M. Ajayan, Nano Lett., 2011, **11**, 1423-1427.
93. S. Shiraishi, M. Kibe, T. Yokoyama, H. Kurihara, N. Patel, A. Oya, Y. Kaburagi and Y. Hishiyama, Appl. Phys. A: Mater. Sci. Process., 2006, **82**, 585-591.

94. M. Endo, Y. J. Kim, T. Chino, O. Shinya, Y. Matsuzawa, H. Suezaki, K. Tantrakarn and M. S. Dresselhaus, Appl. Phys. A: Mater. Sci. Process., 2006, **82**, 559-565.
95. S. Shiraishi, H. Kurihara, K. Okabe, D. Hulicova and A. Oya, Electrochem. Commun., 2002, **4**, 593-598.
96. M. D. Stoller, S. Park, Y. Zhu, J. An and R. S. Ruoff, Nano Lett., 2008, **8**, 3498-3502.
97. G. Milczarek, A. Ciszewski and I. Stepniak, J. Power Sources, 2011, **196**, 7882-7885.
98. D. A. C. Brownson and C. E. Banks, Analyst, 2010, **135**, 2768-2778.
99. D. A. C. Brownson, D. K. Kampouris and C. E. Banks, J. Power Sources, 2011, **196**, 4873-4885.
100. B. J. Yoon, S. H. Jeong, K. H. Lee, H. S. Kim, C. G. Park and J. H. Han, Chem. Phys. Lett., 2004, **388**, 170-174.
101. S. H. Aboutalebi, A. T. Chidembo, M. Salari, K. Konstantinov, D. Wexler, H. K. Liu and S. X. Dou, Energy Environ. Sci., 2011, **4**, 1855-1865.
102. M. Peckerar, Z. Dilli, M. Dornajafi, N. Goldsman, N. Yves, R. B. Proctor, B. J. Krupsaw and D. A. Lowy, Energy Environ. Sci., 2011, **4**, 1807-1812.
103. Y. U. Jeong and A. Manthiram, J. Electrochem. Soc., 2001, **148**, A189-A193.
104. V. Srinivasan and J. W. Weidner, J. Power Sources, 2002, **108**, 15-20.
105. M. Z. Dai, L. Y. Song, J. T. LaBelle and B. D. Vogt, Chem. Mater., 2011, **23**, 2869-2878.
106. C. M. Wu, C. Y. Fan, I. W. Sun, W. T. Tsai and J. K. Chang, J. Power Sources, 2011, **196**, 7828-7834.
107. J. H. Park, O. O. Park, K. H. Shin, C. S. Jin and J. H. Kim, Electrochem. Solid-State Lett., 2002, **5**, H7-H10.
108. N. W. Duffy, W. Baldsing and A. G. Pandolfo, Electrochim. Acta, 2008, **54**, 535-539.
109. V. Srinivasan and J. W. Weidner, J. Electrochem. Soc., 2000, **147**, 880-885.
110. J. Cheng, G.-P. Cao and Y.-S. Yang, J. Power Sources, 2006, **159**, 734-741.
111. W. F. W. W. F. Wei, X. W. Cui, W. X. Chen and D. G. Ivey, Chem. Soc. Rev., 2011, **40**, 1697-1721.
112. S. Yoon, E. Kang, J. K. Kim, C. W. Lee and J. Lee, Chem. Commun., 2011, **47**, 1021-1023.
113. B.-X. Zou, Y. Liang, X.-X. Liu, D. Diamond and K.-T. Lau, J. Power Sources, 2011, **196**, 4842-4848.
114. X. Du, C. Wang, M. Chen, Y. Jiao and J. Wang, J. Phys. Chem. C, 2009, **113**, 2643-2646.
115. M. Salari, K. Konstantinov and H. K. Liu, J. Mater. Chem., 2011, **21**, 5128-5133.
116. C.-T. Hsieh, C.-C. Chang, W.-Y. Chen and W.-M. Hung, J. Phys. Chem. Solids, 2009, **70**, 916-921.
117. A. Jayalakshmi, N. Venugopal, K. P. Raja and M. M. Rao, J. Power Sources, 2006, **158**, 1538-1543.
118. K. R. Prasad and N. Miura, Electrochem. Commun., 2004, **6**, 849-852.

119. I. H. Kim, J. H. Kim, B. W. Cho, Y. H. Lee and K. B. Kim, J. Electrochem. Soc., 2006, **153**, A989-A996.
120. D. Choi, G. E. Blomgren and P. N. Kumta, Adv. Mater., 2006, **18**, 1178-+.
121. G. Wang, L. Zhang and J. Zhang, Chem. Soc. Rev., 2011.
122. S. W. Zhang and G. Z. Chen, Energy Mater., 2008, **3**, 186-200.
123. J. H. Chae, K. C. Ng and G. Z. Chen, Proc. Inst. Mech. Eng. Part A-J. Power Energy, 2010, **224**, 479-503.
124. A. J. Bard and L. R. Faulkner, Electrochemical Methods: Fundamentals and Applications, John Wiley & Sons, 2001.
125. J. W. Long, K. E. Swider, C. I. Merzbacher and D. R. Rolison, Langmuir, 1999, **15**, 780-785.
126. C. K. Min, T. B. Wu, W. T. Yang and C. L. Li, Mater. Chem. Phys., 2009, **117**, 70-73.
127. C.-C. Hu, K.-H. Chang, M.-C. Lin and Y.-T. Wu, Nano Lett., 2006, **6**, 2690-2695.
128. J. P. Zheng, P. J. Cygan and T. R. Jow, J. Electrochem. Soc., 1995, **142**, 2699-2703.
129. B. Messaoudi, S. Joiret, M. Keddam and H. Takenouti, Electrochim. Acta, 2001, **46**, 2487-2498.
130. E. Raymundo-Pinero, V. Khomenko, E. Frackowiak and F. Beguin, J. Electrochem. Soc., 2005, **152**, A229-A235.
131. A. P. Malloy and S. W. Donne, J. Power Sources, 2008, **179**, 371-380.
132. M. Toupin, T. Brousse and D. Belanger, Chem. Mater., 2004, **16**, 3184-3190.
133. A. Yuan, M. Wang, Y. Wang and J. Hu, Electrochim. Acta, 2009, **54**, 1021-1026.
134. J. K. Chang and W. T. Tsai, J. Electrochem. Soc., 2003, **150**, A1333-A1338.
135. P. J. Hall, M. Mirzaeian, S. I. Fletcher, F. B. Sillars, A. J. R. Rennie, G. O. Shitta-Bey, G. Wilson, A. Cruden and R. Carter, Energy Environ. Sci., 2010, **3**, 1238-1251.
136. B. J. Lee, S. R. Sivakkumar, J. M. Ko, J. H. Kim, S. M. Jo and D. Y. Kim, J. Power Sources, 2007, **168**, 546-552.
137. J. M. Miller, B. Dunn, T. D. Tran and R. W. Pekala, J. Electrochem. Soc., 1997, **144**, L309-L311.
138. J. H. Park and O. O. Park, J. Power Sources, 2002, **109**, 121-126.
139. L.-M. Huang, H.-Z. Lin, T.-C. Wen and A. Gopalan, Electrochim. Acta, 2006, **52**, 1058-1063.
140. H. Lee, M. S. Cho, I. H. Kim, J. D. Nam and Y. Lee, Synth. Met., 2010, **160**, 1055-1059.
141. L. Chen, C. Z. Yuan, B. Gao, S. Y. Chen and X. G. Zhang, J. Solid State Electrochem., 2009, **13**, 1925-1933.
142. R. Y. Song, J. H. Park, S. R. Sivakkumar, S. H. Kim, J. M. Ko, D.-Y. Park, S. M. Jo and D. Y. Kim, J. Power Sources, 2007, **166**, 297-301.
143. J. Wen, X. Ruan and Z. Zhou, J. Phys. Chem. Solids, 2009, **70**, 816-820.
144. W. Sugimoto, K. Yokoshima, Y. Murakami and Y. Takasu, Electrochim. Acta, 2006, **52**, 1742-1748.

145. M. Min, K. Machida, J. H. Jang and K. Naoi, J. Electrochem. Soc., 2006, **153**, A334-A338.
146. L. L. Zhang, T. Wei, W. Wang and X. S. Zhao, Microporous Mesoporous Mater., 2009, **123**, 260-267.
147. B. Babakhani and D. G. Ivey, Electrochim. Acta, 2010, **55**, 4014-4024.
148. R. K. Sharma and L. Zhai, Electrochim. Acta, 2009, **54**, 7148-7155.
149. R. K. Sharma, H.-S. Oh, Y.-G. Shul and H. Kim, J. Power Sources, 2007, **173**, 1024-1028.
150. J. M. Ko and K. M. Kim, Mater. Chem. Phys., 2009, **114**, 837-841.
151. R. Amade, E. Jover, B. Caglar, T. Mutlu and E. Bertran, J. Power Sources, 2011, **196**, 5779-5783.
152. J. Yan, Z. Fan, T. Wei, W. Qian, M. Zhang and F. Wei, Carbon, 2010, **48**, 3825-3833.
153. J.-K. Chang, M.-T. Lee, C.-H. Huang and W.-T. Tsai, Mater. Chem. Phys., 2008, **108**, 124-131.
154. K. R. Prasad and N. Miura, Electrochem. Commun., 2004, **6**, 1004-1008.
155. C. Y. Lee, H. M. Tsai, H. J. Chuang, S. Y. Li, P. Lin and T. Y. Tseng, J. Electrochem. Soc., 2005, **152**, A716-A720.
156. M. S. Wu, Appl. Phys. Lett., 2005, **87**.
157. J. N. Broughton and M. J. Brett, Electrochim. Acta, 2005, **50**, 4814-4819.
158. P. Y. Chuang and C. C. Hu, Mater. Chem. Phys., 2005, **92**, 138-145.
159. Q. Huang, X. Wang and J. Li, Electrochim. Acta, 2006, **52**, 1758-1762.
160. V. Subramanian, H. W. Zhu and B. Q. Wei, Electrochem. Commun., 2006, **8**, 827-832.
161. B. Babakhani and D. G. Ivey, J. Power Sources, 2010, **195**, 2110-2117.
162. R. Liu, J. Duay, T. Lane and S. Bok Lee, Phys. Chem. Chem. Phys., 2010, **12**, 4309-4316.
163. E. Lust, A. Janes and M. Arulepp, J. Electroanal. Chem., 2004, **562**, 33-42.
164. A. J. Heeger, Chem. Soc. Rev., 2010, **39**, 2354-2371.
165. T. Sato, G. Masuda and K. Takagi, Electrochim. Acta, 2004, **49**, 3603-3611.
166. C. Largeot, C. Portet, J. Chmiola, P.-L. Taberna, Y. Gogotsi and P. Simon, J. Am. Chem. Soc., 2008, **130**, 2730-2731.
167. Y. W. Park, Chem. Soc. Rev., 2010, **39**, 2428-2438.
168. C. Peng, J. Jin and G. Z. Chen, Electrochim. Acta, 2007, **53**, 525-537.
169. J. W. Y. Lam and B. Z. Tang, Acc. Chem. Res., 2005, **38**, 745-754.
170. R. Huq and G. C. Farrington, J. Electrochem. Soc., 1984, **131**, 819-823.
171. V. Khomenko, E. Frackowiak and F. Beguin, Electrochim. Acta, 2005, **50**, 2499-2506.
172. D. Z. Zhou, G. M. Spinks, G. G. Wallace, C. Tiyapiboonchaiya, D. R. MacFarlane, M. Forsyth and J. Z. Sun, Electrochim. Acta, 2003, **48**, 2355-2359.
173. W. Lu, A. G. Fadeev, B. H. Qi, E. Smela, B. R. Mattes, J. Ding, G. M. Spinks, J. Mazurkiewicz, D. Z. Zhou, G. G. Wallace, D. R. MacFarlane, S. A. Forsyth and M. Forsyth, Science, 2002, **297**, 983-987.
174. E. Frackowiak, Phys. Chem. Chem. Phys., 2007, **9**, 1774-1785.

175. B. R. Saunders, R. J. Fleming and K. S. Murray, Chem. Mater., 1995, **7**, 1082-1094.
176. L. Z. Fan and J. Maier, Electrochem. Commun., 2006, **8**, 937-940.
177. K. Jurewicz, S. Delpeux, V. Bertagna, F. Beguin and E. Frackowiak, Chem. Phys. Lett., 2001, **347**, 36-40.
178. M. Hughes, G. Z. Chen, M. S. P. Shaffer, D. J. Fray and A. H. Windle, Chem. Mater., 2002, **14**, 1610-1613.
179. M. Hughes, G. Z. Chen, M. S. P. Shaffer, D. J. Fray and A. H. Windle, Composites Science and Technology, 2004, **64**, 2325-2331.
180. G. A. Snook, G. Z. Chen, D. J. Fray, M. Hughes and M. Shaffer, J. Electroanal. Chem., 2004, **568**, 135-142.
181. J.-H. Kim, Y.-S. Lee, A. K. Sharma and C. G. Liu, Electrochim. Acta, 2006, **52**, 1727-1732.
182. A. Liu, C. Li, H. Bai and G. Shi, J. Phys. Chem. C, 2010, **114**, 22783-22789.
183. L. L. Zhang, S. Zhao, X. N. Tian and X. S. Zhao, Langmuir, 2010, **26**, 17624-17628.
184. C. Peng, D. Hu and G. Z. Chen, Chem. Commun., 2011, **47**, 4105-4107.
185. H. Li, J. Wang, Q. Chu, Z. Wang, F. Zhang and S. Wang, J. Power Sources, 2009, **190**, 578-586.
186. M. Q. Wu, G. A. Snook, V. Gupta, M. Shaffer, D. J. Fray and G. Z. Chen, J. Mater. Chem., 2005, **15**, 2297-2303.
187. V. Gupta and N. Miura, Mater. Lett., 2006, **60**, 1466-1469.
188. H. Zhang, G. Cao, Z. Wang, Y. Yang, Z. Shi and Z. Gu, Electrochem. Commun., 2008, **10**, 1056-1059.
189. B. L. Groenendaal, F. Jonas, D. Freitag, H. Pielartzik and J. R. Reynolds, Adv. Mater., 2000, **12**, 481-494.
190. K. Lota, V. Khomenko and E. Frackowiak, J. Phys. Chem. Solids, 2004, **65**, 295-301.
191. D. S.-S. John, K. W. Cynthia, A. Nicole, P. C. Andrew, Z. Kyukwan and R. R. John, J. Electrochem. Soc., 2002, **149**, A973-A977.
192. R. Marcilla, F. Alcaide, H. Sardon, J. A. Pomposo, C. Pozo-Gonzalo and D. Mecerreyes, Electrochem. Commun., 2006, **8**, 482-488.
193. K. Liu, Z. L. Hu, R. Xue, J. R. Zhang and J. J. Zhu, J. Power Sources, 2008, **179**, 858-862.
194. G. A. Snook, C. Peng, D. J. Fray and G. Z. Chen, Electrochem. Commun., 2007, **9**, 83-88.
195. R. Liu, S. Il Cho and S. B. Lee, Nanotechnology, 2008, **19**.
196. K. Zhang, L. L. Zhang, X. S. Zhao and J. Wu, Chem. Mater., 2010, **22**, 1392-1401.
197. D. Y. Liu and J. R. Reynolds, ACS Applied Materials & Interfaces, 2010, **2**, 3586-3593.
198. J. D. Stenger-Smith, C. K. Webber, N. Anderson, A. P. Chafin, K. K. Zong and J. R. Reynolds, J. Electrochem. Soc., 2002, **149**, A973-A977.
199. J. Pecher and S. Mecking, Chem. Rev., 2010, **110**, 6260-6279.
200. J. r. Heinze, B. A. Frontana-Uribe and S. Ludwigs, Chem. Rev., 2010, **110**, 4724-4771.
201. P. S. Patil and L. D. Kadam, Appl. Surf. Sci., 2002, **199**, 211-221.
202. S. G. Kandalkar, C. D. Lokhande, R. S. Mane and S.-H. Han, Appl. Surf. Sci., 2007, **253**, 3952-3956.

203. H. Talbi, P. E. Just and L. H. Dao, J. Appl. Electrochem., 2003, **33**, 465-473.
204. C. F. Zhou, S. Kumar, C. D. Doyle and J. M. Tour, Chem. Mater., 2005, **17**, 1997-2002.
205. W. K. Li, J. Chen, J. J. Zhao, J. R. Zhang and J. J. Zhu, Mater. Lett., 2005, **59**, 800-803.
206. A. M. P. Hussain and A. Kumar, J. Power Sources, 2006, **161**, 1486-1492.
207. R. K. Sharma, A. C. Rastogi and S. B. Desu, Electrochim. Acta, 2008, **53**, 7690-7695.
208. M. Selvakumar and D. K. Bhat, J. Appl. Polym. Sci., 2008, **107**, 2165-2170.
209. S. Biswas and L. T. Drzal, Chem. Mater., 2010, **22**, 5667-5671.
210. H. Gomez, M. K. Ram, F. Alvi, P. Villalba, E. Stefanakos and A. Kumar, J. Power Sources, 2011, **196**, 4102-4108.
211. A. K. Mohanty, M. Misra and G. Hinrichsen, Macromol. Mater. Eng., 2000, **276-277**, 1-24.
212. A. K. Mohanty, M. Misra and L. T. Drzal, J. Polym. Environ., 2002, **10**, 19-26.
213. J. P. H. van Wyk, Energy Fuels, 2002, **16**, 1277-1279.
214. R. P. Swatloski, S. K. Spear, J. D. Holbrey and R. D. Rogers, J. Am. Chem. Soc., 2002, **124**, 4974-4975.
215. A. Gandini, Green Chem., 2011, **13**, 1061-1083.
216. M. Samir, F. Alloin and A. Dufresne, Biomacromolecules, 2005, **6**, 612-626.
217. A. Sturcova, I. His, D. C. Apperley, J. Sugiyama and M. C. Jarvis, Biomacromolecules, 2004, **5**, 1333-1339.
218. S. J. Eichhorn, C. A. Baillie, N. Zafeiropoulos, L. Y. Mwaikambo, M. P. Ansell, A. Dufresne, K. M. Entwistle, P. J. Herrera-Franco, G. C. Escamilla, L. Groom, M. Hughes, C. Hill, T. G. Rials and P. M. Wild, J. Mater. Sci., 2001, **36**, 2107-2131.
219. N. L. G. de Rodriguez, W. Thielemans and A. Dufresne, Cellulose, 2006, **13**, 261-270.
220. S. Beck-Candanedo, M. Roman and D. G. Gray, Biomacromolecules, 2005, **6**, 1048-1054.
221. S. Elazzouzi-Hafraoui, Y. Nishiyama, J. L. Putaux, L. Heux, F. Dubreuil and C. Rochas, Biomacromolecules, 2008, **9**, 57-65.
222. J. Araki, M. Wada, S. Kuga and T. Okana, J. Wood Sci., 1999, **45**, 258-261.
223. W. Thielemans, C. R. Warbey and D. A. Walsh, Green Chem., 2009, **11**, 531-537.
224. M. Henriksson, L. A. Berglund, P. Isaksson, T. Lindstrom and T. Nishino, Biomacromolecules, 2008, **9**, 1579-1585.
225. A. Sturcova, G. R. Davies and S. J. Eichhorn, Biomacromolecules, 2005, **6**, 1055-1061.
226. R. Rusli and S. J. Eichhorn, Appl. Phys. Lett., 2008, **93**.
227. P. J. Kim, H. C. Wu, Z. Lin, V. C. Li, B. deLhoneux and S. A. S. Akers, Cem. Concr. Res., 1999, **29**, 201-208.
228. A. S. Herrmann, J. Nickel and U. Riedel, Polym. Degrad. Stab., 1998, **59**, 251-261.

229. G. Siqueira, J. Bras and A. Dufresne, Biomacromolecules, 2009, **10**, 425-432.
230. S. J. Eichhorn, A. Dufresne, M. Aranguren, N. E. Marcovich, J. R. Capadona, S. J. Rowan, C. Weder, W. Thielemans, M. Roman, S. Renneckar, W. Gindl, S. Veigel, J. Keckes, H. Yano, K. Abe, M. Nogi, A. N. Nakagaito, A. Mangalam, J. Simonsen, A. S. Benight, A. Bismarck, L. A. Berglund and T. Peijs, J. Mater. Sci., 2010, **45**, 1-33.
231. Y. Habibi, L. A. Lucia and O. J. Rojas, Chem. Rev., 2010, **110**, 3479-3500.
232. J. R. Capadona, K. Shanmuganathan, S. Triftschuh, S. Seidel, S. J. Rowan and C. Weder, Biomacromolecules, 2009, **10**, 712-716.
233. M. Samir, F. Alloin, J. Y. Sanchez, N. El Kissi and A. Dufresne, Macromolecules, 2004, **37**, 1386-1393.
234. B. Jean, F. Dubreuil, L. Heux and F. Cousin, Langmuir, 2008, **24**, 3452-3458.
235. L. Johnson, W. Thielemans and D. A. Walsh, J. Mater. Chem., 2010, **20**, 1737-1743.
236. B. Braun, J. R. Dorgan and J. P. Chandler, Biomacromolecules, 2008, **9**, 1255-1263.
237. Y. Habibi, A. L. Goffin, N. Schiltz, E. Duquesne, P. Dubois and A. Dufresne, J. Mater. Chem., 2008, **18**, 5002-5010.
238. I. Kvien, J. Sugiyama, M. Votrubec and K. Oksman, J. Mater. Sci., 2007, **42**, 8163-8171.
239. M. J. Bonne, E. Galbraith, T. D. James, M. J. Wasbrough, K. J. Edler, A. T. A. Jenkins, M. Helton, A. McKee, W. Thielemans, E. Psillakis and F. Marken, J. Mater. Chem., 2010, **20**, 588-594.
240. M. J. Bonne, K. J. Edler, J. G. Buchanan, D. Wolverson, E. Psillakis, M. Helton, W. Thielemans and F. Marken, J. Phys. Chem. C, 2008, **112**, 2660-2666.
241. M. J. Sobkowicz, B. Braun and J. R. Dorgan, Green Chem., 2009, **11**, 680-682.
242. M. Tabuchi and Y. Baba, Anal. Chem., 2005, **77**, 7090-7093.
243. J. Hong, X. Ye, Y. Wang and Y. H. P. Zhang, Anal. Chim. Acta, 2008, **621**, 193-199.
244. Q. Li, J. Zhou and L. Zhang, J. Polym. Sci., Part B: Polym. Phys., 2009, **47**, 1069-1077.
245. I. Kvien, B. r. S. Tanem and K. Oksman, Biomacromolecules, 2005, **6**, 3160-3165.
246. L. Goetz, A. Mathew, K. Oksman, P. Gatenholm and A. J. Ragauskas, Carbohydr. Polym., 2009, **75**, 85-89.
247. B. Ly, W. Thielemans, A. Dufresne, D. Chaussy and M. N. Belgacem, Composites Science and Technology, 2008, **68**, 3193-3201.
248. A. B. Elmabrouk, T. Wim, A. Dufresne and S. Boufi, J. Appl. Polym. Sci., 2009, **114**, 2946-2955.
249. A. P. Mathew, W. Thielemans and A. Dufresne, J. Appl. Polym. Sci., 2008, **109**, 4065-4074.
250. G. Morandi, L. Heath and W. Thielemans, Langmuir, 2009, **25**, 8280-8286.
251. M. Labet and W. Thielemans, Cellulose, 2011, **18**, 607-617.

252. O. Paquet, M. Krouit, J. Bras, W. Thielemans and M. N. Belgacem, Acta Mater., 2010, **58**, 792-801.
253. E. h. B. Ly, J. Bras, P. Sadocco, M. N. Belgacem, A. Dufresne and W. Thielemans, Mater. Chem. Phys., 2010, **120**, 438-445.
254. B. Braun and J. R. Dorgan, Biomacromolecules, 2009, **10**, 334-341.
255. M. Labet and W. Thielemans, Cellulose, 2011, **18**, 607-617.
256. M. Nog
271. A. Vuorema, M. Sillanpää, L. Rassaei, M. J. Wasbrough, K. J. Edler, W. Thielemans, S. E. C. Dale, S. Bending, D. Wolverson and F. Marken, Electroanalysis, 2010, **22**, 619-624.

Chapter 2. Experimental

2.1. Electrochemistry and electrochemical techniques

Electrochemical methods were used throughout this project for the synthesis and characterisation of various ECP and ECP nanocomposite materials. In brief, electrochemical methods detect the changes in either potential or current of an electrochemical system, comprised of at least 2 electrodes in an electrolyte, and connected externally through a potentiostat, while the potential or current of one of the 2 electrodes is varied. The response signals depend on both of the electrode material and the electrolyte. Some of the basics of electrochemistry and electrochemical methods will be introduced in the following section.

2.1.1 Fundamentals of electrochemistry

There are two types of electrochemical process, either faradaic processes or non-faradaic processes.[1] A faradaic process involves charge transfer (electrons in most cases) across an interface, resulting in oxidation or reduction of a chemical species. In a non-faradaic process, charge transfer across an interface does not occur, for example the double-layer charging on the surface of an electrode.

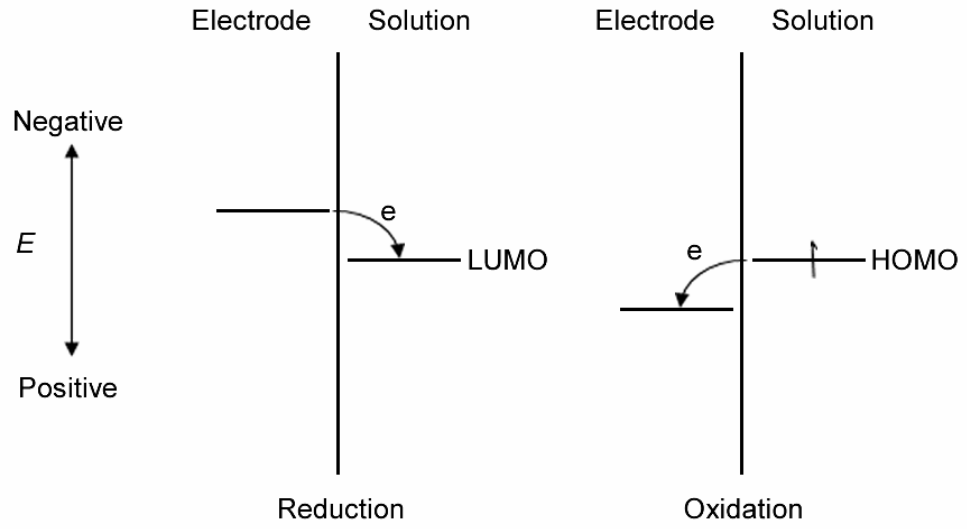

Figure 2.1. A model representing electron transfer processes across an electrode-solution interface, showing reduction and oxidation of a species. Figure from Johnson 2011.[2]

Figure 2.1 shows an idealised representation of electron transfer processes across an electrode-solution interface for oxidation and reduction. In the case of reduction, consider a voltammetric (potential ramp) operation where the potential of the electrode is scanned negatively (cathodic scan, i.e. the potential starts from a high value and is decreased). As the electrode potential decreases, the energy on the electrons becomes higher. When the electrons in the electrode have higher energy than the lowest unoccupied molecular orbital (LUMO) of the chemical species in solution, the electrons will transfer across the electrode-solution interface into the LUMO. The more negative potentials correspond to higher electron energy. Likewise, when the potential is scanned in a positive direction (anodic scan, increasing potential), electron transfer does not occur until the energy of the electrons is lower than that of the highest occupied molecular orbital (HOMO) of the species in

solution. In that case, electrons will be transferred from the HOMO to the electrode.

2.1.2 Electrochemical techniques

The majority of the electrochemical characterisations in this thesis were performed using the 3-electrode system. The cell is comprised of a working electrode, a reference electrode, a counter electrode and an electrolyte solution. The 3-electrode characterisation involves measuring the potential of the working electrode against that of the reference electrode, while the current flows from the counter electrode. This system is favourable in comparison to the 2-electrode system where the current flows from the reference electrode (in this case, it is also the counter electrode). The passage of current can affect the potential of the reference electrode in the case of a 2-electrode system. Thus, the 2-electrode system is not ideal for characterisation where accurate potential measurement is required. In the 3-electrode system, current is not allowed to flow between the reference electrode and the working electrode. Therefore, the potential of the reference electrode stays constant.[1] The use of supporting electrolyte reduces the uncompensated resistance of the circuit, which is manifested as a potential drop of iR_s during the measurement, where R_s is the solution resistance and i is the current flow. The counter electrode is usually made of a material that does not affect the electrolyte solution during its operation, such as platinum.

2.1.2.1 Cyclic voltammetry

Cyclic voltammetry is the most commonly used electrochemical technique that involves sweeping the electrode potential between two preset limits in both negative and positive directions. The cell current is presented as a function of the applied potential. The abbreviation CV is used for both the technique and the experimental output, which is a cyclic voltammogram. The CV technique is the most popular technique among electrochemists due to its simple setup and its ability to provide thermodynamic, kinetic and mechanistic information on either an electrochemical system, or an electrode material.[2]

In CV experiments, the potential waveform applied to the working electrode is triangular, as shown in Figure 2.2. Single or multiple cycles can be used when needed. The potential limits are set to the values where the electroactive species can be detected, i.e. electroactive species are detected when the redox potential is within the potential limits of the scan. A typical CV recorded in a solution containing a redox species is shown in Figure 2.2. The potential scan direction is shown in the figure. The negative potential scan direction is labelled E(-) and the positive potential scan direction is labelled E(+).

The model CV shown in Figure 2.2 is of the type produced for a solution containing a reversible redox mediator, and for a flat disk working electrode. A reversible redox mediator is a species that can be repeatedly oxidised and reduced such that the relative concentration of the oxidised and reduced species at the electrode surface obeys the Nernst equation, which is:

$$E = E^o + \frac{RT}{nF} ln\left(\frac{C_O}{C_R}\right) \quad (2.1)$$

where E^o is the standard potential for the redox mediator, R is the molar gas constant, T is the temperature in Kelvin, n is the number of electrons transferred, F is the Faraday's constant, C_O and C_R are the concentrations of the oxidised and reduced species, respectively.

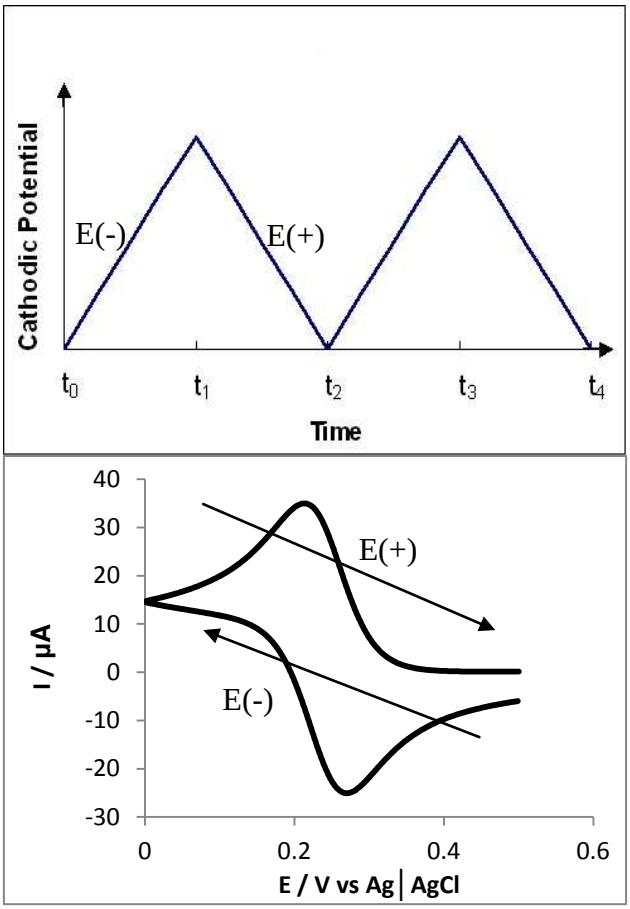

Figure 2.2. Potential step waveform of a CV (top) and a model cyclic voltammogram of a redox mediator in solution.

For the CV technique, the Nernst equation is modified with a potential component defined by the scan rate and it becomes

$$E \pm \frac{dE}{dt} t = E^o \pm \frac{RT}{nF} ln\left(\frac{C_O}{C_R}\right) \quad (2.2)$$

where t is time. In order to maintain the relative concentrations of the oxidised and reduced species as defined by the Nernst equation, the reaction taking place at the electrode surface must occur at a very fast rate. In an ideal case, as the relative concentration of the oxidised or reduced species is determined by the potential of the electrode, so should the current response be, as electrons are added or removed from the redox compound. However, the model CV in Figure 2.2 presents current peak, as a result of depletion of the redox species at the surface of the electrode and subsequently a growing diffusion layer adjacent to the electrode surface. Consider the case in Figure 2.2 for a solution initially only containing the oxidised (O) species. As the potential is scanned negatively, at potential regions near the standard potential, cathodic current is recorded as O is reduced to the reduced species (R) following $O + ne^- \rightarrow R$. The concentration of the O species near the electrode surface decreases. Subsequently, a concentration gradient is generated and diffusion of O species from the bulk occurs spontaneously. The rate of diffusion is given by Fick's first law.

$$J(x,t) = -D \frac{\delta C(x,t)}{\delta x} \quad (2.3)$$

where J is the molecular flux (mol cm^{-2} s^{-1}) of the species down the concentration gradient at distance (x) and time (t), D is the diffusion coefficient of the species (cm^{-2} s^{-1}) and C is the molar concentration (mol cm^{-3}). At the same time, there is a build up of R at the electrode surface. As the potential is scanned more negative, the reduction of O takes place at even faster rate to maintain the equilibrium concentration as outlined in the Nernst equation, so

the cathodic current increases and the concentration gradient becomes steeper and at this point diffusion is enhanced. As O continues to be consumed there is a point where the electrode surface is completely depleted of O, after which all O can only be supplied from the bulk solution through diffusion. As O continues to be consumed, the diffusion layer increases in size. The peak current corresponds to the point at which the diffusion rate of O starts to decrease due to the relaxation effect, and beyond this point the electrochemical reaction becomes limited by diffusion. The diffusion-controlled current, is given by:

$$i = nFAD\left(\frac{\delta C(x,t)}{\delta x}\right)_{x=0} \tag{2.4}$$

For a reversible redox mediator, at 298 K (25˚C), the peak current is:

$$i_p = (2.69 \times 10^5) n^{\frac{3}{2}} A D_o^{\frac{1}{2}} C^{\infty} v^{\frac{1}{2}} \tag{2.5}$$

where C^{∞} is the concentration of the redox species at the bulk solution, and v is the potential scan rate. Equation 2.5, known as the Randles-Sevčik equation, is a solution to the modified Nernst equation (Equation 2.2) and diffusion current equations 2.3 and 2.4. When the potential sweep direction is reversed, at a potential well past the first current peak (cathodic peak for the case we have mentioned), the opposite trend will be observed. The magnitude of the anodic current should be identical to that of the cathodic current during the negative potential sweep, as at this point sufficient R species have built up in the vicinity of the electrode surface due to the reduction during the first sweep. In summary, for an ideally reversible redox mediator, the CVs will have the following features irrespective of the scan rate: (1) the cathodic and anodic peak current separation of 59 mV, (2) reduction and oxidation peak current

ratio of = 1, and (3) a magnitude of the peak current which is linearly proportional to the square root of scan rate (Equation 2.5).

The capacitive current for CVs has been introduced in Chapter 1. Briefly, a rectangular shaped CV is anticipated for electrode materials that exhibit high capacitance. The capacitive current is:

$$i = C\frac{dV}{dt} \tag{2.6}$$

This is the equation that will be used throughout this thesis for calculation of capacitance values of ECPs and ECP nanocomposites.

2.1.2.2 Potential step techniques

Consider a solution containing only an O redox mediator species and initially a positive potential at a working electrode. The reduction of O occurs when the electrode potential is stepped to a value more negative of the standard potential. The concentration of O at the electrode surface instantly becomes depleted, and the current response is diffusion limited. The Cottrell equation describes the variation of current with time:

$$i(t) = \frac{nFAD^{1/2}C^{\infty}}{\pi^{1/2}t^{1/2}} \tag{2.7}$$

Like the Randles-Sevčik equation (Equation 2.5), the Cottrell equation is also a solution to the diffusion limited current, but solved for different boundary conditions. The potential step method assumes instant depletion of a species at the electrode surface. The boundary conditions set for the solution of the diffusion limited equation are as follows:[1]

$$C_o(x, 0) = {C_o}^{\infty} \tag{2.8}$$

$$\lim_{x\to\infty} C_o(x,t) = {C_o}^{\infty} \quad (2.9)$$

$$C_o(0,t) = 0 \quad (2.10)$$

Equation 2.8 and 2.9 apply also for the CV method; however the third condition is exclusive for the potential step case.

The potential step method is also applied during the synthesis of ECP and ECP nanocomposites. However, in those cases the Cottrell equation does not apply as in those cases the process is an electrodeposition rather than simple faradaic charge transfer in solution species. Moreover, the technique can also be used for the characterisation of a capacitive material as the capacitance is given by:

$$C = \frac{dQ}{dV} \quad (2.11)$$

thus integrating the current against time for a given experiment will yield the charge passed after a potential step (the analysis is called coulometry). The capacitance is obtained when the total charge passed was divided by the difference in potential between the initial and final state.

2.1.2.3 Electrochemical impedance spectroscopy (EIS)

EIS is a technique used to study the frequency response of a material or an electrochemical system. The technique involves applying an oscillating potential waveform of small amplitude from high to low frequency, when the potential of the working electrode is held at a certain value. The basics of the characterisation of a capacitive material using this technique have been introduced in Chapter 1. For example, it can be used to determine the turning

point between a resistive and a capacitive response exhibited by an electrode material, or the charge transfer resistance for an electrode material with respect to a certain redox species. For characterising pseudo-capacitive electrode materials, the small amplitude of the applied potential waveform also minimises the contribution of non-capacitive faradaic reactions. This allows a more accurate estimation of the specific capacitance when compared to other methods like CV or the galvanostatic method (explained in next section). It should be noted that when a large potential amplitude is employed in the EIS technique, the characterisation essentially resembles that of the CV technique. In these cases, the high and low frequences correspond to fast and slow potential scan rate in the CV method. The responses recorded at different biased potential also provide valuable information but details will be discussed in the relevant sections in this thesis.

2.1.2.4 Galvanostatic method

The galvanostatic method was used in this thesis for the characterisation of the ECP and ECP nanocomposite materials. In these experiments, a constant anodic or cathodic current is applied to the working electrode. The variation of the electrode potential with time, within a certain positive and negative potential limit, is recorded. A triangular charge-discharge curve is expected for an ideally capacitive material, as discussed in Chapter 1.

2.2. Acid hydrolysis of cotton and oxidised CNXLs from the TEMPO mediated oxidation

This project concerns the making of nanocomposites of ECPs with CNXLs. CNXLs were extracted from native cellulose by hydrolysing the amorphous sections by inorganic acids and retaining the crystalline sections. The CNXLs extracted using H_2SO_4 presents some negative surface charge, due to the introduction of a small amount of surface sulfate half esters ($ROSO_3^-$). When the as-extracted CNXLs are subjected to an oxidation process mediated by the free radical 2,2,6,6,-tetra-methylpiperidine-1-oxyl (TEMPO), all the surface primary hydroxyls are converted to carboxylate functionalities, which significantly increases the amount of negative charges on the CNXL exterior when they are dispersed in water.[4] The negative surface charge on the CNXLs was utilized for the formation of the ECP-CNXL composites.

2.2.1 Materials and apparatus

The cellulose source was cotton wool from Fisher Scientific. All reagents were obtained from Sigma-Aldrich, with the exception of concentrated H_2SO_4 and TEMPO (2,2,6,6-tetra-methylpiperidine-1-oxyl), which were obtained from Alfa Aesar and Amberlite MB 6113 ion exchange resin with colour indicator from Merck. Sonication was performed using a Branson tip sonifier (Branson Ultrasonics Corp., Danbury, Connecticut). Centrifugation was performed using a Refrigerated centrifuge 6K 15 (Sigma®). Deionised water was used for all solutions and procedures unless otherwise stated. Fourier transform infrared spectroscopy (FTIR) was performed with

the KBr pellet technique, using a Bruker Tensor FT-IR spectrometer. Powder x-ray diffraction (PXRD) was performed on a Bruker D8 powder diffractometer operating at 40 kV and 40 mA. Atomic force microscopy (AFM) was performed using a model MFP3D atomic force microscope (Asylum Research Atomic Force Microscopes, Santa Barbara, California) in tapping mode using Olympus AC240TS tips.

2.2.2 Materials preparation and characterisation

The CNXLs were extracted using the method described by Revol.[5] A typical batch process for the extraction of the CNXLs used 400 ml of 64 wt% H_2SO_4 for hydrolysis of 47.1 g of cotton wool (8.75 weight ratio of acid to cotton). The acid was heated to 45˚C using a paraffin oil bath prior to the addition of the cotton wool. The cotton wool was added while the solution was slowly stirred with a mechanical stirrer. When all of the cotton wool was loaded into the solution, the acid-cotton mixture was stirred for 45 minutes for the hydrolysis process to complete. The acid was separated from the CNXLs by a two-step method: (1) dilution and centrifugation at 10˚C and 10000 rpm, which was repeated 3 times with intermittent washing using de-ionised water, and (2) dialysing against a slowly running tap water for at least 48 hours. After the dialysis, the CNXL-containing solution was sonicated for 10 minutes at 20 % sonication amplitude, while ensuring the temperature did not rise above 35˚C. Large unhydrolysed aggregates were removed at this stage by filtering the solution over a No. 2 fritted filter. After the filtration, the CNXL suspension was ion-exchanged with Amberlite MB 6113 overnight to replace

the non H^+ surface cations. After ion-exchange, the suspension was re-filtered, and the ultrasonication was performed again to ensure complete dispersion of the CNXLs in water. These procedures typically resulted in CNXL dispersion of about 1-2 wt%, determined by gravimetric analysis. The suspension could either be freeze dried to yield solid CNXLs, or stored in the refrigerator after addition of a few drops of chloroform to prevent bacterial growth. The CNXLs, prepared as described above, are denoted as S-CNXL, where S represents the surface sulfate half esters.

The TEMPO-mediated oxidation process carried out on the S-CNXLs followed that reported by Habibi et al.[4] Typically, the S-CNXL solution was first diluted to 0.5 wt%. A typical batch process consisted of 400 ml of the 0.5 wt% dispersion of S-CNXLs (2 g of S-CNXL solids). The S-CNXL dispersion was mixed with (in the order mentioned) 648 mg of NaBr, 59 mg of TEMPO free radical, and 5.1 cm^3 of 1 M NaOCl solution. The reaction was carried out at room temperature with the solution stirred and the pH maintained at 10 by dropwise addition of 0.2 M NaOH solutions when required. After 45 minutes reaction time, the process was terminated by adding 2-3 ml of methanol. The pH of the solution was adjusted to 7 with 0.2 M HCl after which the solution was dialysed against de-ionised water for 3 hours. After dialysis, the solution was ion exchanged with Amberlite MB 6113 to replace surface cations with protons, and subsequently it was filtered to separate the ion exchange resins. The solution was then subjected to ultrasonication for 10 minutes to obtain a stable dispersion of the oxidised CNXLs (O-CNXLs). The solution could be stored with a few drops of chloroform added to prevent bacterial growth or freeze dried to obtain O-CNXLs. The solution, at this stage, was typically

0.25-0.4 wt% O-CNXLs. Higher concentrations of the O-CNXL solution could be obtained either by evaporation, or by starting with higher concentration of the S-CNXL, but maintaining the ratios of other chemicals.

FTIR experiments were performed with the KBr pellet technique, where 2 mg of the freeze dried CNXLs were ground with 198 mg of dried KBr, and pressed to form a 13 mm diameter sample disc at 10 tonnes. Conductimetric titration was performed with 50 mg of the O-CNXLs dispersed in 15 ml of 0.03 M HCl and titrated against 0.03 M NaOH. Powder x-ray diffraction (PXRD) experiments were carried out in capillary mode. The diffraction angle (2θ) was scanned from 5˚ to 50˚ using 0.05˚ increments. An O-CNXL film for AFM was prepared by drop coating on a cleaned glassy carbon (GC) plates with 20 μL of 1.5 wt% O-CNXL dispersion and dried at 70˚C for 30 minutes. AFM was performed at a scan speed of 2.5 μm s^{-1}.

The characterisation of the O-CNXLs followed the procedures reported in reference 4. The surface carboxylate groups on the O-CNXLs were identified using FTIR and quantified using conductimetric titration. The conductimetric titration method shows that all surface primary hydroxyls have been converted to carboxylate functionalities.[4] The PXRD results also showed that the crystallinity of the S-CNXLs was preserved after the TEMPO-mediated oxidation process. An AFM image of a drop coated O-CNXL film (Figure 2.3) also resembles that reported in literature, for cotton-derived CNXLs with average elementary crystallite dimensions of 6 × 6 × 150 nm.[6]

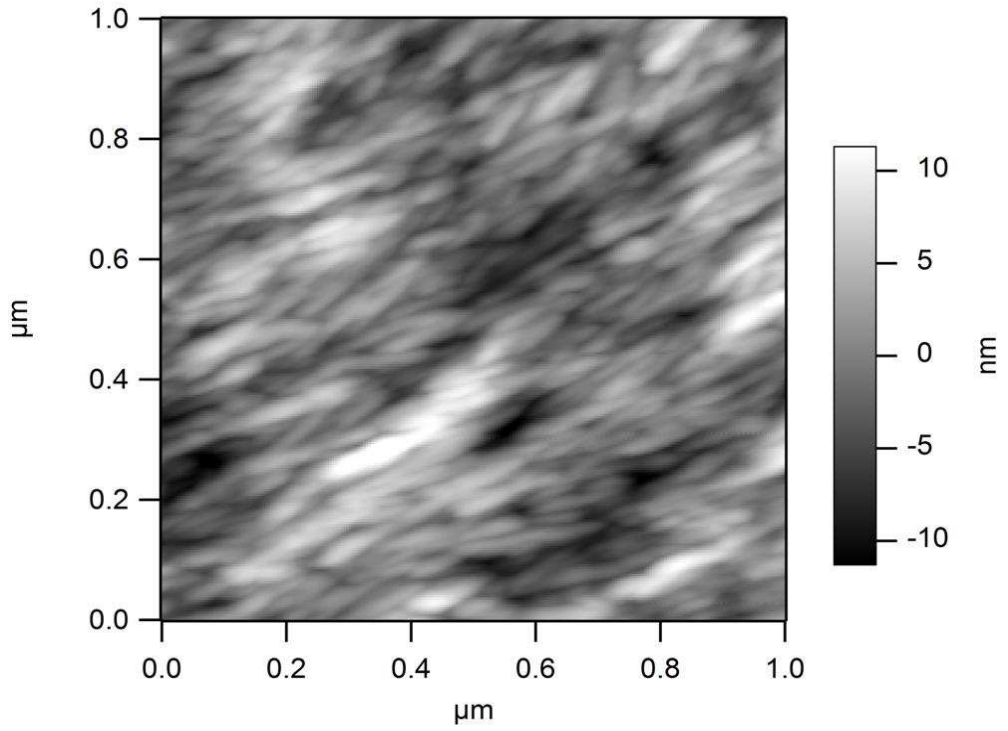

Figure 2.3. Tapping mode AFM height trace image of a drop coated film made of O-CNXLs on glassy carbon plates. Image scan speed was 2.5 µm s^{-1}. The film was drop coated from a 20 µL dispersion of 1.5 wt% O-CNXL and dried in oven at 70˚C for 30 minutes.

2.3. References

1. A. J. Bard and L. R. Faulkner, Electrochemical Methods: Fundamentals and Applications, John Wiley & Sons, 2001.
2. L. Johnson, Synthesis of Nanostructured Metals using Nanocrystals of Cellulose, The University of Nottingham, Nottingham, 2011.
3. K. Lota, V. Khomenko and E. Frackowiak, J. Phys. Chem. Solids, 2004, **65**, 295-301.
4. Y. Habibi, H. Chanzy and M. R. Vignon, Cellulose, 2006, **13**, 679-687.
5. J. F. Revol, H. Bradford, J. Giasson, R. H. Marchessault and D. G. Gray, Int. J. Biol. Macromol., 1992, **14**, 170-172.
6. S. Elazzouzi-Hafraoui, Y. Nishiyama, J. L. Putaux, L. Heux, F. Dubreuil and C. Rochas, Biomacromolecules, 2008, **9**, 57-65.

Chapter 3. Electrochemical co-deposition of PPy-CNXL films and their electrochemical capacitance

3.1. Introduction

As mentioned in the background review in Chapter 1, the attraction of ECPs for supercapacitor applications arises from their relatively low cost, ease of fabrication and high capacitance. The poor potential cycling stability of these ECP materials however, due to weak mechanical properties, poses a practical problem. In the development of devices using ECPs, additives such as metals,[1,2] metal oxides[3] and carbon nanotubes (CNTs)[4-6] are often added to enhance the ECP properties. Perhaps the most remarkable ECP nanocomposites fabricated thus far are those containing CNTs. A particularly promising feature of ECP-CNT nanocomposites is that highly porous structures can be formed from such nanocomposites and the unique electrochemical properties of such materials suggest that they may be suitable for the construction of supercapacitors.[4-11] The CNTs also contribute strength to the ECP-CNT composites as they form the backbone of the composite structure, which significantly enhances the mechanical integrity of the composites.

The main objective of this project is to make use of the strength of CNXLs to replace of CNTs in the preparation of ECP nanocomposites for

supercapacitor applications. The fabrication of ECP-CNXL composites will be achieved using electrochemical co-deposition. Electrochemical co-deposition can produce a more consistent structure for ECP materials, which allows a better comparison with the existing technology.[12,13] Thus, this chapter reports the fabrication of PPy-CNXL nanocomposites using electrochemical co-deposition and their characterisation. The CNXLs used for the work in this chapter were oxidised CNXLs (O-CNXLs), prepared from a TEMPO-mediated oxidation of CNXLs extracted from cotton. As outlined in the project objectives, as the monomer is soluble in water, PPy was chosen due to the relative ease of fabrication.

Composites consisting of cellulose and PPy have been fabricated previously. For example, microstructured cellulose-PPy composites were formed by chemical oxidation of Py monomers in the presence of microfibrillated cellulose from wood.[14] Molecular carboxymethyl cellulose has also been co-electrodeposited into PPy nanocomposites.[15] The major advantage of CNXLs is that, using simple chemistry, a high density of negative charge can easily be introduced to the CNXL surface. It is anticipated that this may allow the incorporation of the CNXLs into the ECP as the counter anions during electrodeposition to form a nanoporous structure as has been achieved previously using CNTs.[6,13]

The PPy-CNXL composites were electrodeposited from a solution of the CNXLs and Py monomers. The resulting PPy-CNXL nanocomposites were characterized using scanning electron microscopy (SEM), thermogravimetric analysis (TGA), cyclic voltammetry and electrochemical impedance spectroscopy (EIS). Cyclic voltammetry and EIS analysis of the

PPy-CNXL nanocomposites showed that the stability and specific capacitance of the nanocomposite materials were higher than those of PPy containing Cl^- anions. The electrochemical performance of the PPy-CNXL nanocomposites was also compared to that of a PPy-CNT composite deposited under the same conditions. The comparison showed that the PPy-CNXL nanocomposites had a similar capacitance to that of the PPy-CNT nanocomposite and was at least as stable as the PPy-CNT nanocomposite. Consequently, the PPy-CNXL nanocomposites showed that ECP nanocomposites containing non-conducting fillers can be equally effective as those containing CNTs. Moreover, the significant cost and environmental benefits that can be achieved by using these inexpensive and sustainable cellulosic nanomaterials for the synthesis of ECP nanocomposites may be very promising for the fabrication of high-performance electrochemical supercapacitors.

3.2. Experimental

3.2.1 Materials and apparatus

Multi-walled CNTs (MWCNTs) with an average diameter of 9.5 nm and an average length 1.5 μm were purchased from Nanocyl, Belgium. Electrochemical depositions and measurements were carried out using a model 760C potentiostat (CH Instruments Inc., Austin, TX), a 3 mm diameter glassy carbon (GC) disk working electrode, an Ag|AgCl reference electrode and a Pt wire counter electrode. Neoprene polishing pads were purchased from Struers A/S., Pedersttupve. Polishing alumina powder (0.3 μm and 1 μm) was purchased from Buehler. Deionised water was used for all solutions and procedures unless otherwise stated. Samples for SEM were prepared by electrodeposition onto GC plates (exposed area = 0.283 cm^2) and SEM analysis was carried out using a Philips XL30 FEG Environmental Scanning Electron Microscope operated at 20 kV. TGA was performed using a TA Instruments TGA Q500, run from 25˚C to 1000˚C in air at ramping speed of 10˚C min^{-1}.

3.2.2 Materials preparation and characterisation

Oxidised CNXLs (O-CNXLs) were used in the work described in this Chapter. Details of this preparation have been described in Chapter 2. To prepare the oxidised MWCNTs, the as-received MWCNTs were dispersed in 2.6 M HNO_3 and refluxed for 48 hours.[16] The resulting suspension was diluted

with water, filtered and washed with deionised water and ethanol. The MWCNTs were then dried under vacuum.[16]

Prior to use, the GC working electrodes were polished with aqueous alumina (0.3 μm) slurries on the Neoprene polishing pads and rinsed with deionized water. The deposition solutions for PPy-CNXL films contained 0.5 M Py in a 0.29 wt% aqueous O-CNXL dispersion. Polypyrrole chloride (PPy-Cl) films were deposited from solutions containing 29 mM KCl and 0.5 M Py. The KCl concentration of 29 mM used for the deposition of PPy-Cl was such that the total charge was approximately 10 times that in the O-CNXL suspension (as determined using the method described in reference 17). The PPy-CNT nanocomposite was electrodeposited from 0.5 M Py in a 0.29 wt% aqueous oxidized MWCNT suspension. The amount of negatively charged surface groups on the oxidised MWCNTs was similar to that of the O-CNXLs, as determined using the same method as for the O-CNXLs. During potentiostatic deposition of the PPy-Cl, PPy-CNXL and PPy-CNT films, electrodeposition was performed at +0.8 V vs Ag|AgCl and stopped when the appropriate amount of charge was passed (0.1 C cm^{-2}, 0.3 C cm^{-2} or 0.5 C cm^{-2}). Electrochemical measurements on the ECP films were performed in either aqueous 0.1 M KCl, 0.1 M tetrapropylammonium chloride (TPACl) or 0.1 M potassium hexafluorophosphate (KPF_6). All preparations and electrochemical measurements were being performed under ambient conditions (ca. 20˚C).

3.3. Results and discussion

3.3.1 Electrochemical Deposition of Polypyrrole-Cellulose Nanocomposites

Figure 3.1A shows the first three cycles of a cyclic voltammogram (CV) obtained at a bare GC electrode in aqueous 0.5 M Py containing 29 mM KCl. Py monomer oxidation began at about 0.7 V and the oxidation current increased on subsequent scans. An oxidation loop was observed in each case, which is common during electropolymerisation of ECPs.[18,19] The presence of the oxidation loop indicates that growth of the polymer on the electrode surface occured by a nucleation and growth mechanism,[15,18] in which ECP deposition on the reverse sweep occurred preferentially on the pre-existing polymer surface.[19] CVs recorded in 0.5 M Py in a 0.29 wt% aqueous O-CNXL dispersion (Figure 3.1B) were very similar to those obtained in KCl. Monomer oxidation also began at about 0.7 V and the CVs also showed an oxidation loop.

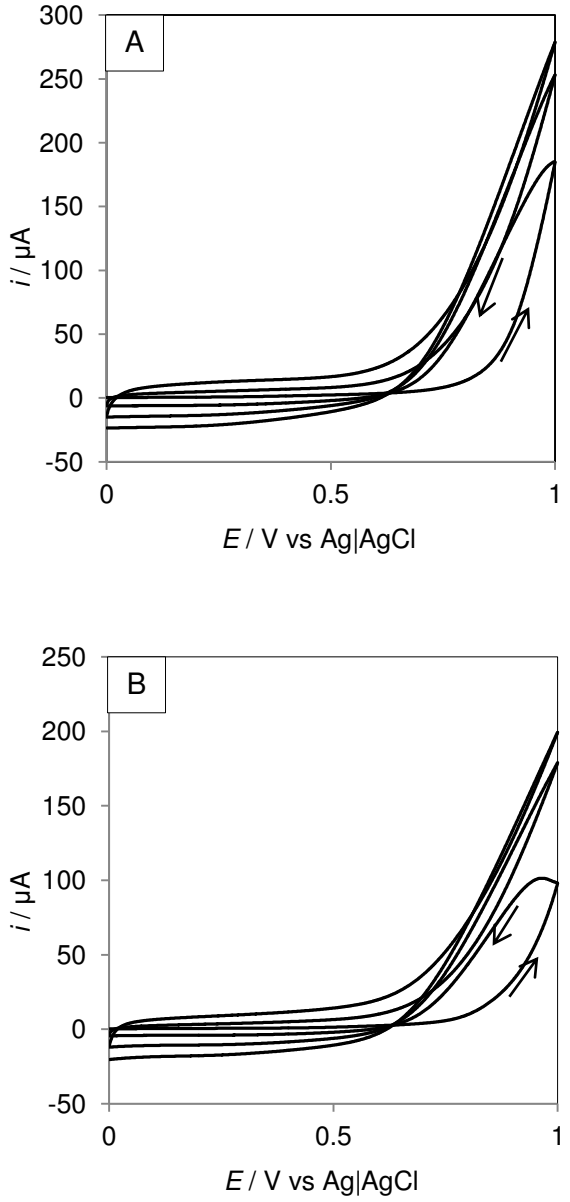

Figure 3.1. (A) First three cycles (lines 1-3) of cyclic voltammograms obtained at a GC electrode in 0.5 M Py in 29 mM KCl (PPy-Cl) (B) First three cycles obtained at a GC electrode in 0.5 M Py in 0.29 wt% O-CNXL dispersion (PPy-CNXL). In each case, the oxidation current increased on successive sweeps, the potential limits were 0.0 V and 1.0 V, the scan rate was 0.1 V s^{-1} and the initial potential was 0.0 V.

During oxidation of Py at the electrode surface, Cl^- anions were incorporated into the polymer to balance the positive charge on the polymer backbone.[13] The similarity of the response obtained in the O-CNXL-containing (Cl^--free) solution indicates that the anionic O-CNXLs acted as the counterion during the electrodeposition, i.e. co-electrodeposition of PPy with O-CNXLs occurred. The oxidation loop in the CV in Figure 3.1B also indicated that the electrodeposition of PPy-CNXL occured by the nucleation and growth mechanism.[13,18,19] In both the solutions, the oxidation current increased on successive scans due to the increased surface area of the conducting polymer coating on the electrode, as was also observed during electrodeposition in aqueous KCl. For subsequent measurements, PPy-CNXL films were prepared using constant potential deposition at 0.8 V unless otherwise mentioned, to prevent over-oxidation of the deposited films and allow good control of the deposition charge.[13]

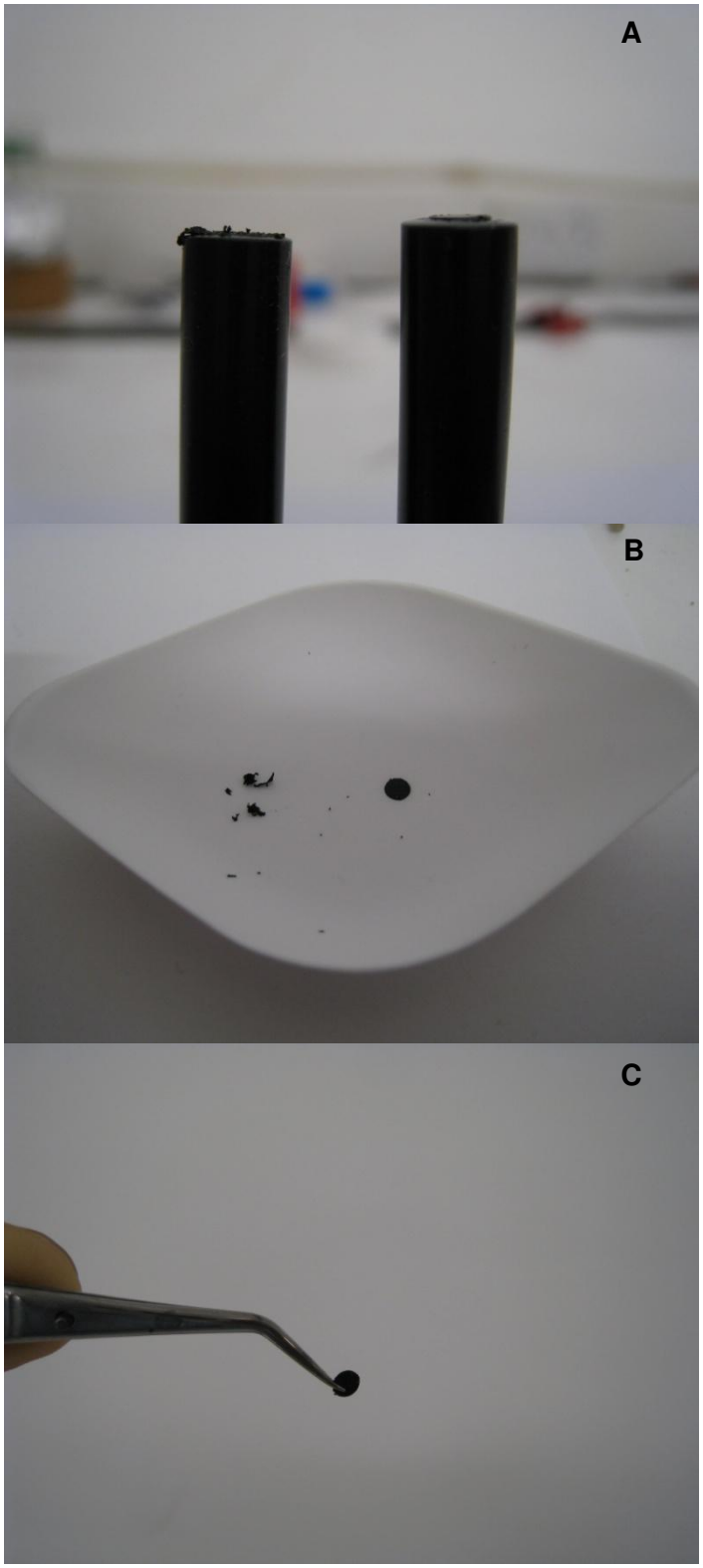

Figure 3.2. Photographs of (A) a PPy-Cl film (left) and a PPy-CNXL film (right) on a GC electrode surface after electrodeposition at 0.9 V until the charge passed was 25 C cm^{-2}. (B) shows the films after removal from the electrode surface. The PPy-Cl film is on the left in (B). (C) shows the PPy-CNXL film held in a pair of tweezers.

Figure 3.2A shows photographs of a PPy-Cl film and a PPy-CNXL film after electrodeposition on the GC electrode surface to a high deposition charge density of 25 C cm^{-2}. The PPy-Cl film appeared very rough on the GC surface in comparison to the PPy-CNXL film. After removal from the electrode using the tip of a spatula (by gently scraping off the films), the PPy-Cl film fell apart. In contrast, the PPy-CNXL film was very robust and remained intact during removal from the electrode and the film was robust enough to be handled using tweezers (Figures 2B and 2C). This observation indicates that incorporation of the O-CNXLs into the PPy structure enhanced the mechanical stability of the polymer and this will be addressed further in a following section. The ability to form a very stable PPy-CNXL film at high deposition charge density is also of significant importance in terms of applications (see Chapter 5).

3.3.2 Scanning Electron Microscopy

Figure 3.3 shows typical SEM images of the surfaces of PPy-Cl and the PPy-CNXL nanocomposite after electrodeposition onto GC surfaces. Electrodeposited PPy-Cl displayed a relatively continuous surface, which was decorated with micron-sized, cauliflower-like or muffin-like aggregates (Figure 3.3A and 3.3B) as has been observed previously for electrodeposited PPy films.[13] In contrast, the surface of the electrochemically co-deposited PPy-CNXL nanocomposite was highly porous (Figure 3.3C) and consisted of a 3D network of interconnected nanofibers. The structure of the PPy-CNXL

nanocomposite was quite uniform across the sample surface (Figure 3.3D) and did not show any dense aggregates such as those observed in the PPy-Cl film.

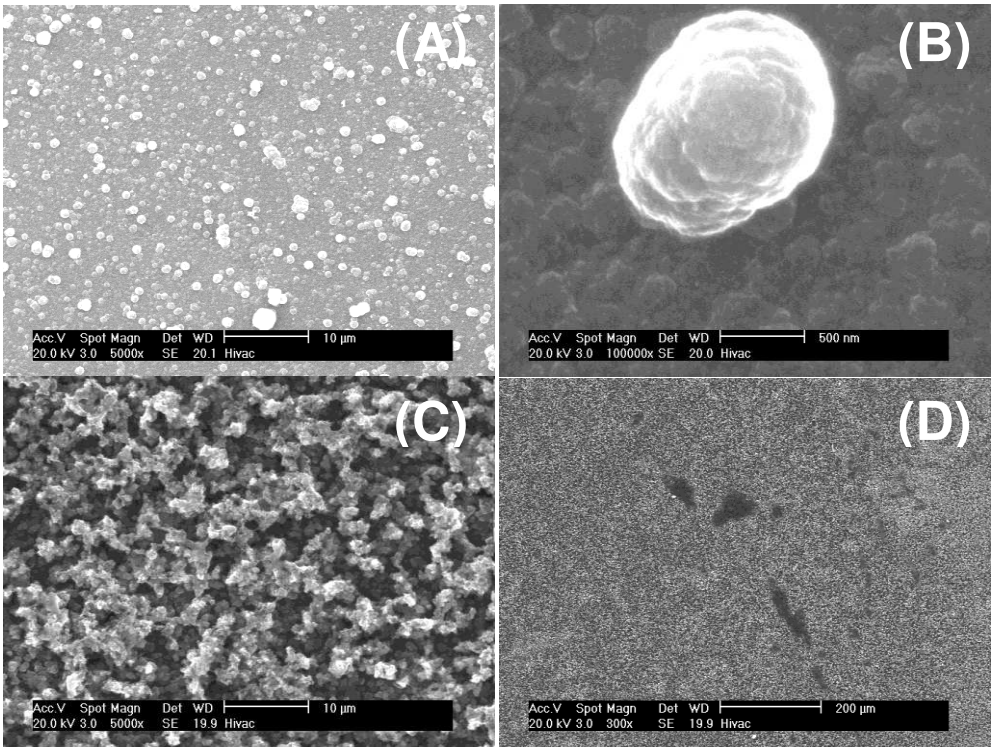

Figure 3.3. Typical SEM images of the surfaces of PPy-Cl (A and B) and a PPy-CNXL nanocomposite (C and D). Each film was deposited at 0.8 V until the total charge passed was 0.5 C cm^{-2}.

Figure 3.4A shows a high resolution image of the PPy-CNXL nanocomposite-coated GC surface. This image clearly illustrates the highly porous nature of the films formed by co-electrodeposition of O-CNXLs and PPy. Figure 3.4B, which is a magnified image of the centre of Figure 3.4A, shows the surface of the PPy-CNXL composite at 400,000× magnification and individual PPy-coated CNXLs can be resolved. From this and similar images, the average width of a PPy-coated CNXL was estimated to be approximately 40 nm. One of these features was highlighted in Figure 3.4B. Therefore, the

estimated average coating thickness of the PPy on the CNXLs was approximately 15 nm, assuming that the features in Figure 3.4B were individual CNXLs crystallites of 6 nm width. The coating thickness was thinner to those previously reported for an electrodeposited PPy-CNT nanocomposite (20-30 nm).[13] A thin PPy coating has been postulated to be advantageous for supercapacitor application as it reduces the diffusion distance for ions in the polymer phase.[13] Generally, the electrochemical performance of ECP nanocomposites is highly dependent on morphology and in the case of ECP-CNT nanocomposites, the electrochemical performance is attributed to the porosity of the structures that are formed, and the low-thickness of the ECP coating on CNTs.[9,13,20] Therefore, the highly porous morphology, and the thin PPy coating of the PPy-CNXL nanocomposites formed in this work may also be very useful for electrochemical applications as discussed in the following sections.

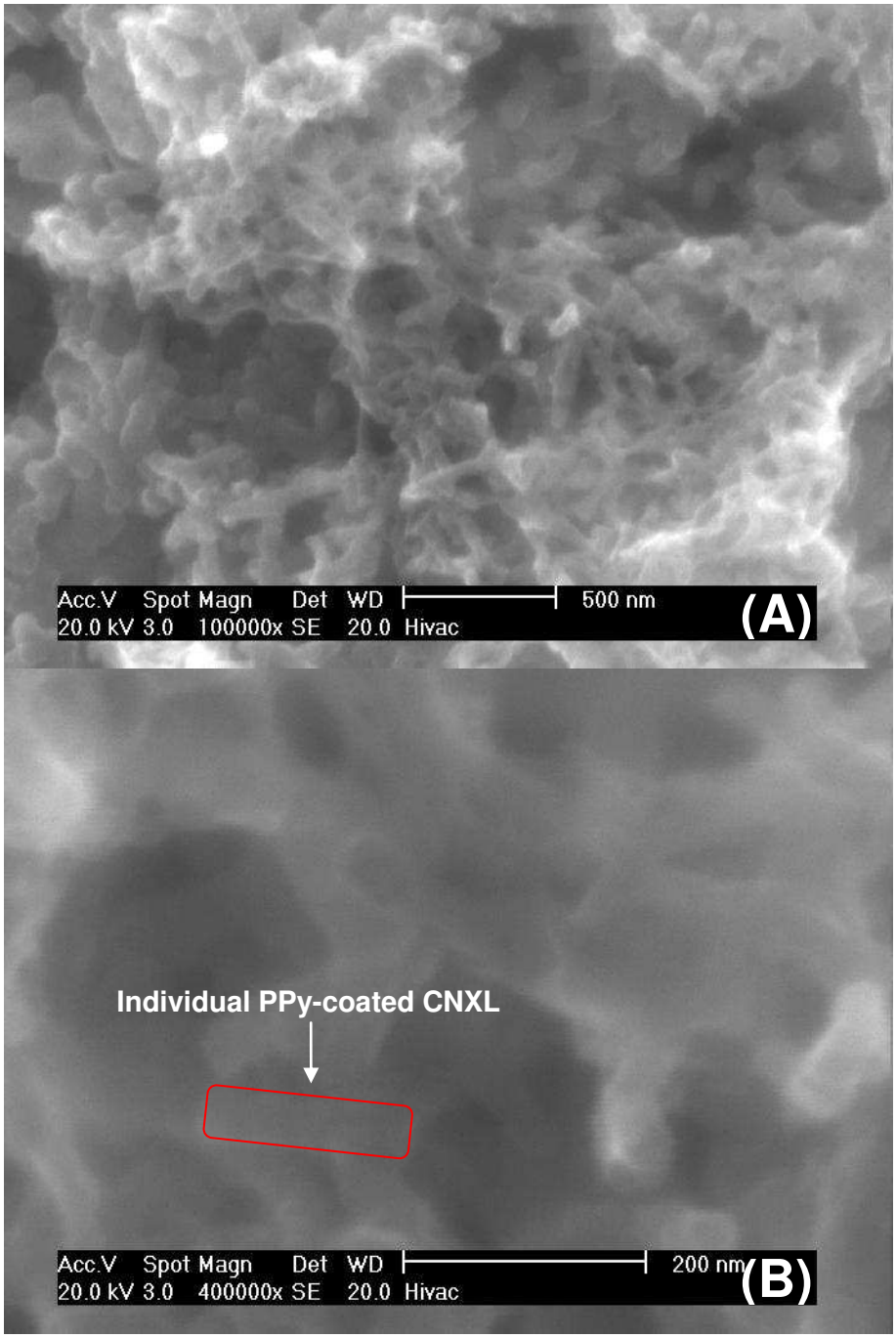

Figure 3.4. High-magnification SEM images of the PPy-CNXL nanocomposite shown in Figure 3.3C. An individual PPy-coated CNXL is highlighted in Figure 3.4B.

The weight percentage of CNXLs in the electrodeposited PPy-CNXL composite can be estimated from the size of a PPy-coated CNXL as characterised by SEM (Figure 3.4B). Assuming that each of the 40 nm-wide PPy-coated nanofeatures consists of an individual CNXL, the density of CNXLs is 1.59 g cm^{-3},[21] and the density of PPy is 0.85 g cm^{-3},[7] the weight percentage of CNXL in the composite should be approximately 3.7 %. The average weight percentage determination was also performed with TGA analysis to clarify with that determined from SEM observations. TGA samples were made by electrodeposition on GC plates and removed after the deposition was completed by gently scraping off the films using the tip of a spatula. The deposition charge density was 27 C cm^{-2}. Figure 3.5 shows the TGA traces for both PPy-Cl and the PPy-CNXL composite. For both of the traces, the small weight loss between 25˚C to 100˚C was due to the evaporation of water.[22] From that point onwards the quicker weight loss in the PPy-CNXL composite in comparison to the PPy-Cl was due to the decomposition of CNXLs at lower temperatures. It has been shown, using TGA of pure CNXLs, that the complete decomposition of CNXLs occured at temperature above 460˚C.[22] At this temperature (460˚C), there is a difference of 7.5 % between the TGA traces of the PPy-Cl and PPy-CNXL. This difference is ascribed to the weight of CNXLs within the composite. In fact, 7.5 weight % of CNXLs corresponds perfectly with calculations based on 2 CNXLs within a coated structure as those shown in the SEM images.

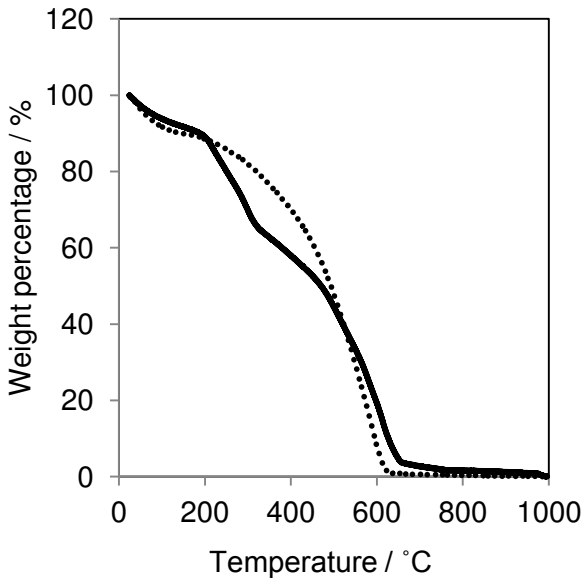

Figure 3.5. TGA traces for PPy-Cl (dotted line) and PPy-CNXL (solid line). The temperature was ramped from 25˚C to 1000˚C at 10˚C min^{-1} in air.

3.3.3 Electrochemical characterisation

Figure 3.6A and 3.6B shows typical CVs obtained at a PPy-Cl film and PPy-CNXL nanocomposite film in 0.1 M KCl. Figure 3.6A shows the actual current recorded while Figure 3.6B shows the current normalised to the mass of PPy in the electrodes. During the anodic sweep in the case of PPy-Cl, a broad oxidation peak was observed at about 0.3 V. During the cathodic sweep, a broad peak was also observed at about -0.1 V and at potentials negative of -0.1 V, the current decreased significantly. This shows that the conductivity of the polymer decreased drastically as it became neutral (undoped).[23] In contrast, in the CV obtained at the PPy-CNXL film, the peak oxidation current was shifted to a more negative potential and a higher current was observed in the negative potential region. Similar behaviour has been observed previously for

capacitive PPy-CNT nanocomposites[13] and it had been suggested that the high conductivity of the CNTs contributed to the high current at negative potentials.[24] However, CNXLs are non-conducting, suggesting that the conductivity of the dopant is not the cause of the high current at low potentials, i.e. when the PPy is reduced. It is more likely that the high current, even at negative potentials, was due to the presence of the negatively-charged CNXLs within the nanocomposite films. This may be explained as follows: when a PPy-Cl film is oxidized, anions from the electrolyte ingress into the film to balance the positive charge on the PPy and, as the film is reduced the anions move out of the film.[13] However, in the case of the PPy-CNXL nanocomposites at negative potentials, the polymer film is neutral but the CNXLs are negatively charged and it is possible that the CNXLs repel the electrons on the PPy chain electrostatically, making their removal easier and resulting in the observed negative shift in the oxidation potential.[13] When the PPy is reduced, the charge on the immobile anionic CNXLs must be balanced by cation ingress from the electrolyte (see below). The mass-specific current CV shows a very high response current (ca. 85 A g^{-1} for the PPy-CNXL) in comparison with the majority of values reported in the literature (Table 1.4 in Chapter 1). The high response mass-specific current recorded at a relatively fast scan rate show that the PPy-CNXL is very promising for high power supercapacitor applications.

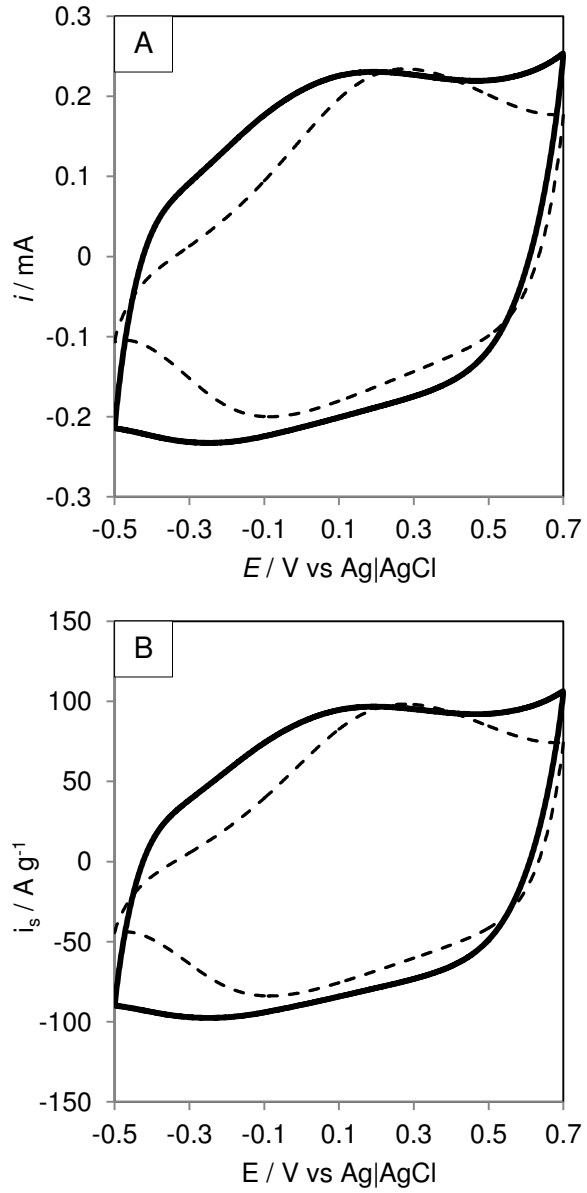

Figure 3.6. Cyclic voltammograms obtained at an electrodeposited PPy-Cl film (dashed line) and PPy-CNXL (solid line) in 0.1 M KCl. (A) Actual current recorded and (B) current normalised to the mass of PPy in each sample. Each film was electrodeposited at 0.8 V until the charge passed was 0.1 C cm^{-2}. The potential limits were -0.5 V and 0.7 V and the scan rate was 0.25 V s^{-1}.

To confirm that cation ingress into the film at negative potentials occurred, CVs were recorded in electrolyte solutions containing large cations and large anions. Figure 3.7 shows CVs recorded at a PPy-CNXL film in KCl, TPACl and KPF_6. The CVs obtained in KCl and KPF_6 were almost identical

but the CV obtained in the electrolyte containing the bulky cation (TPA^+) showed a significant difference. The onset for oxidation of the PPy-CNXL film shifted positive by approximately 200 mV. The current also decreased significantly compared to the response obtained in the K^+-containing electrolyte, suggesting a larger barrier to cation transport out of the film. Therefore, it appears that the presence of the immobile, negatively-charged CNXLs contributed to the high current at negative potentials. Importantly, these results clearly show that ECP composites containing non-conducting additives such as CNXLs can also produce high performance. In the following sections, we discuss the capacitance of PPy-CNXL nanocomposites in more detail.

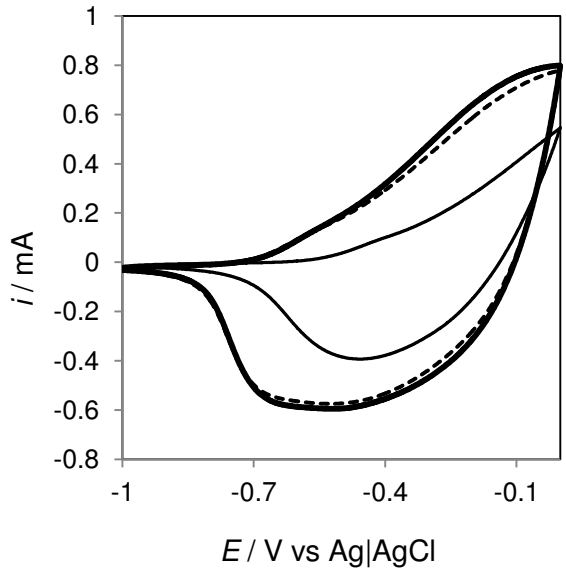

Figure 3.7. Cyclic voltammograms of electrodeposited PPy-CNXL in 0.1 M KCl (thick solid line), 0.1 M KPF_6 (thick dotted line) and 0.1 M TPACl (thin solid line). The potential limits were 0.0 V to -1 V and the scan rate was 0.25 V s^{-1}. The PPy-CNXL film was electrodeposited at 0.8 V vs Ag|AgCl until the charge passed was 0.3 C cm^{-2}.

3.3.4 Electrochemical capacitance and resistance

The CVs shown in Figures 3.6 and 3.7 clearly show pseudo-capacitive processes, resulting in the deviation of the CVs from the rectangular response expected for an ideal capacitor.[25] The potential range in which unfavourable and potentially irreversible pseudo-capacitive effects did not contribute significantly to the measured current was determined using cyclic voltammetry.

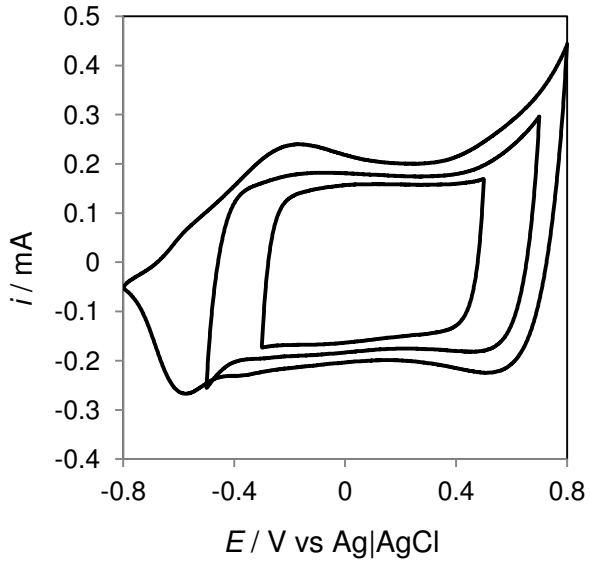

Figure 3.8. Cyclic voltammograms of electrodeposited PPy-CNXL in 0.1 M KCl recorded between potential limits of 0.8 V to -0.8 V, 0.7 V to -0.5 V and 0.5 V to -0.3 V. The scan rate was 0.25 V s^{-1} and the film was electrodeposited at 0.8 V until the charge passed was 0.1 C cm^{-2}.

Figure 3.8 shows CVs recorded at a PPy-CNXL film between a range of potential limits. These CVs demonstrate that the potential range in which the current was predominantly capacitive was approximately -0.45 V to 0.7 V.

Between these potential limits, the CVs showed almost vertical increases in current when the potential sweep direction changed, that is, the CVs were almost rectangular in shape, suggesting fast charging and discharging of the films. This fast charging and discharging is most likely due to the high porosity of the nanocomposite, and the relatively thin PPy film that coats the CNXLs, which results in easy movement of ions and solvent throughout the nanocomposite at the polymer/electrolyte interface and within the polymer phase.[13] The specific capacitance, C (in F g^{-1} based on mass of deposited PPy) was evaluated from the CV data shown in Figure 3.6 using the equation C=I/(dE/dt), where I is the average current, and dE/dt is the potential scan rate. The mass of deposited PPy in each case is Qm/nF, where Q is the deposition charge (C), m is the relative molecular mass of a monomer unit in the polymer, 65 g mol^{-1} for the case of PPy, n is the number of electrons transfer per unit monomer during deposition, which is assumed to be 2 in this case, and F is the Faraday's constant). The estimated specific capacitances from CV currents were 336 F g^{-1} and 258 F g^{-1} for PPy-CNXL and PPy-Cl, corresponding to average mass-specific current of 84 A g^{-1} and 64 A g^{-1}, respectively. The specific capacitance value for the PPy-CNXL compares well with that recently reported for a PPy-graphene nanocomposite (285 F g^{-1}).[26] The average mass-specific current of the PPy-CNXL (84 A g^{-1}) however, was significantly higher than that of the PPy-graphene nanocomposite (0.5 A g^{-1}).[26]

It has been suggested that, as a steady-state-potential technique with a small applied potential variation, electrochemical impedance spectroscopy (EIS) may provide a more accurate estimate of the specific capacitance as it can reduce the influence of faradaic contributions when compared to CV

measurements.[13] Moreover, the capacitance of a given material at different potentials can be studied. EIS experiments were performed on PPy-CNXL and PPy-Cl films at -0.4 V, 0 V and 0.4 V vs Ag|AgCl and the results are shown in Figure 3.9 in the form of Nyquist plots. In most cases, a clear "knee" was observed in the Nyquist plots (indicated by arrows in Figure 3.9). Notably, the Nyquist plots obtained at the PPy-CNXL film at each potential were comparable to those obtained previously for porous ECP-CNT films.[4,6,13,24] At Z' values below the knee, diffusive behaviour dominates, while at Z' values higher than the knee, capacitive behaviour dominates.[13] This diffusive-capacitive feature of the Nyquist plot results from ion intercalation behaviour and is described by fundamentals of the classical finite space Warburg diffusion element.[27] The finite space Warburg element (Z_{FSW}) is,[27]

$$Z_{FSW} = (\tau_d/C)(j\omega\tau_d)^{-p}\coth(j\omega\tau_d)^p \quad (3.1)$$

where $\boldsymbol{\tau}_d$ is the characteristic diffusion time constant, C is the low frequency capacitance associated with the ion intercalation process, ω is the angular frequency, and p = 0.5 for ideal finite space behaviour.[27] In these cases the position of the "knee" relates to $\boldsymbol{\tau}_d$ for the system. For a smaller $\boldsymbol{\tau}_d$, the capacitive behaviour occurs at a higher frequency, according to the hyperbolic cotangent function of the Z_{FSW}. Meanwhile, a smaller $\boldsymbol{\tau}_d$ also results in a lower electrode resistance when $\omega \rightarrow 0$.[27,28] This can be easily identified in the Nyquist plots as the impedance values where the knee occurs. A lower impedance value corresponds to a smaller $\boldsymbol{\tau}_d$, hence more rapid charge transfer.

The exception to the general behaviour was PPy-Cl at -0.4 V (Figure 3.9A), which did not show a clear knee in the Nyquist plot, indicating that PPy-Cl was predominantly resistive at this potential, in agreement with the CV

data described above. At 0.0 V and 0.4 V, the knee in the plot for the PPy-CNXL film appeared at lower impedance values than those for PPy-Cl, indicating a smaller τ_d, and that charge transfer was more rapid in the PPy-CNXL film at each potential. The capacitance of the films were calculated using the equation: $C = -1/(2\pi fZ'')$, where f = frequency (Hz) and Z'' = imaginary component of the complex impedance in ohms at frequency f. At 0.0 V and 0.012 Hz, the specific capacitance was 256 F g^{-1} for the PPy-CNXL compared to 231 F g^{-1} for PPy-Cl. These values are lower than those determined using CV, but which is expected as the non-capacitive faradaic effects are minimised in EIS measurements.[13] However, the general trend was the same as determined using CV, that is, the capacitance of the PPy-CNXL film was higher than that of the PPy-Cl film. The higher capacitance of the PPy-CNXL nanocomposite is most likely due to the highly porous morphology of the nanocomposite and the fact that, within the composite, the PPy coating on the individual CNXLs was very thin which favoured ion transfer across the polymer/electrolyte interface and also within the polymer phase.[13]

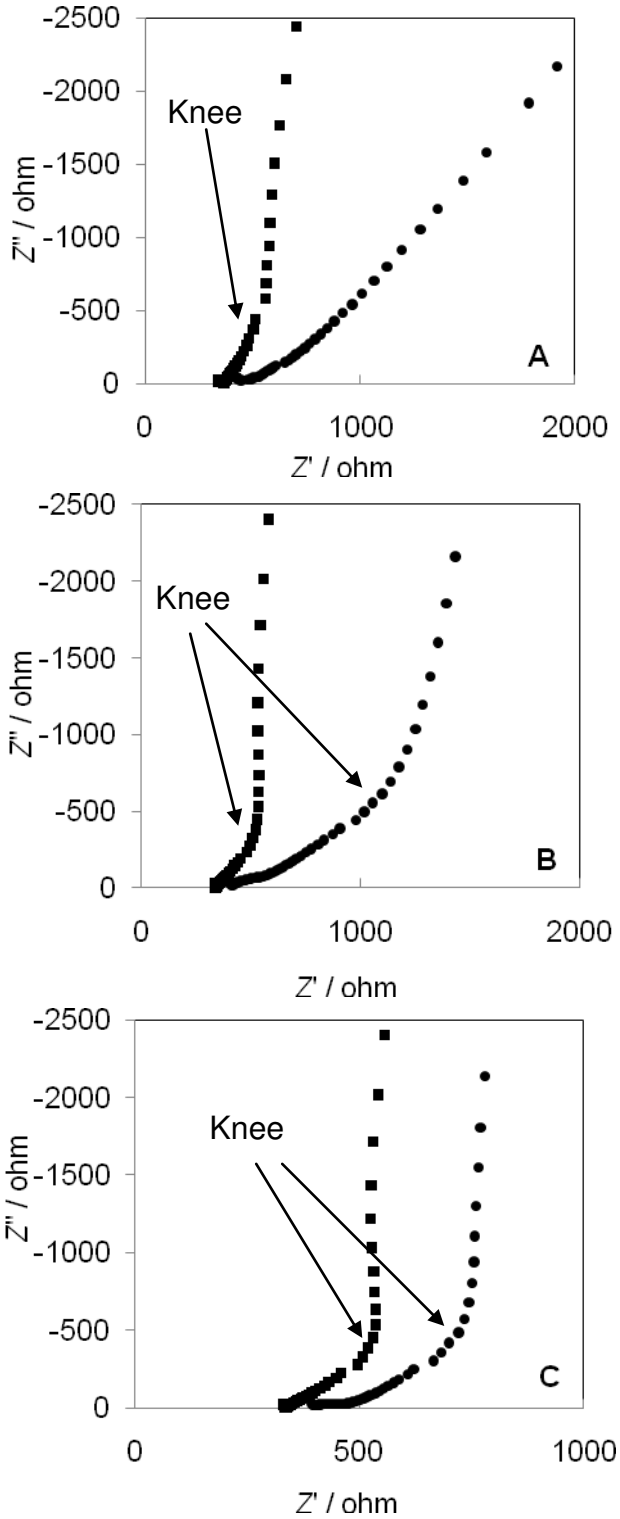

Figure 3.9. Nyquist plots obtained from EIS of electrodeposited PPy-CNXL (solid squares) and PPy-Cl (solid circles) at (A) -0.4 V, (B) 0.0 V and (C) 0.4 V in 0.1 M KCl. The arrows indicate the positions of the "knee". The potential amplitude was 5 mV and the film deposition charge density in each case was 0.1 C cm^{-2}.

3.3.5 Comparison of PPy-CNXL Nanocomposites with PPy-CNT Nanocomposites

In order to show that CNXLs are potentially a viable replacement for CNTs in ECP nanocomposites for supercapacitor applications, we compared the morphology and electrochemical behaviour of a PPy-CNXL nanocomposite and a PPy-CNT nanocomposite. The PPy-CNT nanocomposite was fabricated by electrodeposition from a 0.29 wt% suspension of acid treated MWCNTs containing 0.5 M Py using the same procedure as for the PPy-CNXL nanocomposites.

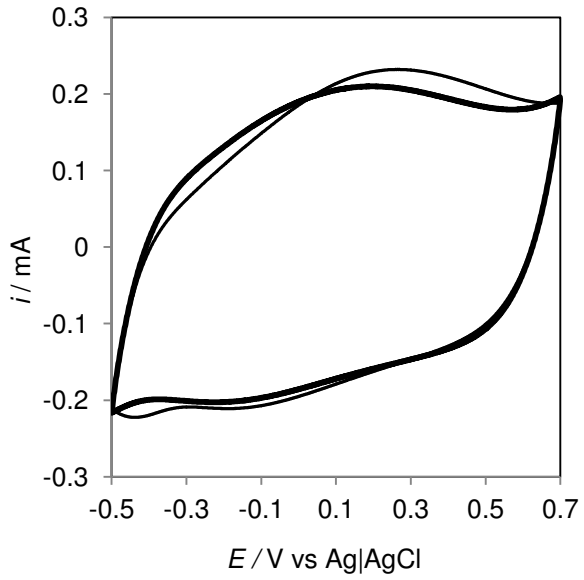

Figure 3.10. Cyclic voltammograms of electrodeposited PPy-CNT (thick line) and PPy-CNXL (thin line) in 0.1 M KCl recorded between potential limits of 0.7 V and -0.5 V at 0.25 V s^{-1}. The films were electrodeposited at 0.8 V until the charge passed was 0.1 C cm^{-2}.

Figure 3.10 shows a typical CV obtained at a PPy-CNT nanocomposite film, which is compared to a CV obtained at a PPy-CNXL nanocomposite film. Generally, the CVs of PPy-CNXL and PPy-CNT overlap very well, indicating the similarities in the electrochemical performance of both nanocomposites. The estimated specific capacitance of the PPy-CNT nanocomposite from CV analysis was 319 F g^{-1}, from an average mass-specific current of 79.8 A g^{-1}. The specific capacitance of the PPy-CNT was close to that estimated by CV for the PPy-CNXL nanocomposite (336 F g^{-1}). SEM analysis of the PPy-CNT film (Figure 3.11) showed some morphological differences to the PPy-CNXL nanocomposite (Figure 3.4A). While both nanocomposites show nanoscopic features, the features of PPy-CNXL composites were significantly smaller.

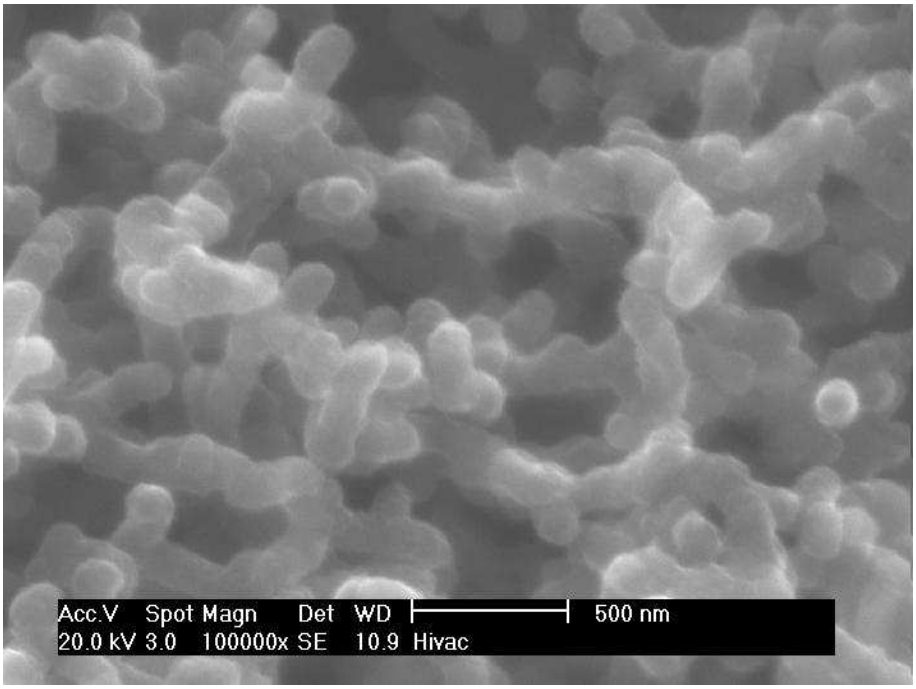

Figure 3.11. SEM image of PPy-CNT film deposited at 0.8 V until the total charge passed was 0.5 C cm^{-2}

The estimated thickness of the PPy layer on the CNTs, considering the fact that the CNTs were 9.5 nm in diameter, was at least 60 nm, which was significantly thicker than the PPy layer on the CNXLs.

3.3.6 Potential cycling stability of composites

An electrochemical stability test was performed to compare the performances of the PPy-CNXL film and the PPy-CNT film. Figure 3.12 shows the CVs recorded at each film before and after the stability test (5000 cycles between 0.5 V and -0.5 V at scan rate of 0.25 V s^{-1}). After the stability test, all films showed lower capacitance, due to degradation of the films during the rapid potential cycling. Notably, the capacitance of the PPy-CNT film decreased significantly more (ca. 60%) than that of PPy-CNXL film (ca. 40%). A PPy-Cl film was also subjected to the potential cycling stability test. The capacitance of the PPy-Cl film after the stability test was negligible compared to those of the nanocomposites (Figure 3.12C). These results indicate that the PPy-Cl is too unstable for the development of durable supercapacitors and that the PPy-CNXL nanocomposite appears to be more stable than the PPy-CNT nanocomposite.

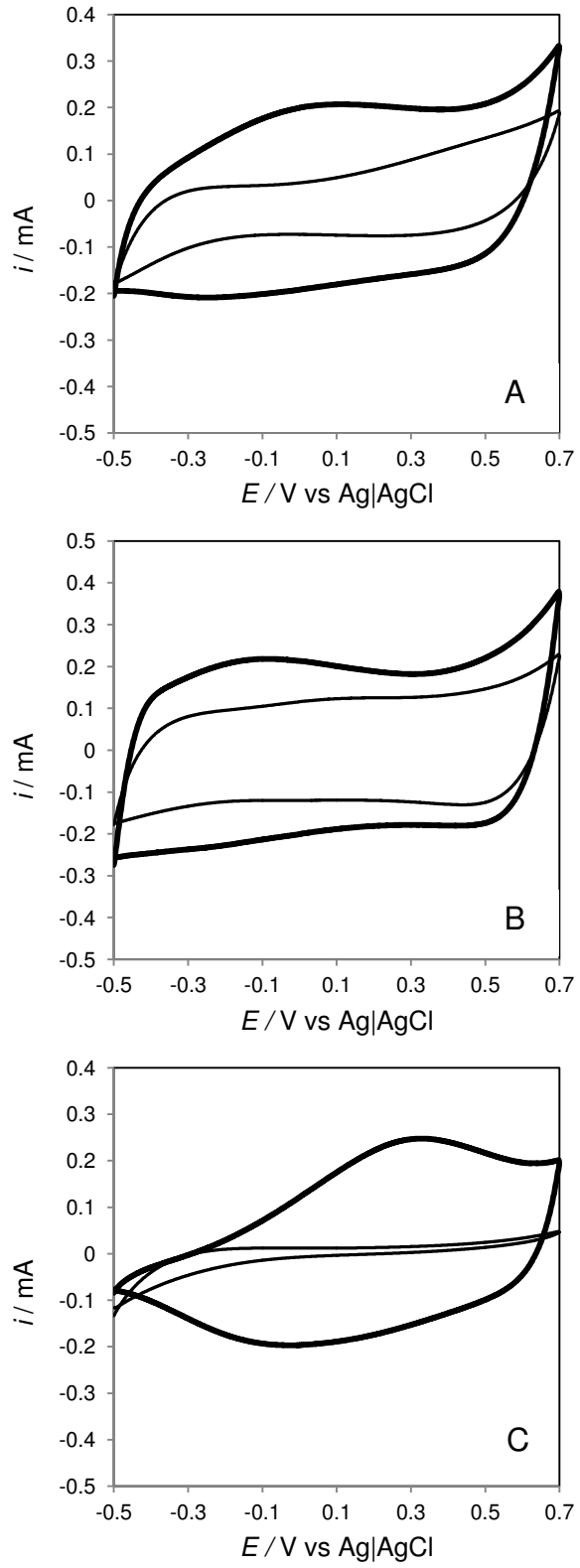

Figure 3.12. Cyclic voltammograms of electrodeposited (A) PPy-CNT, (B) PPy-CNXL and (C) PPy-Cl in 0.1 M KCl before (thick line) and after (thin line) cycling the potential between 0.5 V and -0.5 V 5000 times at 0.25 V s^{-1}. Each film was electrodeposited at 0.8 V until the charge passed was 0.1 C cm^{-2}.

SEM analysis was performed to investigate the effect of potential cycling on the PPy-Cl, PPy-CNT and PPy-CNXL films. Figure 3.13 shows images of each film after cycling 5000 times between 0.5 V and -0.5 V at 0.25 V s^{-1}. Figure 3.13A shows that the morphology of the PPy-Cl film changed significantly upon potential cycling. Prior to potential cycling, the PPy surface was densely decorated with micron-sized, cauliflower-like aggregates (Figure 3.3A and 3.3B). However, the surface of the PPy-Cl film was significantly smoother after potential cycling and it is likely that this smoothing of the surface was a result of mechanical degradation during the test, which also contributed to the loss of capacitance of the PPy-Cl film upon potential cycling. In contrast, the PPy-CNT and PPy-CNXL films did not change significantly during the potential cycling, although some swelling of the polymer is visible after cycling (compare Figure 3.12B and 3.12C with Figures 3.10 and 3.4A, respectively).

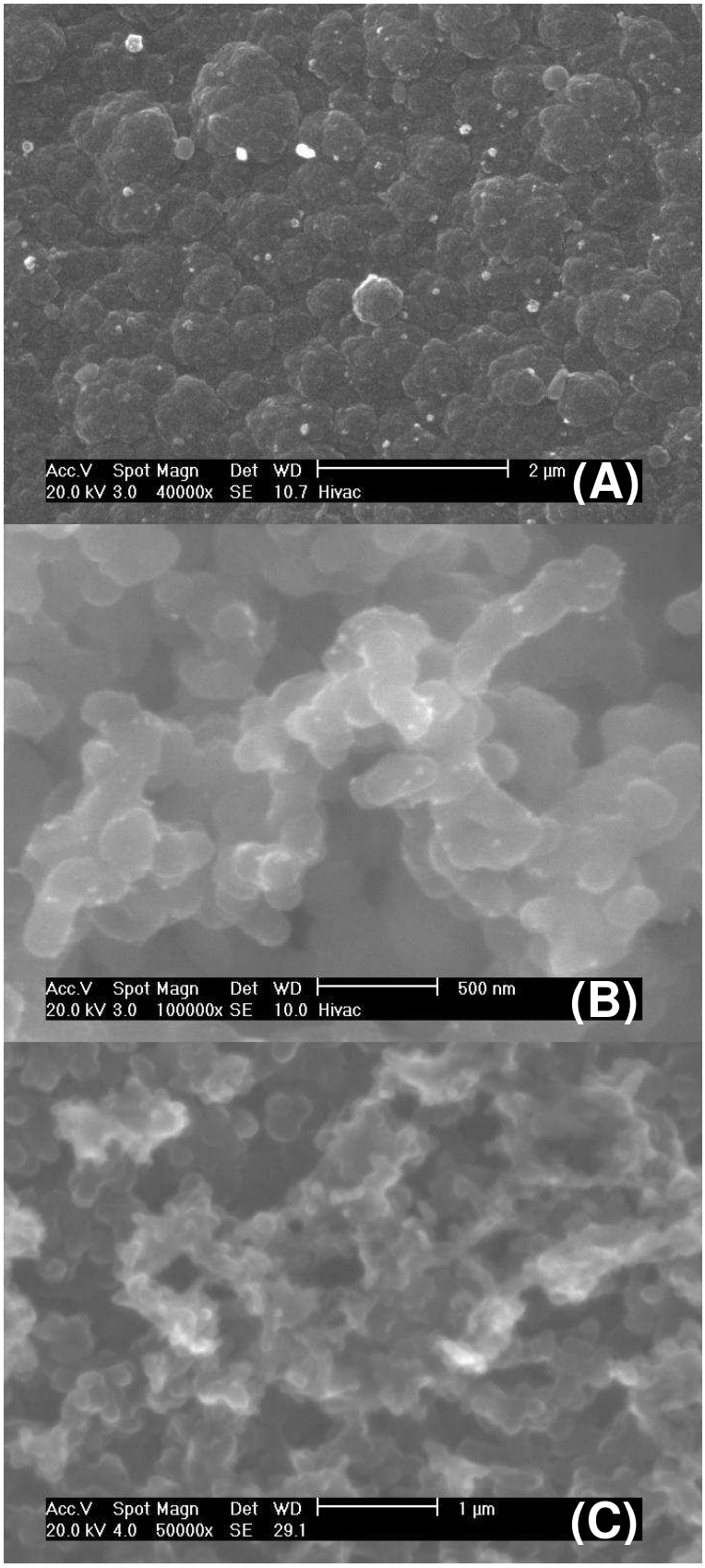

Figure 3.13. SEM images of (A) PPy-Cl, (B) PPy-CNT and (C) PPy-CNXL after cycling the potential between 0.5 V and -0.5 V 5000 times at 0.25 V s^{-1}. Before testing, each film was electrodeposited at 0.8 V until the charge passed was 0.5 C cm^{-2}

As mentioned previously, even before redox cycling, the PPy-Cl nanocomposite was mechanically weaker than the PPy-CNXL nanocomposite, characterised by loose aggregates on the GC electrode after electrodeposition. It appears that the higher electrochemical stability of the PPy-CNT and PPy-CNXL nanocomposites was due to the robustness of the nanocomposite films. It is likely that the higher stability of PPy-CNXL films compared to PPy-Cl upon redox cycling may be due to relatively easier ion and solvent movement through the open, porous nanocomposite structure, with a contribution of strength by the CNXLs within the polymer. This enhancement of the stability of polypyrrole by incorporation of either CNTs or CNXLs is highly encouraging for the development of supercapacitors using these materials. However, considering the benefits of the CNXLs in terms of low cost and renewability, our results suggest that CNXLs may be very promising for the fabrication of very low cost supercapacitors using renewable materials.

3.4. Conclusions

Oxidised CNXLs from cotton were used in the electrochemical synthesis of PPy-CNXL nanocomposites. During electrochemical co-deposition of the CNXLs and PPy, the CNXLs were incorporated into the nanocomposite as the dopant anion. This resulted in a highly porous structure containing CNXLs coated with a thin film of PPy. The high capacitance of the resulting nanocomposite (256 F g^{-1} based on EIS measurements), and its rapid charge/discharge time, were attributed to the high porosity of the 3-D nanocomposite, and the thin coating of PPy on individual CNXL surfaces. The

PPy-CNXL nanocomposite showed a high capacitance at negative potentials, where the PPy was insulating. This was attributed to the negative charge on the CNXLs that was immobilized within the nanocomposite. A similar nanocomposite was prepared using oxidized MWCNTs as an additive and the electrochemical performances of the two nanocomposites were comparable. However, an accelerated stability test indicated that the PPy-CNXL nanocomposite was more durable than the PPy-CNT composite. This is the first time that such a high performance supercapacitor material has been prepared using such non-conducting, renewable and inexpensive nanomaterials. As a result, these cellulosic nanomaterials may be an extremely promising alternative to CNTs for the fabrication of electrochemical supercapacitors based on conducting polymer nanocomposites.

3.5. References

1. A. A. Athawale, S. V. Bhagwat and P. P. Katre, Sens. Actuators B, 2006, **114**, 263-267.
2. H. Bai and G. Q. Shi, Sensors, 2007, **7**, 267-307.
3. R. Gangopadhyay and A. De, Chem. Mater., 2000, **12**, 608-622.
4. M. Q. Wu, G. A. Snook, V. Gupta, M. Shaffer, D. J. Fray and G. Z. Chen, J. Mater. Chem., 2005, **15**, 2297-2303.
5. C. Peng, G. A. Snook, D. J. Fray, M. S. P. Shaffer and G. Z. Chen, Chem. Commun., 2006, 4629-4631.
6. G. Z. Chen, M. S. P. Shaffer, D. Coleby, G. Dixon, W. Z. Zhou, D. J. Fray and A. H. Windle, Adv. Mater., 2000, **12**, 522-526.
7. M. Bozlar, F. Miomandre and J. B. Bai, Carbon, 2009, **47**, 80-84.
8. G. A. Snook, G. Z. Chen, D. J. Fray, M. Hughes and M. Shaffer, J. Electroanal. Chem., 2004, **568**, 135-142.
9. E. Frackowiak, V. Khomenko, K. Jurewicz, K. Lota and F. Beguin, J. Power Sources, 2006, **153**, 413-418.
10. Q. F. Xiao and X. Zhou, Electrochim. Acta, 2003, **48**, 575-580.
11. C. Peng, S. W. Zhang, D. Jewell and G. Z. Chen, Prog. Nat. Sci., 2008, **18**, 777-788.

12. C. Peng, Electrochemical synthesis of composites of conducting polymers and carbon anotubes for supercapacitors, The University of Nottingham, Nottingham, 2007.
13. C. Peng, J. Jin and G. Z. Chen, Electrochim. Acta, 2007, **53**, 525-537.
14. G. Nystrom, A. Mihranyan, A. Razaq, T. Lindstrom, L. Nyholm and M. Stromme, J. Phys. Chem. B, 2010, **114**, 4178-4182.
15. C. R. Alves, P. Herrasti, P. Ocon, L. A. Avaca and T. F. Otero, Polym. J., 2001, **33**, 255-262.
16. G. A. Rance, D. H. Marsh, R. J. Nicholas and A. N. Khlobystov, Chem. Phys. Lett., 2010, **493**, 19-23.
17. Y. Habibi, H. Chanzy and M. R. Vignon, Cellulose, 2006, **13**, 679-687.
18. Z. P. Deng, D. C. Stone and M. Thompson, Analyst, 1997, **122**, 1129-1138.
19. Z. S. Zhao and P. G. Pickup, J. Electroanal. Chem., 1996, **404**, 55-60.
20. V. Khomenko, E. Frackowiak and F. Beguin, Electrochim. Acta, 2005, **50**, 2499-2506.
21. L. Heath and W. Thielemans, Green Chem., 2010, **12**, 1448-1453.
22. L. Johnson, Synthesis of Nanostructured Metals using Nanocrystals of Cellulose, The University of Nottingham, Nottingham, 2011.
23. T. F. Otero, H. J. Grande and J. Rodriguez, J. Phys. Chem. B, 1997, **101**, 3688-3697.
24. M. Hughes, G. Z. Chen, M. S. P. Shaffer, D. J. Fray and A. H. Windle, Chem. Mater., 2002, **14**, 1610-1613.
25. E. Frackowiak and F. Beguin, Carbon, 2001, **39**, 937-950.
26. A. Liu, C. Li, H. Bai and G. Shi, J. Phys. Chem. C, 2010, **114**, 22783-22789.
27. M. D. Levi, C. Wang and D. Aurbach, J. Electroanal. Chem., 2004, **561**, 1-11.
28. E. Barsoukov and J. R. Macdonald, Impedance Spectroscopy Theory, Experiment, and Applications, Wiley-Interscience, 2005.

Chapter 4. Nucleation and Growth Mechanisms during the Redox Switching Dynamics of PPy and PPy-CNXL nanocomposite films

4.1. Introduction

In Chapter 3, the electrochemical capacitance of electrodeposited PPy-CNXL was discussed. In particular, the comparison with a PPy-CNT nanocomposite electrodeposited using a similar procedure showed that the PPy-CNXL may be promising for the application in supercapacitors. The PPy-CNXL nanocomposite withstood a potential cycling stability test better than the PPy-CNT nanocomposite. As the CNXLs were not conducting, the results also suggested that conductivity of the ECP additive may not be necessary for high performance. In contrast, the performance was attributed to the structure and morphology of the composite. Moreover, the large immobile CNXLs embedded within the PPy-CNXL composite also resulted in significantly higher current at the negative potential regions due to charge balancing by cations. However, supercapacitors are not the only electrochemical applications of ECPs that require repeated charging/discharging of the ECP electrodes between different redox states. In similar fashion to supercapacitors,[1-3] electrochromic devices[4-8] and electrochemical actuators[8-10] are typical examples of applications that require repeated charging/discharging the ECP polymer electrodes.

It has been suggested that the charge transfer mechanisms that occur in the ECPs switching between different redox states (it is also the insulating and conducting state) may depend upon the nucleation and the growth of conducting sites in the film.[11-13] Other than electrons, the charge transfer during the redox switching also involves the counter ions and the solvents. Structural changes also occur simultaneously in the process. In fact, although it is apparent that the participating counterions[14-16] and the solvent environment[17,18] both have crucial and rather complex roles during the redox switching, researchers agree that it is the charge balancing ion migration and transport that establishes the dynamics of the process.[12,16,18] Previous examples have also shown that the compactness or morphology of the film have an effect on the dynamics of the process.[17,19,20] However, in these cases the film morphology directly influences the ion migration and transport.[1] Film morphology can be affected by different doping counter ions[21] and also by the different solvents[21,22] employed for the deposition. As a result, the electrochemical performance of ECP films is also affected by the doping counter ions and the solvent used for the deposition.

The phenomenological model of the nucleation and growth mechanism of the conducting sites when ECP films undergo redox switching between insulating and conducting states was recently developed by Randriamahazaka and co-workers.[11] The model has two limiting scenarios, a progressive and an instantaneous nucleation. The quantitative description of each was conveniently written into charge transients, which were functions of time, the growth constants and the nucleation constant. The nucleation constant exists only for the progressive case. The model was employed for the study of

PEDOT films when they undergo redox switching in acetonitrile and ionic liquid media.[11] It was found that the reduction of the films (switching the film from conducting to insulating) proceeds by the instantaneous mechanism in both media whereas the oxidation proceeds by the progressive mechanism in acetonitrile and by the instantaneous mechanism in ionic liquid.[11]

The development and validation of the mechanistic nucleation and growth model, and the interesting insight into the mechanisms that may be present during the redox switching of the ECP films[11] prompted a further study on the properties that appears to be unique to the PPy-CNXL nanocomposite. Due to the non-conducting nature of the CNXLs embedded in the PPy-CNXL nanocomposite, the electronic conductivity of the composite film was solely provided by the PPy portions of the composite. It is interesting to examine and compare the mechanism during the redox switching for the PPy-CNXL composite and PPy. This may further provide insight into the highly capacitive behaviour of the PPy-CNXL composite, and to account for the high oxidative current for the PPy-CNXL at the negative potential region. Furthermore, the nucleation and growth model of the conducting sites may explain the apparent hysteresis that occurs for pure PPy during cyclic voltammetry measurements. The hysteresis is characterised by a mismatch between the reduction or oxidation wave,[23] as the reduction wave tends to be broad and flat while the oxidation wave shows a slow current increase followed by a peak. The PPy-CNXL composites could also be an extremely valuable model system for such a study, as they represent an extremely porous form of PPy due to the structural reinforcement by the immobile CNXLs. Moreover, due to the anionic doping by the immobile CNXLs, the redox

switching process is accompanied by cation movement unlike the redox process of PPy, which is usually accompanied by anions ingress/expulsion (Chapter 3).

In this chapter, the redox switching dynamics of electrodeposited PPy-Cl and PPy-CNXL was reported. The redox switching dynamics of each of the films was investigated using the aforementioned phenomenological model for nucleation and growth of conducting sites within the films. PPy was electrodeposited with Cl^- as the counter anion, while the PPy-CNXL has the negatively charged, immobile CNXLs embedded within the polymer matrix. Potential step measurements were used to identify the nucleation and growth mechanism of the film as they undergo redox transitions between the non-conducting and the conducting state. These results are discussed in section 4.3.1. Instantaneous nucleation was observed for the PPy-CNXL films for both oxidation and reduction potential steps. In contrast, the progressive nucleation occurs for the PPy film during oxidation and instantaneous nucleation was observed for the reduction. The effects of the applied potential on the nucleation and growth rate constants were investigated for all cases, and were discussed in section 4.3.2. The results presented in this chapter show that the nucleation and growth mechanism may explain the apparent hysteresis that occurs for PPy films during cyclic voltammetry. However, the hysteresis does not occur for the PPy-CNXL films.

4.2. Experimental

4.2.1 Materials preparation and characterisation

Oxidised CNXLs (O-CNXLs) were used in the work reported in this Chapter. The preparation of the PPy-CNXL and PPy-Cl films on the 2 mm diameter Pt disk electrode (CH instruments) was similar to that reported for the respective films in Chapter 3. Prior to use, the Pt working electrodes were cleaned by polishing with aqueous alumina slurries on Neoprene polishing pads and rinsed with deionized water. For the electrodeposition of PPy-CNXL films, deposition solutions contained 0.5 M Py in a 0.29 wt% aqueous O-CNXL dispersion. PPy-Cl films were deposited from solutions containing 29 mM KCl and 0.5 M Py. The potentiostatic deposition of the PPy-Cl and PPy-CNXL films were performed at +0.9 V and stopped when 0.5 C cm^{-2} of charge was passed. Electrochemical measurements on the ECP films were performed in aqueous 2 M KCl. All preparations and electrochemical measurements were performed at ambient conditions (ca. room temperature 20˚C).

4.3. Results and discussions

4.3.1 Electrochemical behaviour of PPy-CNXL and PPy-Cl films

Figure 4.1A shows the CVs recorded at a PPy-Cl film and a PPy-CNXL film in 2 M KCl. The PPy-Cl CV had a sharp increase of the cathodic current at the positive potential limits followed by a broad reduction wave, while the anodic current increased much slower at the negative potential limits followed by a peak, which is typical of the hysteresis described for such films.[23] However, the PPy-CNXL CV was much more rectangular. A vertical increase of the current was observed at both ends of the PPy-CNXL CV and the CV current was relatively constant for both the anodic and cathodic process. Notably, both films were electrodeposited to a same charge density but the average current of the PPy-CNXL was higher than that of the PPy-Cl. This shows that the PPy-CNXL film had a higher capacitance. The higher current in the negative potential region for the PPy-CNXL compared to the PPy-Cl film was attributed to cation ingress into the film during the reduction process as the embedded CNXLs were immobile and their surface charge has to be balanced as the PPy portions becomes neutral and uncharged (Chapter 3).

The potential limits chosen for the CVs in Figure 4.1A (0.7 V to -0.5 V vs Ag|AgCl) was within the potential range where both films exhibit reversible pseudo-capacitive behaviour. When these films were subjected to potentials more positive than 0.7 V, over-oxidation may occur and result in degradation of the electrode material. Meanwhile the films become more resistive as the

films were reduced to potentials more negative of -0.5 V. For the purpose of this study, however, the primary interest was placed on the redox transition between the insulating and the conducting state of the ECP. Therefore, the negative potential limit needed to be extended further to identify the potential where the ECP films were completely reduced and exhibited resistive behaviour.

Figure 4.1B shows the CVs recorded at a PPy-Cl film and a PPy-CNXL film also in 2 M KCl. In these CVs the negative potential limits were extended to -1 V. The CV of the PPy-Cl film in Figure 4.1B retained its respective features as in Figure 4.1A when the negative potential limit was extended. However, a significant difference was observed for the PPy-CNXL CV at the extended negative potential region (-0.5 V to -1 V). The cathodic current dropped sharply after the negative potential sweep reached ca. -0.6 V, which is an indication that the PPy-CNXL film became resistive as it was reduced. In addition, the oxidation sweep response of PPy-CNXL, starting from a completely reduced film, was also strikingly different when compared to that of the PPy-Cl. The anodic current of the PPy-CNXL film increased steeply after the positive potential sweep reached ca. -0.6 V, in contrast to the gradual anodic current increase presented by the PPy-Cl during the oxidation sweep. In other words, the typical hysterisis as presented by CVs recorded at the PPy-Cl film was not observed for the PPy-CNXL. The switch from an insulating to conducting PPy-CNXL film was much more rapid and the shape of the CV suggest that different mechanisms may be present for the redox switch in both of the films. Moreover, to the best of my knowledge, the

behaviour observed for the PPy-CNXL was never reported before for PPy, or any porous ECP composites with a non-conducting nanofiller.

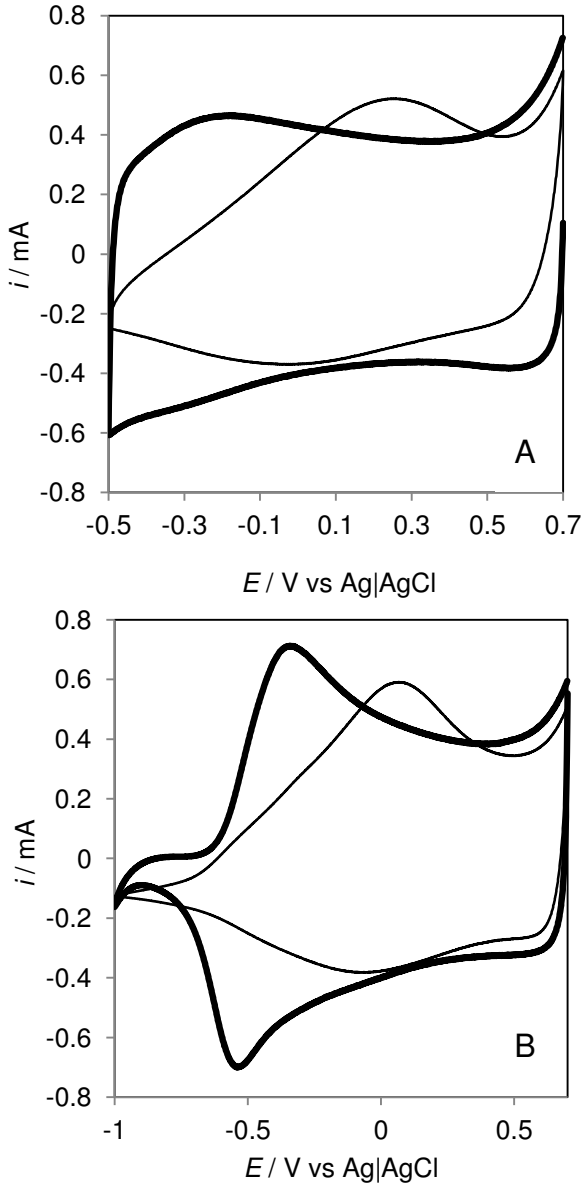

Figure 4.1. Cyclic voltammograms recorded at a PPy-Cl film (thin line) and a PPy-CNXL film (thick line) in 2 M KCl. The potential limits of the scans were (A) between 0.7 V to -0.5 V and (B) between 0.7 V to -1 V. The scan rate was 0.25 V s^{-1}. The films were electrodeposited at 0.9 V to a charge density of 0.5 C cm^{-2}.

The mechanisms of the redox switching can be identified using potential step experiments using charge-time transients. There are two limiting cases: the instantaneous nucleation or the progressive nucleation and growth. The nucleation and growth rate constants can be obtained by fitting the charge-time transients to the appropriate mechanistic descriptions.[11] The equation that describes the charge Q_t, at time t, when the ECP undergoes redox transition by the instantaneous nucleation and growth mechanism is:

$$Q_t = Q_T \times (1-\exp(-k_G^i \times t)) \quad (4.1)$$

where Q_T is the total charge consumed and k_G^i is the growth constant for the instantaneous mechanism. The equation for the progressive nucleation and growth mechanism is:

$$Q_t = Q_T \times \{1-\exp[-k_G^p \times t+(k_G^p/k_n^p) \times (1-\exp(-k_n^p t))]\} \quad (4.2)$$

where k_G^p is the growth rate constant and k_n^p is the nucleation rate constant for the progressive mechanism.[11] Therefore, the charge transient for the instantaneous nucleation and growth mechanism is a first-order response while that for the progressive nucleation and growth mechanism is of a multiple-order response. In fact, for a progressive nucleation it is infinite order if the exponential terms were expanded. However, the actual response may be a composite response of either two identical mechanisms, or a mixture of both of the mechanisms in which one of them has a predominant effect.[11]

Figure 4.2A shows the current transients for the PPy-Cl film and PPy-CNXL film when the potential of the films were stepped to -0.4 V after polarizing the films at -0.9 V. At -0.9 V, both films were in their reduced,

insulating state as identified in Figure 4.1B. In each case, the anodic current transients were very different. The initial current recorded at the PPy-CNXL film was significantly higher, and decreased immediately. Meanwhile the initial current recorded at the PPy-Cl film was much lower. The current at the PPy-Cl film also increased slightly for a very short period of time before decreasing again. Importantly, the current recorded at the PPy-CNXL film at any point of time was nearly twice that of the PPy-Cl, which is a manifestation of more effective charging.

The corresponding charge-time transient for the potential step was presented in Figure 4.2B. It is obvious that the total charge passed during the anodic step increased much faster for the PPy-CNXL film than the PPy-Cl film. Notably, the charge recorded using the PPy-CNXL film increased immediately after the potential step (at time 0) and followed a first-order transient, while the charge increased much more slowly for the PPy-Cl film. The charge transient for the PPy-Cl film also had an increasing slope at short times after the potential step which then decreased. The inflection point for this charge transient was around t = 0.05 s. Such behaviour was typical of a multiple-order transient. The predominant nucleation and growth mechanisms which occurred at the ECP films during the anodic potential step can be easily determined from such observations, i.e. instantaneous nucleation and growth occurred at the PPy-CNXL film, while the conducting sites within the PPy-Cl film underwent a progressive nucleation and growth.

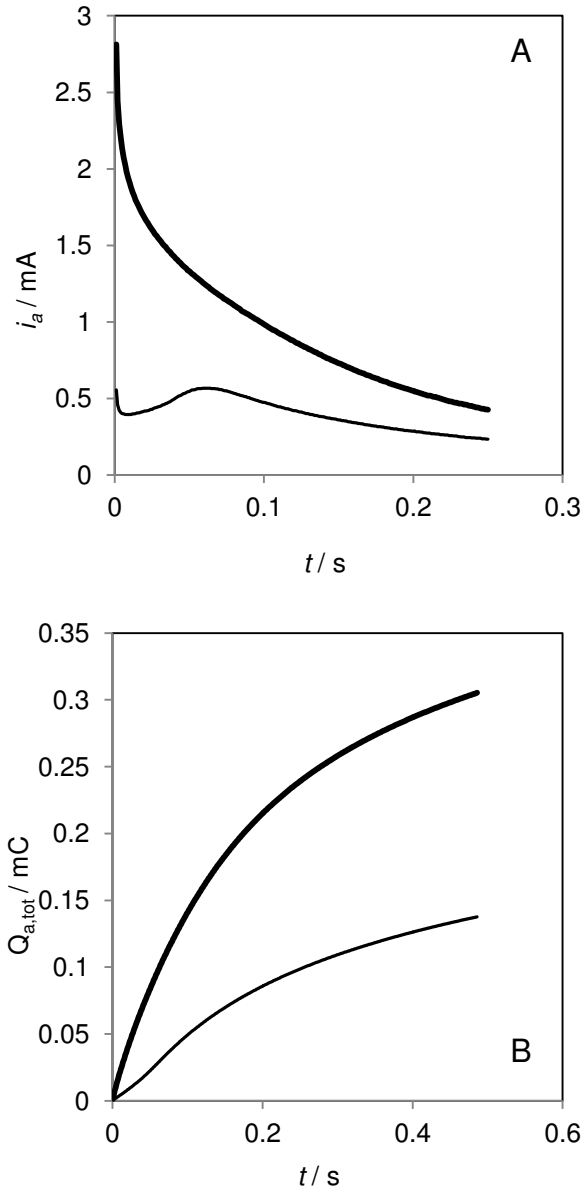

Figure 4.2. (A) Anodic chronoamperograms recorded at a PPy-Cl film (thin line) and a PPy-CNXL (thick line) at -0.4 V after the films were being polarized at -0.9 V for 10 seconds. (B) Respective overall charge-time profile for the potential step experiment in (A). The films were electrodeposited at 0.9 V to a charge density of 0.5 C cm^{-2}. The electrolyte was 2 M KCl.

Figure 4.3 shows the anodic current transients recorded at a PPy-Cl film (Figure 4.3A) and a PPy-CNXL film (Figure 4.3B) at different applied potentials after polarization at -0.9 V for 10 seconds. Figure 4.4 shows the corresponding anodic charge-time transients for both of the films. The initial current (also the peak current for the case of the PPy-Cl) recorded at each film increased with more positive applied potential, which suggest that the rate of the nucleation and growth may be different at different potentials.[11] Nevertheless, it is clear that the initial currents recorded at the PPy-CNXL film at each potential were much higher than those for the PPy-Cl. The charge-time transients in each case also showed features similar as those shown for the respective films in Figure 4.2B, hence the predominant mechanism was obvious.

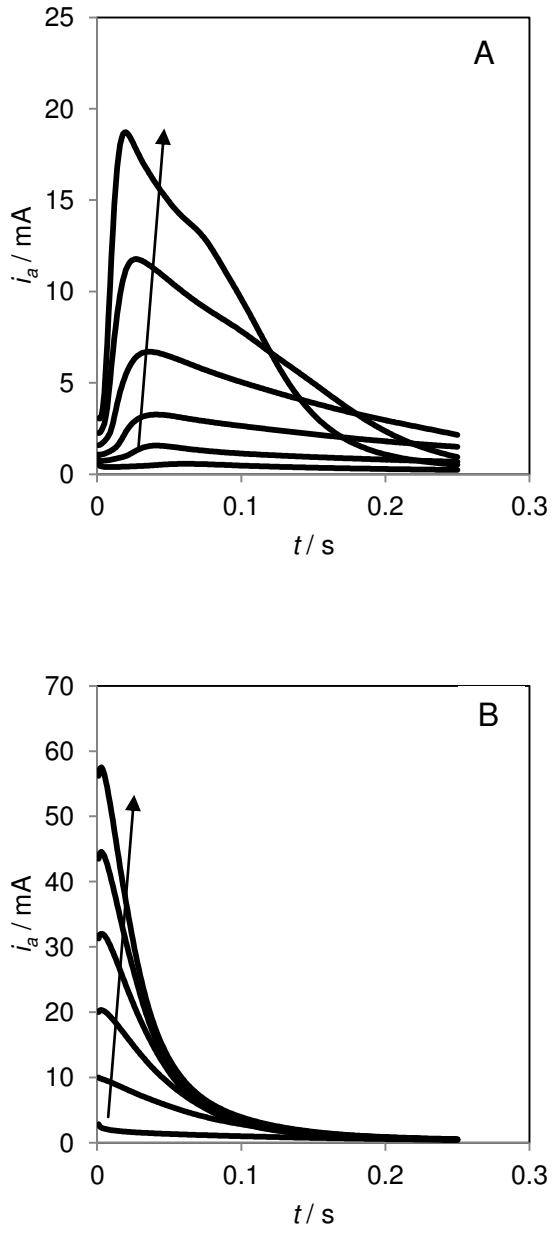

Figure 4.3. (A) Anodic chronoamperograms recorded at a PPy-Cl film at -0.4, -0.2, 0, 0.2, 0.4 and 0.6 V. (B) Anodic chronoamperograms recorded at a PPy-CNXL film at -0.4, -0.2, 0, 0.2, 0.4 and 0.6 V. The increasingly more positive anodic potentials were indicated with arrows. Each of the anodic potential steps was performed after polarizing the films at -0.9 V for 10 seconds. The films were electrodeposited at 0.9 V to a charge density of 0.5 C cm^{-2}. The electrolyte used was 2 M KCl.

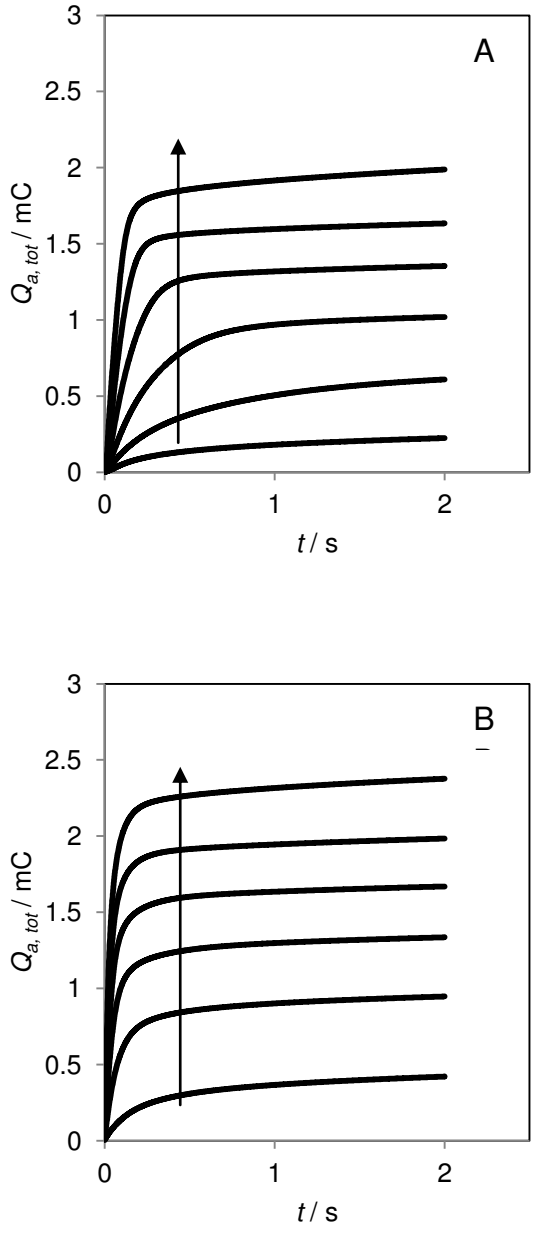

Figure 4.4. (A) Overall anodic charge-time profile corresponding to the chronoamperograms recorded at a PPy-Cl film in Figure 4.3A at -0.4, -0.2, 0, 0.2, 0.4 and 0.6 V. (B) Overall anodic charge-time profile corresponding to the chronoamperograms recorded at a PPy-CNXL film in Figure 4.3B at -0.4, -0.2, 0, 0.2, 0.4 and 0.6 V. The increasingly more positive anodic potentials were indicated with arrows. Each of the anodic potential steps was performed after polarizing the films at -0.9 V for 10 seconds. The films were electrodeposited at 0.9 V to a charge density of 0.5 C cm^{-2}. The electrolyte was 2 M KCl.

Figure 4.5 shows the plot of the total anodic charge passed versus applied potential after polarizing the ECP films at -0.9 V for 10 seconds. The total anodic charge increased with increasingly positive potentials for both PPy-Cl and PPy-CNXL films, indicating the capacitive nature of these films as $C = dQ/dV$, where dQ is the differential charge between two potential points (dV) within the capacitive region. By extrapolation, the onset potential of the capacitive response for either of the films was determined, at -0.59 V and -0.7 V for the PPy-Cl and PPy-CNXL film, respectively. The more negative onset potential for the PPy-CNXL film can be explained by the anionic doping effect provided by the immobile CNXLs which repel electrons on the PPy chain electrostatically, making their removal easier, as has been discussed in Chapter 3. The average specific capacitance evaluated from the gradient of the plot in Figure 4.5 for the PPy-Cl film was 316 F g^{-1}, while for the PPy-CNXL film (considering deposited PPy only) was 350 F g^{-1}. The specific capacitance values deduced from the potential step experiments agree well with those determined using the CV method in Chapter 3.

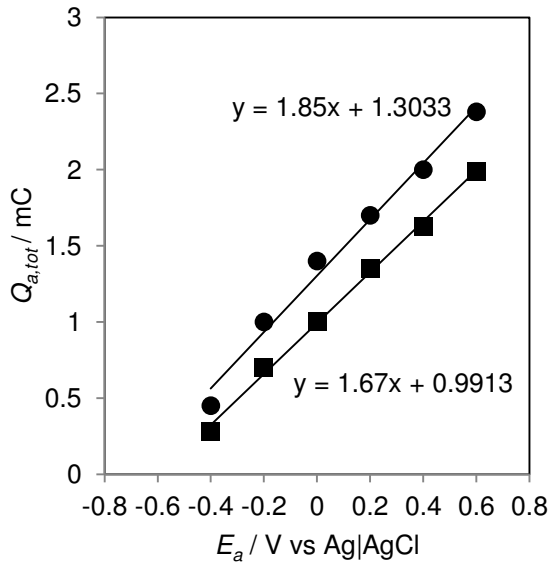

Figure 4.5. Total anodic charge passed vs the anodic potentials for PPy-Cl (squares) and PPy-CNXL (circles). Each of the anodic potential steps was performed after polarizing the films at -0.9 V for 10 seconds. The films were electrodeposited at 0.9 V to a charge density of 0.5 C cm^{-2}. The electrolyte was 2 M KCl.

Figure 4.6A shows the current transients for the PPy-Cl film and PPy-CNXL film when the potential of the films were stepped to 0.4 V after polarizing the films at 0.6 V. At 0.6 V, both films were in their oxidised, conducting state as shown in Figure 4.1B. The cathodic current transients for both of the films were similar. As the potential step was applied, both films responded immediately and the current decreased. The corresponding charge-time transient for the potential step was presented in Figure 4.6B. Notably, the total charge passed during the anodic step increased much faster for the PPy-CNXL film than the PPy-Cl film. However, both of the transient responses were typical of a first-order process, thus the instantaneous nucleation and growth mechanism was predominant at both of the ECP films during the cathodic potential step.

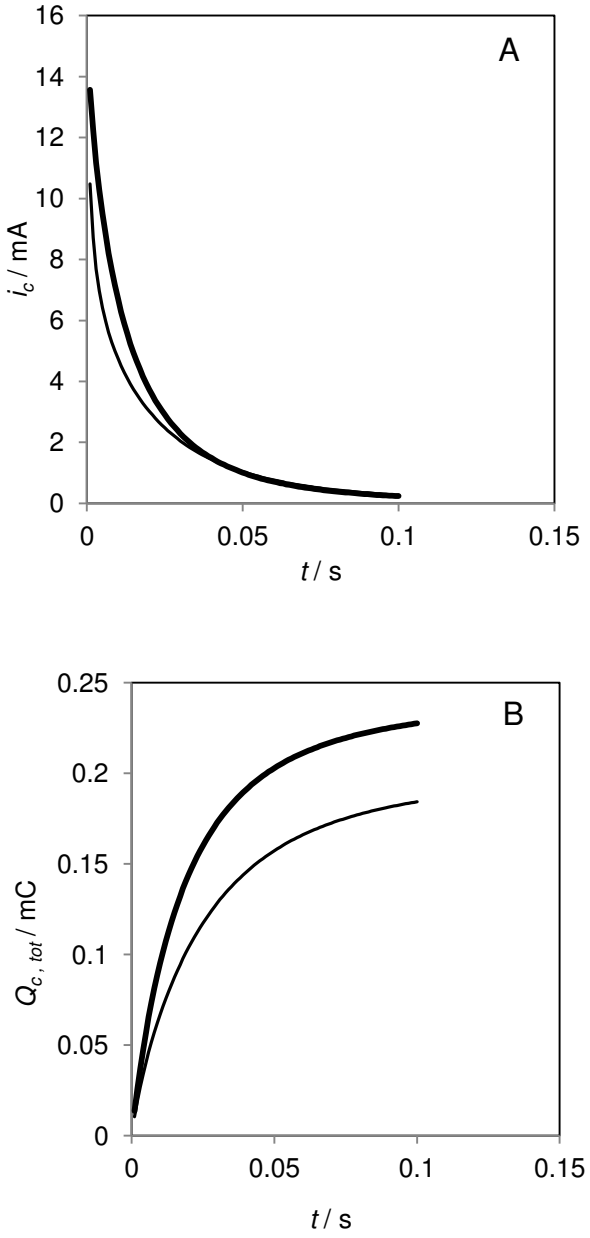

Figure 4.6. (A) Cathodic chronoamperograms recorded at a PPy-Cl film (thin line) and a PPy-CNXL (thick line) at 0.4 V after the films were being polarized at 0.6 V for 10 seconds. (B) Respective overall charge-time profile for the potential step experiment in (A). The films were electrodeposited at 0.9 V to a charge density of 0.5 C cm^{-2}. The electrolyte was 2 M KCl.

Figure 4.7 shows the cathodic current transients recorded at a PPy-Cl film (Figure 4.7A) and a PPy-CNXL film (Figure 4.7B) at different applied potentials after polarizing at 0.6 V for 10 seconds, while Figure 4.8 shows the corresponding anodic charge-time transients for both of the films. The initial currents recorded at both of the films were higher when the applied potential steps were more negative, similar to the effects observed for the anodic potential steps (Figure 4.3). The cathodic charge-time transients recorded in the range of applied potentials also showed features similar as those shown for the respective films in Figure 4.6B. Hence the instantaneous nucleation and growth mechanism was predominant for the reduction of the films. Figure 4.9 shows the plot of the total cathodic charge passed versus applied potential after polarizing the ECP films at 0.6 V for 10 seconds. The total cathodic charge increased with more increasingly positive potentials for both PPy-Cl and PPy-CNXL films, which is identical to the trend observed for the anodic charges (Figure 4.5).

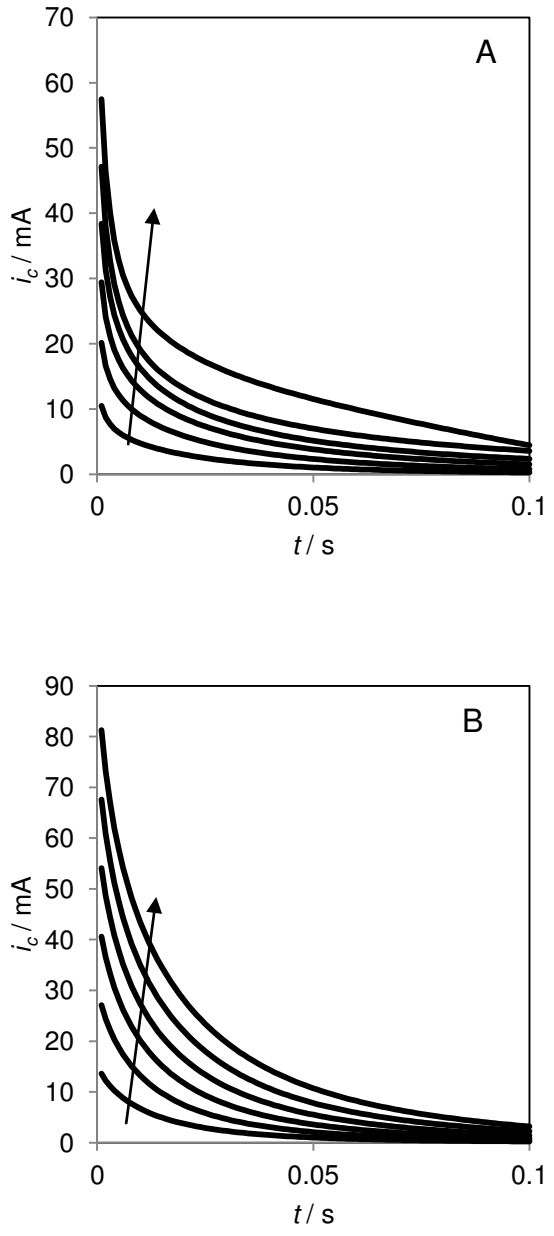

Figure 4.7. (A) Cathodic chronoamperograms recorded at a PPy-Cl film at 0.4, 0.2, 0, -0.2, -0.4 and -0.6 V. (B) Cathodic chronoamperograms recorded at a PPy-CNXL film at 0.4, 0.2, 0, -0.2, -0.4 and -0.6 V. The increasingly more negative cathodic potentials are indicated with arrows. Each of the cathodic potential step was performed after polarizing the films at 0.6 V for 10 seconds. The films were electrodeposited at 0.9 V to a charge density of 0.5 C cm^{-2}. The electrolyte was 2 M KCl.

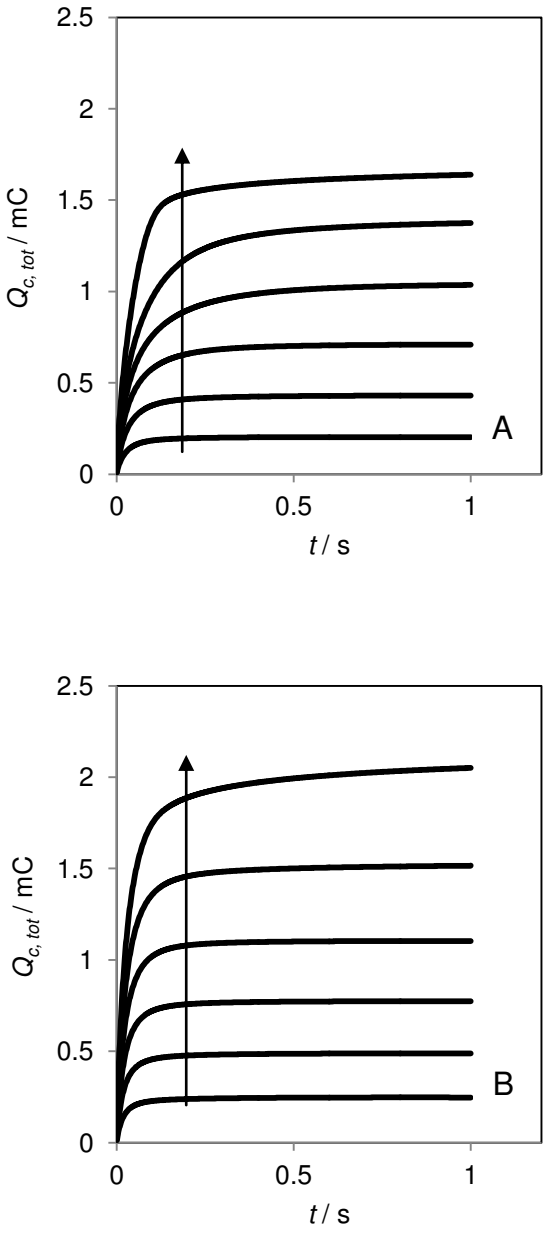

Figure 4.8. (A) Overall cathodic charge-time profile corresponding to the chronoamperograms recorded at a PPy-Cl film in Figure 4.7A at 0.4, 0.2, 0, -0.2, -0.4 and -0.6 V. (B) Overall cathodic charge-time profile corresponding to the chronoamperograms recorded at a PPy-CNXL film in Figure 4.7B at 0.4, 0.2, 0, -0.2, -0.4 and -0.6 V. The increasingly more negative cathodic potentials were indicated with arrows. Each of the anodic potential step was performed after polarizing the films at 0.6 V for 10 seconds. The films were electrodeposited at 0.9 V to a charge density of 0.5 C cm^{-2}. The electrolyte was 2 M KCl.

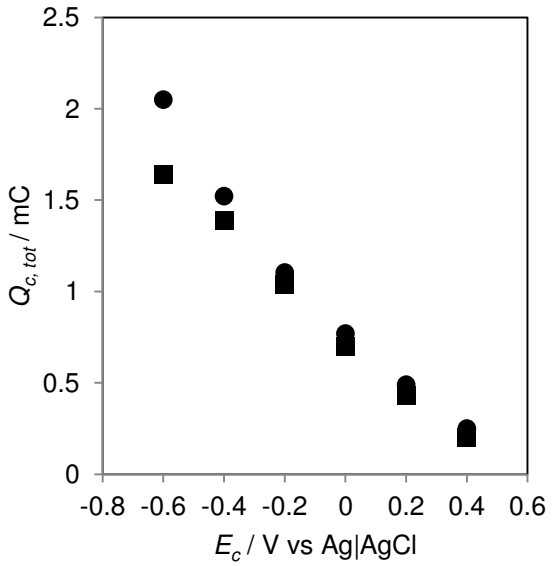

Figure 4.9. Total cathodic charge passed vs the cathodic potentials for PPy-Cl (squares) and PPy-CNXL (circles). Each of the anodic potential steps was performed after polarizing the films at 0.6 V for 10 seconds.

4.3.2 Nucleation and growth rate constants determination

4.3.2.1 Progressive nucleation and growth dominant response

The variation of the nucleation and growth rate constants for the anodic potential steps at a PPy-Cl film (Figure 4.4A) with different applied anodic potentials, E_a, was obtained when the charge transients were analyzed by the following time function, which is a combination of the mechanisms described by Equation 4.1 and 4.2,[11]

$$Q_{tot,t} = Q_T^{open} \times \{1-\exp[-k_G^p \times t + (k_G^p/k_n^p) \times (1-\exp(-k_n^p t))]\} + Q_T^{comp} \times (1-\exp(-k_G^i \times t)) \quad (4.3)$$

Q_T^{open} is the total charge consumed from the open part of the film or fast charging pathway, Q_T^{comp} is the total charge consumed from the compact part of the film or slow charging pathway, k_G^p is the growth rate constant and k_n^p is the nucleation rate constant for the progressive mechanism associated with the open part of the film; and k_G^i is the growth constant for the instantaneous mechanism associated with the compact part of the film.[11] The experimental charge transients have been closely fitted to the equation above with the correlation coefficient squared, $R^2 > 0.98$. An example plot of the model $Q_{tot,t}$ versus the experimental $Q_{tot,t}$ is shown in Figure 4.10.

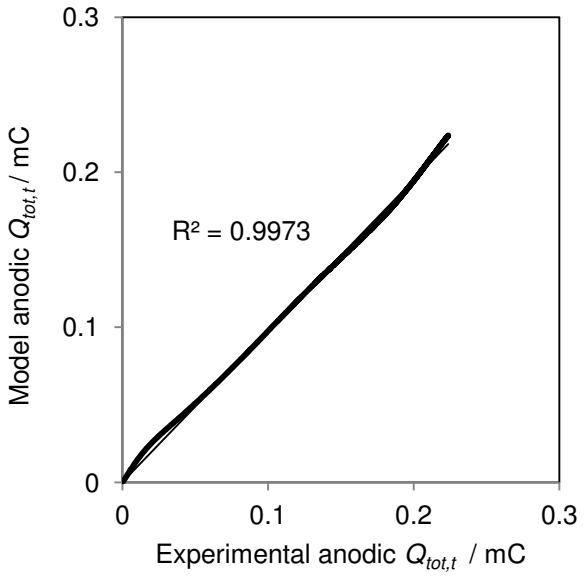

Figure 4.10. Plot of model $Q_{tot,t}$ versus experimental $Q_{tot,t}$ for the anodic potential step to -0.4 V using a PPy-Cl film.

The model fitting began with determining the quantity of Q_T^{open} and Q_T^{comp}. The sum of Q_T^{open} and Q_T^{comp} was the total anodic charge as indicated in Figure 4.5, and their proportion was determined using current vs charge

curves.[24] An example is presented in Figure 4.11 for both the PPy-Cl film and the PPy-CNXL film during the potential step to -0.4 V after polarizing at -0.9 V for 10 seconds. The individual curves can be rationalised as a combination of two linear sections. Q_T^{open} is the intersection of the first linear section with the charge axis, and Q_T^{comp} is the remainder of the charges.[24] In most cases Q_T^{open} has a larger value than Q_T^{comp}. As Q_T^{open} is contributed by the initial current of a potential step response, it is associated with the predominant mechanism in all cases. For example, the progressive mechanism is the predominant mechanism for the oxidation of PPy-Cl from an insulating state as being identified from the step response (Figure 4.2B). This can be easily rationalised, as the open fraction of the film is where the charge transfers start taking place due to more electrolyte accessibility. In the case of PPy-Cl, which showed a progressive nucleation mechanism, charge transfer does not occur until the initial conducting sites are nucleated. This further justifies the association of Q_T^{open} with the progressive mechanism. As Q_T^{comp} occurs later, at that stage the conductive sites within the PPy-Cl film would have nucleated. Therefore Q_T^{comp} is associated with an instantaneous nucleation mechanism.

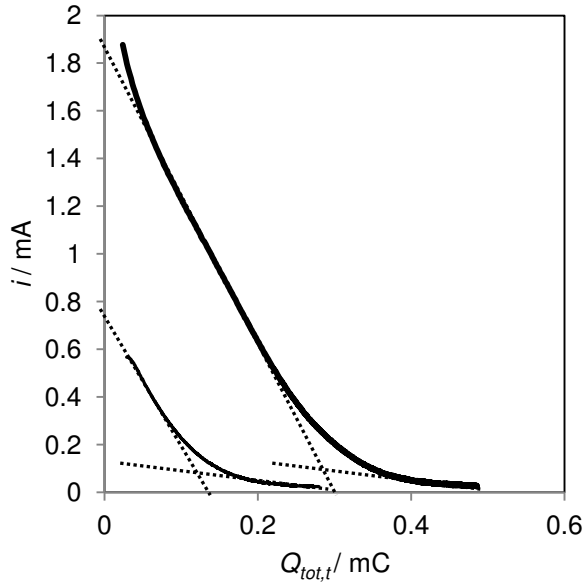

Figure 4.11. Variation of current vs charge for the PPy-Cl film (thin line) and the PPy-CNXL film (thick line) during the potential step to -0.4 V after polarizing at -0.9 V for 10 seconds. The dotted lines show the best fits of two linear sections for either of the curves. The films were electrodeposited at 0.9 V to a charge density of 0.5 C cm^{-2}. The electrolyte was 2 M KCl.

The fractions of Q_T^{open} and Q_T^{comp} for all the anodic potential steps for both PPy-Cl and PPy-CNXL are presented in Table 4.1. The anodic Q_T^{open} and Q_T^{comp} fraction values for PPy-Cl was used with Equation 4.3 to describe the progressive mechanism (Figure 4.12), but the anodic Q_T^{open} and Q_T^{comp} fraction values for PPy-CNXL was used with Equation 4.4 (see next section) due to the instantaneous mechanism during oxidation of PPy-CNXL (Figure 4.13). The fraction of charge that is consumed for either of the pathways gives no indication of the rate of the redox conversion, as the increase in charge Q in Figure 4.11 is dependent on the current.[24] It can be seen that the fractions of Q_T^{open} for the oxidation of PPy-Cl increased with the more positive applied potentials, presumably as the result of the structural opening of the PPy-Cl at more positive applied potentials. Ingress of anions can cause the structure of

the film to swell, and therefore create more passages for subsequent ions and solvent transfers.[23] It has been suggested that the cause of the structural deformation of the ECPs, especially during the initial stages of the anodic process when they were held previously at highly cathodic potentials for long time, may be due to conformational relaxation.[19,20,25] Meanwhile, others also suggested that it may be due to ion movements.[26,27] However, considering applications such as supercapacitors or electrochromic devices, in which the ECPs are subjected to charging/discharging rapidly and are rarely polarized at extreme potentials/voltages, it can be said that the structural changes almost certainly were due to ion and solvent uptake.[11] The potential step experiments in this study were performed after polarizing at the same potentials for the same length of time in each case. Hence it can be assumed that the initial structural configuration was the same for the films prior to all the potential step experiments.

Table 4.1. Fractions of Q_T^{open} and Q_T^{comp} at different applied potentials for the oxidation of PPy-Cl and PPy-CNXL films.

Applied potential, V vs Ag|AgCl	PPy-Cl		PPy-CNXL	
	Q_T^{open} fraction	Q_T^{comp} fraction	Q_T^{open} fraction	Q_T^{comp} fraction
-0.4	0.50	0.50	0.65	0.35
-0.2	0.57	0.43	0.80	0.20
0	1.00	0.00	0.85	0.15
0.2	0.95	0.05	0.85	0.15
0.4	0.95	0.05	0.90	0.10
0.6	0.95	0.05	0.90	0.10

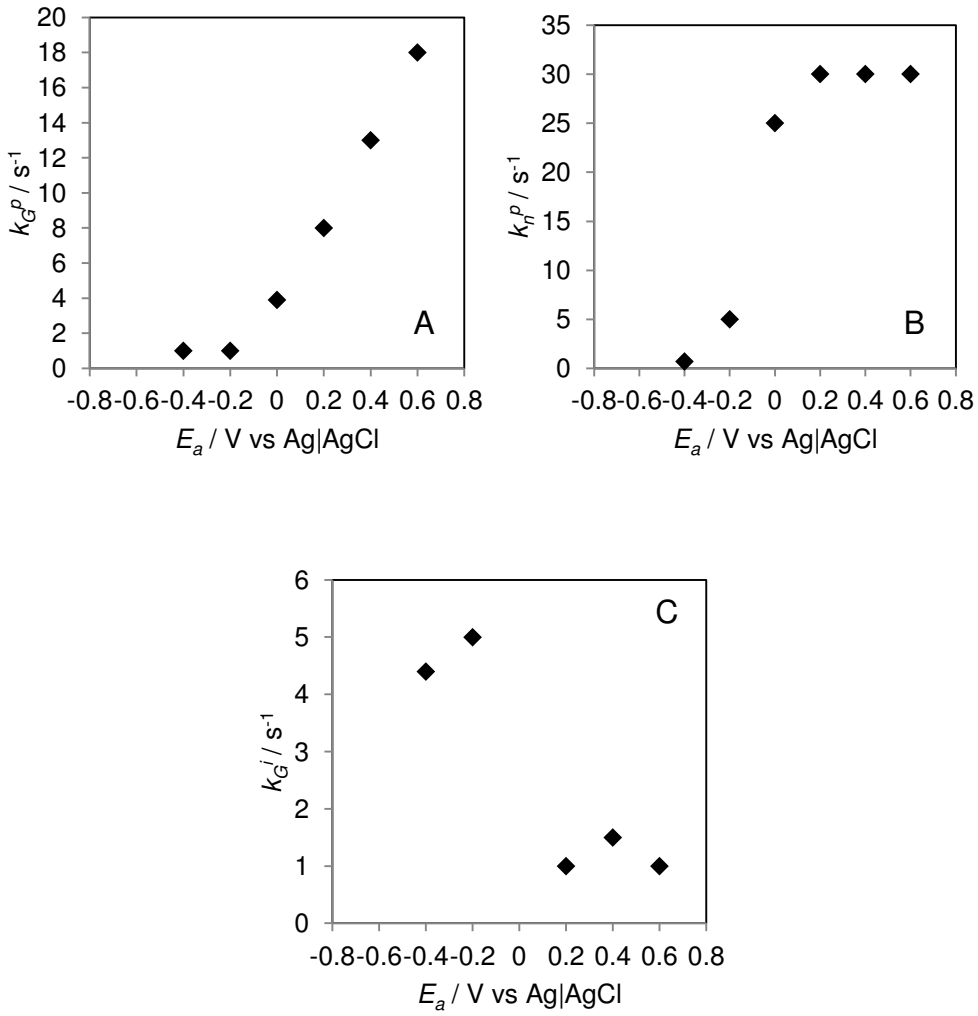

Figure 4.12. Variation of (A) growth rate constants and (B) nucleation rate constants corresponding to the progressive nucleation mechanism and (C) growth rate constants corresponding to the instananeous nucleation mechanism of PPy-Cl during the anodic potential steps, as a function of the anodic potential (horizontal axes). The Q_T^{open} and Q_T^{comp} fraction values at each potentials were shown in Table 4.1. Prior to each potential step the film was being polarized at -0.9 V for 10 s. The PPy-Cl film was electrodeposited at 0.9 V to a charge density of 0.5 C cm^{-2}. The electrolyte was 2 M KCl.

The variation of the best fit nucleation and growth constants for the oxidation of the PPy-Cl film are shown in Figure 4.12. In conjunction with higher fraction of the Q_T^{open} at more positive applied potentials, the PPy-Cl film also had higher nucleation and growth rate constants when the applied potential was more positive. Meanwhile, the growth rate constant for the

instantaneous mechanism had a lower value at more positive applied potential, notably as the fraction of the Q_T^{comp} was also lower at those applied potentials. Thus, the structural change of the PPy-Cl film during a potential step has an effect on the overall charge transient and the rate constants.

4.3.2.2 Instantaneous nucleation and growth response

The variation of the growth rate constants for the anodic potential steps at a PPy-CNXL film (Figure 4.4B) with the applied anodic potential, E_a, and the cathodic potential steps at both PPy-CNXL and PPy-Cl films (Figure 4.8) with different applied cathodic potentials, E_c, were obtained when the charge transients were analyzed by the following function:[11]

$$Qtot,t = Q_T^{open}\times(1-\exp(-k_G^{i,open}\times t))+ Q_T^{comp}\times(1-\exp(-k_G^{i,comp}\times t)) \quad (4.4)$$

Q_T^{open} is the total charge consumed from the open part of the film, Q_T^{comp} is the total charge consumed from the compact part of the film, $k_G^{i,open}$ is the growth rate constant for the instantaneous mechanism associated with the open part of the films; and $k_G^{i,comp}$ is the growth constant for the instantaneous mechanism associated with the compact part of the films.[11] In all cases the best fit was achieved with $R^2 > 0.98$. The values of Q_T^{open} and Q_T^{comp} were also approximated from the experimental data as described above (Figure 4.11). Table 4.2 shows the values of the fractions of Q_T^{open} and Q_T^{comp} for the reduction potential steps for both PPy-Cl and PPy-CNXL at different applied potentials.

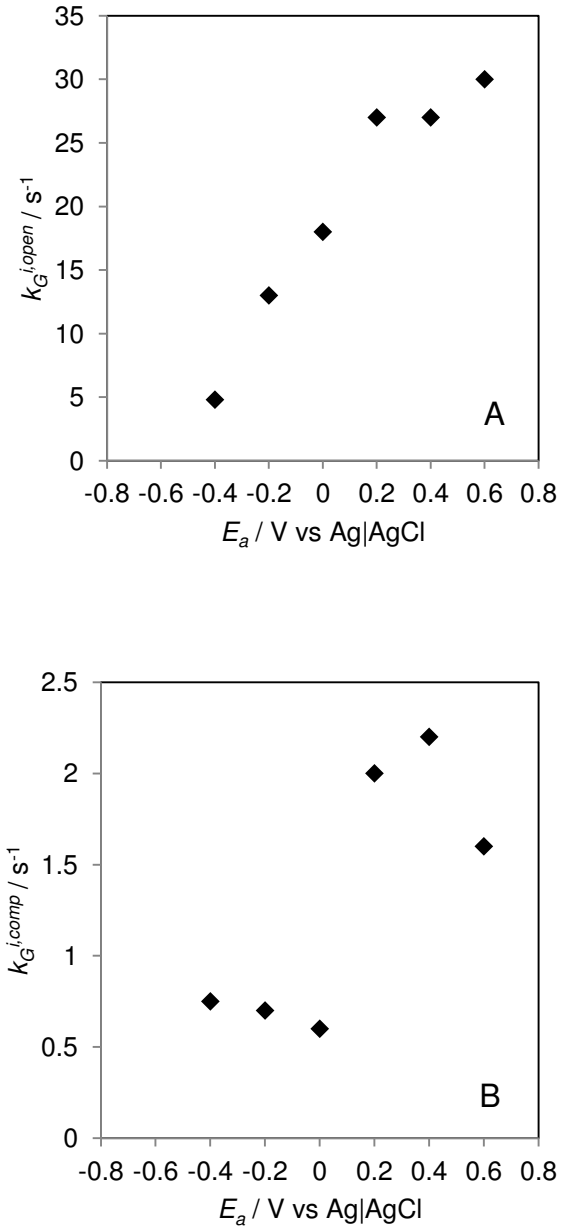

Figure 4.13. Variation of growth rate constants for the instantaneous nucleation mechanism of PPy-CNXL film for the (A) fast charging and (B) slow charging pathways during the anodic potential steps, as a function of the anodic potential (horizontal axes). The Q_T^{open} and Q_T^{comp} fraction values at each potentials were shown in Table 4.1. Prior to each potential step the film was being polarized at -0.9 V for 10 s. The PPy-CNXL film was electrodeposited at 0.9 V to a charge density of 0.5 C cm^{-2}. The electrolyte was 2 M KCl.

Table 4.2. Fraction of Q_T^{open} and Q_T^{comp} at different applied potentials for the reduction of PPy-Cl and PPy-CNXL films.

Applied potential, V vs Ag|AgCl	PPy-Cl		PPy-CNXL	
	Q_T^{open} fraction	Q_T^{comp} fraction	Q_T^{open} fraction	Q_T^{comp} fraction
0.4	0.5	0.5	0.8	0.2
0.2	0.5	0.5	0.8	0.2
0	0.5	0.5	0.8	0.2
-0.2	0.5	0.5	0.8	0.2
-0.4	0.4	0.6	0.8	0.2
-0.6	0.4	0.6	0.7	0.3

The variation of the best fit growth constants for the oxidation of the PPy-CNXL film, and the reduction of both the PPy-Cl and PPy-CNXL films were shown in Figures 4.13, 4.14 and 4.15. The growth rate constants for both the open and compact part of the PPy-CNXL film during oxidation had higher values when the applied potential was more positive (Figure 4.13). For the reduction steps at both PPy-Cl and PPy-CNXL films, the growth rate constants associated with both Q_T^{open} and Q_T^{comp} generally decreased when the applied potentials were more negative (Figure 4.14 and Figure 4.15). There is an exception for the $k_G^{i,comp}$ of the PPy-Cl film, where a minimum value was determined at -0.2 V, but increased when the final potentials were -0.4 and -0.6 V. However, that occurred as the fractions of Q_T^{comp} for the PPy-Cl reduction step at those potentials were also higher.

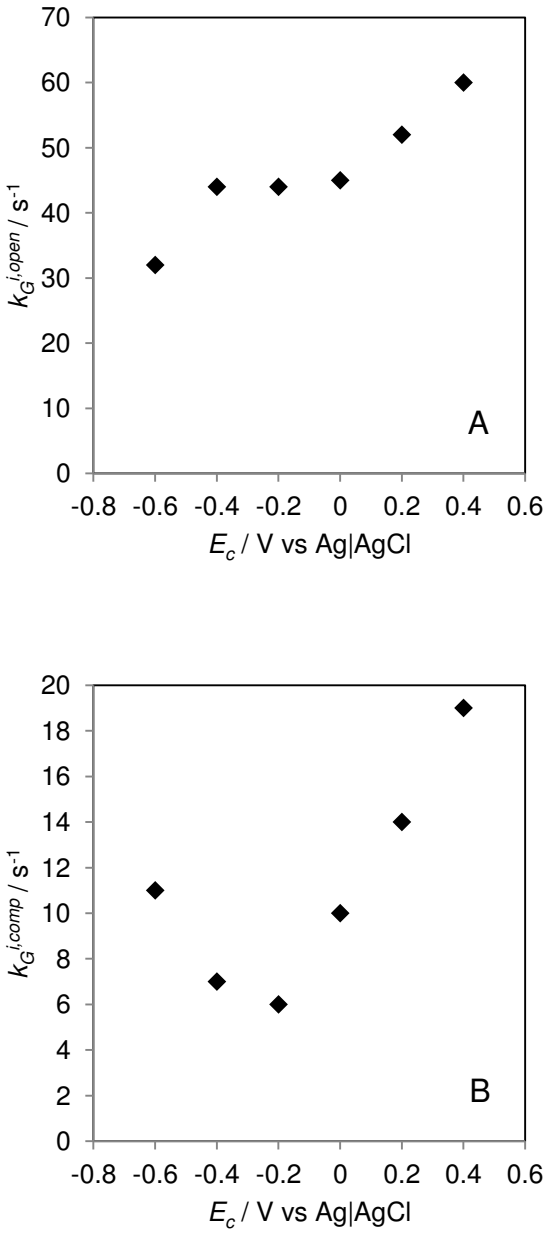

Figure 4.14. Variation of growth rate constants for the instantaneous nucleation mechanism of PPy-Cl film for the (A) fast charging and (B) slow charging pathways during the cathodic potential steps, as a function of the cathodic potential (horizontal axes). The Q_T^{open} and Q_T^{comp} fraction values at each potentials were shown in Table 4.2. Prior to each potential step the film was being polarized at 0.6 V for 10 s. The PPy-Cl film was electrodeposited at 0.9 V to a charge density of 0.5 C cm^{-2}. The electrolyte was 2 M KCl.

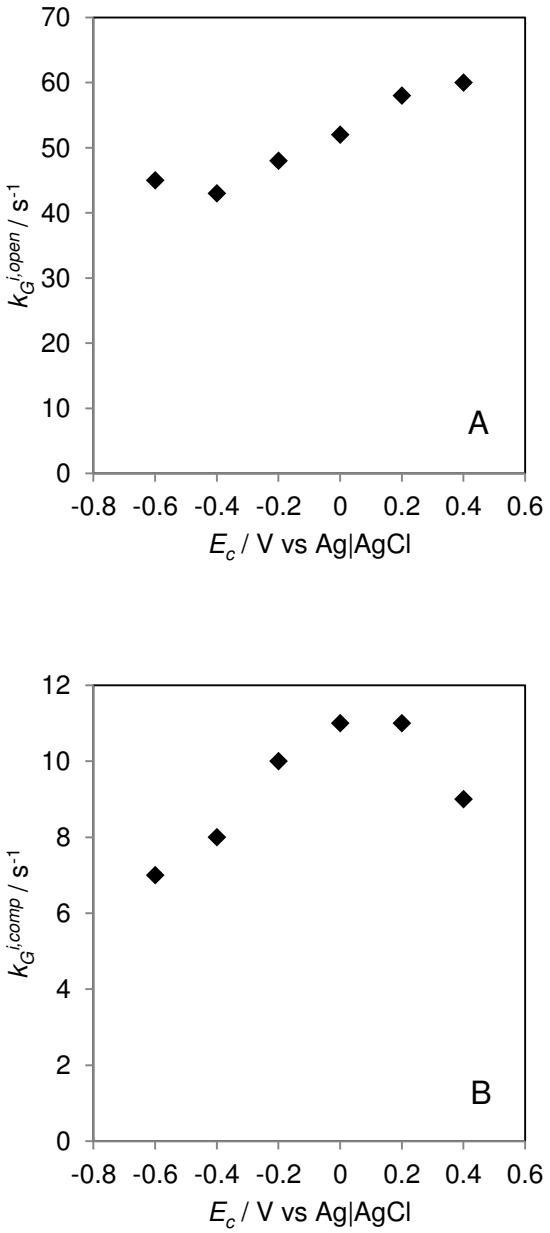

Figure 4.15. Variation of growth rate constants for the instantaneous nucleation mechanism of PPy-CNXL film for the (A) fast charging and (B) slow charging pathways during the cathodic potential steps, as a function of the cathodic potential (horizontal axes). The Q_T^{open} and Q_T^{comp} fraction values at each potentials were shown in Table 4.2. Prior to each potential step the film was being polarized at -0.9 V for 10 s. The PPy-CNXL film was electrodeposited at 0.9 V to a charge density of 0.5 C cm^{-2}. The electrolyte was 2 M KCl.

The differences between the values of growth rate constants for the oxidation and reduction of both of the films were obvious. Significantly higher values were obtained for the reduction than for the oxidation, indicating that the reduction process was much faster. For example, while the fraction of Q_T^{open} was similar for both the oxidation and reduction potential steps, the reduction growth rate constants for the PPy-CNXL were near twice those of the oxidation at each potential. Such behaviour has been previously reported.[11,24] The growth rate constants depend on the initial fraction of the polymer involved in the nucleation process for the transition from an insulating state to the conducting state, even for the case of the instantaneous nucleation mechanism.[11] For the reduction process however, the conducting sites were already present in the film, thus the fraction of the ECP film involved in the reduction process can be said to be constant.[11] The slight variation of the values of the growth constants were due to the slight structural differences at different potentials, which affected the counter-ion movements during the potential steps. In the case of reduction, anion expulsion occurs for the PPy-Cl and cation ingress occurs for the PPy-CNXL. The fact that the transition for PPy-CNXL from an insulating state to the conducting state follows the instantaneous mechanism was also due to the active sites already being present in the film at the reduced state; i.e. the sites where the cations are present. During the reduction however, where no ions were present in the initial conducting state of the PPy-CNXL film, instantaneous nucleation was achieved due to the highly porous structure of the composite film attributed to the strength of the embedded immobile CNXLs. The thin PPy coating of the individual CNXLs within the composite also reduced the ion transport

resistance across the polymer/electrolyte interface, resulting in higher growth constants when compared to PPy-Cl.

A striking coincidence was observed between the best-fit nucleation constants for the oxidation of PPy-Cl and the oxidation current recorded in the CVs (Figure 4.1). The nucleation constants for the oxidation of the PPy-Cl film increased with more positive applied anodic potentials and reached a plateau at +0.2 V (Figure 4.12B). Similarly, the oxidation current at the PPy-Cl CV only started to increase at potential around -0.4 V in the same way as the nucleation rate constants increased with the applied potentials. In contrast, the oxidation current for the PPy-CNXL increased almost vertically after the potential sweep reached -0.6 V. At the moment, a clear relationship between the oxidation CV current and the nucleation rate constants cannot be determined, as CV is a potentiodynamic method while the rate constants were determined from a potentiostatic method. However, the results suggest that the hysteresis observed in the CV for PPy-Cl films may be due to the slow nucleation of the conducting sites as the film undergoes oxidation by the progressive nucleation and growth mechanism. For the PPy-CNXL film, of which both the oxidation and reduction processes occurs by the instantaneous nucleation mechanism, the typical hysteresis was not observed in the CVs.

4.4. Conclusions

The redox switching dynamics of electrodeposited PPy with chloride anions (PPy-Cl) and nanocomposites consisting of PPy and cellulose nanocrystals (CNXLs) (PPy-CNXL) were investigated using the phenomenological model for nucleation and growth of conducting sites within the films. The nucleation and growth mechanism of the conducting sites within the films as they undergo the insulating-conducting transition was easily identified using the potential step measurements. The instantaneous nucleation mechanism has a typical first-order charge-time response whereas the progressive nucleation and growth mechanism has a multiple-order charge-time response. Instantaneous nucleation was observed for the PPy-CNXL films for both oxidation and reduction potential steps. On the PPy-Cl film, progressive nucleation occured during oxidation from the initially non-conducting state, while instantaneous nucleation was observed for the reduction. The effect of the applied potential towards the nucleation and growth rate constants was investigated for all cases. The growth rate constant values for both films were significantly higher during reduction than during oxidation, indicating that the reduction takes place much faster than the oxidation for both films. While the growth rate constants during the oxidation was dependent on the applied potential, the reduction growth rate constants appeared to be independent of the applied potential, due to the already present conducting sites within the films. I also showed that the nucleation and growth mechanism may explain the apparent hysteresis that occurs for PPy-Cl films

during the cyclic voltammetry measurements. However, the hysteresis does not occur for the PPy-CNXL films.

4.5. References

1. C. Peng, J. Jin and G. Z. Chen, Electrochim. Acta, 2007, **53**, 525-537.
2. V. Khomenko, E. Frackowiak and F. Beguin, Electrochim. Acta, 2005, **50**, 2499-2506.
3. E. Frackowiak, V. Khomenko, K. Jurewicz, K. Lota and F. Beguin, J. Power Sources, 2006, **153**, 413-418.
4. S. Bhandari, M. Deepa, S. Singh, G. Gupta and R. Kant, Electrochim. Acta, 2008, **53**, 3189-3199.
5. M. Deepa, S. Bhandari, M. Arora and R. Kant, Macromol. Chem. Phys., 2008, **209**, 137-149.
6. S. Ahmad and S. Singh, Electrochem. Commun., 2008, **10**, 895-898.
7. J. L. Boehme, D. S. K. Mudigonda and J. P. Ferraris, Chem. Mater., 2001, **13**, 4469-4472.
8. M. Dobbelin, R. Marcilla, C. Pozo-Gonzalo and D. Mecerreyes, J. Mater. Chem., 2010, **20**, 7613-7622.
9. J. Ding, D. Z. Zhou, G. Spinks, G. Wallace, S. Forsyth, M. Forsyth and D. MacFarlane, Chem. Mater., 2003, **15**, 2392-2398.
10. D. Z. Zhou, G. M. Spinks, G. G. Wallace, C. Tiyapiboonchaiya, D. R. MacFarlane, M. Forsyth and J. Z. Sun, Electrochim. Acta, 2003, **48**, 2355-2359.
11. H. Randriamahazaka, T. Bonnotte, V. Noel, P. Martin, J. Ghilane, K. Asaka and J. C. Lacroix, J. Phys. Chem. B, 2011, **115**, 205-216.
12. F. Miomandre, M. N. Bussac, E. Vieil and L. Zuppiroli, Chem. Phys., 2000, **255**, 291-300.
13. F. Miomandre, M. N. Bussac, E. Vieil and L. Zuppiroli, Electrochim. Acta, 1999, **44**, 2019-2024.
14. M. D. Levi, C. Lopez, E. Vieil and M. A. Vorotyntsev, Electrochim. Acta, 1997, **42**, 757-769.
15. M. A. Vorotyntsev, E. Vieil and J. Heinze, J. Electroanal. Chem., 1998, **450**, 121-141.
16. M. A. Careem, Y. Velmurugu, S. Skaarup and K. West, J. Power Sources, 2006, **159**, 210-214.
17. T. F. Otero, I. Cantero and H. Grande, Electrochim. Acta, 1999, **44**, 2053-2059.
18. K. P. Vidanapathirana, M. A. Careem, S. Skaarup and K. West, Solid State Ionics, 2002, **154**, 331-335.
19. H. Grande and T. F. Otero, Electrochim. Acta, 1999, **44**, 1893-1900.
20. T. F. Otero, H. Grande and J. Rodriguez, J. Phys. Chem. B, 1997, **101**, 8525-8533.

21. A. S. Sarac, M. Ates and E. A. Parlak, J. Appl. Electrochem., 2006, **36**, 889-898.
22. S. Carquigny, O. Segut, B. Lakard, F. Lallemand and P. Fievet, Synth. Met., 2008, **158**, 453-461.
23. G. Z. Chen, M. S. P. Shaffer, D. Coleby, G. Dixon, W. Z. Zhou, D. J. Fray and A. H. Windle, Adv. Mater., 2000, **12**, 522-526.
24. H. Randriamahazaka, C. Plesse, D. Teyssie and C. Chevrot, Electrochim. Acta, 2005, **50**, 1515-1522.
25. X. W. Chen, K. Z. Xing and O. Inganas, Chem. Mater., 1996, **8**, 2439-2443.
26. M. J. R. Presa, D. Posadas and M. I. Florit, J. Electroanal. Chem., 2000, **482**, 117-124.
27. Q. B. Pei and O. Inganas, J. Phys. Chem., 1993, **97**, 6034-6041.

Chapter 5. High electrode capacitance PPy-CNXL

5.1. Introduction

It has previously been suggested that, in supercapacitor development, reporting only mass specific capacitances (C_M) may be misleading because the total electrode capacitance (C_E) may not increase linearly with increasing amounts of the electrodeposited material.[1-3] C_E is the practically accessible electrode capacitance, normalised to the geometric area of the supercapacitor material (F cm^{-2}). This is an especially important issue because, in the development of supercapacitors, a high C_E value is necessary because it translates directly into the device capacitance.[4] A high C_M achieved by some materials may not be useful if the C_E is impractically low. For example, Lota measured C_M values for very thin films of poly(3,4-ethylenedioxythiophene) (PEDOT), which were as high as 180 F g^{-1}.[5] However, this value reduced to 80-100 F g^{-1} when larger amounts of the material (10-20 mg) were pressed into pellet form. A poly(2,2-dimethyl-3,4-propylene-dioxythiophene) (PProDOT-Me_2) based electrode material although has appreciable C_M, 55 F g^{-1} in a 2 electrode configuration, but the C_E was only 6.5 mF cm^{-2}, which is extremely low for practical use.[6] In another study, a PEDOT-PProDOT and ionic liquid based supercapacitor which demonstrated high performance had only 1.35 mC cm^{-2} (2.7 mF cm^{-2}) per unit electrode area.[7] For these materials, unless the

scale up can be proven to achieve a high C_E, the high C_M is of questionable usefulness. In contrast, C_E on the order of Farads per cm^2 have been widely reported for many other ECP materials.[1,2,8] In this respect, Peng[2] pointed out the importance of the C_E as a complementary performance indicator to C_M for electrode materials should they be proposed for the fabrication of electrochemical supercapacitors.

In this chapter, the effect of the deposition charge density on the electrochemical capacitance of PPy-CNXL films electrochemically synthesized on GC surfaces is described. The capacitive properties of PPy-CNXL films with varying deposition charge were characterised using CV, electrochemical impedance spectroscopy (EIS) and galvanostatic charge/discharge analysis. The average C_M of the PPy-CNXL nanocomposite was 240 F g^{-1} while the C_E was as high as 1.54 F cm^{-2} based on EIS data, which is unprecedented for conducting polymer films of this type. In comparison, C_E value of about 1.0 F cm^{-2} has been reported for state-of-the-art electrodeposited PPy-CNT films and around 0.7 F cm^{-2} for PPy-Cl films.[1] More recently, C_E of 2.35 F cm^{-2} has been reported for a PPy-CNT film.[2] However, the C_E reported was based on CV results which usually give a higher value.[2] The low C_E achieved by the PPy-Cl also shows the disadvantage of using pure ECP in supercapacitor applications, i.e. to achieve the same capacitance requires more surface area of the current collector, and hence a higher cost. A high C_E is dependent on the ability to form a highly porous structure of the ECP throughout the thickness of the material which allows electrolyte access throughout the volume of the ECP during the charging process. High porosity also favours higher potential cycling stability. As the

ion and solvent transfers are facilitated by the porous structure, the ECP becomes more stable volumetrically and thus a more stable performance is achieved. The capacitance values that can be attained using the PPy-CNXL nanocomposite, even when relatively thick films of the material are used, demonstrates that PPy-CNXL nanocomposites are very attractive materials for the fabrication of high performance supercapacitors.

This chapter also reports on the fabrication of a symmetric supercapacitor based on two PPy-CNXL nanocomposite electrodes. The supercapacitor assembly was tested at a cell voltage of 1 V using the CV method and the galvanostatic method. The supercapacitor had comparable specific energy to supercapacitors constructed with different ECP-CNT nanocomposites characterised at similar mass specific current loading. An accelerated stability test revealed that the supercapacitor had a good stability over at least 10000 cycles. After cycling for 50000 cycles, the supercapacitor still retained about half of its initial capacity.

5.2. Experimental

5.2.1 Materials preparation and characterisation

The preparation of the PPy-CNXL and PPy-Cl films on the GC electrodes is similar to that reported for the respective films in Chapter 3. Prior to use, the GC working electrodes were polished with aqueous alumina (0.3 μm) slurries on felt polishing pads and rinsed with deionized water. The

deposition solutions for PPy-CNXL films contained 0.5 M Py in a 0.29 wt% aqueous CNXL dispersion. During potentiostatic deposition of the PPy-CNXL nanocomposites, electrodeposition was performed at +0.9 V vs Ag|AgCl and stopped when the appropriate amount of charge was passed (see text for further details). Electrochemical measurements on the PPy-CNXL films were performed in aqueous 2 M KCl. The laboratory supercapacitor was constructed using two GC electrodes coated with electrodeposited PPy-CNXL to a charge density of 25 C cm^{-2}. The electrodes were connected in a tube cell with aqueous 2 M KCl as the electrolyte.[9] Samples for scanning electron microscopy SEM were prepared by electrodeposition onto GC plates (exposed area = 0.283 cm^2)

5.3. Results and discussions

5.3.1 Electrochemical responses at PPy-CNXL and PPy-Cl films

Figure 5.1 shows the cyclic voltammograms (CV) obtained at a GC electrode coated with PPy-CNXL and PPy-Cl films in 2 M KCl. The films were formed with a deposition charge of 5 C cm^{-2}. The shapes of the CVs were similar to those previously reported for both films formed using a much lower deposition charge (0.1 C cm^{-2}) in Chapter 3. The CV indicates that both the PPy-CNXL and PPy-Cl films were pseudo-capacitive, characterised by the slight deviation from the rectangular shaped response, expected for a purely capacitive material.[10]

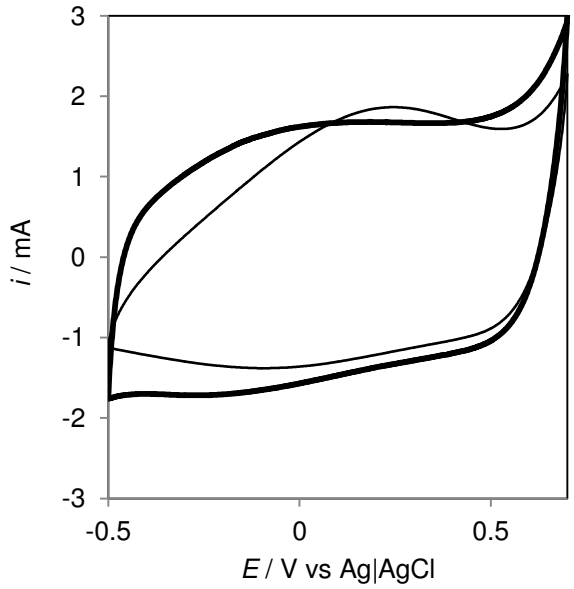

Figure 5.1. Cyclic voltammograms recorded at a PPy-CNXL film (heavy line) and a PPy-Cl film (light line) between potential limits of 0.7 V and -0.5 V. The scan rate was 0.05 V s^{-1}. Both films were electrodeposited at 0.9 V until charge passed was 5 C cm^{-2}. Experiments were carried out in aqueous 2 M KCl.

The CV current recorded at the PPy-CNXL film was higher than that recorded at the PPy-Cl film, indicating that the capacitance of the PPy-CNXL film was higher. Moreover, the sharp rise in current for the PPy-CNXL during the potential switch at the limits indicates that the film can be charged rapidly, unaffected by the diffusion limitation that is posed by counter ions participation.[2] Also noteworthy was at potentials negative of 0 V, the charging/discharging of the PPy-CNXL film was accompanied by cation ingress. This is due to the embedded CNXLs which were immobile and their negative surface charge which has to be balanced when the PPy portions of the composite become neutral. As a result, the PPy-CNXL film exhibited high conductivity and high capacitance at the negative potential region, where the PPy-Cl film became insulating. The charge transfer process that occured on the PPy-CNXL was much more rapid than that occurred on the PPy-Cl film

(Chapter 4). The C_M estimated from the CV in Figure 5.1 for the PPy-CNXL film was 263 F g^{-1} (on the basis of the mass of deposited PPy). The corresponding average mass-specific current and the C_E for the PPy-CNXL CV in Figure 5.1 were 65.8 A g^{-1} and 0.44 F cm^{-2}, respectively. These values are very impressive in comparison with many of those widely reported for other ECP materials. In the literature, many ECPs displayed comparable C_M, however they correspond to significantly lower mass-specific current or loading, and considerably lower C_E (Table 1.4, Chapter 1). The best example for this comparison is a co-electrodeposited PPy-graphene nanocomposite to a charge density of 2 C cm^{-2} which displayed C_M of 285 F g^{-1} when characterised with a current loading of 0.5 A g^{-1}.[11] The current loading of 0.5 A g^{-1} was significantly lower than the response current of 65.8 A g^{-1} in this work.[11] Moreover, when the same characterisation was performed using a PPy-graphene film deposited to 4 C cm^{-2}, the C_M reduced to 215 F g^{-1}.[11] However, the deposition charge was still lower than 5 C cm^{-2} used to fabricate the PPy-CNXL film which the CV in Figure 5.1 was recorded from.

The frequency responses of PPy-CNXL and PPy-Cl films were studied using electrochemical impedance spectroscopy (EIS). Typical Nyquist plots for capacitive ECP materials present a "knee" which separates the plot into two distinctive region.[2] In this case, the "knee" frequency relates to the characteristic diffusion time constant for a system which undergoes charging/discharging cycles accompanied by ion movement.[12] In the development of supercapacitors, films with high knee frequencies are favoured as they can be charged and discharged more rapidly, as high knee frequencies

correspond to short diffusion time constant relating to the Warburg diffusion element.[1,2,12-14]

Figure 5.2A shows a Nyquist plot obtained using a PPy-CNXL film and a PPy-Cl film electrodeposited to charge density of 5 C cm^{-2}, in which the "knee" is indicated with an arrow. EIS was performed at a bias potential of 0.0 V vs Ag|AgCl in each case. The "knee" position occured at a significantly lower real impedance value when the PPy-CNXL film was used compared to when the PPy-Cl film was used indicated a smaller diffusion time constant for the PPy-CNXL film. This is due to significantly shorter diffusion distance for the intercalating ions in the porous PPy-CNXL and consequently, charge transfer occurs more rapidly on the PPy-CNXL.[12] At frequencies below the knee, i.e. the vertical portion of the Nyquist plot, the film capacitance is related to the frequency, f (Hz), by $C = -1/(2\pi fZ'')$, where Z'' is the imaginary component of the complex impedance in ohms. C was evaluated from the gradient of a plot of Z'' at low frequency vs. f^{-1} (Figure 5.2B). C was 0.0293 F and 0.0266 F, for the PPy-CNXL and the PPy-Cl films, respectively. Converting these values to C_M and C_E gives values of 246 F g^{-1} and 0.414 F cm^{-2} for the PPy-CNXL film, and 223 F g^{-1} and 0.376 F cm^{-2} for the PPy-Cl film. The C_M values agreed with those found for much thinner versions of either of the films synthesized using a deposition charge of 0.1 C cm^{-2} discussed in Chapter 3, and also with the value determined using CV, as discussed above (Figure 5.1).

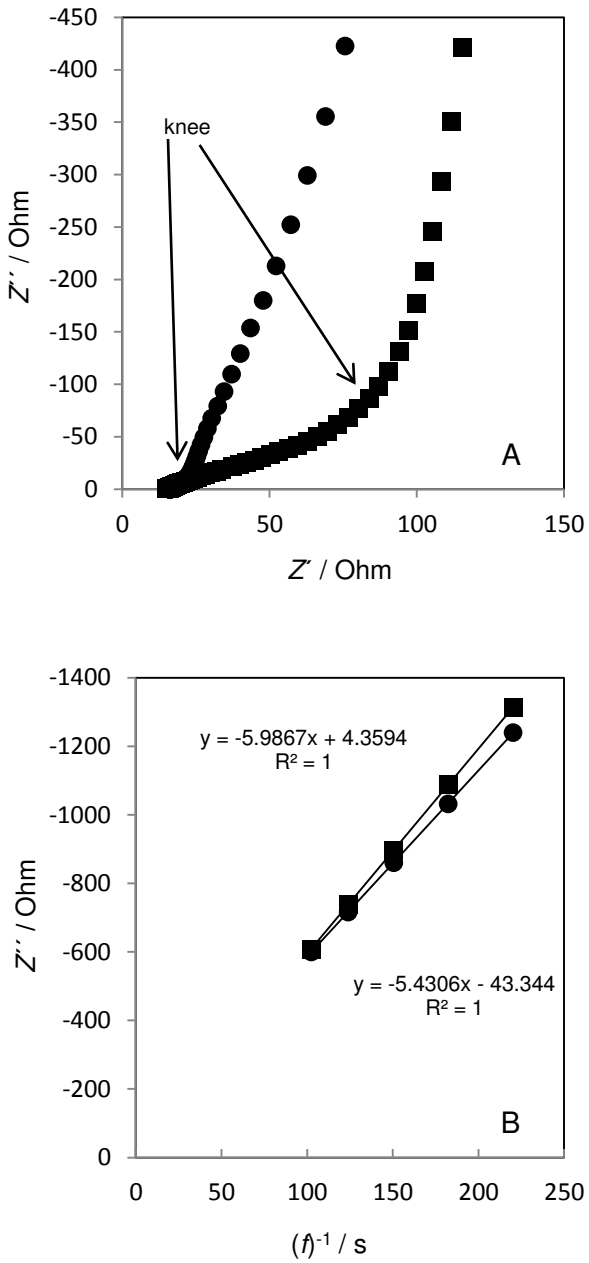

Figure 5.2. Comparison of a PPy-CNXL film (solid circles) and a PPy-Cl film (solid squares). (A) Nyquist plots obtained from EIS at bias potential of 0 V, and with a potential amplitude of 5 mV. (B) Plot of the imaginary component of impedance, at low frequency, versus the inverse of frequency. Both films were electrodeposited at 0.9 V until charge passed was 5 C cm^{-2}. Experiments were carried out in aqueous 2 M KCl.

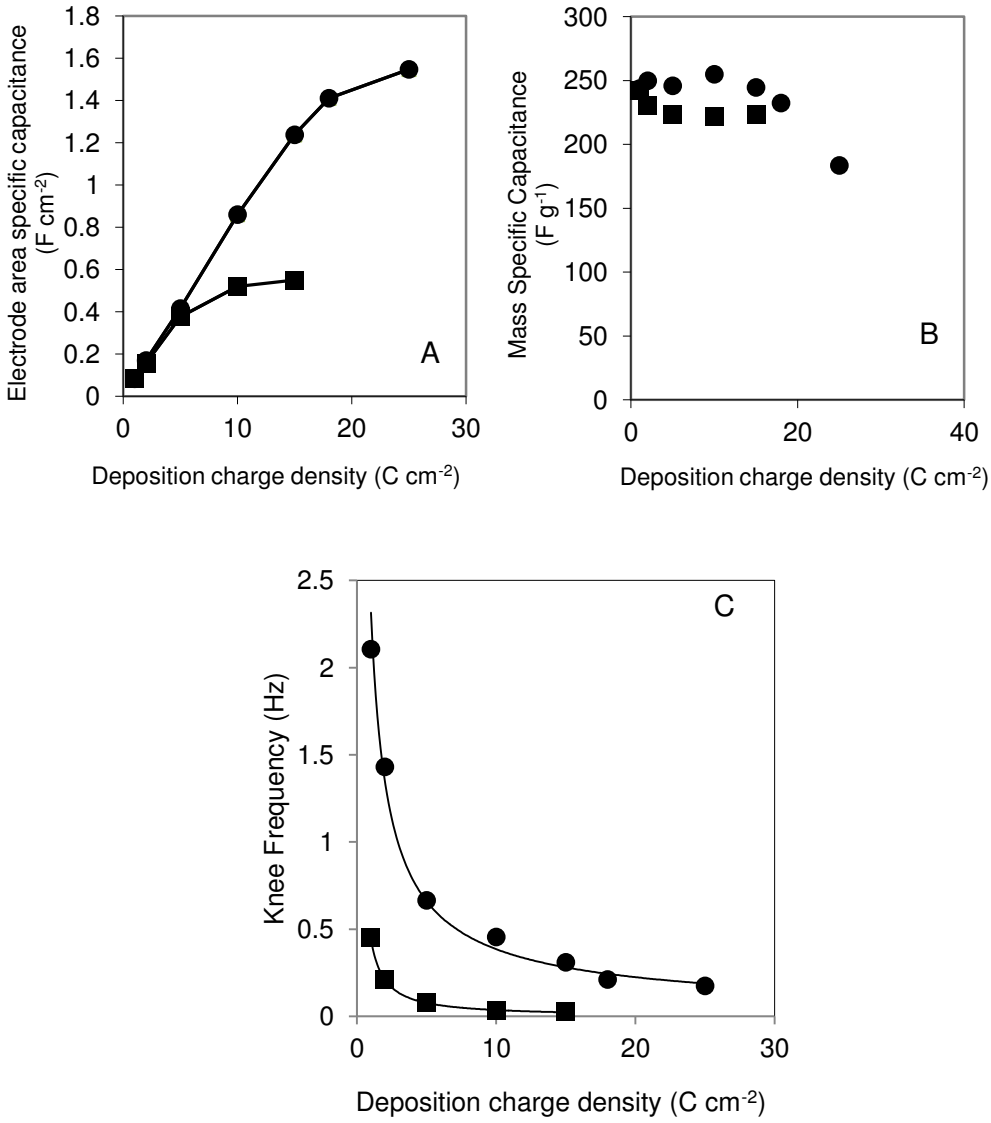

Figure 5.3. Relationship between deposition charge density and (A) low frequency C_E, (B) low frequency C_M, and (C) knee frequency of PPy-CNXL films (solid circles) and PPy-Cl films (solid squares). All films were characterised in 2 M KCl aqueous electrolyte solutions. EIS was performed at bias potential of 0 V with a potential amplitude of 5 mV.

While the C_M and C_E values obtained for films that were deposited at a deposition charge density of 5 C cm^{-2} were still comparable, major differences were revealed when higher deposition charge densities were used, i.e. when thicker films were formed. The low frequency C_E and corresponding C_M values at 0 V vs Ag|AgCl for PPy-CNXL and PPy-Cl films formed at different film formation charges are shown in Figures 5.3A and 5.3B. C_E value as high as 1.54 F cm^{-2} were observed for the PPy-CNXL while the PPy-Cl film yielded an upper C_E limit of about 0.5 F cm^{-2}. The C_E value of 1.54 F cm^{-2} for the PPy-CNXL was unprecedented. Previously, the upper-limit values of about 1.0 F cm^{-2} was reported for the state-of-the-art electrodeposited PPy-CNT films and 0.7 F cm^{-2} for PPy-Cl films, characterised using EIS.[1] Using CV data, a C_E of 2.35 F cm^{-2} was reported for a PPy-CNT nanocomposite film.[2] However, as the CV current may also include the contributions of non-capacitive Faradaic current, the values obtained are usually higher.[2] The upper limit of C_E for the PPy-Cl film of 0.5 F cm^{-2} in this work was however lower than that previously reported (0.7 F cm^{-2}).[1] In this study, radial growth was observed for the PPy-Cl films electrodeposited to deposition charges above 10 C cm^{-2} (Figure 5.4A and 5.4B), which resulted in larger effective electrode surface area for the respective samples.

In this study, the apparent electrode surface area (average diameter indicated in Figure 5.4A and 5.4B) was employed in the C_E calculations for the PPy-Cl films deposited with charges of 10 C cm^{-2} and 15 C cm^{-2}. Analysis of the effect of increasing film formation charge on C_E was not performed beyond deposition charge densities of 15 C cm^{-2}, because at higher film formation charges the growth of the PPy-Cl film became inconsistent and reliable

estimates of the surface area could not be performed. An example of a PPy-Cl film electrodeposited with a charge density of 25 C cm^{-2}, and which has an ill-defined geometrical shape, was shown in Figure 3.2 in Chapter 3. In contrast to the non-uniform growth observed for the PPy-Cl films on GC electrodes, radial growth of the PPy-CNXL films was not observed, even when using deposition charge densities as high as 25 C cm^{-2} (Figure 5.4C, and Figure 3.2 in Chapter 3). The PPy-CNXL films films covered only the underlying GC electrode and the geometric area of the PPy-CNXL film was assumed to be equal to that of the GC electrode.

The presence of an upper limit of the C_E for the PPy-CNXL with increasing film formation charge and the deviation from the initially linear relationship between the C_E and film formation charge was similar to that previously reported for electrodeposited PPy-CNT composites.[1] This behaviour was attributed to inaccessibility of the lower levels of the thick films to the electrolyte such that the film was only partially charged within the timeframe of the measurement.[1] The significant extension of the linear relationship between C_E and the film formation charge (up to around 15 C cm^{-2}) for the PPy-CNXL composite films compared to the PPy-Cl films was a result of uniform growth of the PPy-CNXL composite and also due to the porous morphology of PPy-CNXL films (see below). Within the linear region of the plot of C_E vs film formation charge, an average C_M of approximately 240 F g^{-1} was achieved for the PPy-CNXL nanocomposite (Figure 5.3B).

The effect of the extended uniform growth on the capacitance of ECP nanocomposites is most obvious upon comparison of the 'knee' frequencies in the impedance Nyquist plots. As mentioned above, the 'knee' (indicated by

arrows in Figure 5.2A) is where the high frequency region (diffusion type response) can be distinguished from the low frequency region (capacitive response).[1,13,14] Therefore, the knee frequency is the highest frequency where capacitive behaviour is observed for the ECP films. It is clear from Figure 5.3C that the knee frequencies of the PPy-CNXL films were about four times higher than that of the PPy-Cl films, for a range of films electrodeposited at different charge densities. As discussed before, the higher knee frequency indicates that charge transfer for the PPy-CNXL films was faster than for the PPy-Cl films. This effect is attributed to the highly porous film structure that facilitates ion and electrolyte transfer, as well as the thin coating of the PPy on the individual CNXLs that favours ion transfer across the electrolyte/polymer interface which will be discussed in a later section.[2,12] When a deposition charge density of 25 C cm^{-2} was employed, the PPy-CNXL film exhibited a knee frequency of 0.2 Hz, which is a practically accessible value.[3]

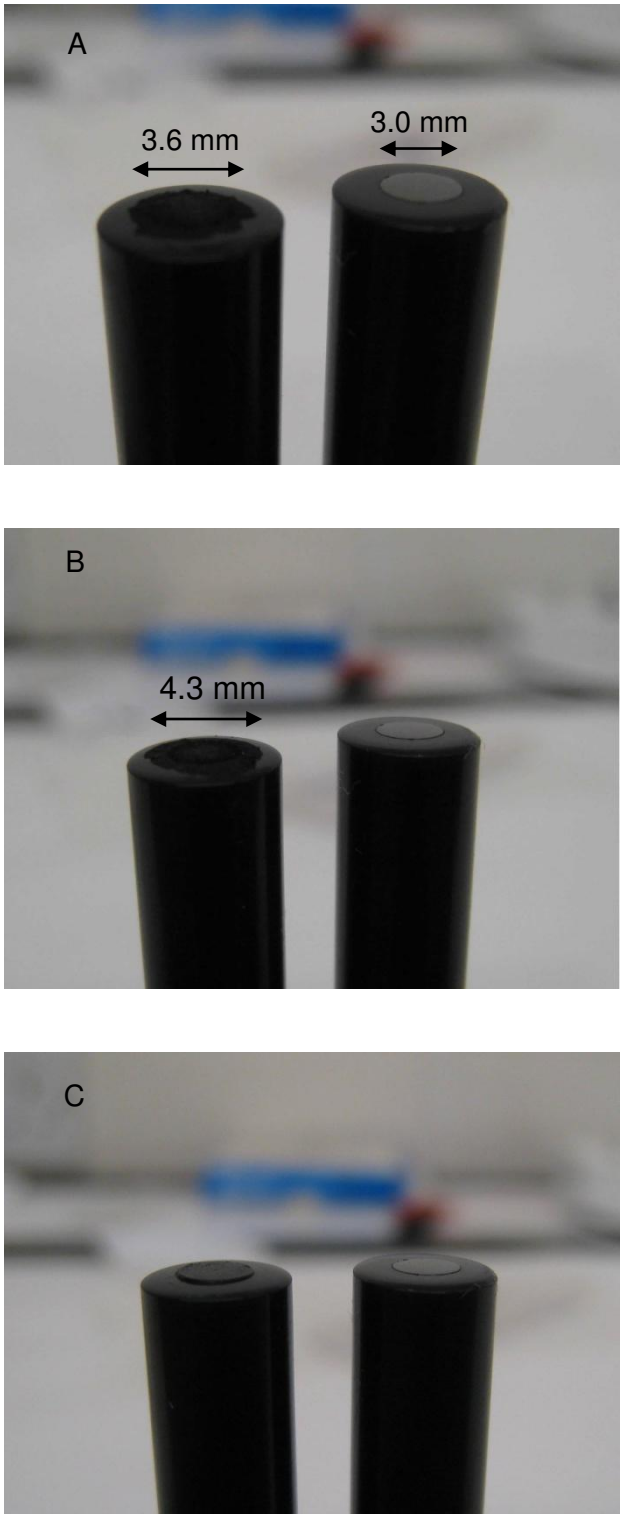

Figure 5.4. Photographs of PPy-Cl films deposited at charge densities of (A) 10 C cm^{-2} and (B) 15 C cm^{-2}. (C) Photograph of a PPy-CNXL film deposited at a charge density of 25 C cm^{-2}. In each image, the left image shows the film coated GC electrode and the right image shows the bare GC electrode. All films were electrodeposited at 0.9 V.

The fast charging capability of the PPy-CNXL films as characterised by the higher knee frequency in comparison with PPy-Cl (Figure 5.3C) was obvious when cyclic voltammetry was performed at relatively fast potential scan rates. Figure 5.5 shows CVs obtained at PPy-CNXL and PPy-Cl coated GC electrodes, where the deposition charge density was 5 C cm^{-2} (Figure 5.5A) and 10 C cm^{-2} (Figure 5.5B) and the potential scan rate employed was 0.25 V s^{-1}. The difference between Figure 5.5A and Figure 5.1 should be noted. Figure 5.1 showed CVs for essentially the same films, but when the potential scan rate was much slower (0.05 V s^{-1}). The CV recorded using the PPy-CNXL film in Figure 5.5A had a more rectangular shape, which suggested that the film was capacitive even at a relatively high scan rate. In contrast, the PPy-Cl film did not respond to fast charging as the shape of the CV indicates that it was more resistive. The difference was even more obvious for the films deposited with charge density of 10 C cm^{-2} as shown in Figure 5.5B when an even larger difference between the CV currents was observed. Therefore, the fast charging capability, in addition to the high C_E values that can be achieved by the PPy-CNXL films indicates that PPy-CNXL nanocomposites are promising electrode materials for the fabrication of electrochemical supercapacitors.

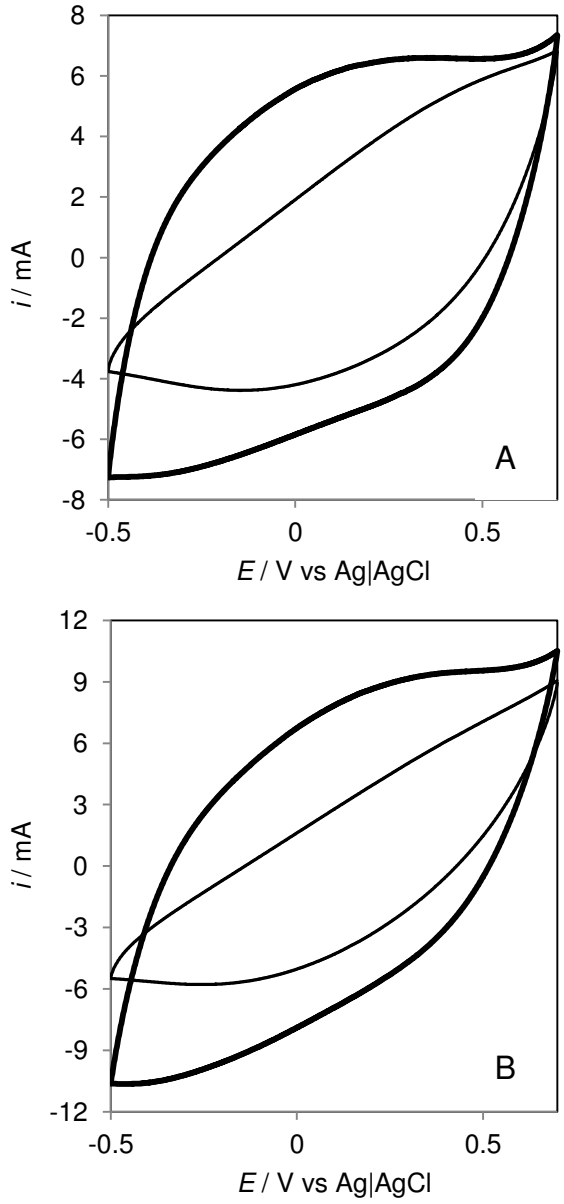

Figure 5.5. Cyclic voltammograms of electrodeposited PPy-CNXL (heavy lines) and PPy-Cl (light lines) in 2 M KCl recorded between potential limits of 0.7 V and -0.5 V at 0.25 V s^{-1}. The films were electrodeposited at 0.9 V until the charge passed was (A) 5 C cm^{-2} and (B) 10 C cm^{-2}.

5.3.2 SEM of PPy-CNXL films

Figure 5.6 shows SEM images of the surface (Figure 5.6A and 5.6B) and the cross-section (Figure 5.6C and 5.6D) of PPy-CNXL films. The PPy-CNXL films were electrodeposited to a charge density of 5 C cm^{-2}. The surface of the PPy-CNXL film (Figure 5.6A and 5.6B) was highly uniform and porous, consisting of individual CNXLs coated with a thin layer of PPy. Such structure and morphology was thought to be extremely favourable for a supercapacitor electrode material as it facilitated ion and solvent movement, and which was discussed in detail in Chapter 3.[2,15,16] While the film was electrodeposited to quite a high charge density (5 C cm^{-2}), Figure 5.6A and 5.6B indicated that the film growth was uniform when the morphology was compared with the much thinner version of the film discussed in Chapter 3 (Figure 3.4), which was formed at a charge density of 0.5 C cm^{-2}. Moreover, as a result of the strength and robustness of these PPy-CNXL films they can be easily removed from the electrode surface without breaking (Figure 3.2 in Chapter 3). A PPy-CNXL film formed at a charge density of 5 C cm^{-2} was removed from the electrode surface after completion of the electrodeposition process. A cross-section in the middle of the film was created by tearing the film gently. By tearing the film apart, the cross section feature of the film was better preserved. Several attempts at creating the cross-section were made by cutting using either a sharp blade or a pair of scissors however they resulted in blunting of the film cross-section due to the shear motion across and also compression during the cutting.

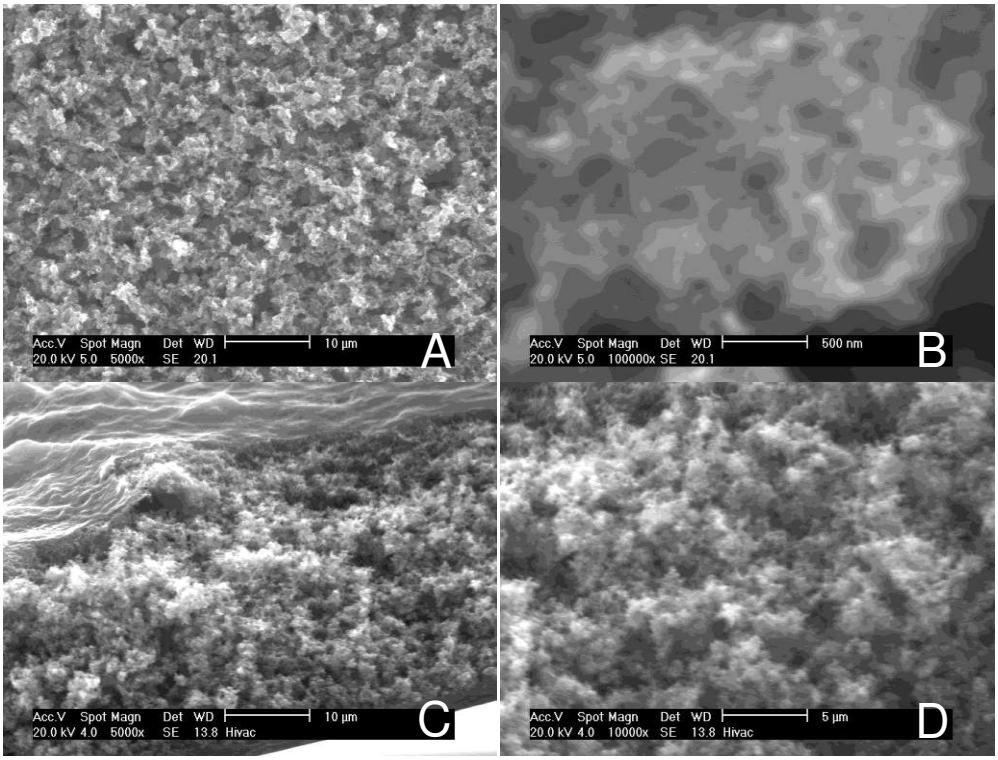

Figure 5.6. SEM images of (A and B) a PPy-CNXL film surface and (C and D) a fractured PPy-CNXL film cross-section. The PPy-CNXL film was electrodeposited at 0.9 V until the charge passed was 5 C cm^{-2}. The cross section surface was created by tearing the PPy-CNXL film after its removal from the GC electrode surface when deposition was completed.

The cross-section SEM images of the PPy-CNXL film (Figure 5.6C and 5.6D) showed that the film cross-section had a homogenous structure throughout the thickness of the film, which was consistent with the film surface structure and morphology (Figure 5.6A and 5.6B). The highly porous film structure throughout not only facilitates ion and electrolyte movement, but the thin coating of PPy on individual CNXLs also favours ion transfer across the electrolyte/polymer interface.[2] Both effects were reported to give rise to a short characteristic diffusion time constant for ion intercalation.[12] Thus, the exceptionally high C_E for the PPy-CNXL film was a result of uniform growth of the porous films at high deposition charges. The achievement of highly porous structure throughout the PPy-CNXL film thickness can be attributed to

the exceptional strength of the CNXLs[17,18] as the polymer filler that has prevented the composite structures from collapsing during prolonged deposition. The cases for the ECP-CNT nanocomposites reported in the literature were essentially the same like the PPy-CNXL.[1,2] High C_E was achieved due to the ability to form an extended porous ECP structure at higher deposition charge density.[1,2] In contrast, the growth of PPy-Cl films were inconsistent when they were deposited to high deposition charge densities, and therefore a uniform structure could not be achieved. These interesting observations and insights, in conjunction with the electrochemical results, highlight the potential application of CNXLs for the fabrication of high capacitance electrode material. The average thickness measured for 3 PPy-CNXL films deposited to 25 C cm^{-2} charge density was 130 ± 5 μm, which gives the thickness per unit deposition charge density of about 5 μm (C $cm^{-2})^{-1}$. This value compares reasonably with the value of 4 μm (C $cm^{-2})^{-1}$ for pure PPy films[19] due to the more porous structure of the PPy-CNXL.

5.3.3 Galvanostatic charging of PPy-CNXL films

To support the EIS analysis of the capacitance of PPy-CNXL films deposited at varying deposition charges, galvanostatic charge/discharge curves were recorded using PPy-CNXL films deposited to 5, 10, 15 and 25 C cm^{-2} at a current density of 10 mA cm^{-2} (Figure 5.7). The charge/discharge curves had slightly asymmetrical shapes. For PPy-CNXL films, the potential increased much slower after reaching 0.5 V when the constant anodic current was

applied. This behaviour agreed with the CV response (Figure 5.1) as higher anodic currents were recorded at potentials positive of 0.5 V.

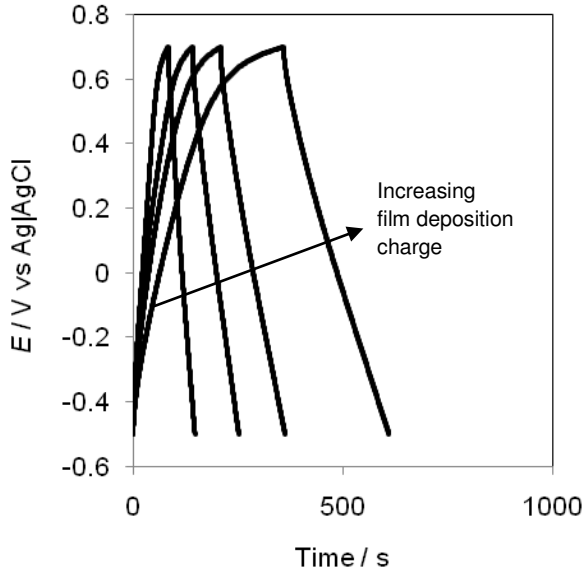

Figure 5.7. Galvanostatic charge/discharge curves at current density of 10 mA cm^{-2} using PPy-CNXL films deposited to charge densities of 5, 10, 15 and 25 C cm^{-2} (increasing film deposition charge indicated with arrow). The potential limits were 0.7 V to -0.5 V. All films were electrodeposited at 0.9 V. The electrolyte was 2 M KCl.

The average C_M determined for the films of different thicknesses from the galvanostatic charge/discharge curve (using the equation C = I/(dE/dt), dE = 2.4 V (one cycle) and dt was the time taken to complete the cycle) was 318 F g^{-1} (262 F g^{-1} based on the discharging curve only) which is slightly higher than that determined using EIS and the CV method described above (Figure 5.1 and Figure 5.3B). However, the average CV current density, normalised to the geometrical area of the electrode (Figure 5.1), was 22 mA cm^{-2}, which is more than twice that used for the galvanostatic experiment. As expected, the capacitance of an electrode material is higher when measurements were performed at lower current loadings.[20] Indeed, the C_M values calculated from the range of techniques used in this study can be considered each agreeing with another, considering also that the non-capacitive faradaic contributions to the

current are not excluded in the galvanostatic method as they are in the EIS analysis. As a result, this could lead to a slight overestimation of the capacitance using the galvanostatic charge/discharge method, in comparison with the EIS method. However, the fact that C_M was consistent for films fabricated using different deposition charge densities as shown using the galvanostatic method (Figure 5.7) indicates that the capacitance of the PPy-CNXL films increased linearly with increasing amount of the electrode material. The highest C_E measured using the galvanostatic method was 2.55 F cm^{-2} (2.1 F cm^{-2} based on discharge curve) from the PPy-CNXL film electrodeposited to 25 C cm^{-2}.

5.3.4 Symmetric supercapacitor based on PPy-CNXL nanocomposite electrodes

Figure 5.8A and 5.8B show the three electrode cell CVs and galvanostatic charge/discharge curves of two PPy-CNXL films electrodeposited to a charge density of 25 C cm^{-2}. These electrodes were used to assemble a laboratory supercapacitor. Figure 5.8A and 5.8B show that the capacitance of the resulting films for large deposition charge density was highly reproducible. This is very important because it it shows that electrochemical fabrication is a reliable process for making high C_E PPy-CNXL nanocomposites. Using the galvanostatic charge/discharge curves, C_M and C_E for electrodes 1 and 2 were 282 and 263 F g^{-1}, and 2.3 and 2.2 F cm^{-2}, respectively. The mass-averaged current loading was 1.19 A g^{-1} in each case. Figure 5.8C shows the CV of the symmetric supercapacitor

assembly when measured in the two-electrode configuration. The test voltage of 1 V was slightly smaller than the potential range of the individual electrodes (≈ 1.2 V). The CV shows highly capacitive response as a result of the fast charging capability of the individual electrodes.[15]

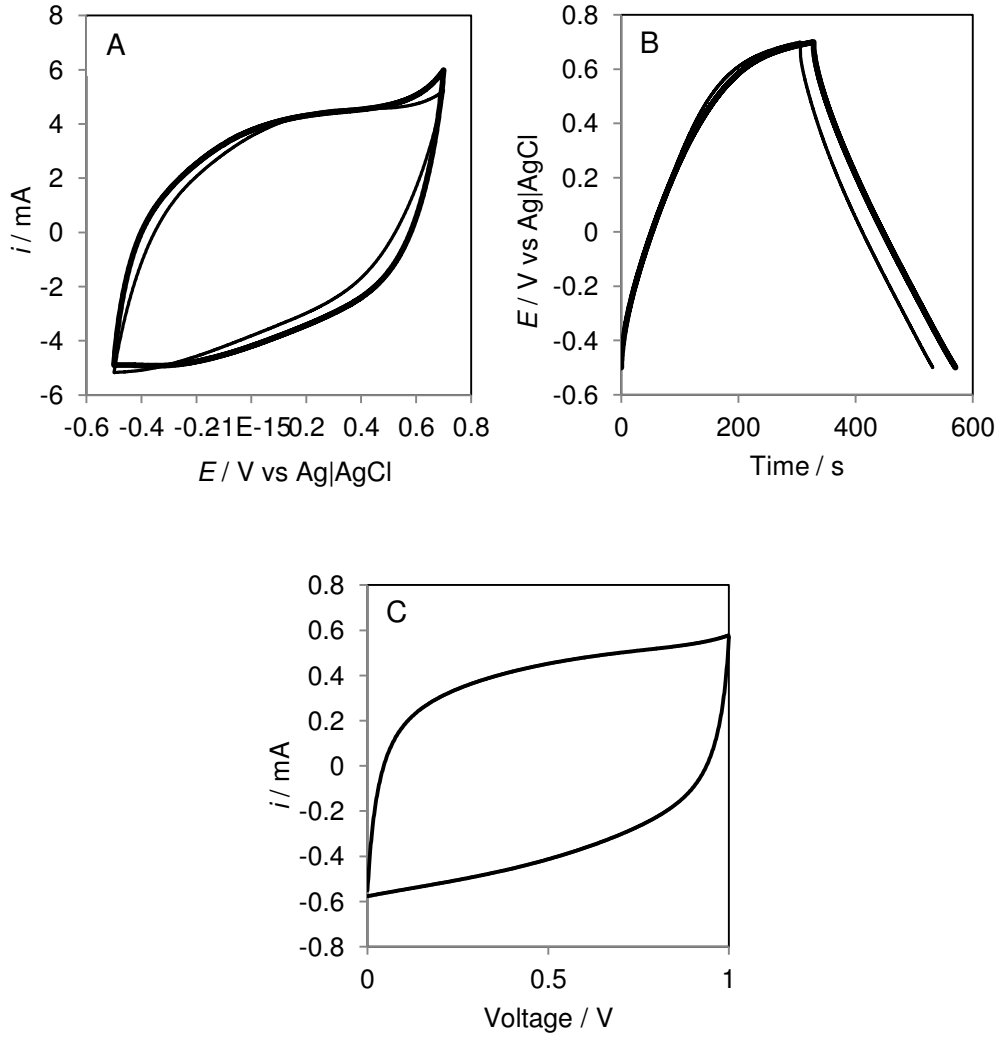

Figure 5.8. (A) Cyclic voltammograms of two PPy-CNXL films electrodeposited at 0.9 V to a charge density of 25 C cm^{-2} in 2 M KCl, recorded between potential limits of 0.7 V and -0.5 V at a scan rate of 0.1 V s^{-1}. The thick line corresponds to electrode 1; thin line corresponds to electrode 2. (B) Galvanostatic charge/discharge curves at current density of 10 mA cm^{-2} for the same PPy-CNXL films used to record the cyclic voltammograms in part (A). The potential limits were 0.7 V to -0.5 V. (C) Cyclic voltammogram of a symmetric supercapacitor constructed using both the PPy-CNXL electrodes characterised in part (A) and (B). The electrolyte in the supercapacitor is 2 M KCl. The cyclic voltammogram was recorded between 0 to 1 V at 0.01 V s^{-1}.

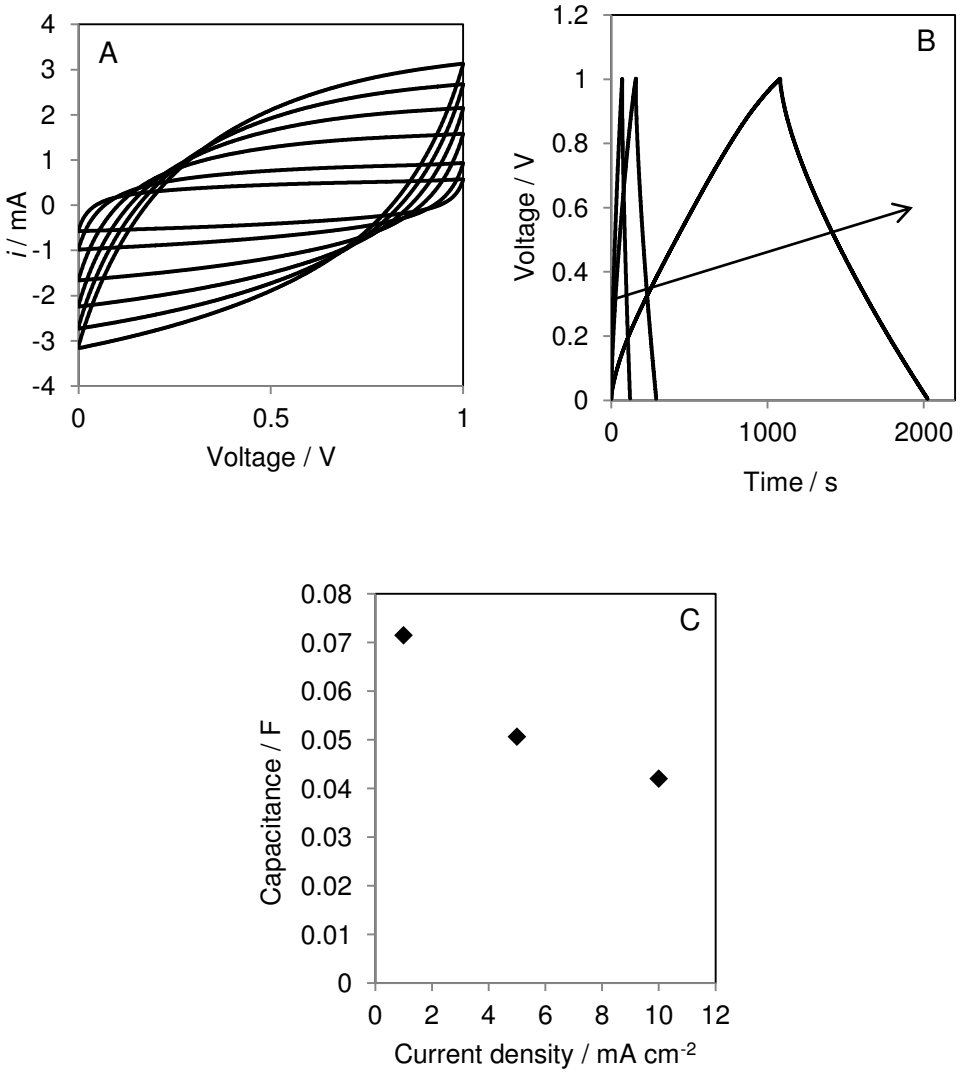

Figure 5.9. (A) Cyclic voltammograms of the symmetric supercapacitor recorded between 0 to 1 V at scan rates of 10 mV s^{-1} (innermost curve, increasing scan rate indicated with arrow), 20 mV s^{-1}, 40 mV s^{-1}, 60 mV s^{-1}, 80 mV s^{-1} and 100 mV s^{-1}. (B) Galvanostatic charge/discharge curves recorded using the symmetric supercapacitor between 0 to 1 V at current densities of 10 mA cm^{-2}, 5 mA cm^{-2} and 1 mA cm^{-2}. The arrow indicates the decreasing current density. (C) The relationship between the device capacitance measured using the galvanostatic method against the current density applied for the measurement. The symmetric supercapacitor consists of 2 PPy-CNXL electrodes which were prepared by electrodeposition at 0.9 V until a charge density of 25 C cm^{-2} was reached. The electrolyte in the supercapacitor was 2 M KCl.

On increasing scan rate, the average CV current increased proportionally (Figure 5.9A). At faster scan rate however, the vertical current increase at the potential limits was no longer observed but instead a significant voltage drop (iR drop) was observed. The is due to the relatively thick individual PPy-CNXL films used for the supercapacitor assembly which has a large diffusion distance for ions to reach the lower levels of the films, as discussed earlier Section 5.3.1.[1] Galvanostatic charge/discharge curves were also produced for the supercapacitor at different current loadings (Figure 5.9B). At the discharge current density of 1 mA cm^{-2} (119 mA g^{-1} based on the mass of PPy electrodeposited on a single electrode), the average mass specific capacitance, C_{AMC} of the electrode materials was 240 F g^{-1}, calculated using the equation $C_{AMC}=4C_{Cell}/M_T$ where C_{AMC} is the average mass specific capacitance, C_{Cell} is the cell capacitance, M_T is the total mass of the electrode materials (both electrodes, considering PPy mass only).[20] The C_{AMC} was very close to the C_M values for each of the individual electrodes, showing equal and near maximum utilization of the capacitance on each of the electrodes (in the three-electrode case) in the supercapacitor assembly.[20] The calculation of specific energy was performed using the equation $W_{sp}=0.5C_{ssp}V^2$ where W_{sp} is the specific energy in J g^{-1}, C_{ssp} is the cell total mass specific capacitance (F g^{-1}) which is C_{Cell}/M_T, V is the working voltage of the supercapacitor, which is 1 V in this case.[20] The calculation resulted in a specific energy of 8.34 Wh kg^{-1} for the symmetric PPy-CNXL supercapacitor which is comparable to that of supercapacitors built using different ECP-CNT nanocomposites, and characterised at similar mass specific current loading.[15] More importantly, these results were produced using relatively thick PPy-CNXL films with high

C_E, which is unprecedented, and that really demonstrates the practical aspects of these films.

The capacitance degradation of the supercapacitor was studied by continuously cycling the supercapcitor between 0 and 1 V at a scan rate of 0.05 V s^{-1}. The potential cycling stability test reported and discussed previously in Chapter 3 was performed on relatively thin films (deposition charge of 0.1 C cm^{-2}), whereas the films made for the supercapacitor in this chapter were deposited to charge densities 250 times higher (25 C cm^{-2}). The potential cycling stability of such thick ECP films, or supercapacitor devices made with such thick electrodeposited ECP films has thus far not yet been reported. Galvanostatic charge/discharge curves were recorded before the cycling test and after the number of cycles as indicated in Figure 5.10. The capacitance loss was fastest at the early stages of the stability test, where 14% of capacitance was lost in the initial 1000 cycles. From the 1000^{th} cycle until the 10000^{th} cycle a further 16% of capacitance was lost; and another 23% lost in the next 40000 cycles. In other words, the supercapacitor retained 70% of its initial capacity after being cycled for 10000 times and 47% of its capacity after 50000 cycles. As most ECP based supercapacitors have typical cycle-life of a few thousand cycles,[4] the PPy-CNXL supercapacitor performance can be considered very stable as it retained almost half its original capacity after 50000 cycles. The exceptional potential cycling stability for the supercapacitor is attributed to the stability of the individual electrodes, due to:

(1) the highly porous structure of the PPy-CNXL nanocomposite and the thin coating of PPy on individual CNXLs, which facilitates the ion and solvent

movements during the charge/discharge cycles and consequently more stable volumetrically, and

(2) contribution of strength by the exceptionally strong CNXLs as has been discussed in Chapter 3.

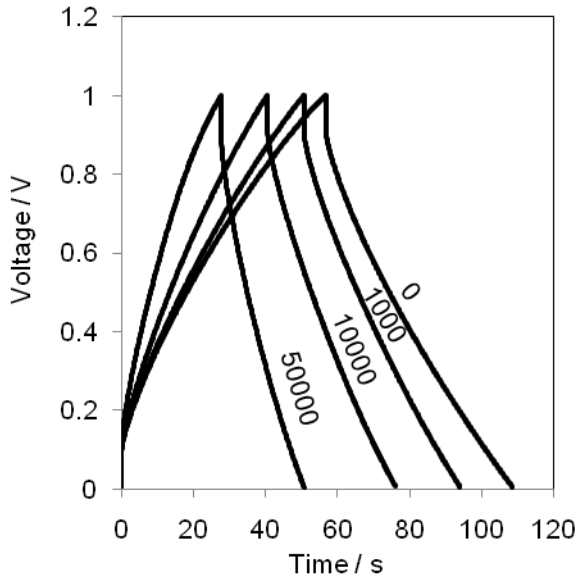

Figure 5.10. Galvanostatic charge/discharge curves of the symmetric supercapacitor recorded before (indicated '0') and after a number of potential cycles (number of cycles indicated on the curves) at 10 mA cm^{-2}. The potential cycling was performed between the voltage of 0 to 1 V at a scan rate of 50 mV s^{-1}. The symmetric supercapacitor consists of 2 PPy-CNXL electrodes which was prepared by electrodeposition at 0.9 V until a charge density of 25 C cm^{-2} was reached. The electrolyte in the supercapacitor was 2 M KCl.

5.4. Conclusions

Cellulose nanocrystals (CNXLs) from cotton were used in the electrochemical synthesis of polypyrrole (PPy)-cellulose nanocomposite (PPy-CNXL) films for the construction of a symmetrical supercapacitor. The mass specific capacitance (C_M) and electrode specific capacitance (C_E) of the PPy-CNXL nanocomposite films were examined for a range of film formation charges using low frequency impedance data supported by galvanostatic charge/discharge data. C_E of 1.54 F cm^{-2} was recorded for the PPy-CNXL nanocomposite, for a film electrodeposited to 25 C cm^{-2} of charge. This is the highest C_E determined for any PPy composite using EIS while an average mass specific capacitance of about 240 F g^{-1} was recorded across the range of deposition charges examined. The EIS results showed that the PPy-CNXL films can be charged 4 times faster than PPy-Cl. Moreover, the PPy-CNXL film electrodeposited using 25 C cm^{-2} of charge still displayed a practical knee frequency of 0.2 Hz. The exceptionally high electrode capacitance and the rapid charge transfer in these materials is attributed to the highly porous film structure throughout, which facilitates ion and electrolyte movement, as well as the relatively thin coating of PPy on individual CNXLs that favours ion transfer across the electrolyte/polymer interface.

A symmetrical supercapacitor was constructed using two PPy-CNXL electrodes and tested at an operating voltage of 1 V. The specific energy of the symmetrical cell at an electrode area specific current density of 1 mA cm^{-2} (mass specific current density of 118 mA g^{-1}) was 8.34 Wh/kg. This value is comparable to that of similar supercapacitors constructed with various different

ECP-CNT nanocomposites, and characterised at similar current loading. An accelerated stability test also showed that the PPy-CNXL supercapacitor was stable for at least up to 50000 cycles where 47 % of its initial capacity was retained. For the first time a supercapacitor device was constructed using a high performance nanocomposite containing non-conducting CNXLs. I believe the results may be of significant interest to the wide community considering the ever increasing demand in application of green, cost effective and environmentally friendly materials.

5.5. References

1. M. Hughes, G. Z. Chen, M. S. P. Shaffer, D. J. Fray and A. H. Windle, Chem. Mater., 2002, **14**, 1610-1613.
2. C. Peng, J. Jin and G. Z. Chen, Electrochim. Acta, 2007, **53**, 525-537.
3. G. A. Snook, C. Peng, D. J. Fray and G. Z. Chen, Electrochem. Commun., 2007, **9**, 83-88.
4. G. A. Snook, P. Kao and A. S. Best, J. Power Sources, 2011, **196**, 1-12.
5. K. Lota, V. Khomenko and E. Frackowiak, J. Phys. Chem. Solids, 2004, **65**, 295-301.
6. D. Y. Liu and J. R. Reynolds, ACS Applied Materials & Interfaces, 2010, **2**, 3586-3593.
7. J. D. Stenger-Smith, C. K. Webber, N. Anderson, A. P. Chafin, K. K. Zong and J. R. Reynolds, J. Electrochem. Soc., 2002, **149**, A973-A977.
8. G. A. Snook, G. Z. Chen, D. J. Fray, M. Hughes and M. Shaffer, J. Electroanal. Chem., 2004, **568**, 135-142.
9. D. Hu, C. Peng and G. Z. Chen, ACS Nano, 2010, **4**, 4274-4282.
10. E. Frackowiak and F. Beguin, Carbon, 2001, **39**, 937-950.
11. A. Liu, C. Li, H. Bai and G. Shi, J. Phys. Chem. C, 2010, **114**, 22783-22789.
12. M. D. Levi, C. Wang and D. Aurbach, J. Electroanal. Chem., 2004, **561**, 1-11.
13. W. J. Albery, Z. Chen, B. R. Horrocks, A. R. Mount, P. J. Wilson, D. Bloor, A. T. Monkman and C. M. Elliott, Faraday Discuss., 1989, **88**, 247-259.
14. D. J. Guerrero, X. M. Ren and J. P. Ferraris, Chem. Mater., 1994, **6**, 1437-1443.
15. E. Frackowiak, V. Khomenko, K. Jurewicz, K. Lota and F. Beguin, J. Power Sources, 2006, **153**, 413-418.

16. V. Khomenko, E. Frackowiak and F. Beguin, Electrochim. Acta, 2005, **50**, 2499-2506.
17. M. Samir, F. Alloin and A. Dufresne, Biomacromolecules, 2005, **6**, 612-626.
18. M. Samir, F. Alloin, J. Y. Sanchez, N. El Kissi and A. Dufresne, Macromolecules, 2004, **37**, 1386-1393.
19. M. Bozlar, F. Miomandre and J. B. Bai, Carbon, 2009, **47**, 80-84.
20. K. C. Ng, S. W. Zhang, C. Peng and G. Z. Chen, J. Electrochem. Soc., 2009, **156**, A846-A853.

Chapter 6. PANi-CNXL and PEDOT-CNXL composite films

6.1. Introduction

Amongst all ECPs, PANi and PEDOT are among some of the most important and widely studied.[1] This is especially true in the development of ECP supercapacitors. Together with PPy, PANi and PEDOT are the most widely studied ECPs due to their high capacitance, their ease of fabrication and their relatively low cost. For example, PANi films can reach a very high mass specific capacitance (up to 775 F g^{-1}),[2] while PEDOT is known for its improved stability compared to PANi and PPy,[3-5] and has a stable redox response towards relatively large potential perturbations.[6] However, these ECPs share a common weakness, which is the poor potential cycling stability. The poor stability of these ECPs has been significantly improved by forming composite materials in particularly those with CNTs.[3,7] The improved capacitance and stability was attributed to the high porosity of the ECP-CNT composites which facilitated the ions and solvent transport during the charging and discharging.[3] The stability enhancement was also due to the excellent mechanical properties of CNTs which form the backbone structure in those composites.[3]

In Chapter 3, 4 and 5, the advantages of the PPy-CNXL nanocomposite have been demonstrated. The capacitance and stability of PPy was enhanced

by the highly porous structure of the PPy-CNXL that facilitates ion and solvent movements, resulting in a shorter electrolyte transport distance.[3,8,9] Moreover, the instantaneous nucleation of the conducting sites during oxidation allowed a much more rapid charging of the composite films compared to the PPy films electrodeposited with small anions as the counter ion (PPy-Cl).[3,10] Owing to the strength of the CNXLs as the structural backbone of these nanocomposites, PPy-CNXL composite films of unprecedented C_E have been fabricated electrochemically (Chapter 5).

It is important to investigate whether the performance improvement that was provided by the CNXLs on PPy could also be extended to PANi and PEDOT. Such a comparison study allows generalisation of the CNXLs contribution in ECP-CNXL composites to be established. PANi-CNXL and PEDOT-CNXL nanocomposite films were electrochemically synthesized at platinum and glassy carbon (GC) surfaces, respectively. The performances of these nanocomposite films were compared to those of the ECP films containing small anions (ECP-X). CNXLs extracted from cotton using sulphuric acid hydrolysis (S-CNXLs) were used for the fabrication of PANi-CNXL composite. The S-CNXLs were used due to the highly acidic media (0.5 M HCl) that was required to dissolve the aniline (ANi) monomers. In that acidic environment, both S-CNXLs and O-CNXLs become protonated, as a result they 'crash out' from the initially, charge-stabilised dispersions to form suspensions. The suspensions of S-CNXLs were more stable than O-CNXL suspensions as the S-CNXLs did not precipitate and is therefore used for the fabrication of the PANi-CNXL. These details will be further discussed in the results section. For the PEDOT-CNXL composite, O-CNXLs were used

as the negative surface charge density of O-CNXLs was higher than that of S-CNXLs.

The PANi-CNXL films were electrodeposited from a solution of S-CNXLs, HCl and the ANi monomers. The PEDOT-CNXL composites were electrodeposited from a solution of O-CNXLs, $LiClO_4$ and ethylenedioxythiophene (EDOT) monomers. The CNXLs were incorporated at the same time as the supporting electrolytes during electrodeposition of both nanocomposites. The resulting nanocomposite films were characterized using scanning electron microscopy (SEM), cyclic voltammetry, electrochemical impedance spectroscopy (EIS) and galvanostatic charge-discharge analysis. The results show that the electrochemical performance and stability of the ECP-CNXL nanocomposites was much improved compared to the respective ECP-X, in agreement with the case for the PPy-CNXL. Moreover, a linear increase of the electrode capacitance was demonstrated using the thick PANi-CNXL film electrodeposited to a high charge density. The thick PANi-CNXL film also showed much faster charging (more than an order of magnitude) than the thick pure PANi film. The electrosynthesis of thick PEDOT-CNXL film was unfortunately not successful. These results show that the PANi-CNXL nanocomposite was especially promising for the fabrication of inexpensive, high performance electrochemical supercapacitors, as evident from the CV and electrochemical impedance spectroscopy (EIS) results.

6.2. Experimental

6.2.1 Materials preparation and characterisation

Both S-CNXLs and O-CNXLs are used in the work reported in this Chapter. For the deposition of PANi-CNXL nanocomposite films, the S-CNXLs were used. For the deposition of PEDOT-CNXL nanocomposite films, the O-CNXLs were used. PANi-CNXL films were electrodeposited from solutions containing 0.25 M ANi in 0.5 wt% S-CNXL suspension in 0.5 M HCl. For comparison, PANi films were electrodeposited from a deposition solution containing 0.25 M ANi in 1 M HCl. PEDOT-CNXL films were electrodeposited solutions containing 38 mM EDOT in a mixture of 5:2 aqueous 50 mM $LiClO_4$ in a 0.79 wt% O-CNXL dispersion/acetonitrile. PEDOT films were deposited from solutions comprised of 38 mM EDOT in a mixture of 5:2 aqueous 100 mM $LiClO_4$/acetonitrile. All the deposition solutions were prepared through ultrasonication for 10 minutes.

Prior to use, the Pt and GC working electrodes were cleaned by polishing with aqueous alumina (0.3 μm) slurries on the Neoprene polishing pads and rinsed with deionized water. The films were electrodeposited potentiostatically. For the PANi and PANi-CNXL nanocomposites, electrodeposition was performed at + 0.9 V vs Ag|AgCl; for the PEDOT and PEDOT-CNXL nanocomposites electrodeposition was performed at +1.1 V vs Ag|AgCl. The deposition potential was determined using the CV method (for full details see section 3.1). The deposition charge density employed for the PANi and PANi-CNXL nanocomposite was either 0.2 C cm^{-2} or 10 C cm^{-2}

while the deposition charge density for the PEDOT and PEDOT-CNXL was 1 C cm^{-2}. After the deposition, the electrodes were rinsed gently with water before characterisation. Electrochemical measurements on the PANi and PANi-CNXL films were performed in 1 M HCl, while for the PEDOT and PEDOT-CNXL films the measurements were performed in 2 M KCl unless otherwise indicated. All the electrodeposition and electrochemical characterisation of the ECP and ECP composites were performed under ambient conditions (ca. 20˚C). Samples for scanning electron microscopy (SEM) were prepared by electrodeposition onto GC plates (exposed area = 0.283 cm^2). PANi-CNXL and PANi samples for TGA were electrodeposited using a Pt wire as the working electrode. TGA was performed using a TA Instruments TGA Q500, run from 25˚C to 1000˚C under the flow of air at 10˚C min^{-1}.

6.3. Results and discussions

6.3.1 Electrochemical Deposition of PANi-CNXL and PEDOT-CNXL Nanocomposites

Figure 6.1 shows CVs obtained at Pt disk electrodes for the electrodeposition of PANi and PANi-CNXL films (Figure 6.1A) and at GC disk electrodes for the electrodeposition of PEDOT and PEDOT-CNXL films (Figure 6.1B). It is obvious that an oxidation current loop was present for both films which indicated nucleation and growth of the ECP and ECP composites,[11,12] where deposition on pre-existing polymer surfaces was preferred compared to clean Pt or GC electrode surfaces.[13] However,

supporting electrolytes were present in the deposition solution for PANi-CNXL and PEDOT-CNXL. That was due to the insolubility of both the ANi and EDOT monomers in pure de-ionised water. In the case of deposition solution for PEDOT-CNXL, EDOT was dissolved in acetonitrile. Because the O-CNXLs do not disperse in pure acetonitrile, a mixed water/acetonitrile solvent system was employed for the deposition of PEDOT-CNXL films.[3] Poor voltammetric responses were recorded for the deposition of PEDOT-CNXL in the absence of supporting $LiClO_4$ in the deposition solution. Therefore, a small amount of the supporting $LiClO_4$ was added to aid the co-deposition. In the case of the PANi-CNXL deposition solution, HCl was required to dissolve the ANi monomer. In the acidic environment (pH = 0.3 for 0.5 M H_2SO_4), the majority of surface groups on both O-CNXLs (carboxylate groups with pKa ≈ 4.8) and S-CNXLs (assuming pKa of 1.03 for sulfonate groups on polymers[14]) became protonated. As a result, they were no longer dispersed in the solution but instead formed a suspension. The suspension of S-CNXLs was however more stable compared to the suspension of O-CNXLs, as the S-CNXLs did not precipitate and settle at the bottom of the container like the O-CNXLs did. Therefore, S-CNXLs are used for the deposition of PANi-CNXL.

In the presence of supporting electrolytes, the deposition CVs does not confirm the formation of the ECP composites. However, the successful formation of the ECP composites was shown using a range of techniques discussed in the following sections. For subsequent measurements, the PANi and PANi-CNXL films were prepared using constant potential deposition at 0.9 V while the PEDOT and PEDOT-CNXL films were prepared using

constant potential deposition at 1.1 V, which prevents over-oxidation of the deposited films and allows good control of the deposition charge.[3]

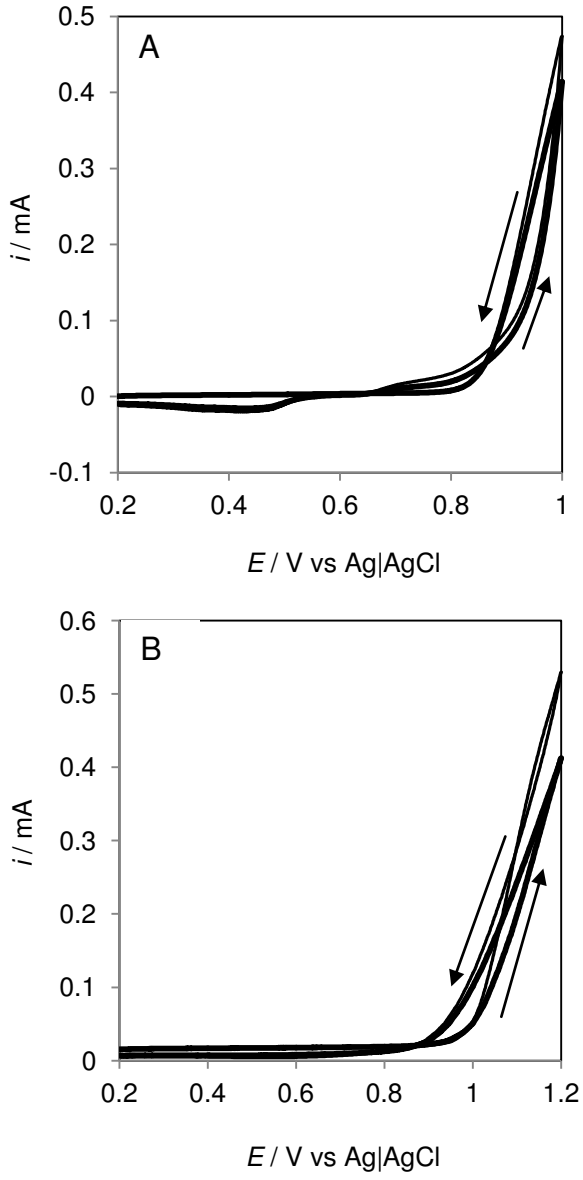

Figure 6.1. (A) Cyclic voltammograms recorded at a Pt electrode in 0.25 M ANi in 1 M HCl (thin line) and in 0.25 M ANi in 0.5 wt % CNXL suspension in 0.5 M HCl (thick line). (B) Cyclic voltammograms recorded at a GC electrode in 38 mM EDOT in a mixture of 5:2 aqueous 100 mM $LiClO_4$/acetonitrile (thin line) and in 38 mM EDOT in a mixture of 5:2 aqueous 50 mM $LiClO_4$ in a 0.79 wt. % CNXL dispersion/acetonitrile. The potential scan rate for A) was 0.1 V s^{-1} and for B) was 0.05 V s^{-1}. The initial potential was 0.2 V and the potential range was as indicated by the horizontal axis.

6.3.2 Structural characterisation of films

Figure 6.2 shows SEM images at low magnification of PANI, PANi-CNXL, PEDOT and PEDOT-CNXL (Figure 6.2A – 6.2D, respectively). The SEM images showed clear differences between the film surface of the ECP-X and the respective ECP-CNXL composite. For instance, the PANi-CNXL film had notably rougher features, and was more porous than the pure PANi. The difference between the PEDOT and PEDOT-CNXL film was even more striking. The PEDOT film had a porous surface containing relatively thick aggregates at the surface which is typical of electrodeposited PEDOT,[3,15] while the PEDOT-CNXL had a relatively smooth surface with pores only slightly visible.

At higher magnification (40000 times) it can be seen that the PANi-CNXL film had a significantly more open structure than the PANi film (compare Figure 6.3D to Figure 6.3A). A more open structure was thought to be favourable for electrochemical applications as it facilitates ion and solvent transport during the charging/discharging cycle.[3] Moreover, at this magnification, the features of CNXL in the PANi-CNXL were obvious. Pure PANi was fibrillar in structure, in agreement with the previously reported structure for PANi.[2,3] However, the PANi-CNXL composite showed more linear structures which is thought to be the result of coating of the monocrystalline CNXL nanorods by the PANi.

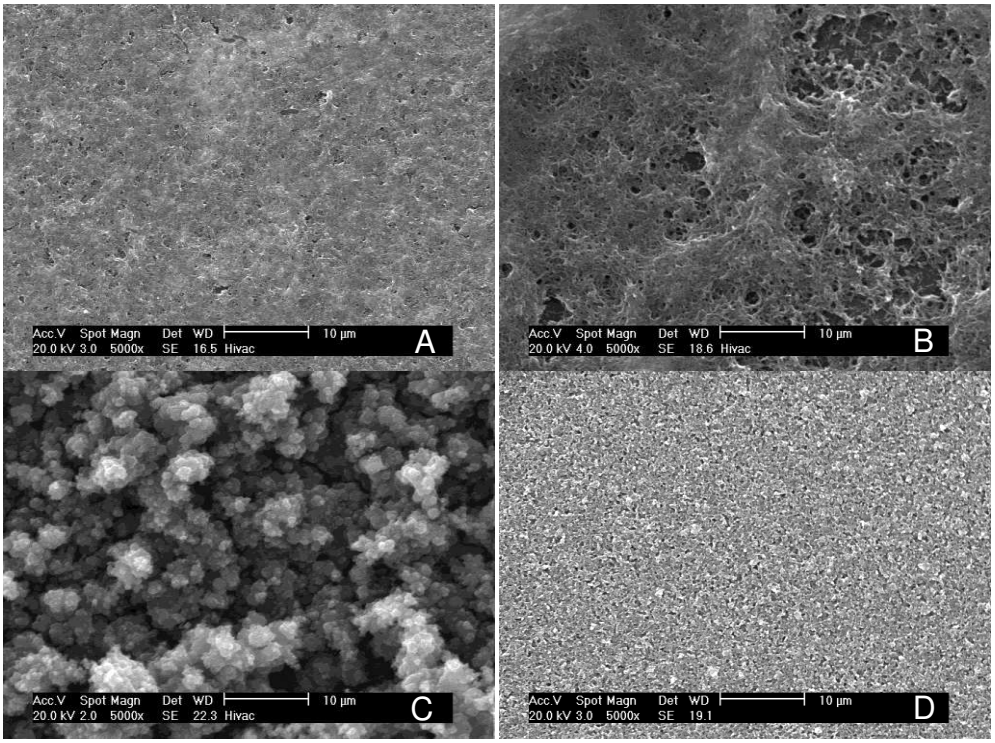

Figure 6.2. SEM images of (A) PANi, (B) PANi-CNXL, (C) PEDOT and (D) PEDOT-CNXL at 5000 times magnification. The PANi and PANi-CNXL films were electrodeposited at 0.9 V to a charge density of 0.2 C cm^{-2} while the PEDOT and PEDOT-CNXL films were electrodeposited at 1.1 V to a charge density of 1 C cm^{-2}.

As the deposition solution for PANi-CNXL nanocomposites also contained HCl, the CNXLs were not the only counter anion present during the electrodeposition. The PANi-CNXL nanocomposites also contained large amount of Cl^- ions. It was thought that TGA may provide invaluable information about the composition of the PANi-CNXL composite, as the presence of the CNXLs may be identified from the TGA curves due to its lower decomposition temperature. PANi and PANi-CNXL samples for TGA were electrodeposited on a platinum wire as the working electrode for 10 hours.

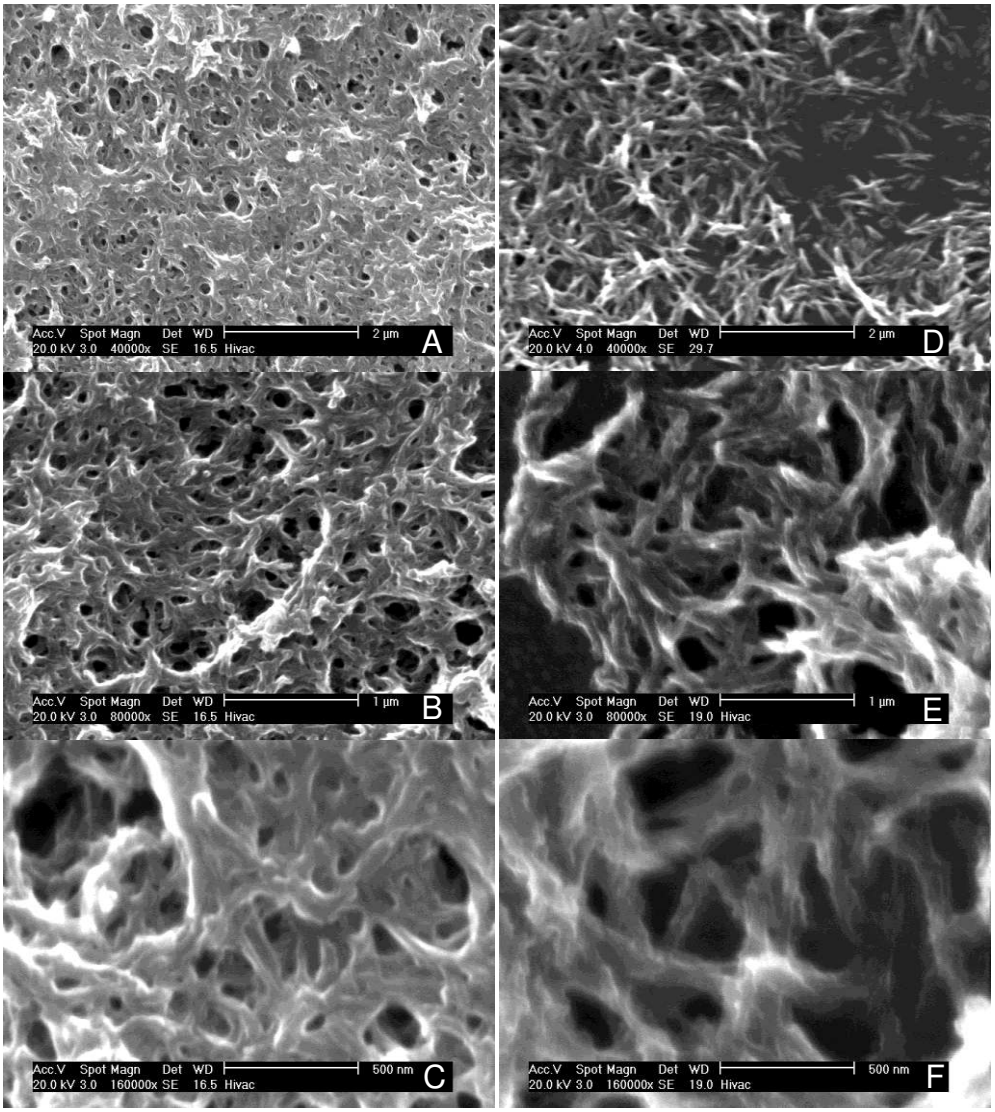

Figure 6.3. High magnification SEM images of (A, B and C) PANi and (D, E and F) PANi-CNXL. The films were electrodeposited at 0.9 V to a charge density of 0.2 C cm^{-2}.

Figure 6.4 shows the TGA traces for both the PANi and PANi-CNXL composite. Unexpectedly, both the traces overlap for almost the entire temperature range from the initial temperature (25 ˚C) to the temperature where complete decompostion occurred (ca. 700 ˚C). The results show that the quantity of CNXLs in the composite may be undetectably small. However, this behaviour may be explained from comparison with the PPy-CNXL nanocomposite (Section 3.3.2). When CNXLs are used as the sole counter

anion during the electrochemical co-deposition of PPy-CNXLs, the weight percentage determined using TGA was only 7.5 %. The case is different for the PANi-CNXL nanocomposite where the deposition solution contained large amount of Cl^- anions which also participated in the electrodeposition process. Furthermore, in the highly acidic environment of the PANi-CNXL deposition solution, the surface sulfonate groups on the S-CNXLs were protonated and therefore S-CNXLs were present as uncharged particles. In this case, the PANi-CNXL formed when the uncharged S-CNXLs diffused to the electrode surface and were coated by the PANi-Cl. As a result, the PANi-CNXL can be expected to contain predominantly PANi-Cl and only a small amount of CNXLs. Furthermore, as the TGA samples were prepared by electrodeposition for a long period due to the sample amount required, the long deposition time favoured formation of PANi-Cl due to diffusion limitation posed by the large S-CNXLs. Instead, the SEM samples were electrodeposited to a same charge density as those films that were characterised electrochemically. For these samples, the electrodeposition was typically completed within a few minutes (to a charge density of 0.2 C cm^{-2}). From this point of view, the SEM analysis may provide more useful information as those samples were more similar to those that were tested electrochemically.

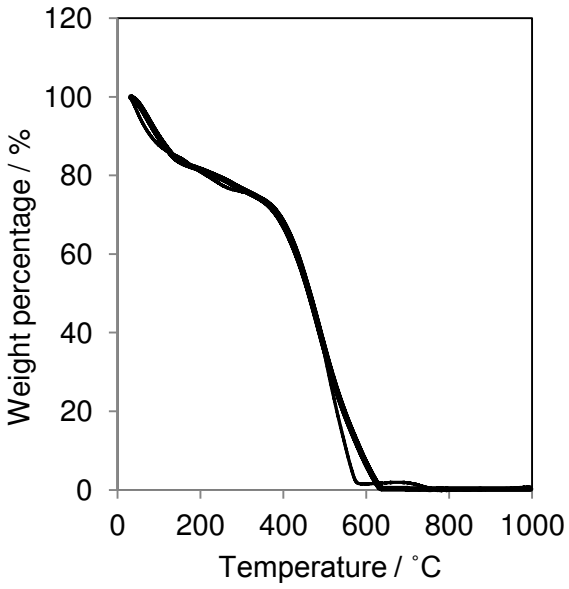

Figure 6.4. TGA traces for PANi (thin line) and PANi-CNXL (thick line). The temperature was ramped from 25˚C to 1000˚C at 10˚C min^{-1} in air.

At high magnification, the morphological differences between the PEDOT-CNXL composite and the PEDOT film was obvious (compare Figure 6.5B to 6.5A). It is also evident that the PEDOT-CNXL film showed a much more continuous structure, compared to the PEDOT. The PEDOT-CNXL film contained a high number of nanopores which were expected to improve the electrochemical performance.

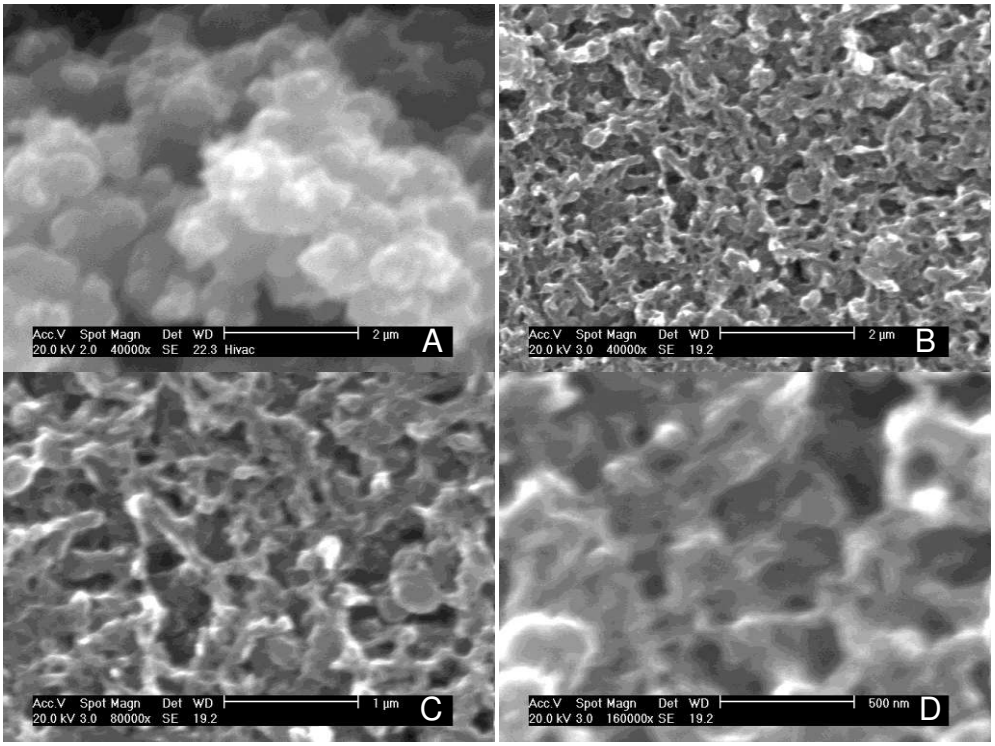

Figure 6.5. High magnification SEM images of (A) PEDOT and (B, C and D) PEDOT-CNXL. The films were electrodeposited at 1.1 V to a charge density of 1 C cm^{-2}.

6.3.3 Electrochemical characterisation of ECP-CNXL composite and ECP-X films

Figure 6.6A shows the CVs recorded at a PANi-CNXL film and a PANi film in 1 M HCl after a stable response was obtained for both the films. Both the CVs were rectangular in shape, showing fast redox switching at the potential limits and broad current waves.[16] At the more positive potential however, the PANi-CNXL film exhibited a higher current and showed a faster current increase as the potential switched at the positive limit. The S-CNXLs in the PANi-CNXL deposition solution were uncharged due to protonation in the highly acidic solution (0.5 M HCl). However, it was evident from the SEM analysis that although the S-CNXLs were uncharged, still the PANi-CNXL composites were formed using the same deposition methods as

for the PANi containing Cl^- only. It was the same case for the electrodeposited PANi-CNT composite films previously described in the literature.[3] Acid treated multi-walled CNTs were successfully co-deposited with PANi from an acidic deposition solution in which the surface functional groups on the CNTs were protonated, resulting in uncharged CNTs for the co-deposition process.[3] Thus any charged doping by the CNXLs on the PANi was unlikely. However, the current at the positive potential recorded at the PANi-CNXL film was significantly higher than that of the PANi. If the PANi-CNXL composite was only structurally different compared to pure PANi, the higher current may be explained as follows: As pure PANi was charged from neutral to positive (the anodic sweep), the accompanying counter anions ingress into the polymer will cause swelling of the polymer.[17] As the film swells, some of the interconnected pores may be blocked. As a result, the mass transfer barrier for subsequent anion ingress was increased. In that scenario, the PANi-CNXL composite was highly favourable. Firstly, the more open structure of the PANi-CNXL compared to the pure PANi, as indicated by the SEM characterisation, may allow more swelling (for the anodic sweep) while maintaining the interconnected porous network in the film for subsequent ion ingress. Secondly, the structural reinforcement offered by the strong CNXLs may reduce the extent of swelling and thus maintain a very open structure as the film charges.

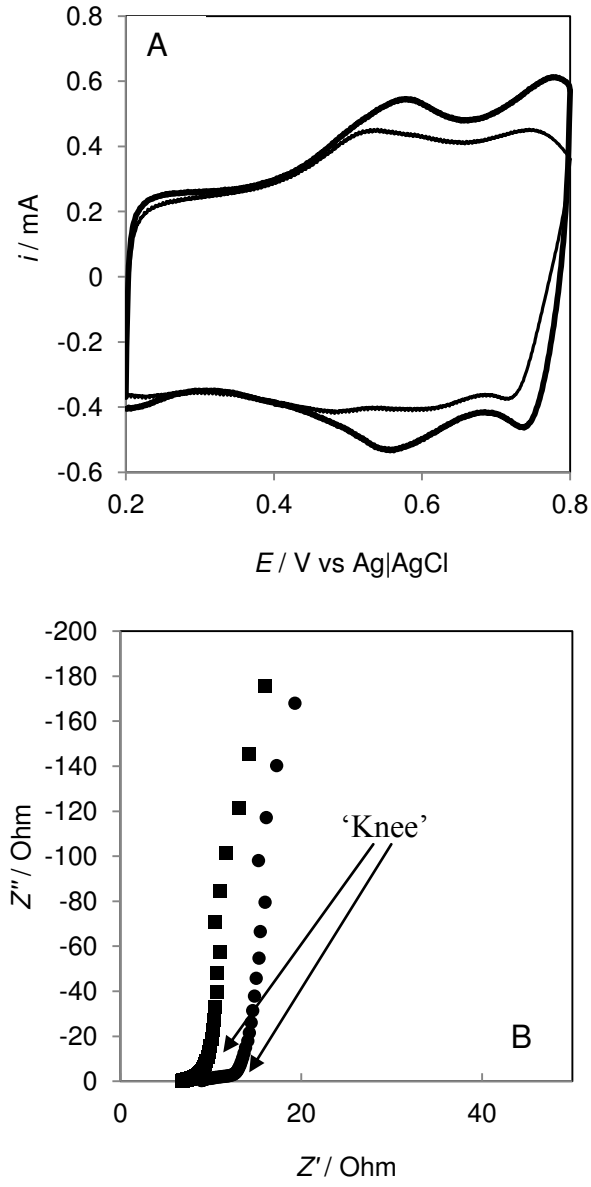

Figure 6.6. (A) Cyclic voltammograme obtained at an electrodeposited PANi-CNXL film (thick line) and a PANi film (thin line) in 1 M HCl. The potential limits were 0.2 V and 0.8 V and the scan rate was 0.25 V s^{-1}. (B) Nyquist plots obtained from EIS of the PANi-CNXL film (squares) and the PANi film (circles) at + 0.6 V in 1 M HCl with a potential amplitude of 5 mV. Each film was electrodeposited at 0.9 V to a charge density of 0.2 C cm^{-2}.

The effect of the facilitated ion transport in the PANi-CNXL film was evident from the electrochemical impedance spectroscopy (EIS) results. EIS was used to provide a more accurate estimate of the capacitance.[3] More

importantly, the EIS technique also allow easy comparison for the rate of charge transfer between the films from the Nyquist plots using the 'knee frequency' comparison, or by comparing the real impedance value as the films exhibit capacitive behaviour.

Figure 6.6B shows the Nyquist plots obtained from the EIS of a PANi-CNXL film and a PANi film. These plots show that both films exhibited typical diffusive-capacitive behaviour from high to low applied frequency. The knee frequency determined for the PANi-CNXL nanocomposite from the EIS data was 37 Hz compared to 21 Hz for the PANI film. The higher knee frequency at the PANi-CNXL film indicates that the charging of the PANi-CNXL can take place at much faster rate than the PANi. In the low frequency region, where the film had a capacitive behaviour (characterised by the near vertical Nyquist plot), the capacitance of the films were evaluated using the equation: $C = -1/(2\pi fZ'')$, where f = frequency (Hz) and Z'' = imaginary component of the complex impedance in ohms at frequency f. At 0.12 Hz, the capacitance of the PANi-CNXL film was 1.45 mF and that of the PANi film was 1.06 mF. Converting these values to the mass specific capacitance (considering weight of PANi only) gives a value 488 F g^{-1} for the PANi-CNXL composite and 358 F g^{-1} for the PANi film. The higher capacitance and the improvement on the charge transfer rate of the PANi-CNXL nanocomposite was ascribed to the more open porous structure of the nanocomposite compared to the PANi film.

Figure 6.7A shows the CVs recorded at a PEDOT-CNXL composite film and a PEDOT film. The CVs overlapped generally except at the negative

potential region where a significantly higher current was recorded at the PEDOT-CNXL film. For the PEDOT film, the lower current recorded at the negative potentials was due to a higher resistance of the film in its reduced state.[3] However, the higher current at the negative potentials of the PEDOT-CNXL film can be attributed to the presence of the large and immobile negatively charged CNXLs within the nanocomposite film (Chapter 3). As the CNXLs repelled electrons on the PEDOT chain electrostatically, the electron removal became easier and resulted in the observed negative shift of the oxidation potential.[3]

The EIS Nyquist plots in Figure 6.7B show that the PEDOT-CNXL film exhibited a more capacitive behaviour at low frequencies compared to the pure PEDOT film at -0.6 V, characterised by the significantly more vertical plot. At 0.6 V, the Nyquist plots almost overlap, indicating similar activity of the two films. The bending of the Nyquist plots at high frequencies was unusual for ECP materials. It was thought that they are most likely the inductive artefacts caused by the wire leads of the potentiostat that may have been damaged over many years of use.[18] The low frequency capacitance calculated from EIS data recorded at 0 V (data not shown), where the average current was observed at the CV (Figure 6.7A) and at 0.045 Hz, was 69 F g^{-1} for the PEDOT-CNXL and 58 F g^{-1} for the pure PEDOT. These values were slightly lower than those previously reported for PEDOT (Table 1.4, Chapter 1).

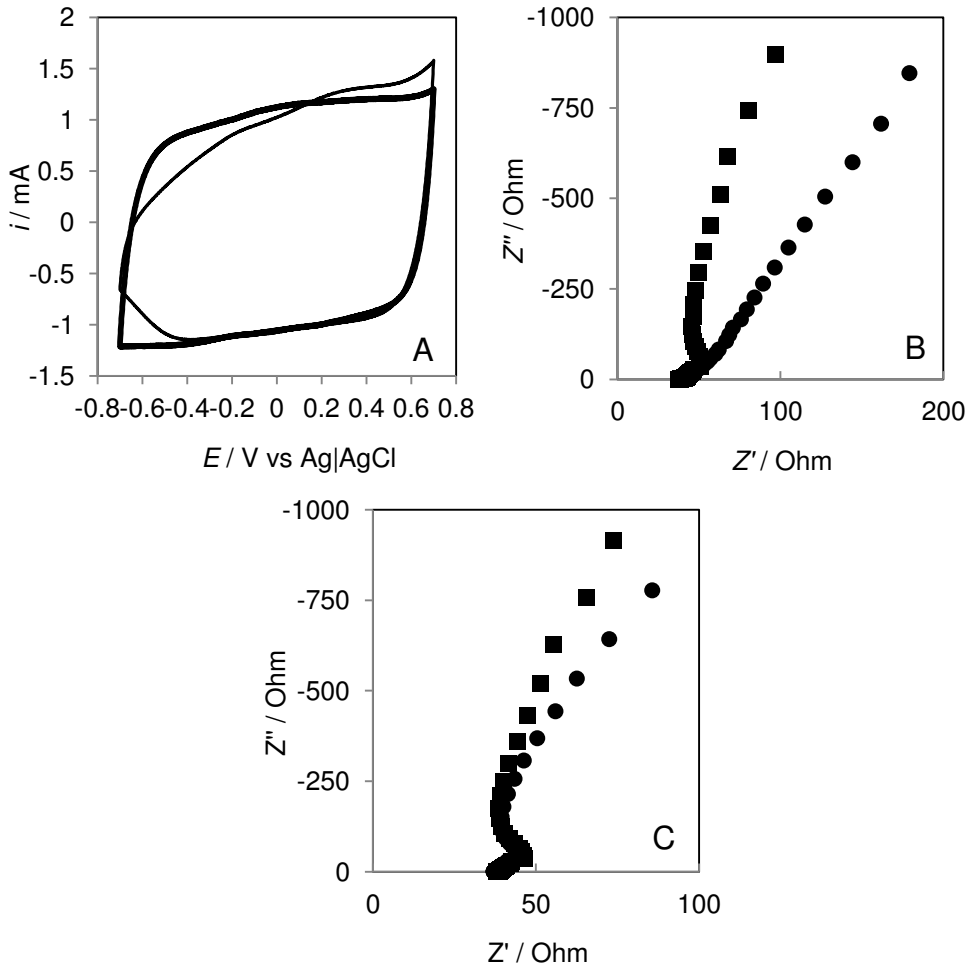

Figure 6.7. (A) Cyclic voltammograms obtained at an electrodeposited PEDOT-CNXL film (thick line) and a PEDOT film (thin line) in 2 M KCl. The potential limits were –0.7 V and 0.7 V and the scan rate was 0.25 V s^{-1}. (B and C) Nyquist plots obtained from EIS of the PEDOT-CNXL film (squares) and the PEDOT film (circles) at (B) -0.6 V and (C) +0.6 V in 2 M KCl with a potential amplitude of 5 mV. Each film was electrodeposited at 1.1 V until the charge passed was 1 C cm^{-2}.

To show that the reduction of the PEDOT-CNXL film was accompanied by cation ingression, CVs were recorded in electrolyte solutions containing large cations and large anions. Figure 6.8 shows CVs recorded at PEDOT-CNXL films in KCl, tetrapropylammonium chloride (TPACl) and potassium hexafluorophosphate (KPF_6). The CV currents recorded in KCl and KPF_6 (small cation but varied anion size) were significantly larger than the

current recorded in the TPACl solution (large cation). The oxidation onset for the PEDOT-CNXL film also shifted significantly to a more positive potential in the presence of bulky cations, suggesting that a larger barrier to cation transport when the PEDOT-CNXL was oxidised. This simple experiment confirms that the immobile, negatively-charged CNXLs were the cause of the higher current at negative potentials. As the PEDOT-CNXL nanocomposites were also deposited in the presence of a supporting electrolyte, these results also showed that the charge effects present on the CNXLs was significant for the electrochemical behaviour of the resulting PEDOT-CNXL films. However, it is unsurprising that the voltammetric response in the more positive potential range as shown in Figure 6.7A is similar for both the PEDOT and the PEDOT-CNXL, as the PEDOT-CNXL composite can be expected to also contain a significant amount of PEDOT-ClO_4.

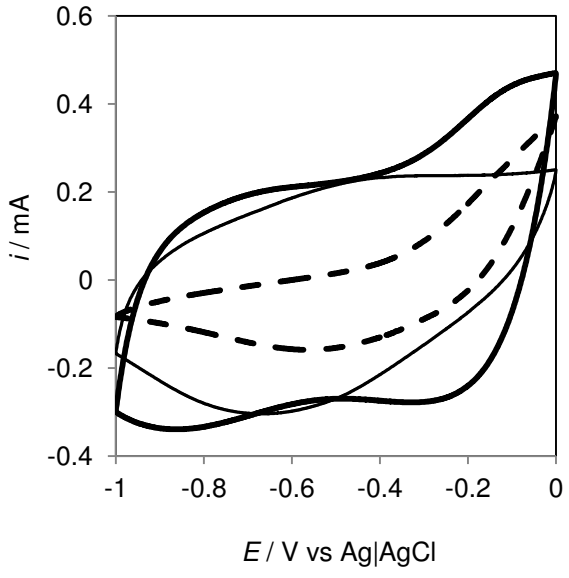

Figure 6.8. Cyclic voltammograms obtained at an electrodeposited PEDOT-CNXL in 0.1 M KCl (thick solid line), 0.1 M KPF_6 (thin solid line) and 0.1 M TPACl (thick dashed line). The potential limits were 0.0 V to -1.0 V and the scan rate was 0.25 V s^{-1}. The PEDOT-CNXL film was electrodeposited at 1.1 V until the charge passed was 1 C cm^{-2}.

6.3.4 Potential cycling stability tests of ECP-CNXL composite and ECP-X films

The potential cycling stabilities of both the PANi-CNXL and the PEDOT-CNXL films were compared to those of the PANi and PEDOT films. Galvanostatic charge/discharge curves were recorded using the films before and after they were subjected to the potential cycles. Figure 6.9A shows the galvanostatic charge/discharge curves for the PANi-CNXL and PANi film before the potential cycle test at current density of 1 mA cm^{-2}. The near symmetrical shapes of the charge/discharge curves recorded using both films show that both films had ideal capacitive behaviour within the potential limits. The longer time taken for the PANi-CNXL film to complete the charge/discharge cycle was due to the higher capacitance of the film, as capacitance C = I/(dE/dt), where I is the constant applied current, and dE/dt is the resulting change of potential with time to accommodate the current loading. As the potential limits were set for the galvanostatic experiment, the longer time required to complete a cycle means a higher capacitance of the film.

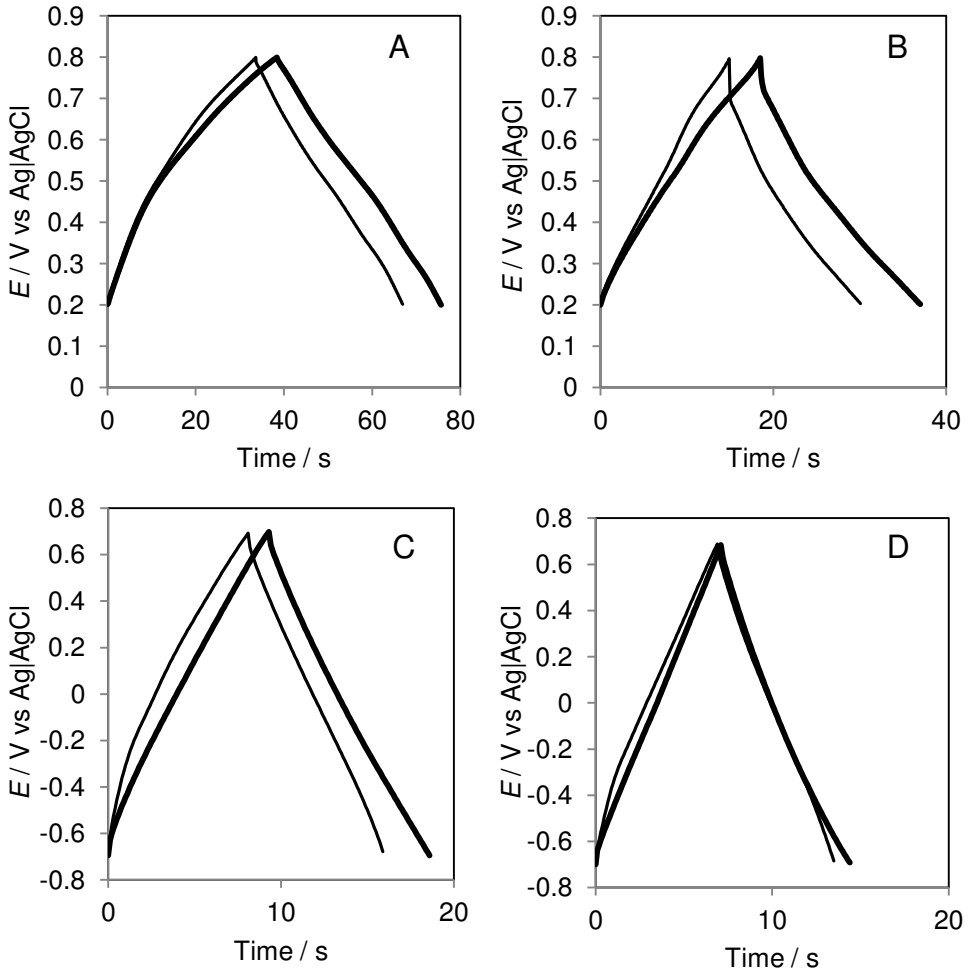

Figure 6.9. Galvanostatic charge/discharge curves obtained at (A and B) PANi-CNXL (thick line) and PANi (thin line) films at a current density of 1 mA cm^{-2} (A) before and (B) after subjecting the films to the potential cycling test. The potential limits were 0.2 V to 0.8 V and the electrolyte was 1 M HCl. The films were deposited at 0.9 V to charge densities of 0.2 C cm^{-2}. The potential cycle test comprised of 5000 potential cycles between 0.2 V and 0.8 V at a scan rate of 0.05 V s^{-1}. (C and D) Galvanostatic charge/discharge curves obtained at PEDOT-CNXL (thick line) and PEDOT (thin line) films at a current density of 10 mA cm^{-2} (C) before and (D) after subjecting the films to a potential cycle test. The potential limits were 0.7 V to -0.7 V and the electrolyte was 2 M KCl. The films were electrodeposited at 1.1 V to charge densities of 1 C cm^{-2}. The potential cycle test comprised of 5000 potential cycles between 0.7 V and -0.7 V at a scan rate of 0.25 V s^{-1}.

Figure 6.9B shows the charge/discharge curves recorded after the rapid potential cycling, recorded at the same current density and potential limits. Firstly, the time required to complete the charge/discharge cycles for both films reduced, due to the degradation of the films as they were repeatedly

cycled leading to capacitance loss. However, it was also obvious that the PANi-CNXL film remained more capacitive at the end of the potential cycling test. The capacitance of the PANi-CNXL film decreased by 51 % compared to 55 % for the pure PANi film. As this result was obtained from only one experiment, the slight stability improvement may be within the margin of experimental errors. Figure 6.9C shows the charge/discharge curves at current density of 10 mA cm^{-2} for the PEDOT-CNXL and the PEDOT film before the potential cycling test. The charge/discharge curves show that the PEDOT-CNXL film was more capacitive compared to the PEDOT film, agreeing with the EIS results discussed earlier. After the potential cycling test, the capacitance of both films had decreased (Figure 6.9D). However, in this instance it was the PEDOT-CNXL film which degraded slightly more (22 %) compared to the PEDOT film (15%). This effect may be due to the initially higher capacitance of the PEDOT-CNXL film. When subjected to the same potential cycling test the 'relative activity/stress' experienced by the PEDOT-CNXL film was higher than that of the pure PEDOT film due to more counter ion transport in the film. A similar trend was also observed for a previously reported PEDOT-CNT nanocomposite where the percentage capacitance degradation over a 5000 potential cycles was higher than for a pure PEDOT film.[3] Nevertheless the PEDOT-CNXL film was still more capacitive than the PEDOT film at the end of the potential cycling test. The results also show that PEDOT films were relatively more stable compared to PANi films which is attributed to higher electrochemical stability of PEDOT.[4,5]

6.3.5 PANi-CNXL film electrodeposited at high charge density

To show that the electrodeposited ECP-CNXL nanocomposites are suitable materials for the construction of high performance, cost effective supercapacitors, the mass specific capacitance reported for films deposited at low charge density is an insufficient indicator because it does not translate to device capacitance.[3,15,19] A good supercapacitor electrode material should not only have a high mass specific capacitance, but very importantly, it has to allow for a proportional increase of the electrode capacitance when a higher amount of the material (higher deposition charge for this case) is deposited on an electrode.[3] The measurement of interest in this case is the electrode specific capacitance, C_E, in the units of F cm^{-2}. High electrode specific capacitance is dependent on the ability to form a highly porous structure of the ECP/ECP composite that allows electrolyte access throughout the volume of the material as the redox charging process of ECPs depends on the chemical affinity of the counter ions.[3,15,16,19] In the case of the ECP-CNXL nanocomposites, it is important that the porous structure can be extended when films are synthesized at high deposition charge, and the success of electrodepositing a high C_E PPy-CNXL nanocomposite was demonstrated in Chapter 5.

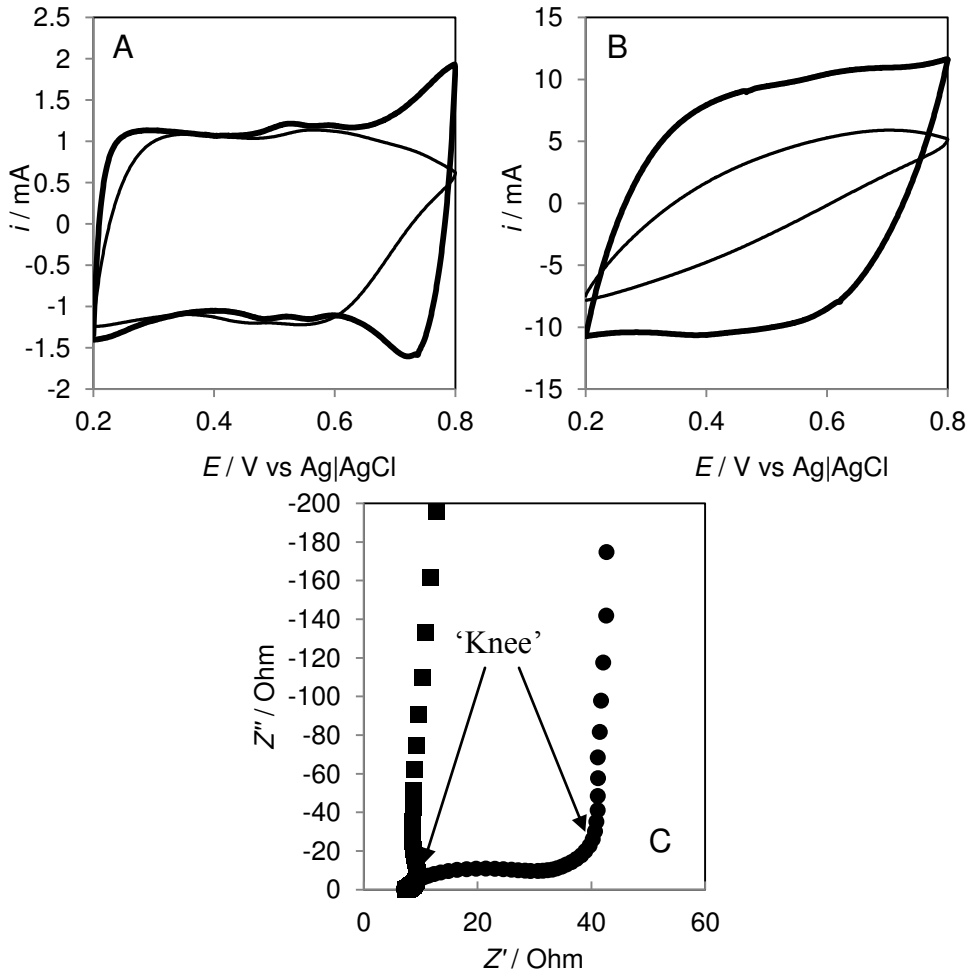

Figure 6.10. (A and B) Cyclic voltammograms obtained at an electrodeposited PANi-CNXL film (thick line) and a PANi film (thin line) in 1 M HCl. The potential limits were 0.2 V and 0.8 V and the scan rate was (A) 0.02 V s^{-1} and (B) 0.25 V s^{-1}. (C) Nyquist plots obtained from EIS of the PANi-CNXL film (squares) and the PANi film (circles) at + 0.6 V in 1 M HCl with a potential amplitude of 5 mV. Each film was electrodeposited at 0.9 V to a charge density of 10 C cm^{-2}.

Figure 6.10A shows the slow scan rate CVs (at 0.02 V s^{-1}) recorded at a PANi-CNXL film and a PANi film electrodeposited at a charge density of 10 C cm^{-2} (50 times the charge employed for the films used in Figure 6.6). The CVs showed similar features compared to the CVs shown in Figure 6.6. The current increased vertically for the PANi-CNXL at the potential limits showing the fast charging capability of the PANi-CNXL film, whereas the current

increased much slower in the case of the PANi film. The relatively fast charging effect on the PANi-CNXL film was more striking when the same comparison was made for CVs recorded at faster scan rates (0.25 V s^{-1} in Figure 6.10B). At this scan rate, the PANi-CNXL film still produced a near rectangular response, suggesting that the film was highly capacitive even at a relatively high scan rate. In contrast, the PANi film did not respond to fast charging, as the slope of the CV indicates resistive behaviour. At 0.02 V s^{-1}, the capacitance of the films was evaluated using the equation C = I/(dE/dt), where I is the average current, and dE/dt is the potential scan rate. The mass and electrode specific capacitance for the thick PANi-CNXL film was 440 F g^{-1} and 2.07 F cm^{-2}, respectively. For the thick PANi film, the mass and electrode specific capacitance was 285 F g^{-1} and 1.34 F cm^{-2}, respectively. It is important to note that the average CV current, normalised to mass, for the PANi-CNXL film was 8.8 A g^{-1}, which was very high for films of this thickness and which displayed such a high C_E. The mass specific capacitance of the thick PANi-CNXL agrees with the value obtained using the thin films (440 F g^{-1} vs 488 F g^{-1}), showing a proportional increase of electrode capacitance at higher deposition charge density. However, the mass specific capacitance of the thick PANi film decreased significantly from 358 F g^{-1} reported for the thin film in Figure 6.6. The possibility to form the extended porous structure for the PANi-CNXL composite, similar to PPy-CNXL (Chapter 5), was attributed to the strength of the CNXL which prevented the structure from collapsing in the deposition process. Meanwhile, PANi fibres were mechanically weak and were thus not able to support an extended highly porous structure. Figure 6.10C shows the EIS Nyquist plots for the thick

PANi-CNXL and PANi film. It is evident that the PANi-CNXL can be charged more efficiently judging from the position of the knee occuring at significantly lower impedance value than that of the pure PANi film. The knee frequency determined from the EIS results for the thick PANi-CNXL film was 5.5 Hz compared to 0.3 Hz for the pure PANi film. The results show that the thick PANi-CNXL film can be charged at at least an order of magnitude faster than the pure PANi film. This effect was also manifested in the CVs shown in Figure 6.10A and 6.10B.

Numerous attempts to form the PEDOT-CNXL film at a high deposition charge density were unfortunately not successful as initially anticipated. The thick PEDOT-CNXL film (deposited for a charge density of 10 C cm^{-2}) formed a thick gel rather than a robust film when removed from the deposition solution upon completion, and had a poor voltammetric response. This effect may be due to the water/acetonitrile mixture used for the preparation of the deposition solution. In the water/acetonitrile mixture deposition solution, the EDOT monomers and the CNXL may be preferentially dissolved/dispersed in separate phases although the solution was visibly single-phased. Assuming that the EDOT monomers were accompanied by many acetonitrile molecules, when the monomers were polymerised on the electrode surface, the polymerisation will thus leave the solution layers adjacent to the electrode surface enriched in acetonitrile. The CNXLs then have to travel through the acetonitrile-rich phase to complete the charge balancing process on the electrode surface. The effect may be less pronounced for the deposition of a film at low deposition charge. However, when films were electrodeposited for a long period of time, the acetonitrile built up at the areas adjacent to the

electrode surface would have formed a layer. Therefore, the CNXLs could not travel through to complete the charge balancing process. The formation of the gel was thus due to the CNXL 'crashing out' from the stable water dispersion into the acetonitrile rich layers. Similar effects were also reported for the unsuccessful formation of thick PEDOT-CNT nanocomposites.[3,20]

6.4. Conclusions

CNXLs from cotton were used for the electrochemical synthesis of PANi-CNXL films and PEDOT-CNXL nanocomposite films. CNXLs were incorporated into the nanocomposites during the electrochemical deposition of each conducting polymers. In the case of the PEDOT-CNXL nanocomposite, the negatively charged CNXLs were incorporated as the dopant anion. More interestingly, PANi-CNXL can be deposited from a solution containing uncharged CNXLs. In this case, the CNXLs only affected the structure and morphology of the resulting PANi-CNXL films. Both the ECP-CNXL nanocomposites showed higher capacitance and faster charge/discharge rates compared to the respective ECP-X, due to the high porosity (and a more open structure in the case of PANi-CNXL) of the nanocomposites. Moreover, the PEDOT-CNXL nanocomposite was capacitive at negative potentials where pure PEDOT was resistive, due to the negative charge on the immobilised CNXLs within the nanocomposite. Both the PANi-CNXL and the PEDOT-CNXL were also highly stable when subjected to a rapid potential cycling test. Thicker PANi-CNXL nanocomposite films also exhibited ideal capacitive behaviour and highly responsive to fast charging (440 F g^{-1} and 2.07

F cm^{-2}, at average mass-specific current of 8.8 A g^{-1}). In contrast, the thick pure PANi film was much more resistive when subjected to the same tests. Not only was the thick PANi-CNXL film significantly more capacitive, the rate of charge transfer for the thick PANi-CNXL film was more than an order of magnitude higher than that of the thick PANi film. The ability to form an extended porous structure for the PANi-CNXL films at high deposition charge, which facilitates ion and solvent movement, was attributed to the strength of the CNXLs as the composite filler. Unfortunately the scaling up of PEDOT-CNXL was unsuccessful due to complications of the solvent system employed to dissolve the EDOT monomer while maintaining a dispersion of the O-CNXLs. The work in this chapter compliments the previous in Chapter 3, 4 and 5, and underlines the strength of CNXLs as an extremely promising material for fabrication of conducting polymer composites for supercapacitor applications.

6.5. References

1. A. J. Heeger, Chem. Soc. Rev., 2010, **39**, 2354-2371.
2. V. Gupta and N. Miura, Mater. Lett., 2006, **60**, 1466-1469.
3. C. Peng, J. Jin and G. Z. Chen, Electrochim. Acta, 2007, **53**, 525-537.
4. K. Lota, V. Khomenko and E. Frackowiak, J. Phys. Chem. Solids, 2004, **65**, 295-301.
5. R. Liu, S. Il Cho and S. B. Lee, Nanotechnology, 2008, **19**.
6. B. L. Groenendaal, F. Jonas, D. Freitag, H. Pielartzik and J. R. Reynolds, Adv. Mater., 2000, **12**, 481-494.
7. E. Frackowiak, V. Khomenko, K. Jurewicz, K. Lota and F. Beguin, J. Power Sources, 2006, **153**, 413-418.
8. C. Peng, S. W. Zhang, D. Jewell and G. Z. Chen, Prog. Nat. Sci., 2008, **18**, 777-788.
9. V. Khomenko, E. Frackowiak and F. Beguin, Electrochim. Acta, 2005, **50**, 2499-2506.
10. B. E. Conway, V. Birss and J. Wojtowicz, J. Power Sources, 1997, **66**, 1-14.
11. Z. P. Deng, D. C. Stone and M. Thompson, Analyst, 1997, **122**, 1129-1138.
12. C. R. Alves, P. Herrasti, P. Ocon, L. A. Avaca and T. F. Otero, Polym. J., 2001, **33**, 255-262.
13. Z. S. Zhao and P. G. Pickup, J. Electroanal. Chem., 1996, **404**, 55-60.
14. H. Ding and S. M. Park, J. Electrochem. Soc., 2003, **150**, E33-E38.
15. G. A. Snook, C. Peng, D. J. Fray and G. Z. Chen, Electrochem. Commun., 2007, **9**, 83-88.
16. E. Frackowiak and F. Beguin, Carbon, 2001, **39**, 937-950.
17. H. Yan, K. Tomizawa, H. Ohno and N. Toshima, Macromol. Mater. Eng., 2003, **288**, 578-584.
18. S. Fletcher, Electrochem. Commun., 2001, **3**, 692-696.
19. M. Hughes, G. Z. Chen, M. S. P. Shaffer, D. J. Fray and A. H. Windle, Chem. Mater., 2002, **14**, 1610-1613.
20. C. Peng, G. A. Snook, D. J. Fray, M. S. P. Shaffer and G. Z. Chen, Chem. Commun., 2006, 4629-4631.

Chapter 7. Final conclusions

The work discussed in this thesis concerns the use of nanomaterials from biomass (cotton), in the form of cellulose nanocrystals (CNXLs), for making nanocomposites with electronically conducting polymers (ECPs) for electrochemical supercapacitors with improved stability and performance. Specifically, a range of ECPs such as polypyrrole (PPy), polyaniline (PANi) and poly-(3,4-ethylenedioxythiophene) (PEDOT) were chosen for making such composites because of their relative high specific capacitance and also because of the ease of their electro-synthesis. The utilization of CNXLs in these nanocomposite materials is aimed at making a class of ECP nanocomposites as alternatives to those containing highly conducting support materials such as carbon nanotubes (CNTs) and graphene. Based on the understandings developed from the ECP-CNT and ECP-graphene nanocomposite materials, the non-conductivity of the CNXLs poses a major challenge and could limit the ECP-CNXL nanocomposite performance. Aside from the conductivity issue, it can be said that CNXLs may be just as ideal as either CNTs or graphene for the fabrication of ECP nanocomposites due to their size, strength, surface chemistry and high aspect ratio. Consequently, this work showed that the ECP support does not need to be conductive for high performance. This is a major finding for the ECP-based supercapacitor field.

The different ECP-CNXL nanocomposites were electrodeposited from solutions containing the corresponding monomers and dispersed CNXLs. Electrodeposition was chosen as the fabrication method due to the ease of controlling the deposition amount and also the ability to form a consistent composite structure which is ideal for lab-scale characterisation and device electrode fabrication. During the electrodeposition process, the positive charge on the deposited ECPs required charge balancing by anionic species from the solution. As the CNXLs were negatively charged, they were simultaneously incorporated into the polymer matrices as the charge balancing component, i.e. they were co-deposited during the electrodeposition process. The exception was when PANi-CNXL was also co-electrodeposited when the CNXLs were uncharged. As the CNXLs were co-electrodeposited with the ECPs, they formed the backbone of the nanocomposite structure, which resulted in a significantly more porous structure in comparison with pristine ECPs electrosynthesized using small anions for charge balancing. Such porous structures were highly favourable for enhanced capacitance and stability performance due to the facilitated electrolyte transport which resulted in higher capacitance and less volumetric stress for higher stability.

Among all the ECP-CNXL nanocomposites reported in this thesis, PPy-CNXL nanocomposites were the most extensively studied. This is due to the relative ease of fabrication, as the monomers are soluble in de-ionised water. Secondly, it is because PPy composites are the most widely studied ECP for supercapacitor applications, which makes it a good model for study. The capacitances of the PPy-CNXL nanocomposites have been studied in detail using thin films formed using low deposition charge and thick films

formed using high deposition charge. Remarkably, the capacitance of the PPy-CNXL film increased linearly with deposition charge, resulting in constant mass-specific capacitance for deposition charges over 20 C cm^{-2}. As a result, the electrode area specific capacitance of the PPy-CNXL reached unprecedented values of 1.54 F cm^{-2}, measured using electrochemical impedance spectroscopy (EIS), compared with a previous high of 1 F cm^{-2} achieved using a PPy-CNT nanocomposite. The cause of such a high film capacitance is ascribed to the strength of the CNXLs which supported the composite film structure during the prolonged electrodeposition process. Attempts to form pristine PPy films with the same high deposition charge were unsuccessful, as the film growth was inconsistent.

In conjunction with the porous structure, the anionic doping by the CNXLs in the PPy-CNXL nanocomposites also favours more rapid charge transfer. This was characterised by the instantaneous nucleation and growth during the switching from an insulating state to the conducting state of the PPy-CNXL nanocomposites. In comparison, the transition from insulating to conducting state for PPy-Cl proceeds by the slower progressive nucleation and growth pathway. Remarkably, the performance of the PPy-CNXL nanocomposites was comparable to that of a PPy-CNT nanocomposite fabricated using a similar procedure. Moreover, the PPy-CNXL nanocomposite performed better in a durability test. This comparison shows that conductivity of the ECP nanocomposite filler is not necessary. This finding raises very interesting fundamental question, and could challenge current understanding which was developed primarily from previously reported ECP-CNT work. Nevertheless in this thesis, the capacitance, and

rapid charge removal corresponds very well with the structure and morphology of the film, and perhaps they are the main factors for high performance of ECP nanocomposite films. Consequently, a laboratory protype supercapacitor was assembled from two high capacitance PPy-CNXL and the durability of this protype was tested for 50000 cycles which in the end it retained half of its initial capacity. That was very good performance as usually supercapacitors based on ECPs only last a few thousand cycles. Moreover, the example was the first of a supercapacitor device assembled from high performance ECP nanocomposites containing CNXLs, and which shows the promising prospects of such nanocomposites for such applications.

The PANi-CNXL and PEDOT-CNXL composites reported in the last chapter shows that high performance was not unique only to PPy-CNXL and, in fact, apparently any combination of the commonly used high capacitance ECP with CNXLs can be a synergistic one. In particular, the PANi-CNXL showed the similar behaviour as the PPy-CNXL. In this case, the CNXLs were uncharged due to protonation of the CNXL surface groups in the highly acidic mixture used to dissolve the ANi monomer. Even so, the PANi-CNXL composite still produced a remarkable performance. For example, a thick PANi-CNXL film showed mass-specific capacitance of 440 F g^{-1} and corresponding electrode area specific capacitance 2.07 F cm^{-2}, at average mass-specific current of 8.8 A g^{-1}. This combination of values is unprecedented. Unfortunately the same cannot be said for the PEDOT-CNXL as attempts to synthesize thick films were unsuccessful, due to problems posed by solvent separation during the deposition.

Last but not least, the combination of ECPs with CNXLs in this thesis is novel, and noble. Such materials are not only fundamentally interesting but most importantly they are practical, and certainly offers a more environmentally friendly, and cost effective version of ECP nanocomposites for supercapacitor applications in the future.

Chapter 8. Future work

In this thesis, I have reported the success of making ECP-CNXL nanocomposites for the supercapacitor applications and I have done so with a very thorough study. However, it is only fair to say that there are always areas that I think can be further improved based on the current work. So the following are my suggestions for immediate attention:

1. To optimize of the wt% of O-CNXL in the dispersion for the fabrication of PPy-CNXL.
2. To study the nucleation and growth mechanism present for the redox charging of ECP-CNT nanocomposites.
3. To fit the EIS data based on the finite space Warburg (Z_{FSW}) element.
4. To look at other deposition methods for the fabrication of thick PEDOT-CNXL nanocomposites.